Exploring Anisotropic Noise and Fast Gates with Superconducting Qubits

by

David A. Rower

B.S., University of California, Santa Barbara, 2019

Submitted to the Department of Physics
in partial fulfillment of the requirements for the degree of

Doctor of Philosophy in Physics

at the

MASSACHUSETTS INSTITUTE OF TECHNOLOGY

February 2025

Authored by:	David A. Rower Department of Physics December 2, 2024
Certified by:	William D. Oliver Professor of EECS and Physics Thesis Supervisor
Certified by:	Riccardo Comin Professor of Physics Thesis Supervisor
Accepted by:	Lindley Winslow Associate Department Head of Physics

Exploring Anisotropic Noise and Fast Gates with Superconducting Qubits

by

David A. Rower

Submitted to the Department of Physics
on December 2, 2024 in partial fulfillment of the requirements for the degree of

Doctor of Philosophy in Physics

ABSTRACT

Rapid recent progress in the engineering of quantum systems across multiple platforms has enabled quantum science at never-before-seen precision and scale, and may yield useful quantum technology. However, two major challenges slow such progress: (1) decoherence from interactions between target systems and uncontrolled external degrees of freedom, and (2) errors in the control of target systems, which often arise from physics beyond the models used to design control protocols. We report on three novel results addressing both coherence and control, utilizing superconducting qubits.

Our first result is the characterization of superconducting qubit flux noise, a primary source of decoherence, under the influence of weak, in-plane magnetic fields. We reveal two trends which serve as a novel experimental benchmark for microscopic theories of flux noise: (1) a $1/f$ to approximately Lorentzian transition in the noise power spectral density below 1 Hz, and (2) noise suppression above 1 MHz.

Our second result is the suppression of coherent qubit-control errors induced by the counter-rotating component of strong, linearly-polarized drives. We establish two complementary protocols for mitigating such errors, which previously limited the speed of single-qubit gates for low-frequency qubits. The first protocol realizes circularly-polarized drives in circuit quantum electrodynamics. The second protocol—commensurate pulses—uses pulse-timing restrictions to homogenize counter-rotating errors and enable their mitigation with conventional calibration routines. With commensurate pulses, we demonstrate world-class single-qubit gate fidelities reliably exceeding 99.997%.

Our third result is the observation of a novel signature in the decoherence dynamics of qubits subject to anisotropic transverse noise. Through injected noise experiments with a fluxonium qubit, we directly observe time-domain state-purity oscillations at twice the qubit frequency arising from the intrinsic qubit Larmor precession. We probe the oscillation dependence on noise anisotropy, lab-frame orientation, and power spectral density. Such oscillations are a result of physics beyond standard qubit-decoherence models within the rotating-wave approximation, and were previously unobserved in experiment.

Thesis supervisor: William D. Oliver
Title: Professor of EECS and Physics

Thesis supervisor: Riccardo Comin
Title: Professor of Physics

Acknowledgments

This work is the culmination of much more than just my last several years in Cambridge. I acknowledge all the family, friends, mentors, teachers, and others I have had in my journey, academic and otherwise. To be specific…

I thank my advisor Will. EQuS is a magical group: I see it as a reflection of Will's friendly spirit and dedication to clarity and enjoying (while not short-cutting) the process. I thank Will for inspiring with his leadership, cultivating the environment of EQuS, and offering insightful perspectives on physics, writing, presenting, career advice, and all else. I especially appreciate Will's guidance in times of deep stress when I lost touch with my own common sense. Along with Will, I thank Simon, Terry, Jeff, Kyle, and Joel, all of whom are integral to the identity and spirit of EQuS and functioned as kind mentors throughout my PhD. Beyond scientific support, I relied on their encouragement and advice during unsure times. I especially thank Terry and Will for their thorough feedback in editing this thesis. Also integral to the EQuS family, I thank Mirabella, Chihiro, and Lenore, who facilitated all the details that allowed me to glide through MIT with no hitches.

Now, I thank the other professors involved in my PhD. Riccardo, also my advisor, consistently provided positive support: I often reflect on my arrival to MIT and his wise advice to listen to myself when I was excited by many others' ideas and didn't yet have a clear direction. I thank the members of my thesis committee, Martin and Pablo, for their support and helpful feedback through the dissertation process. I also thank the professors at universities beyond MIT I have had the opportunity to discuss science with and gather feedback from: Rogério de Sousa (and his student José Alberto Nava Aquino) and Lorenza Viola.

I thank Dr. B, who helped me find the spirit of physics during my formative years as a student at UCSB. This spirit—that of community, fun, and selfless pursuit of understanding—has become the foundation of my relationship with physics. As he shared this wonderful spirit with me, I have aspired to share it with others, especially mentees.

On to my friends and collaborators. It takes a village to raise a scientist. The village I was raised in, EQuS, was vibrant. My first interactions were with Leon and Jochen, who had infinite patience for my questions (e.g., "what's that squiggle in the GDS file?"). Then came Youngkyu, who introduced me to fridge handiwork, taught me proper experimental habits, and bestowed upon me L3. Next was Bharath, who took me under his wing as we were building the new lab space 13-3080, and acted as my PhD guardian angel. His pragmatic advice is worth its weight in gold. I had the pleasure of being raised in 3080 alongside Aziza, who brought energy to the lab that made the work exciting and enjoyable every day.

I thank those who played a major role when I was first figuring out how to run my own experiment. These people provided selfless support that helped me find my footing: Kyle, Jochen, Bharath, Antti, Leon, Patrick, Young, Tim, and others. During this time, I had the pleasure of mentoring Lauren Li, who quickly mastered the practices of lab research, and as quickly outgrew the calculations I gave her to work on. As the project got exceedingly heavy to bear on my own with failure after failure to find a signal, Lamia joined the effort. I am deeply grateful for her sanity-preserving personal and scientific support, which resulted in the project becoming my first paper. I thank Jeff for his crucial role editing this paper (and all others): his feedback significantly improved my scientific writing.

After that experiment, I began to work with Leon. Leon's setup was the gift that kept on giving, a reflection of his high-quality work, enabled by his deep understanding of physics. Doing science with him is a true joy. Among other things, he taught me how to approach gates, and helped me find my Bloch-sphere intuition at a level that enabled our world-class single-qubit gates and my final project on anisotropic noise. Helin joined as Leon left, and immediately began to help me as a sounding-board for my fruitless attempts to achieve five nines fidelity. He is the one who first suggested the idea for commensurate pulses, and I therefore believe he is largely to blame for the success I encountered in the last 1.5 years of my PhD. In a similar spirit, I thank Max, Junyoung, Lamia, Miguel, Jorge, Patrick, Ilan, and Reouven, all of whom were always available to entertain my questions and ideas for any and all projects. Beyond their availability, they positively received my enthusiasm always, and shared it with me. I especially thank Miguel and Jorge, whose passion for error correction and thorough knowledge inspired and fed new scientific interests.

After the gate project finished and I was in the midst of job hunting, Kotaro arrived. I thank Kotaro for his dedication to our brief but fruitful collaboration, which was a highlight of my PhD. His positive spirit and ability to adapt quickly as our project developed gave rise to a wonderful synergy in our working together. The miraculous match of our experimental personalities led to a miraculously fast and fun experiment.

Beyond those I have had the chance to work closely with, I thank all members of EQuS, old and new, for providing community. I have many wonderful memories from trips, socials, celebrations, wild Wednesdays, etc. I am especially fond of the house parties during my first few years when I was making my first friends in the group (and everyone was re-learning how to socialize post-COVID). This is where I learned that grad school could be fun. Thanks especially to Sarah, Amir, John, Bharath, and T. Tim.

Throughout my journey, I had the wonderful priviledge of working with some of my close friends. My friends-turned-collaborators Sam, Dolev, Chris, Robbie, and James constantly inspire me to realize a deeper understanding of physics, keep me excited with the discussion of new ideas and perspectives, and offer unwavering positive support, both professionally and personally. Dolev's perspective and advice was integral to my development as a scientist. Sam's humbling pursuit of understanding shaped my interaction with knowledge.

I thank all other friends for helping me maintain perspective and sanity, keeping me grounded in the low times and celebrating in the high: Ben, Daniel, Jasmin, Morgan, Caolan, Paul, Oriol, Nisarga, Maddie, Marcin, Nishad, Mark, Kenny, and many others.

I especially thank Lamia, whose role in this journey was uniquely unique. She has been a steadfast source of love and support. This is only the beginning of a wonderful story.

Last, I thank my family. This thesis is the fruit of a lifetime of opportunities thanks to them. A lifetime I intend to make the most of, to honor grandpa. I know he would have loved to see this. Thanks mom, dad, Nathan, grandma, Bella, and Levy.

Contents

List of Figures

List of Tables

Chapter 1

Introduction

> The behavior of things on a very tiny scale is simply different. An atom does not behave like a weight hanging on a spring and oscillating. Nor does it behave like a miniature representation of the solar system with little planets going around in orbits. Nor does it appear to be somewhat like a cloud or fog of some sort surrounding the nucleus. It behaves like nothing you have seen before.
>
> *Richard P. Feynman* [1]

Quantum mechanics provides a description of nature at small scales. The most basic quantum system is one comprising two states, referred to as a quantum bit or "qubit." Qubits are likely the most studied quantum system and are extremely well understood. In this thesis, we even further augment this understanding through access to novel regimes with engineered (rather than naturally abundant) quantum systems comprising superconducting circuits. Our results are directly applicable to the ambitious present-day quest to build a quantum computer—a machine that stores and manipulates qubits, as a conventional computer stores and manipulates bits—with the promise of enabling science and technology that are otherwise inaccessible. The aim of this chapter is to motivate this quest and frame our contributions.

We will start by introducing quantum physics and the many-body problem. Then, we will introduce the idea of quantum computation as (among other things) a promising solution to this problem. We proceed with the present-day progress towards building a quantum computer and its associated challenges. Armed with this perspective, we will highlight the three core results of this thesis in their respective contexts. In the following chapters, we will develop a more rigorous picture to enable appreciation of the results in full detail.

1.1 Quantum Physics and the Many-Body Problem

At the beginning of the 20th century, a few outstanding physical phenomena (most prominently the light emitted by hot objects [2], the ejection of electrons from irradiated materials [3], and the structure of absorbed and emitted light from atoms [4]) were irreconcilable with the established physics of the time, namely classical electrodynamics given by Maxwell's equations. Quantum mechanics [5] was born to explain these phenomena, but came with far-reaching implications that wildly departed from the prior intuition of classical physics. After decades of development and experimental success, quantum mechanics took its place as the fundamental description of nature on the scale of atoms. The most remarkable aspects of quantum mechanics are the action of measurement, which irreversibly changes the state of a system, and the appearance of entanglement, i.e., correlations between subsystems such that measurements of one instantaneously affect the other.

Although the rules of quantum mechanics can be written down readily, the behavior of quantum systems is only well understood in a relatively small (but rapidly growing) number of model scenarios (e.g., the famous hydrogen atom). As stated so well by Anderson, more is different [6]: writing down a fundamental set of rules does not yield a full understanding of a system's behavior at larger sizes and increasing complexity, i.e., its emergent behavior. For quantum physics, the investigation of such behavior is called the **many-body problem**. This problem lies at the heart of understanding how quantum-mechanical effects give rise to remarkable large-scale behaviors. One of the most intriguing examples of this is high-temperature superconductivity, the discovery of which in 1986 [7] won the following year's Nobel prize. To this day, this phenomenon has eluded theoretical understanding due to its many-body nature. Such an understanding might enable the engineering of even higher-temperature superconductors, with the potential to revolutionize electronic technology[1]. Beyond this example, many-body physics plays a key role in various scientific fields including quantum chemistry, condensed-matter physics, atomic physics, and nuclear physics. Although approximate methods have been developed to understand many-body physics in various contexts [8, 9], theoretical methods are limited in their applicability, and algorithmic approaches with conventional computers are limited by computational resources [10, 11].

To understand why the many-body problem cannot be solved with conventional computers, we give a simple argument here before diving into the details of quantum mechanics in Chapter 2. The state of a system of N classical bits can be specificed with N binary digits as $k_0k_1\cdots k_N$, where $k_i \in \{0,1\}$. In contrast, the state of a quantum system of N qubits generally takes the form

$$|\Psi\rangle = \alpha_{00\cdots 00}\,|00\cdots 00\rangle + \alpha_{00\cdots 01}\,|00\cdots 01\rangle + \cdots + \alpha_{11\cdots 11}\,|11\cdots 11\rangle\,, \tag{1.1}$$

where $\alpha_x \in \mathbb{C}$: the N-qubit system is specified with 2^N complex numbers. The memory resources required to store the state of a quantum system grow exponentially with its size, rather than linearly as in the classical case.

Although a computer using classical (binary) bits can simulate quantum systems in principle, the exponential memory complexity generally prevents the simulation of large quantum systems[2]. This limitation presents an intriguing opportunity.

---

[1] We note that current electronic technology already relies on a quantum-mechanical device, the semiconductor-based transistor.

[2] Entanglement plays a key role in the computational complexity of quantum systems. We can see this by considering N qubits with no entanglement, which is described by a state of the form $|\Psi\rangle = (a_0\,|0\rangle + b_0\,|1\rangle) \otimes (a_1\,|0\rangle + b_1\,|1\rangle) \otimes \cdots \otimes (a_N\,|0\rangle + b_N\,|1\rangle)$. Such an unentangled state requires only $2N$ complex numbers to specify, rather than 2^N as in the entangled case. Leveraging the entanglement structure of specific systems can alleviate the classical resources required to simulate them [10].

1.2 Quantum Computers

A large quantum system with sufficient measurement and control capabilities could be programmed to evolve in a way that would, at most, take exponentially more resources to classicaly compute. One could view the quantum evolution as performing a computational task, and design evolutions to solve specific problems [12, 13]. Such a machine is called a **quantum computer**, and its evolution (including state preparation and measurement) a **quantum computation**. Ref. [14] explicitly considers the requirements for implementing such a machine, referred to as the **DiVincenzo criteria**.

Beyond probing many-body physics (i.e., performing quantum simulations [15]), a quantum computer could be used to perform other algorithmic tasks with speedup over classical computers [16, 17]. The most celebrated example of this idea is Shor's algorithm [18] for factoring integers on a quantum computer with exponential time advantage over the best known classical algorithms. This application is particularly motivating, since one of the most widely used cryptosystems, Rivest-Shamir-Adleman (RSA) [19], relies on the difficulty of the factoring problem for classical computers. For a proper introduction to quantum algorithms, we refer to Refs. [16, 20], and note that the field is under rapid development.

1.2.1 Fault-Tolerance

Building a quantum computer is extremely difficult. The core of the challenge is that quantum information is fragile, and a quantum computer could be easily overrun by errors from either (1) unwanted interactions with its environment, or (2) imperfect control. We will make these ideas more precise in Chapter 2 and Chapter 3 with the notions of quantum state purity, noise, and decoherence. When severe enough, errors kill the exponential benefit of quantum computers by enabling their polynomial-time classical simulation [21].

To maintain their advantage, quantum computations must be performed in a way that is **fault-tolerant**, i.e., resilient to errors. From a purely theoretical point of view, the problem of fault-tolerant quantum computation has already been solved with the idea of **error-correcting codes** [16, 22, 23], which leverage redundant encoding of quantum information across many physical qubits to form error-corrected logical qubits, along with schemes to perform fault-tolerant operations between logical qubits. However, there is significant distance to cover between an idea and its physical implementation.

1.3 The Age of Quantum Engineering

After a century of development in experiments probing quantum physics, we have arrived in an era of rapid progress across multiple platforms (superconducting circuits [24], neutral atoms [25], trapped ions [26], photonic devices [27], solid-state defects [28], and semiconductor spins [29]) giving access to quantum systems at never-before-seen precision and scale. This has been referred to as a **second quantum revolution**. Recent landmark experiments [25, 30] have heralded the era of early small-scale fault-tolerance: at the time of writing, systems can be designed and manipulated with high fidelity on the scale of $10-100$ [30, 31] qubits with circuit depths of up to 10^6 [30], and the regime of 1000+ qubits appears to be on the not-so-distant horizon [25]. Current hardware error rates (within an order-of-magnitude or two variation across platforms) lie in the range $10^{-2}-10^{-5}$ [30, 32, 33], enabled by significant engineering achievements.

However, orders-of-magnitude more qubits and further mitigation of hardware errors are required to realize large-scale fault-tolerant quantum computation [20], demanding careful engineering of next-generation systems and approaches that alleviate space-time costs [34–36]. In other words, scaling, coherence, and control are the central challenges facing the present-day quantum engineer [14]. Although each platform comes with unique obstacles, the abstraction of a specific system as a qubit or multi-qubit system enables platform-agnostic results, e.g., control or characterization techniques that can benefit multiple platforms. Most of this thesis falls into the platform-agnostic category.

1.4 Thesis Overview

In this work, we present three distinct results which address the topics of qubit decoherence and high-fidelity control, using superconducting quantum circuits [37–39]. We summarize these results below, and outline the remaining thesis chapters at the end of this section.

1.4.1 $1/f$ Flux Noise in Applied Magnetic Fields

One of the major sources of decoherence for superconducting qubits is low-frequency magnetic flux noise with a power-spectral density (PSD) scaling with $1/f$ where f is frequency. Such $1/f$ PSDs are ubiquitous in electronic devices, as well as in several disparate fields including biology [40], geology [41], language [42], music [43], and others. Despite its ubiquity, we will see in Chapter 4 that there is no notion of a unified theory for this frequency scaling. Rather, $1/f$ PSDs arise from different mechanisms in different contexts.

For today's superconducting circuits, the physics behind $1/f$ flux noise is still a mystery. Since its first observation in superconducting quantum interference devices (SQUIDs) in the 1980s [44], consensus has been formed around the relevance of magnetic defects residing on the surfaces and interfaces of devices [45]. It is typically believed that high-frequency $1/f$ flux noise emerges from spin-diffusion dynamics [46–49], while a distinct mechanism is responsible for the low-frequency flux noise, such as longer-time fluctuations of the net magnetization of clusters [47, 48]. Although theoretical models have found success, the exact physics remains ambiguous. In large part, this arises from the ambiguity of experiments: microscopic theories contain free parameters which can be adjusted to accommodate experimental observations, but these free parameters cannot be controlled in the experiments themselves (e.g., a spin-spin coupling strength). Further experiments with different tuning knobs are therefore required to pin down a precise description and rule out various proposed models.

To this end, we have measured the evolution of $1/f$ flux noise as a function of applied in-plane magnetic field [Fig. 1.1]. We have uncovered two novel signatures to serve as benchmarks for theories of superconducting circuit flux noise. Our results are qualitatively consistent with the current understanding of spin diffusion and clustering. However, no quantitative theory has been developed yet which accommodates all features of our data [50].

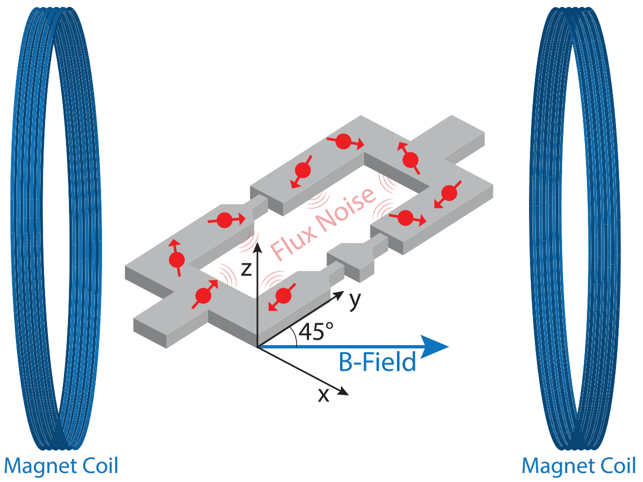

Figure 1.1: **Cartoon schematic of $1/f$ noise in magnetic fields experiment.** The Josephson-junction (JJ) loop (gray) of a flux qubit is placed in a uniform magnetic field provided by Helmholtz coils (blue). The field is oriented in the plane of the device, and the device is tilted at a 45° in-plane angle relative to the field. Surface spins (red) in proximity to the loop generate flux noise which dephases the qubit. The applied-field dependence of the dephasing noise yields clues about the microscopic physics of $1/f$ flux noise.

1.4.2 Pushing the Speed of Gates for Low-Frequency Qubits

As introduced earlier in this chapter, one of the most significant barriers to building a quantum computer is errors in qubit control. In general, the error associated with performing a gate operation in a time t_g will be proportional to t_g/T_{coh} where T_{coh} is the relevant coherence timescale. In order to decrease errors, one can then take two paths: making the gate faster by decreasing t_g, or increasing the coherence T_{coh}. The first approach has the added benefit of reducing the run-time of algorithms which may be significant for useful quantum computations requiring deep circuits [20].

Decreasing the control timescale comes with challenges. The most common method of single-qubit control relies on resonant (Rabi) driving [51] and requires that the duration of the gate be much longer than the period of the drive [52] and the timescale set by the anharmonicity of the qubit [53]. For the most developed superconducting qubit of today, the transmon [54], low anharmonicity limits the gate duration through leakage errors: when pulses become fast, their high bandwidth leads to spurious transitions to states beyond the qubit subspace. To mitigate leakage errors, a technique called derivative removal by adiabatic gate (DRAG) [53] has been widely adopted in the transmon community.

The fluxonium qubit has recently been established as a strong alternative to the transmon for building a quantum processor [55–59]. Unlike the transmon, the fluxonium has a much lower qubit frequency (less than one gigahertz, rather than several gigahertz for the transmon), and much higher anharmonicity (several gigahertz, rather than several hundred megahertz for the transmon). As a consequence, fast single-qubit fluxonium gates are limited by spurious dynamics related to the breakdown of the famous rotating-wave approximation [52] and associated counter-rotating errors, rather than leakage.

In Chapter 6, we establish two complementary techniques for suppressing counter-rotating errors, enabling gates as fast as the timescale set by the qubit frequency f_{01}, referred to as the Larmor period $\tau_L = 1/f_{01}$. Our results lead to state-of-the-art single-qubit gates for the superconducting qubit platform, summarized in Table. 1.1 with the records for other platforms, along with the prior superconducting record.

1.4.3 Elucidating the Effect of Anisotropic Transverse Noise

The physics of qubit decoherence is of fundamental interest. Beyond enabling the further understanding of quantum systems coupled to environments (i.e., **open quantum systems**), the study of decoherence enables the design of techniques to understand and mitigate coherence-limiting noise [65–67]. While the study of open quantum systems is well-established [68], conventional models of qubit decoherence often assume that the environ-

Table 1.1: **Present-day record single-qubit gate errors for different quantum computing platforms.** For superconducting circuits, we include the prior record that was achieved with transmons [60], and the current record that was achieved with fluxoniums in this work [61]. For neutral atoms, we note that techniques beyond conventional optical trapping can be leveraged to achieve global single-qubit gate errors on the order 10^{-5} [62].

Qubit	f_{01}	Gate time	Technique	Error
Semiconductor Spin [63]	2 GHz	30 ns	Rabi	$\sim 10^{-4}$
Neutral Atom (Cs) [32]	9.2 GHz	250 ns 4 us	Diff. Light Shift (local Z) Rabi (global)	$\sim 10^{-3}$ $\sim 10^{-4}$
Superconducting Transmon [60]	4 GHz	20 ns	Rabi + DRAG	$\sim 10^{-4}$
Superconducting Fluxonium (this work)	250 MHz	4 ns ($1/f_{01}$)	Rabi + Commensurate	$\sim 10^{-5}$
Trapped Ion [64]	3.2 GHz	12 us	Rabi	$\sim 10^{-6}$

mental noise is symmetric with respect to the quantization axis of the qubit. We depict this in Fig. 1.2 with the Bloch-sphere picture, which we will explicitly develop in Chapter 2.

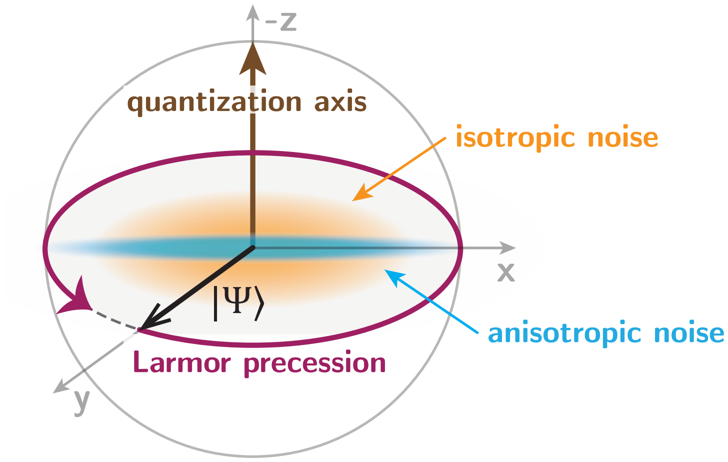

Figure 1.2: **Bloch sphere picture of isotropic and anisotropic transverse noise.** A qubit is represented in the Bloch-sphere picture, where the quantization axis (brown arrow) is depicted along the $-z$ axis. The qubit state (black) precesses around the quantization axis (purple). Usual models of decoherence assume isotropic transverse noise that is symmetrically distributed in the Bloch-sphere XY plane (orange). Anisotropic transverse noise (blue) is commonly encountered across experimental platforms, and leads to novel dynamics on the scale of the qubit Larmor precession period.

This symmetry assumption is commonly broken for realistic noise in leading experimental platforms including superconducting qubits, neutral atoms, and trapped ions (e.g., from control electronics or optics used for single-qubit manipulations [24, 69]). The decoherence dynamics from realistic, asymmetric transverse noise sources are not captured by conventional isotropic noise models [70], including those that utilize the ubiquitous rotating-wave approximation (RWA) [71, 72]. Signatures of broadband transverse noise anisotropy in qubit decoherence, representing physics beyond the RWA, would advance our understanding of decoherence and provide a new means to diagnose noise in experiments.

In this work, we study the decoherence of qubits subject to injected anisotropic transverse noise. We directly observe purity oscillations at twice the Larmor frequency in the state of a fluxonium qubit. We probe the oscillation dependence on noise anisotropy, lab-frame orientation, and power-spectral density. This signature elucidates the impact of realistic noise on qubit decoherence. Although the signature is relatively small for strong noise, we expect it may be useful as a diagnostic tool for extremely low-frequency qubits with low coherence.

1.4.4 Remaining Chapters

The rest of this thesis is structured as follows. Chapter 2 introduces quantum mechanics, single-qubit control, and superconducting qubits. Chapter 3 introduces noise and qubit decoherence. Chapter 4 introduces $1/f$ noise. The main results are then presented in Chapter 5 ($1/f$ flux noise in magnetic fields [73]), Chapter 6 (fast gates with low-frequency qubits [61]), and Chapter 7 (novel signatures from anisotropic transverse noise [74]). We conclude in Chapter 8 with an outlook.

Chapter 2

Quantum Mechanics & Qubits

In this chapter, we provide an introduction to the physics necessary to understand the experimental results of this thesis. As I have often needed to explain quantum mechanics to interested non-physicists with some mathematical background, I begin with a quick pedagogical crash-course on quantum mechanics in Section 2.1 which I hope will serve the interested reader. We proceed by detailing the relevant physics for the thesis results. We introduce the main system of study, the qubit, in Section 2.2 and how we control them in Section 2.3. We finish this chapter with a description of the experimental platform used in this thesis, superconducting circuits, in Section 2.4.

2.1 Quantum Mechanics

2.1.1 From Classical to Quantum

To introduce quantum mechanics, I find it most helpful to draw an analogy with classical mechanics which we are intuitively familiar with from everyday life. Let's consider a single particle, e.g. a billiard ball, as an illustrative example. In broad strokes, we can model the system as a state (its position and momentum, $\{\vec{x}, \vec{p}\}$) which evolves according to an equation of motion (for classical mechanics, the equations of motion are determined by

Newton's second law $\vec{F} = d\vec{p}/dt$). Once we write down the forces acting on the billiard ball, we are equipped to model how it behaves in time with all the detail we desire within the framework of classical mechanics.

We can now pitch quantum mechanics simply: instead of a state consisting of position and velocity, we introduce an object called the **wavefunction**, $|\Psi\rangle$, which is a normalized vector in a **Hilbert space** $\mathcal{H}$ (the inner product $\langle\Psi|\Psi\rangle = 1$). The equation of motion is determined by the **Schrödinger equation**,

$$i\hbar\frac{\partial}{\partial t}|\Psi\rangle = \hat{H}|\Psi\rangle, \tag{2.1}$$

where the **Hamiltonian** $\hat{H}$ determines the dynamics of the system. The Hamiltonian must be **Hermitian**, $\hat{H} = \hat{H}^\dagger$, in order for the time-evolution to conserve normalization of the wavefunction. We can represent how a state evolves with the **time-evolution operator** $\hat{U}(t)$: $|\Psi(t)\rangle = \hat{U}(t)|\Psi(0)\rangle$, which for a time-independent Hamiltonian is given by:

$$\hat{U}(t) = e^{-i\hat{H}t/\hbar}. \tag{2.2}$$

Thanks to the Hermiticity of the $\hat{H}$, we can see that $\hat{U}(t)$ is **unitary**: $\hat{U}(t)^\dagger = \hat{U}(t)^{-1}$.

2.1.2 Measurement

For classical systems like our billiard ball, we are used to measuring quantities such as its position or momentum without affecting the quantity in the process. This is no longer the case when measuring a quantum system. Measurable quantities are associated with an **observable** operator $\hat{O}$. When measuring $\hat{O}$, we will find an eigenvalue $o_m \in \mathbb{R}$ and the quantum state will **collapse** into the associated eigenstate of $\hat{O}$, $|m\rangle$, with probability given by the **Born rule**:

$$p(o_m) = |\langle m|\Psi\rangle|^2. \tag{2.3}$$

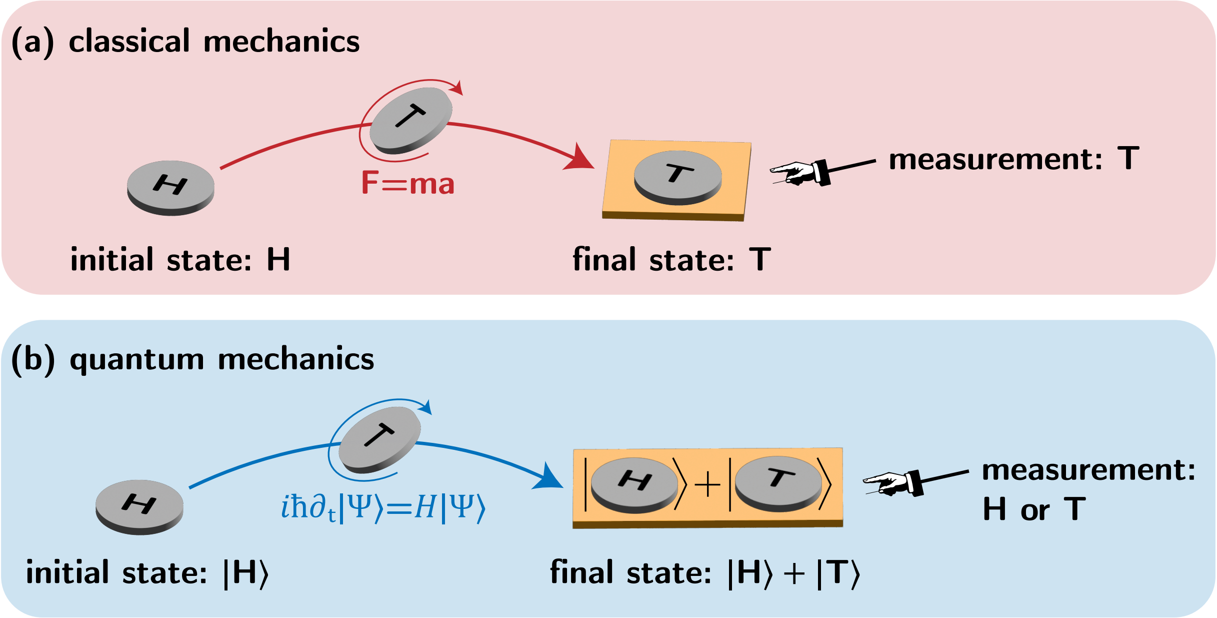

Figure 2.1: **Classical vs quantum mechanics, in the analogy of a coin flip. (a)** Classical mechanics: an initial state of the coin, H, undergoes motion according to Newton's second law. Once the coin lands, it is in a final state given by either H or T. Measuring the coin, we will always find the same final state T. **(b)** Quantum mechanics: an initial wavefunction of the coin, $|H\rangle$, undergoes motion according to the Schrödinger equation. Once the coin lands, it can be in a superposition of H and T: $a\,|H\rangle + b\,|T\rangle$, where $a, b \in \mathbb{C}$ and $|a|^2 + |b|^2 = 1$. Measuring the coin, we will find H with probability $|a|^2$, and T with probability $|b|^2$. Measurement is a process which now affects the state of the quantum system.

Since measured values must be real, observables must be Hermitian operators.

The **expectation value** of an operator, defined as the average value over an ensemble of identical states, is given by

$$\begin{aligned} \langle \hat{O} \rangle &= \sum_m p(o_m) o_m && (2.4)\\ &= \langle \Psi | \left(\sum_m o_m \, |m\rangle \langle m| \right) |\Psi\rangle && (2.5)\\ &= \langle \Psi | \, \hat{O} \, |\Psi\rangle \, . && (2.6) \end{aligned}$$

We have used the fact that we can express a Hermitian operator in the **eigenbasis** given by its eigenstates $\{|0\rangle, |1\rangle, \cdots\}$: $\hat{O} = \sum_m o_m \, |m\rangle \langle m|$.

Here we note that the Hamiltonian of a system $\hat{H}$ is the observable corresponding to energy: for an eigenvector $|E\rangle$ of $\hat{H}$, $\hat{H}\,|E\rangle = E\,|E\rangle$ where E is the energy associated with the state $|E\rangle$. The eigenbasis of $\hat{H}$ yields the complete set of orthogonal states accessible by the quantum system and their corresponding energies, the respective eigenvalues.

2.1.3 Density Matrix

In this subsection, we motivate a statistical description of quantum systems and the formalism to accommodate such descriptions; that of **density operators**. The representation of the density operator in a given basis is referred to as the **density matrix**.

So far in our description of quantum systems, we have used a state vector $|\Psi\rangle$ to characterize the state of the system. However, in practice one can imagine (and often encounters) a scenario in which the quantum system is found in $|\Psi_i\rangle$ with probability p_i. For an observable $\hat{O}$ with eigenvalues O_m and corresponding eigenvectors $|m\rangle$, the average measurement outcome is then computed with the statistical ensemble of states:

$$\begin{aligned} \langle \hat{O} \rangle &= \sum_i p_i \langle \Psi_i | \hat{O} | \Psi_i \rangle && (2.7) \\ &= \sum_m O_m \langle m | \left(\sum_i p_i |\Psi_i\rangle \langle \Psi_i| \right) |m\rangle \, . && (2.8) \end{aligned}$$

where we have used the expression $\hat{O} = \sum_m O_m |m\rangle \langle m|$. We see that the statistical nature of the quantum state is captured by the operator in the parenthesis of the last line, which we define below.

Definition 2.1: Density Operator

The **density operator** of a quantum system described by a statistical ensemble of states $|\Psi_i\rangle$ each with probability p_i is given by

$$\hat{\rho} = \sum_i p_i |\Psi_i\rangle \langle\Psi_i| . \tag{2.9}$$

For a given eigenbasis $|n\rangle$, the **density matrix** has elements $\rho_{ij} = \langle i| \hat{\rho} |j\rangle$. The density matrix is Hermitian, as $\rho_{ij} = (\rho_{ji})^*$. Diagonal elements correspond to the occupancy of each state in the ensemble, and are referred to as **populations**. Summing over the diagonal elements, we see $\mathrm{tr}(\hat{\rho}) = \sum_i p_i = 1$. Off-diagonal elements correspond to the correlations between states, and are typically referred to as the **coherences**.

We can now derive a simple expression for the expectation value of $\hat{O}$, with a further simplification utilizing our favorite trick of inserting an identity in the form of another eigenbasis $|n\rangle$, $\hat{I} = \sum_n |n\rangle \langle n|$,

$$\begin{aligned} \langle\hat{O}\rangle &= \sum_m \sum_n O_m \langle m|n\rangle \langle n| \hat{\rho} |m\rangle && (2.10) \\ &= \sum_n \langle n| \hat{\rho}\hat{O} |n\rangle && (2.11) \\ &= \mathrm{tr}(\hat{\rho}\hat{O}). && (2.12) \end{aligned}$$

Pure & Mixed States

For a quantum system described by a state $|\Psi\rangle$, the density operator is simply $\hat{\rho} = |\Psi\rangle \langle\Psi|$. Since there is no need for a statistical ensemble to describe such a state, we refer to it as a **pure state**. For pure states, $\hat{\rho}^2 = \hat{\rho}$, and so $\mathrm{tr}(\hat{\rho}^2) = 1$.

If we instead need a statistical ensemble, we refer to the state as a **mixed state**. One can show that for such states, $\hat{\rho}^2 \neq \hat{\rho}$, and $\mathrm{tr}(\rho^2) < 1$. We can see that the quantity $\mathrm{tr}(\hat{\rho}^2)$ is a useful indicator of the purity of a quantum state, and define it below.

Definition 2.2: Purity

The **purity** of a quantum system described by a density operator $\hat{\rho}$ is

$$\gamma \equiv \mathrm{tr}(\hat{\rho}^2). \tag{2.13}$$

The purity takes on values $\frac{1}{d} \leq \gamma \leq 1$ where d is the dimension of the Hilbert space. The upper bound is saturated by **pure states** when $\hat{\rho}$ can be expressed as $\hat{\rho} = |\Psi\rangle\langle\Psi|$ for some state $|\Psi\rangle$. States which are described by a statistical ensemble are referred to as **mixed states** and have $\gamma < 1$. Such states can arise from e.g. decoherence or imperfect state preparation.

We emphasize that there are two general cases in which mixed states describe a quantum system, shown in Fig. 2.2.

1. Consider an ensemble of pure states, where each state $|\Psi_i\rangle$, encountered with probability p_i, is different due to imperfect preparation: $\hat{\rho} = \sum_i p_i |\Psi_i\rangle\langle\Psi_i|$. As an example, consider a qubit in its ground state which is subject to either a π pulse or no pulse due to, e.g., an irresponsible child (or adult) touring your lab and wiggling a loose cable. We will find the qubit in its ground or excited state with a probability of 0.5 for both, and the density operator describing this ensemble is $\hat{\rho} = 0.5\,|0\rangle\langle 0| + 0.5\,|1\rangle\langle 1|$.

2. Considering an ensemble consisting of identical copies of a pure state $|\Psi\rangle$ for a system with constituent subsystems A and B, the description of subsystem A will be a mixed state if the subsystems are **entangled**. In this case, the **reduced density operator** describing subsystem A is given by the **partial trace** of the full system density operator: $\hat{\rho}_A = \mathrm{tr}_B(\hat{\rho})$, where $\mathrm{tr}_B(\cdot)$ is defined as summing over an eigenbasis spanning the Hilbert space of subsystem B. As an example, consider a system of two qubits prepared in a Bell state: $|\Psi\rangle = (|00\rangle + |11\rangle)/\sqrt{2}$. The density operator for either of the qubits will then be $\hat{\rho} = 0.5\,|0\rangle\langle 0| + 0.5\,|1\rangle\langle 1|$, as in the prior example. However,

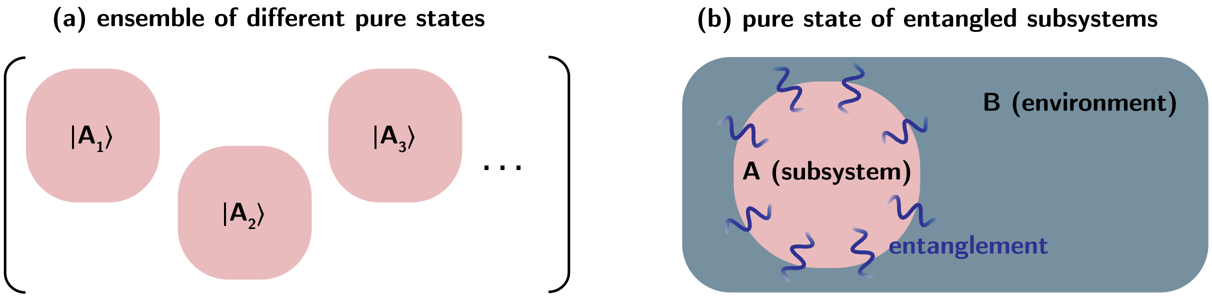

Figure 2.2: **Cartoon showing two kinds of mixed quantum states requiring description with density matrices.** **(a)** An ensemble consisting of different pure states, $\{|A_0\rangle, |A_1\rangle, \cdots\}$, each of which is different, must be described by a density matrix. **(b)** A subsystem A of a system described by a single pure state $|\Psi_{AB}\rangle$ comprised of entangled subsystems A and B must be described by a density matrix.

the origin of the state impurity is intrinsically quantum mechanical.

Congratulations, you have now completed this mini crash course on quantum mechanics! You should understand enough of the basic principles to appreciate the experimental contents of this thesis. From this point onwards, we slightly change our notation. We began by expressing all operators with hats, e.g., $\hat{O}$. Moving forward, we drop the hats, as one can deduce from the context of an equation which objects are operators.

2.2 Qubits

Now, we are ready to dive into the physics of quantum systems comprising two possible states, known as **qubits** – the focus of this thesis. Put another way, the Hilbert space in which a qubit state lives has dimension $d = 2$, so a qubit state can be expressed as the linear combination of two vectors with complex coefficients,

$$|\Psi\rangle = a\,|0\rangle + b\,|1\rangle\,, \tag{2.14}$$

where $\langle 0|0\rangle = \langle 1|1\rangle = 1$ and $\langle 0|1\rangle = 0$.

It is convenient choose $\{|0\rangle, |1\rangle\}$ corresponding to the eigenbasis of the Hamiltonian of the qubit (recall that for a Hermitian operator, the eigenvectors are orthonormal and comprise a basis of the Hilbert space). For a qubit with states of energy difference $E_1 - E_0 = \hbar\omega_{01}$, the Hamiltonian in this eigenbasis is given by

$$H = \frac{\hbar\omega_{01}}{2}(|1\rangle\langle 1| - |0\rangle\langle 0|), \tag{2.15}$$

where the ground (lowest energy) and excited (highest energy) states are given by $|0\rangle$ and $|1\rangle$, respectively.

Now, let's consider the dynamics of an arbitrary state $|\Psi_0\rangle = a_0|0\rangle + b_0|1\rangle$. Writing down the Schrödinger equation for this system, we find two uncoupled differential equations for $a(t)$ and $b(t)$. Solving them yields

$$|\Psi(t)\rangle = a_0 e^{i\frac{\omega_{01}t}{2}}|0\rangle + b_0 e^{-i\frac{\omega_{01}t}{2}}|1\rangle. \tag{2.16}$$

Now we can define the convenient notation used in the bulk of this thesis, ever thankful that our Hilbert space is conveniently small. We introduce the **Pauli matrices**,

$$\sigma_x = \begin{pmatrix} 0 & 1 \\ 1 & 0 \end{pmatrix}, \quad \sigma_y = \begin{pmatrix} 0 & -i \\ i & 0 \end{pmatrix}, \quad \sigma_z = \begin{pmatrix} 1 & 0 \\ 0 & -1 \end{pmatrix}, \tag{2.17}$$

with the properties that $\sigma_i^2 = 1$, $\mathrm{tr}(\sigma_i) = 0$, and $[\sigma_i, \sigma_j] = 2i\epsilon_{ijk}\sigma_k$ where ϵ_{ijk} is the Levi-civita symbol.

We can express Eq. (2.15) as

$$H = -\frac{\hbar\omega_{01}}{2}\sigma_z, \tag{2.18}$$

with eigenstates given by

$$|0\rangle = \begin{pmatrix} 1 \\ 0 \end{pmatrix}, \quad |1\rangle = \begin{pmatrix} 0 \\ 1 \end{pmatrix}. \tag{2.19}$$

The time-evolution operator, $U(t) = e^{-\frac{i\sigma_z t}{2}}$, allows us to calculate the evolution as a matrix multiplication yielding the same result as Eq. (2.16):

$$|\Psi(t)\rangle = \begin{pmatrix} e^{i\frac{\omega_{01}t}{2}} & 0 \\ 0 & e^{-i\frac{\omega_{01}t}{2}} \end{pmatrix} \begin{pmatrix} a_0 \\ b_0 \end{pmatrix} = \begin{pmatrix} a_0 e^{i\frac{\omega_{01}t}{2}} \\ b_0 e^{-i\frac{\omega_{01}t}{2}} \end{pmatrix}. \tag{2.20}$$

2.2.1 Qubit Geometry: the Bloch Sphere

In this section, we detail a geometric representation of a two-level quantum system, which is incredibly useful in understanding the physics of qubit control and decoherence. As described previously, a pure qubit state is specified by two complex numbers

$$|\Psi\rangle = a\,|0\rangle + b\,|1\rangle\,, \tag{2.21}$$

where $a, b \in \mathbb{C}$. Apparently, there are 4 degrees of freedom to specify corresponding to the real and imaginary parts of both numbers. We now recall two constraints,

1. state normalization, $|a|^2 + |b|^2 = 1$, and
2. unobservability of global phases, $|\Psi\rangle \leftrightarrow e^{i\delta}\,|\Psi\rangle$ for $\delta \in \mathbb{R}$.

Without loss of generality, the second constraint allows us to choose a global phase such that $a \in \mathbb{R}$. Motivated by the normalization condition, we can parameterize our state with two angles:

$$a = \cos(\theta/2) \tag{2.22}$$

$$b = e^{i\varphi}\sin(\theta/2) \tag{2.23}$$

where $0 \leq \theta \leq \pi$ and $0 \leq \varphi < 2\pi$. Calculating the expectation values for the Pauli matrices with this paramterization, we identify the cartesian components of a vector $\vec{r}$ on the unit sphere with polar angle θ and azimuthal angle φ:

$$\vec{r} \equiv \begin{pmatrix} \langle \sigma_x \rangle \\ \langle \sigma_y \rangle \\ \langle \sigma_z \rangle \end{pmatrix} = \begin{pmatrix} \cos(\varphi)\sin(\theta) \\ \sin(\varphi)\sin(\theta) \\ \cos(\theta) \end{pmatrix}. \tag{2.24}$$

This parameterization gives us a geometric picture of a pure qubit state, referred to as the Bloch sphere. We draw the Bloch sphere in Fig. 2.3, labelling the states on all poles. We refer to $\vec{r}$ as the **Bloch vector**.

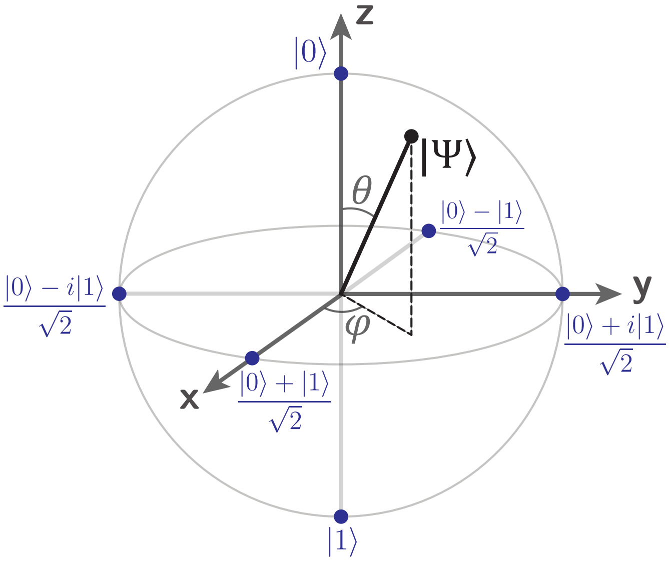

Figure 2.3: **Bloch sphere representation of a qubit state.** States corresponding to the poles (blue dots) represent the eigenstates of the Pauli matrix of that axis.

As an illustrative example, we can now visualize the dynamics of the qubit state Eq. (2.16), prepared in state $|\Psi_0\rangle = |+\rangle = \frac{1}{\sqrt{2}}(|0\rangle + |1\rangle)$

$$\vec{r}_{\text{bare evolution}} \equiv \begin{pmatrix} \cos(\omega_{01}t) \\ -\sin(\omega_{01}t) \\ 0 \end{pmatrix}. \tag{2.25}$$

Starting along the $+\hat{x}$ axis, the Bloch vector spins in a clockwise circle about the $+\hat{z}$ axis.

This behavior is analogous to that of a magnet with angular momentum along the direction of its dipole moment when placed in a static magnetic field, which can be understood entirely with the physics of classical electromagnetism. The magnetic moment will gyrate about the axis of the static field, referred to as **Larmor precession**. Inspired by this physics analogy, it is typical to use this name for the precession of any qubit about the axis given by its ground and excited states in the Bloch sphere picture, also known as its **quantization axis**.

2.2.2 Mixed States

For pure states, we note that $|\vec{r}| = 1$ – the Bloch vector lies on the unit sphere. However, we also learned that density operators can be used to describe states which are not pure. In a Hilbert space of dimension $d = 2$, the density matrix will have four elements, but three degrees of freedom due to the normalization condition. Noting that the Pauli matrices along with the identity matrix comprise a basis for the space of 2×2 Hermitian matrices, we can express a qubit density matrix as

$$\begin{aligned} \rho &= \frac{1}{2}(I + \vec{r} \cdot \vec{\sigma}) && (2.26) \\ &= \frac{1}{2}(I + r_x\sigma_x + r_y\sigma_y + r_z\sigma_z). && (2.27) \end{aligned}$$

With this convention, we conveniently find $\langle\sigma_i\rangle = r_i$. The purity is given by

$$\begin{aligned} \mathrm{tr}(\rho^2) &= \frac{1}{2} + \frac{\langle\sigma_x\rangle^2 + \langle\sigma_y\rangle^2 + \langle\sigma_z\rangle^2}{2} && (2.28) \\ &= \frac{1 + |\vec{r}|^2}{2}. && (2.29) \end{aligned}$$

Recall that for an impure state, $\mathrm{tr}(\rho^2) < 1$, implying $|\vec{r}| < 1$. In other words, Bloch vectors inside the unit sphere represent impure states. The maximally mixed state, $\rho \to I/2$, corresponds to the center.

2.2.3 Rotations

Any unitary operation we perform on a qubit will be described by a 2 × 2 unitary matrix. We can imagine these unitary operations as rotations of the Bloch vector. For a rotation of angle ϕ about an axis $\hat{n}$, we can express the rotation operator as

$$R_{\hat{n}}(\phi) = e^{-i\frac{\phi}{2}\hat{n}\cdot\vec{\sigma}} = \cos(\phi/2)I - i\sin(\phi/2)\hat{n}\cdot\vec{\sigma}. \tag{2.30}$$

Some of the most common rotations, or **gates**, utilized in experiments are π rotations about the cardinal axes along with arbitrary rotations about $\hat{z}$ and the **Hadamard gate** which is a rotation of $\theta = \pi$ about the $\hat{x} + \hat{z}$ axis:

$$X_\pi = -i\sigma_x \tag{2.31}$$

$$Y_\pi = -i\sigma_y \tag{2.32}$$

$$Z_\theta = \begin{pmatrix} e^{-i\theta/2} & 0 \\ 0 & e^{i\theta/2} \end{pmatrix} \tag{2.33}$$

$$H = \frac{1}{2}\begin{pmatrix} 1 & 1 \\ 1 & -1 \end{pmatrix} \tag{2.34}$$

We can now ask the question, given a qubit prepared in a particular state, how do we implement a rotation? This is the bread, butter, and main entree of this thesis.

2.3 Qubit Control

In this section, we describe the common control paradigm of qubits, that of control via the application of oscillating fields that are resonant with the qubit frequency. We discuss the physics of such control, its breakdown in the limit of fast operations, and the frequency shifts a system inherits from such fields.

2.3.1 Linear Drives

We begin by deriving the workhorse result of this thesis: when a qubit defined by Hamiltonian $H_{\text{qubit}} = -\frac{\hbar\omega_{01}}{2}\sigma_z$ is subject to an oscillating field coupled transversely, $H_{\text{drive}}(t) = \hbar\Omega\cos(\omega t)\sigma_x$, the qubit state will begin to oscillate between $|0\rangle$ and $|1\rangle$. This behavior is known as **Rabi flopping**.

Let us start with the time-dependent system Hamiltonian,

$$\begin{aligned} H &= H_{\text{qubit}} + H_{\text{drive}}(t) && (2.35)\\ &= -\frac{\hbar\omega_{01}}{2}\sigma_z + \hbar\Omega\cos(\omega t)\sigma_x && (2.36)\\ &= \hbar\begin{pmatrix} -\frac{\omega_{01}}{2} & \Omega\cos(\omega t) \\ \Omega\cos(\omega t) & \frac{\omega_{01}}{2} \end{pmatrix}. && (2.37) \end{aligned}$$

We now introduce a trick that greatly simplifies solving the Schrödinger equation for many time-dependent Hamiltonians like the one above.

Rotating-Frame Transformation

We can consider the dynamics in a **rotating frame** determined by a **unitary transformation** $U_{\text{rf}}(t)$ of the Hamiltonian. If we pick a rotating frame such that the effective Hamiltonian $\tilde{H}$ in the new frame is time-independent, the calculation becomes extremely simple.

Here we derive the effective Hamiltonian $\tilde{H}$ corresponding to a frame defined by our choice of $U_{\text{rf}}(t)$. We remember the Schrödinger equation written down with no transformation, in the so-called **laboratory frame**, for our state $|\Psi\rangle$:

$$i\hbar\frac{\partial}{\partial t}|\Psi\rangle = H|\Psi\rangle\,. \tag{2.38}$$

Let us define our rotating-frame state as $|\tilde{\Psi}\rangle = U_{\mathrm{rf}}(t)\,|\Psi\rangle$ (so $|\Psi\rangle = U^{\dagger}_{\mathrm{rf}}(t)\,|\tilde{\Psi}\rangle$), and note that

$$i\hbar\frac{\partial}{\partial t}\left(U_{\mathrm{rf}}(t)\,|\Psi\rangle\right) = i\hbar\frac{\partial U_{\mathrm{rf}}}{\partial t}\,|\Psi\rangle + U_{\mathrm{rf}}\left(i\hbar\frac{\partial}{\partial t}\,|\Psi\rangle\right) \tag{2.39}$$

$$i\hbar\frac{\partial}{\partial t}\,|\tilde{\Psi}\rangle = i\hbar\frac{\partial U_{\mathrm{rf}}}{\partial t}U^{\dagger}_{\mathrm{rf}}\,|\tilde{\Psi}\rangle + U_{\mathrm{rf}}HU^{\dagger}_{\mathrm{rf}}\,|\tilde{\Psi}\rangle \tag{2.40}$$

$$= \tilde{H}\,|\tilde{\Psi}\rangle\,. \tag{2.41}$$

We now define our rotating-frame transformation succinctly below.

Definition 2.3: Rotating-Frame Transformation

For a system with laboratory-frame Hamiltonian H and wavefunction $|\Psi\rangle$, we define a **rotating-frame transformation** by a unitary $U_{\mathrm{rf}}(t)$ such that the state in the rotating frame,

$$|\tilde{\Psi}\rangle = U_{\mathrm{rf}}(t)\,|\Psi\rangle\,, \tag{2.42}$$

evolves according to a Schrödinger equation with an effective Hamiltonian $\tilde{H}$ given by

$$\tilde{H} = U_{\mathrm{rf}}HU^{\dagger}_{\mathrm{rf}} + i\hbar\frac{\partial U_{\mathrm{rf}}}{\partial t}U^{\dagger}_{\mathrm{rf}}. \tag{2.43}$$

Armed with this trick, we can now choose a frame rotating about σ_z at the drive frequency (recalling the unitary transformation corresponding to rotations, Eq. (2.30)):

$$U_{\mathrm{rf}}(t) = e^{-i\omega t\sigma_z/2}. \tag{2.44}$$

Defining a detuning $\delta = \omega - \omega_{01}$, the effective Hamiltonian becomes

$$\tilde{H} = \hbar\begin{pmatrix} \frac{\delta}{2} & \frac{\Omega}{2}\left(1+e^{-2i\omega t}\right) \\ \frac{\Omega}{2}\left(1+e^{2i\omega t}\right) & -\frac{\delta}{2} \end{pmatrix} \tag{2.45}$$

$$= \hbar\left[\frac{\delta}{2}\sigma_z + \Omega\left(\frac{\sigma_x}{2} + \frac{\cos(2\omega t)\sigma_x + \sin(2\omega t)\sigma_y}{2}\right)\right] \tag{2.46}$$

The effective Hamiltonian still contains time dependence, now oscillating at twice the qubit frequency. We can understand the off-diagonal terms with the observation that a linear drive field, $\cos(\omega t)\sigma_x$, can be decomposed into two circularly polarized components:

$$\cos(\omega t)\sigma_x = \frac{\cos(\omega t)\sigma_x - \sin(\omega t)\sigma_y}{2} + \frac{\cos(\omega t)\sigma_x + \sin(\omega t)\sigma_y}{2} \tag{2.47}$$

The first term in Eq. (2.47) corresponds to a field oscillating clockwise about σ_z in the Bloch sphere picture. We refer to this term as **co-rotating**, as it rotates in the same direction as the qubit Bloch vector evolving with H_{qubit} (Eq. (2.25)). Inspecting the unitary transformation of the drive Hamiltonian, we can see that the co-rotating component becomes static in the rotating frame:

$$U_{\text{rf}}\left(\frac{\cos(\omega t)\sigma_x - \sin(\omega t)\sigma_y}{2}\right)U_{\text{rf}}^{\dagger} = \frac{\sigma_x}{2}. \tag{2.48}$$

In contrast, the second term of Eq. (2.47) corresponds to a field oscillating in the counter-clockwise direction, which we refer to as **counter-rotating**. The counter-rotating term in the rotating-frame now oscillates at twice the frequency:

$$U_{\text{rf}}\left(\frac{\cos(\omega t)\sigma_x + \sin(\omega t)\sigma_y}{2}\right)U_{\text{rf}}^{\dagger} = \frac{\cos(2\omega t)\sigma_x + \sin(2\omega t)\sigma_y}{2} \tag{2.49}$$

We can understand these components geometrically in the Bloch sphere picture, presented in Fig. 2.4.

In the limit that $\delta \ll \omega_{01}$ (near resonance) and $\Omega \ll \omega_{01}$ (weak coupling), the dynamics at 2ω are fast compared to the dynamics of the qubit state, and we can discard the fast oscillating terms in an approximation known as the **rotating-wave approximation**. Starting in $|\Psi_0\rangle = |0\rangle$, we find

$$|\Psi(t)\rangle = \begin{pmatrix} \cos\left(\frac{\sqrt{\Omega^2+\delta^2}t}{2}\right) - \frac{i\delta}{\sqrt{\Omega^2+\delta^2}}\sin\left(\frac{\sqrt{\Omega^2+\delta^2}t}{2}\right) \\ -\frac{i\Omega}{\sqrt{\Omega^2+\delta^2}}\sin\left(\frac{\sqrt{\Omega^2+\delta^2}t}{2}\right) \end{pmatrix}. \tag{2.50}$$

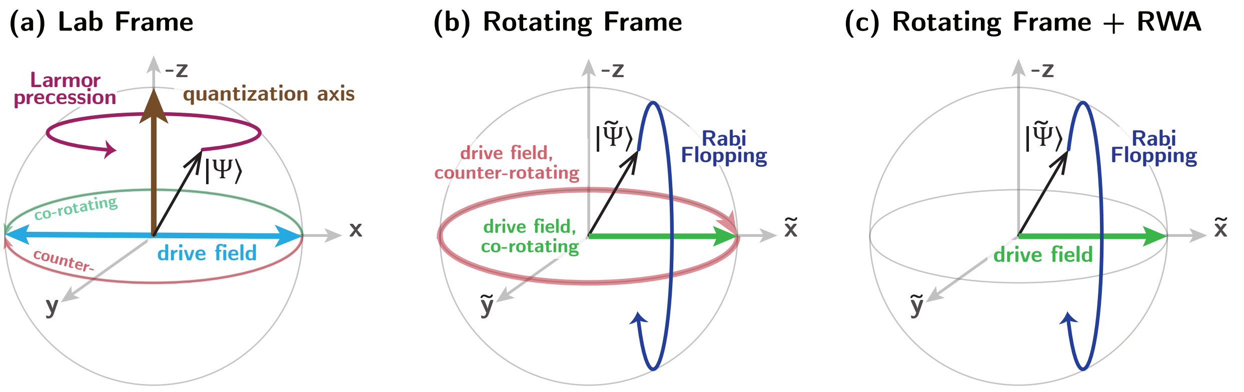

(a) Lab Frame **(b) Rotating Frame** **(c) Rotating Frame + RWA**

Figure 2.4: **Bloch sphere picture of linearly polarized driving.** **(a)** Laboratory-frame Bloch sphere cartoon depicting a qubit with state $|\Psi\rangle$ (black) subjected to a linearly-polarized drive field (blue). The drive field can be expressed as the combination of co- (green) and counter-rotating (red) components. In the laboratory frame, the qubit will undergo Larmor precession (purple) about its quantization axis. **(b)** Entering a frame co-rotating with the qubit, the co-rotating component of the drive (green) becomes static, and the counter-rotating component oscillates at twice the qubit frequency. The Larmor precession is captured by the rotating frame, so the rotating-frame state $|\tilde{\Psi}\rangle$ appears static in the absence of the drive. The static, co-rotating component of the drive generates rotations of the qubit state. **(c)** Making the rotating-wave approximation (RWA) is equivalent to disregarding the fast-oscillating counter-rotating component of the original linear drive.

and corresponding population of the excited state

$$p_{|1\rangle}(t) = |\langle 1|\Psi(t)\rangle|^2 = \frac{\Omega^2}{\Omega^2+\delta^2}\sin^2\left(\frac{\sqrt{\Omega^2+\delta^2}t}{2}\right). \tag{2.51}$$

We plot Eq. (2.51) in Fig. 2.5. The population of the qubit under the influence of an oscillating linearly polarized drive field exhibits oscillations $|0\rangle \leftrightarrow |1\rangle$ with an amplitude and frequency determined by the detuning of the drive frequency $\delta = \omega - \omega_{01}$. The frequency of these oscillations is known as the **Rabi frequency**. The maximum amplitude and frequency correspond to a **resonant** pulse, when $\omega = \omega_{01}$. We can understand the oscillations geometrically by inspecting the Hamiltonian Eq. (2.45) – discarding the fast-oscillating terms, the qubit will rotate about the static field along the rotating-frame Bloch sphere $\delta\hat{z} + \Omega\hat{x}$ axis. In other words, detuning the drive has the effect of tilting the static field about which the qubit oscillates (flops) in the rotating frame.

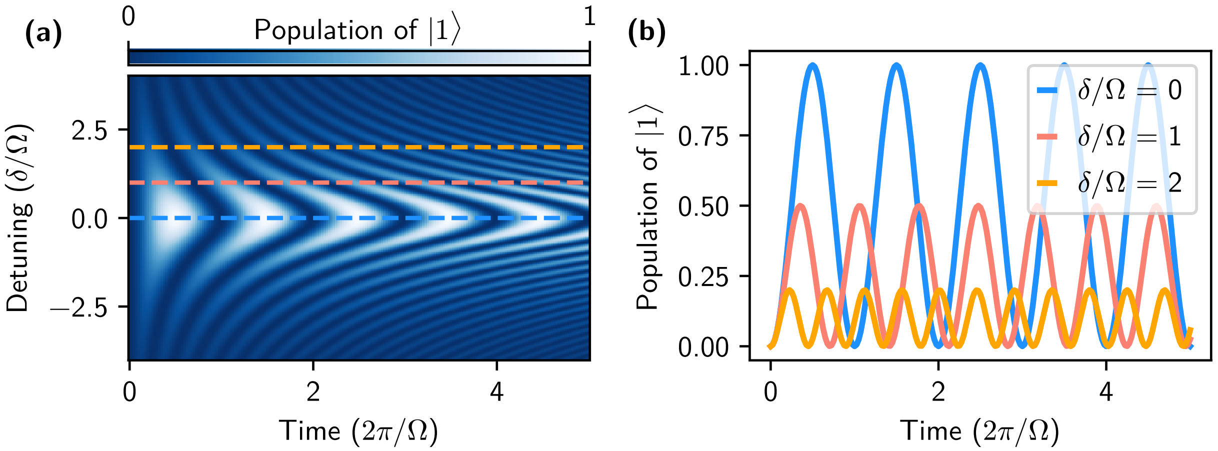

Figure 2.5: **Rabi oscillations.** **(a)** Dynamics of the qubit excited state population when prepared in $|\Psi_0\rangle = |0\rangle$ and subject to a drive of strength Ω, as a function of detuning δ, as given by Eq. (2.51). **(b)** Linecuts for different values of the detuning. Larger drive detuning leads to smaller amplitude oscillations at a higher frequency.

Armed with the physics of Rabi flopping, we can now ask, what are the limitations of controlling a qubit with a resonant drive field? As we have learned in the previous section on density matrices, the purity of a quantum state depends sensitively on how well we can prepare an identical ensemble or mitigate entanglement with the environment. In general, as we leave a quantum system alone, it will become more mixed or impure due to unwanted interactions with external degrees of freedom. This process is called **decoherence** as the coherence (off-diagonal) elements of the density matrix tend to zero with time. To mitigate decoherence and perform high-quality operations, it is important to implement gates which are fast.

To implement fast Rabi gates, we must be mindful – the rotating-wave approximation we made to derive Eq. (2.51) breaks down as the drive strength becomes comparable to the qubit frequency $\Omega \to \omega_{01}$. We plot the simulated dynamics of a qubit subject to a drive field of increasing strength (Rabi frequency) in Fig. 2.6. We can see that for weak drives $\Omega \ll \omega_{01}$, the population dynamics are well described by a sinusoidal oscillation as in Eq. (2.51), as the RWA is a good approximation. As the drive strength becomes comparable to the qubit frequency, we can see deviations from a sinusoidal oscillation. In particular, fast dynamics at the counter-rotating frequency $2\omega_{01}$ become significant. When implementing gates with strong linearly polarized drives, these fast dynamics can lead to significant errors associated with the counter-rotating component of the drive, which we call **counter-rotating errors**. Such errors become especially important to consider when using low-frequency qubits.

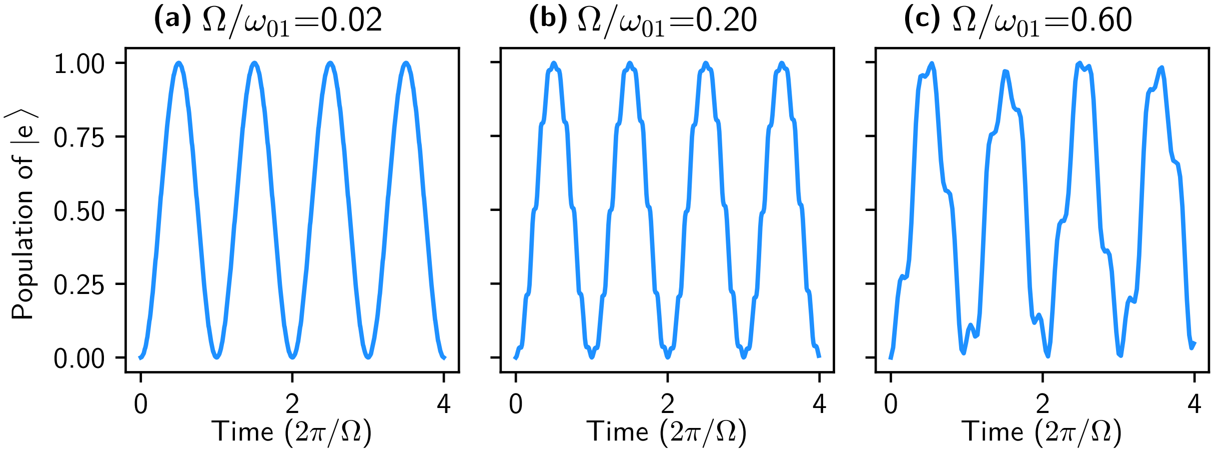

Figure 2.6: **Breakdown of the rotating-wave approximation for strong drives.** Simulated dynamics of a qubit excited state population when prepared in $|\Psi_0\rangle = |0\rangle$ and subject to a resonant linearly polarized drive of strength Ω, for **(a)** $\Omega/\omega_{01} = 0.02$, **(b)** $\Omega/\omega_{01} = 0.2$, and **(c)** $\Omega/\omega_{01} = 0.6$.

2.3.2 Preview: Suppressing Counter-Rotating Errors for Fast Gates

We now are equipped to appreciate the results presented in Chapter 6. There, we introduce and experimentally demonstrate two complementary methods for suppressing counter-rotating errors which arise from strong driving, breaking the weak-coupling assumption made in the RWA. Our methods enable high-fidelity Rabi gates at times approaching the timescale set by the qubit frequency, the **Larmor period**:

$$\tau_L \equiv 2\pi/\omega_{01}. \tag{2.52}$$

The first method involves the implementation of a purely co-rotating drive, which natively contains no counter-rotating component. The second method utilizes timing restrictions to make counter-rotating errors uniform for all gates, reducing the error to a systematic rotation which is corrected for in typical calibrations.

2.3.3 Resonant Control

Advertisement aside, we now explain how we can generate specific gates with the physics of Rabi flopping. To realize a gate, i.e., a specific unitary operation, we must be able to turn our control on and off as well as rotate around different axes of the Bloch sphere. Let's consider a resonant drive term with two new aspects: (1) time-dependence in the Rabi frequency $\Omega(t)$, and (2) a variable phase φ of the drive tone,

$$H_{\text{drive}} = \hbar\Omega(t)\cos(\omega t + \varphi)\sigma_x. \tag{2.53}$$

The qubit + drive Hamiltonian in the frame co-rotating with the qubit is given by

$$\tilde{H} = \hbar\Omega(t)\left[\frac{\cos(\varphi)\sigma_x - \sin(\varphi)\sigma_y}{2} + \frac{\cos(2\omega t + \varphi)\sigma_x + \sin(2\omega t + \varphi)\sigma_y}{2}\right]. \tag{2.54}$$

Performing the rotating-wave approximation amounts to dropping the 2ω oscillations,

$$\tilde{H}_{\text{RWA}} = \hbar\frac{\Omega(t)}{2}\left(\cos(\varphi)\sigma_x - \sin(\varphi)\sigma_y\right). \tag{2.55}$$

The time-evolution generated by this Hamiltonian is given by

$$\tilde{U}(T) = e^{-\frac{i}{\hbar}\int_0^T \tilde{H}_{\text{RWA}} t dt} \tag{2.56}$$

$$= e^{-i(\cos(\varphi)\sigma_x - \sin(\varphi)\sigma_y)\cdot\frac{1}{2}\int_0^T \Omega(t)dt}. \tag{2.57}$$

Recalling that the unitary corresponding to a rotation about axis $\hat{n}$ by angle θ takes the form $R_{\hat{n}}(\theta) = e^{-i\frac{\theta}{2}\hat{n}\cdot\vec{\sigma}}$, we see that applying a drive tone with phase φ enables us to generate rotations about any axis on the equator of the rotating-frame Bloch sphere, with a rotation angle given by the total area under the Rabi-frequency envelope:

$$\hat{n} = \cos(\varphi)\hat{\tilde{x}} - \sin(\varphi)\hat{\tilde{y}} \tag{2.58}$$

$$\theta = \int_0^T \Omega(t)dt \tag{2.59}$$

where we have used $\tilde{\cdot}$ to denote a rotating-frame axis.

To conclude this subsection, we highlight that it is possible to generate rotations about orthogonal axes of the rotating-frame Bloch sphere by applying drive tones that are 90° out of phase, referred to as **orthogonal quadratures**. This trick comprises the most common control paradigm for high-frequency qubits including trapped ions, neutral atoms, and superconducting circuits. We refer to gates generated using the physics of resonant control as **Rabi gates**.

2.3.4 Frequency Shifts

Before finishing this section, we highlight another phenomenon which becomes significant in practice: frequency-shifts arising from drives. So far, we have explored the population dynamics of a qubit from a weak, resonant drive ($\Omega \ll \omega_{01}$ and $\delta = \omega - \omega_{01} = 0$). Here, we point out that drives can, in addition to inducing Rabi flopping, modify the eigenstates and eigenenergies of a system. The modified system is referred to as the **dressed** system. We introduce the two typical frequency shifts encountered when applying drive fields to a quantum system below.

Bloch-Siegert Shift

Here, we answer the following question: does applying a strong drive to a qubit shift its effective resonance frequency? Let's start with our usual qubit + drive Hamiltonian Eq. (2.35) with $\omega = \omega_{01}$. We can gain some insight by performing a rotating-frame transformation, this time into the frame counter-rotating with the qubit,

$$U_{\mathrm{rf}}(t) = e^{i\omega t\sigma_z/2}, \tag{2.60}$$

with the effective Hamiltonian given by

$$\tilde{H} = \hbar\left[-\frac{(\omega+\omega_{01})}{2}\sigma_z + \Omega\left(\frac{\sigma_x}{2} + \frac{\cos(2\omega t)\sigma_x - \sin(2\omega t)\sigma_y}{2}\right)\right]. \tag{2.61}$$

The $\Omega\frac{\sigma_x}{2}$ term was the original counter-rotating field, now static in this frame. We are interested in the effective frequency of the two-level system, which is shifted due to the slight tilt in the quantization axis given by the static term $\Omega\frac{\sigma_x}{2}$. Discarding the fast oscillating terms (which, in this frame, one might call a counter-rotating wave approximation), we find eigenvalues and the effective resonance frequency in this frame

$$\tilde{\omega}_\pm = \pm\frac{\sqrt{\Omega^2 + (\omega+\omega_{01})^2}}{2}, \tag{2.62}$$

$$\tilde{\omega} = \tilde{\omega}_+ - \tilde{\omega}_- = \sqrt{\Omega^2 + (\omega+\omega_{01})^2}. \tag{2.63}$$

As our frame is rotating at ω, the effective resonance frequency in the laboratory frame, ω_{eff}, will be shifted by $-\omega$. We can see this by noting that a frequency shift arises in our rotating-frame from the second term of Eq. (2.43), $-i\frac{\partial U_{\mathrm{rf}}(t)}{\partial t}U^\dagger_{\mathrm{rf}}(t) = -\omega\frac{\sigma_z}{2}$. Considering a resonant drive $\omega = \omega_{01}$ and expanding in $\frac{\Omega}{\omega_{01}}$, we find

$$\omega_{\mathrm{eff}} = \sqrt{\Omega^2 + 4\omega_{01}^2} - \omega_{01} \tag{2.64}$$

$$= \omega_{01}\left(1 + \frac{\Omega^2}{4\omega_{01}^2}\right) + \mathcal{O}\left(\frac{\Omega^4}{\omega_{01}^4}\right). \tag{2.65}$$

To summarize, we have found that the counter-rotating component of a resonant drive does not only create fast dynamics at 2ω – it also **dresses** the system, slightly modifying the eigenstates and eigenenergies. The frequency shift above, $\Delta\omega_{\mathrm{BS}} = \frac{\Omega^2}{4\omega_{01}}$, is known as the

Bloch-Siegert shift, derived by the pair in 1940 [52].

Off-Resonant AC-Stark Shift

We now must step back and make an admission – in practice, most qubits comprise a dimension-2 subspace of a quantum system with a much larger Hilbert space. By picking two levels with a unique energy difference, one can address those two levels selectively (e.g. with a drive that is resonant with the transition of interest, but no other transitions) while ignoring the rest of the original Hilbert space. However, we now bring up an important effect of the other levels: dressing of the qubit subspace from the off-resonant driving of non-target transitions.

We follow the same rough procedure as in the last subsection, considering the qubit + drive Hamiltonian Eq. (2.35), but now with detuning $\omega = \omega_{01} + \delta$. In the frame co-rotating with the qubit, we find

$$\tilde{H} = \hbar \left[\frac{\delta}{2}\sigma_z + \Omega \left(\frac{\sigma_x}{2} + \frac{\cos(2\omega t)\sigma_x + \sin(2\omega t)\sigma_y}{2} \right) \right]. \tag{2.66}$$

Similarly discarding the fast-oscillating terms, and inspecting the difference in dressed eigenstates given by the difference in eigenenergies, we find

$$\begin{aligned} \omega_{\text{eff}} &= \sqrt{\Omega^2 + \delta^2} - (\omega_{01} + \delta) \qquad (2.67) \\ &= \omega_{01} + \frac{\Omega^2}{2\delta} + \mathcal{O}\left(\frac{\Omega^3}{\delta^3} \right). \qquad (2.68) \end{aligned}$$

We have found that an off-resonant drive will shift the effective energy of a qubit by $\Delta\omega_{\text{AC}} = \frac{\Omega^2}{2\delta}$. Let's now consider the case where we have a target qubit comprised of levels $\{|0\rangle, |1\rangle\}$ with resonance frequency ω_{01}, and a non-target qubit comprised of one level of the target qubit, and another separate level, e.g. $\{|1\rangle, |2\rangle\}$ with resonance frequency ω_{12}. The application of a drive at frequency ω_{01} will dress the $\{|1\rangle, |2\rangle\}$ subspace, leading to a frequency shift of the $|1\rangle$ state.

2.4 Qubits from Superconducting Circuits

Before finishing this chapter, we introduce the experimental platform of the qubits utilized in this thesis: **superconducting circuits**. As our results are largely platform-agnostic, we introduce the platform and highlight the ideas relevant to this thesis while pointing to some of the many existing resources for more thorough treatments [75–78]. In this section, we first introduce the idea of circuits which require quantum-mechanical descriptions, then discuss some of the most popular qubits derived from such circuits.

2.4.1 Introduction to Quantum Circuits

Quantum mechanics was initially developed to understand the discrete (or quantized) energy spectra of atoms: microscopic systems containing only a handful of fundamental particles. Creating qubits from electronic circuits might seem counter-intuitive for two reasons: a circuit is a much larger system, comprising (at least) billions of atoms or fundamental particles, and circuits are conventionally understood with classical electromagnetism (e.g. Kirchoff's laws). When does a circuit require a quantum-mechanical description? This is the case when a circuit (1) has discrete energy levels [37], and (2) the energy levels maintain coherence [79]. Circuits meeting these conditions are referred to as **artificial atoms**. The field of study centered around these circuits is known as **circuit quantum electrodynamics** [75, 80].

An essential ingredient for realizing such circuits is **cryogenic temperatures**, which allows circuits made of superconducting materials to avoid conventional dissipation mechanisms associated with thermal fluctuations [81][1]. Before proceeding, we must now define the tools required to write a quantum description of circuits, starting with the **Lagrangian** and **Hamiltonian** formulations of classical mechanics.

---

[1] This requirement shapes the infrastructure of superconducting qubit experiments, comprising dilution refrigerators which cool samples to the $\sim 10\,\mathrm{mK}$ temperature scale, and microwave electronics with proper cryogenic signal conditioning.

Definition 2.4: Lagrangian & Hamiltonian Mechanics

Given a system described by a set of coordinates $\vec{q} = \{q_0, q_1, \cdots, q_N\}$, the **Lagrangian** $\mathcal{L}$ is a function of the coordinates and their time derivatives $\dot{\vec{q}} = \frac{d\vec{q}}{dt}$ which yields the correct equations of motion of the system from the **Euler-Lagrange equations**:

$$\frac{d}{dt}\left(\frac{\partial \mathcal{L}}{\partial \dot{q}_i}\right) = \frac{\partial \mathcal{L}}{\partial q_i}. \tag{2.69}$$

Solving these equations yields a **path** $\{\vec{q}(t), \dot{\vec{q}}(t)\}$ corresponding to the classical motion of the system. For non-relativistic systems without electromagnetic fields, the $\mathcal{L}$ is given by the difference in kinetic (T) and potential (U) energies:

$$\mathcal{L} = T - U. \tag{2.70}$$

Lagrangian mechanics gives us a new interpretation of classical physics: systems evolve on paths of **stationary action**: $\delta S = 0$, where the action S is the time-integral of the Lagrangian over a given path and $\delta(\cdot)$ is the functional derivative of S with respect to perturbations of the path.

The Lagrangian of a system is related to the **Hamiltonian** by a **Legendre transformation**, yielding an equivalent formulation of mechanics:

$$H = \sum_i p_i \dot{q}_i - \mathcal{L}, \text{ where } p_i = \frac{\partial \mathcal{L}}{\partial \dot{q}_i}, \tag{2.71}$$

with equations of motion

$$\frac{dq_i}{dt} = \frac{\partial H}{\partial p_i}, \quad \frac{dp_i}{dt} = -\frac{\partial H}{\partial q_i}. \tag{2.72}$$

The coordinate q_i and momentum p_i are referred to as **conjugate** variables, as they satisfy the **Poisson bracket** relation $\{p_i, q_i\} = \delta_{ij}$ (intuitively, changes in one generate displacements of the other), where $\{f, g\} = \sum_i \frac{\partial f}{\partial q_i}\frac{\partial g}{\partial p_i} - \frac{\partial f}{\partial p_i}\frac{\partial g}{\partial q_i}$.

We can now sketch out the general procedure for writing down the quantum-mechanical description of a circuit.

1. Get the circuit Lagrangian. This can be approached by writing down Kirchoff's laws for the circuit and working backwards, or directly with developed procedures such as the method of nodes (see e.g. [82]).
2. Get the circuit Hamiltonian by calculating the Legendre transform of the Lagrangian.
3. Promote the Hamiltonian to a quantum operator by promoting the classical conjugate variables to operators, and replacing the Poisson bracket they satisfy with a commutation relation: $\{q, p\} = 1 \rightarrow [\hat{q}, \hat{p}] = \hat{q}\hat{p} - \hat{p}\hat{q} = i\hbar$ [5].

2.4.2 Quantum Circuit Ingredients

In order to write down the Lagrangians for our favorite superconducting qubits, we must develop the "kinetic" and "potential" energies appearing in Eq. (2.70) associated with circuit elements. As atoms comprise a small number of constituent particles (electrons, protons, and neutrons), superconducting artificial atoms analogously comprise a small number of building blocks: **capacitors**, **inductors**, and **Josephson junctions**. Capacitors and inductors store energy in the electric and magnetic fields, respectively. The Josephson junction, a circuit element defined by two superconducting terminals separated by a thin barrier, has a current-voltage relationship determined by the **Josephson equations**.

Now, we develop the energies of these elements and establish what is "kinetic" vs "potential". First, we define notation for two-terminal circuit elements. The **branch voltage** is given by the line integral of the electric field across an element, and the **branch current** is given by the line integral of the magnetic field in a closed path around the element [Fig. 2.7]:

$$V(t) = \int_{\text{start}}^{\text{end}} \vec{E} \cdot d\vec{l}, \tag{2.73}$$

$$I(t) = \oint_{\text{around}} \vec{B} \cdot d\vec{l}. \tag{2.74}$$

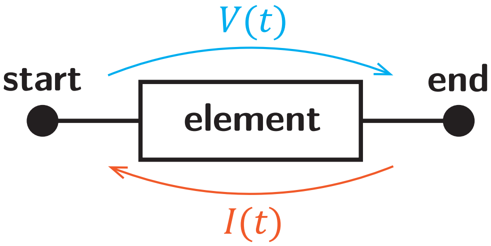

Figure 2.7: **Two-terminal circuit element.** Cartoon showing a two-terminal circuit element and sign conventions for its associated branch voltage and current, given by Eq. (2.73) and Eq. (2.74), respectively.

The energy stored in an element at a time t is

$$E(t) = \int_{-\infty}^{t} V(t')I(t')dt'. \tag{2.75}$$

We can express the energy of any element as a function of either

1. the **branch flux** $\Phi(t) = \int_{-\infty}^{t} V(t')dt'$ and its derivative $\dot{\Phi}(t) = V(t)$, or
2. the **branch charge** $Q(t) = \int_{-\infty}^{t} I(t')dt'$ and its derivative $\dot{Q}(t) = I(t)$.

Picking one or the other choice amounts to treating either the flux Φ or charge Q as a "position coordinate" q, with conjugate momentum then given by $\frac{\partial \mathcal{L}}{\partial \dot{q}}$. Both options result in equivalent physics. Our choice simply determines which energies are termed kinetic or potential: potential (kinetic) energies are a function of q ($\dot{q}$). We choose (1), consistent with the convention in our field.

The energy of an element can be derived from its **constitutive equation**, which specifies the relationship between current and voltage. We enumerate circuit elements, their constitutive equations, and associated energies in Table. 2.1. Given our choice (1), energies which are a function of $\dot{\Phi}$ (Φ) are deemed kinetic (potential).

Table 2.1: **Circuit elements and their energies.** The Josephson junction stands apart from classical capacitors and inductors, as the constitutive equations—the Josephson relations—rely on the quantum-mechanical physics of superconductivity. The flux Φ across a Josephson junction is related to the collective state of the electrons in the superconductor (referred to as the Ginzburg-Landau order parameter). In a superconductor, pairs of electrons form bound states, called **Cooper pairs**, with charge $-2e$ where $-e$ is the electron charge. The total flux around a closed superconducting loop is quantized as integer values of the **flux quantum** $\Phi_0 = h/2e$, with $h = 2\pi\hbar$.

Element	Constitutive Equation	Energy
Capacitor	$Q = CV$	$\frac{1}{2}C\dot{\Phi}^2$
Inductor	$\Phi = LI$	$\frac{1}{2L}\Phi^2$
Josephson junction	$I = I_c \sin\left(2\pi\frac{\Phi}{\Phi_0}\right)$, $V = \frac{d\Phi}{dt}$	$-\frac{\Phi_0 I_c}{2\pi}\cos\left(2\pi\frac{\Phi}{\Phi_0}\right)$

2.4.3 Classical to Quantum Resonator

We are now ready to consider the most ubiquitous and simple quantum circuit: the LC oscillator comprising an inductor and capacitor in parallel. Following the procedure outlined in the previous subsection, we can write the Lagrangian Eq. (2.70) with the circuit element energies in Table. 2.1, yielding

$$\mathcal{L} = \frac{1}{2}C\dot{\Phi}^2 - \frac{1}{2L}\Phi^2, \tag{2.76}$$

with the canonical momentum $p = \frac{\partial\mathcal{L}}{\partial\dot{\Phi}} = C\dot{\Phi}$, which is simply equal to the charge Q for this circuit. The classical circuit Hamiltonian is then

$$\begin{aligned} H &= C\dot{\Phi}\cdot\dot{\Phi} - \mathcal{L} && (2.77)\\ &= \frac{1}{2}C\dot{\Phi}^2 + \frac{1}{2L}\Phi^2 && (2.78)\\ &= \frac{Q^2}{2C} + \frac{\Phi^2}{2L}. && (2.79) \end{aligned}$$

This circuit yields equations of motion for $Q(t)$ and $\Phi(t)$ identical to a particle of mass C on a spring with stiffness $1/L$. Such a system is referred to as a **simple harmonic oscillator**, as the classical motion (derived by solving Eq. (2.72)) is given by sinusoidal oscillations or "simple harmonic motion" with an angular frequency $\omega = 1/\sqrt{LC}$.

Our final step involves promoting the charge and flux from classical coordinates to quantum operators: $Q \to \hat{Q}$ and $\Phi \to \hat{\Phi}$, obeying the commutation relation $[\hat{Q}, \hat{H}] = i\hbar$. We have now arrived at the quantum Hamiltonian:

$$\hat{H} = \frac{\hat{Q}^2}{2C} + \frac{\hat{\Phi}^2}{2L}. \tag{2.80}$$

In order to gather insight about the energy level structure of this circuit, we introduce new coordinates following Dirac's ladder-operator approach:

$$\hat{Q} = -i\sqrt{\frac{\hbar}{2Z_0}}(a - a^\dagger) \tag{2.81}$$

$$\hat{\Phi} = \sqrt{\frac{\hbar Z_0}{2}}(a + a^\dagger), \tag{2.82}$$

where $Z_0 = \sqrt{L/C}$ is the **characteristic impedance** of the circuit, and a and $a^\dagger$ are the famous annihilation and creation operators, respectively. We find the famous form of the **quantum harmonic oscillator** Hamiltonian,

$$\hat{H} = \hbar\omega\left(a^\dagger a + \frac{1}{2}\right). \tag{2.83}$$

We draw the circuit and plot the associated potential energy and eigenenergies of the Hamiltonian in Fig. 2.8. We can understand the eigenstates analytically with clever manipulations of $\hat{H}$, a, $a^\dagger$, and $N \equiv a^\dagger a$. With $|n\rangle$ denoting the eigenstate with the n-th highest energy (and remembering that the eigenstates of a Hermitian operator yield an orthonormal

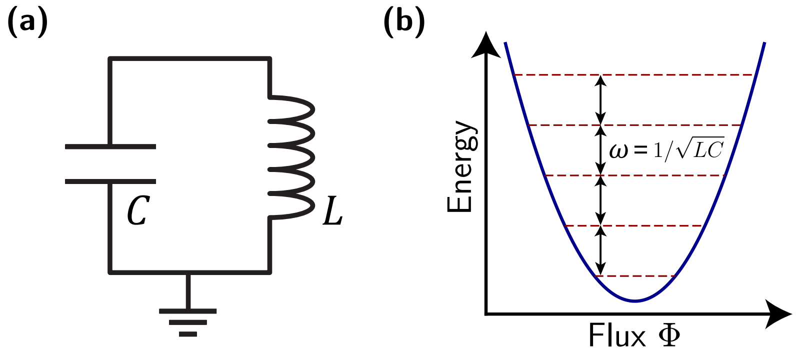

Figure 2.8: **LC circuit.** **(a)** Circuit diagram with a capacitor (capacitance C) and inductor (inductance L) in parallel. **(b)** The potential energy of the circuit, with the convention of treating the flux Φ as the position coordinate, is given by $\frac{\Phi^2}{2L}$ (blue). The energy levels (red, dashed) are equally spaced apart by the resonance frequency of the circuit, $\hbar\omega = \hbar/\sqrt{LC}$.

basis), we have

$$\begin{aligned}
\hat{H}\left|n\right\rangle &= \hbar\omega\left(n+\frac{1}{2}\right)\left|n\right\rangle \\
N\left|n\right\rangle &= n\left|n\right\rangle \\
a\left|n\right\rangle &= \begin{cases} 0 \quad \text{for } n=0 \\ \sqrt{n}\left|n-1\right\rangle \quad \text{for } n>0 \end{cases} \\
a^\dagger\left|n\right\rangle &= \sqrt{n+1}\left|n\right\rangle .
\end{aligned}$$

The states $\{\left|0\right\rangle, \left|1\right\rangle, \cdots\}$ are termed the **Fock states** or **number states**, with the interpretation that $\left|n\right\rangle$ corresponds to a state with n **excitations** (also called **particles**). In our case, the Hamiltonian Eq. (2.83) describes an electromagnetic field, so we call the excitations **photons**[2]. We can now appreciate a basic feature of quantum mechanics: bound states (those with energies in the potential well [Fig. 2.8(b)] have discrete energy levels. In

---

[2] Hamiltonians like Eq. (2.83) show up in nearly all fields of physics and the excitations are given names according to the context. In condensed matter physics, these excitations typically describe the collective behavior of many constituent particles, and are called **collective excitations** or **quasiparticles**. For example, vibrations in a solid yield a similar Hamiltonian, and the excitations are labelled phonons. Eq. (2.83) only describes excitations that behave like **bosons**. In the field of superconducting quantum circuits, the word quasiparticle is used almost exclusively to denote excitations in the state of the superconductor corresponding to breaking up Cooper pairs, yielding unpaired electrons: these are **fermions**, not described by Eq. (2.83).

our case, $|n\rangle$ corresponds to a state with n photons, and the energy levels have a spacing given by the **energy quantum** $\hbar\omega$.

We are close to completing our construction of qubits with superconducting circuits, as we have found an artificial atom with discrete energy levels. However, to operate the circuit as a qubit, we need to pick two energy levels that we can selectively address. This is not possible with the LC circuit considered – the difference between any two energy levels is not unique since all levels are spaced apart by the same amount. We must change the Hamiltonian in order to break the harmonic level structure of Eq. (2.83).

Aside on Fluctuations

Before building qubits with circuits, we highlight one additional feature of Eq. (2.83) in the charge and phase fluctuations of the state with zero photons, $|0\rangle$, referred to as the **vacuum**:

$$\Phi_{\mathrm{zpf}} \equiv \sqrt{\langle 0|\,\Phi^2\,|0\rangle} = \sqrt{\frac{\hbar Z_0}{2}} \tag{2.84}$$

$$Q_{\mathrm{zpf}} \equiv \sqrt{\langle 0|\,Q^2\,|0\rangle} = \sqrt{\frac{\hbar}{2Z_0}}. \tag{2.85}$$

The fluctuations are known as **zero-point fluctuations** or **vacuum fluctuations**, and are an essential feature of quantum mechanics[3]. In the classical description at zero temperature, such that there are no thermal fluctuations, a particle starting with $Q = 0$, $\Phi = 0$ will simply stay at rest. The zero-point fluctuations indicate that, even at zero temperature, a quantum mechanical system will have a finite variance in measured quantities due to the nature of the wavefunction. These fluctuations are associated with the **Heisenberg uncertainty principle**, which mandates a minimum amount of fluctuations for any two canonically conjugate observables,

$$\langle \Phi^2 \rangle \langle Q^2 \rangle \geq \frac{\hbar}{4}. \tag{2.86}$$

---

[3] Such fluctuations are not physical fluctuations of the system: they correspond to the finite variance of measured observables from the delocalized nature of the wavefunction.

One can immediately appreciate that the inequality can be satisfied by suppressing the fluctuations for one observable, while enhancing the fluctuations for the other. States with this property are termed **squeezed** [83, 84]. We broadly explore the ideas of such **anisotropic** fluctuations and the impact they have on qubit decoherencee in Chapter 7.

2.4.4 Common Superconducting Qubits

Back to the main quest of this section, to realize qubits with superconducting circuits. We have established that the LC circuit yields a quantum harmonic oscillator with equally-spaced energy levels. To break that harmonic structure, we can consider adding potential energies of the system deviating from $\frac{\Phi^2}{2L}$. Such a deviation is provided by the Josephson junction.

We can understand the effective behavior of a Josephson junction in a circuit by noting that a classical inductor obeys $V = L\frac{dI}{dt}$, and the Josephson junction obeys

$$\frac{dI}{dt} = I_c \cos\left(2\pi\frac{\Phi}{\Phi_0}\right) \cdot \frac{2\pi}{\Phi}\frac{d\Phi}{dt} \tag{2.87}$$

$$= \frac{V}{L_{\text{eff}}} \tag{2.88}$$

$$V = L_{\text{eff}} \cdot \frac{dI}{dt} \tag{2.89}$$

where $L_{\text{eff}} = \frac{\Phi_0}{2\pi\cos(\phi)}$, with $\phi = 2\pi\frac{\Phi}{\Phi_0}$ referred to as the **reduced flux**. The above equation tells us that a Josephson junction will behave as an inductor with an effective inductance L_{eff} which depends on the phase difference (or current) across the junction. The effective energy, with $E_J = \frac{\Phi_0 I_c}{2\pi}$, is given by $E_{JJ}(\phi) = -E_J\cos(\phi)$. Expanding the Josephson junction energy around $\phi = 0$, we find

$$E_{JJ}(\phi) = -E_J\left(1 - \frac{\phi^2}{2} + \frac{\phi^4}{4!} + \cdots\right). \tag{2.90}$$

We see that the Josephson junction gives us an element which behaves as an inductor at lowest order, but adds higher-order perturbations to the potential[4].

Before detailing the most common qubits of today, we pay homage to the decades-long history of superconducting qubits [86–89]. From the first experimental landmark of observing quantum coherence in these systems [37, 79], the field has flourished and become one of the leading contenders to realizing quantum computation [90]. Along the way, many qubits have been invented and experimentally realized. In the rest of this chapter, we offer a concise overview of the most common superconducting qubits of today which establish the physics relevant for this thesis, noting that our treatment is far from a comprehensive review.

Charge Qubit

By simply replacing the linear inductor of an LC circuit with with a Josephson junction of energy E_J, we find the circuit corresponding to the first experimentally realized superconducting qubit: the **Cooper-pair box** or **charge qubit** [38, 79], with Hamiltonian

$$\hat{H} = 4E_C(\hat{n} - n_g)^2 - E_J \cos(\hat{\phi}). \tag{2.91}$$

We have introduced the capacitive charging energy $E_C \equiv \frac{e^2}{2C}$, the **charge operator** $\hat{n} = \frac{\hat{Q}}{2e}$ (which counts the number of excess Cooper pairs on one of the superconducting islands), and an additional offset-charge $n_g = C_g V_g$ which arises from capacitively coupling a voltage V_g to the circuit. Unfortunately, the first realizations of this circuit suffered from severe dephasing due to extreme sensitivity of the energy levels to the offset charge.

Transmon

By using a larger shunt capacitor with the charge qubit, moving to the regime $E_J/E_C \gg 1$ of the Hamiltonian Eq. (2.91), the offset-charge sensitivity is suppressed. In this regime, we

---

[4] In fact, the Josephson energy is only approximated as $\cos(\phi)$, but in reality contains higher-order corrections referred to as **Josephson harmonics** which can also affect the energy level structure of superconducting qubits [85].

refer to the circuit as a **transmon** [91]. The transmon displays significantly higher coherence due to its insensitivity to charge noise.

We can add one more feature by replacing the single Josephson junction with two junctions in parallel, referred to as a **DC superconducting quantum interference device (SQUID)** [Fig. 2.9(a)]. Through some algebraic manipulations, we can understand the circuit as yielding the same Hamiltonian as Eq. (2.91), but now with an effective Josephson energy E_J which depends on flux. We refer to this as a **flux-tunable transmon**, with Hamiltonian

$$\hat{H} = 4E_C\hat{n}^2 - E_J(\Phi_{\text{ext}})\cos(\hat{\phi}), \tag{2.92}$$

where Φ_{ext} is a flux applied in the DC-SQUID loop (typically supplied with a small solenoid mounted near the circuit, or an on-chip flux line inductively coupled to the loop), and

$$E_J(\Phi_{\text{ext}}) = (E_{J1} + E_{J2})\cos\left(\frac{\pi\Phi_{\text{ext}}}{\Phi_0}\right)\sqrt{1 + d^2\tan^2\left(\frac{\pi\Phi_{\text{ext}}}{\Phi_0}\right)}. \tag{2.93}$$

We have introduced the **junction asymmetry** $d = (E_{J1} - E_{J2})/(E_{J1} + E_{J2})$.

Flux Qubit

Alongside the charge qubit, the **flux qubit** was developed, comprising a circuit with a small Josephson junction in parallel with two large Josephson junctions [92, 93]. The eigenstates of this circuit correspond to superpositions of persistent current states around the JJ loop, resulting in high sensitivity to applied flux. Early versions of this qubit suffered from issues in reproducibility and low coherence. These issues were largely solved with the inclusion of a capacitive shunt, leading to the **C-shunt flux qubit** [94].

Fluxonium

Although the transmon and C-shunt flux qubits represented significant steps in terms of coherence over the early-generation charge and flux qubits, advances in the understanding of Hamiltonian engineering with circuits has given rise to qubits with improved coherence and control properties [95, 96]. The current rising star in the superconducting qubit world is the **fluxonium** [55], comprising a capacitor, inductor, and Josephson junction in parallel [Fig. 2.9(c)], yielding the Hamiltonian

$$\hat{H} = 4E_C\hat{n}^2 - E_J\cos(\hat{\phi} - \phi_{\text{ext}}) + \frac{1}{2}E_L\phi^2. \tag{2.94}$$

We can view this circuit as an extension of the C-shunt flux qubit, with the two large junctions now replaced with a large junction array realizing an effectively linear inductance. We note that experimentally, the inductance L usually comprises an array of Josephson junctions, however so-called "superinductances" made with 2D materials or geometric inductors [97] are also being explored. At the bias point $\phi_{\text{ext}} = 0.5$, also called the **flux-frustration point**, typical fluxonium qubit frequencies are less than 1 GHz, and coherence times can readily reach the millisecond timescale [58, 98, 99][5].

Numerical Treatment

It is only possible to analytically solve for the energy levels of a Hamiltonian in simple cases such as the LC circuit. As a consequence, numerical tools are generally required to understand the behavior of more complex circuits. In broad strokes, one must pick a finite basis, e.g. $\{|0\rangle, |1\rangle, \cdots, |N\rangle\}$, yielding a representation of the Hamiltonian in that basis $H_{ij} = \langle i|\hat{H}|j\rangle$. Diagonalizing the matrix H then yields the energy levels of the Hamiltonian $\hat{H}$. For superconducting circuits, this is often done by picking either the Fock basis (eigenvectors of $a^\dagger a$), the charge basis (eigenvectors of $\hat{n}$), or the phase basis (eigenvectors of $\hat{\phi}$). For a wonderful thorough treatment of circuit numerical diagonalization, we point to Ref. [78]. From numerical diagonalization of the tunable transmon [Eq. (2.92)] and fluxonium [Eq. (2.94)], we calculate the $|0\rangle \leftrightarrow |1\rangle$ and $|1\rangle \leftrightarrow |2\rangle$ transition energies and plot them

---

[5] Operation of a fluxonium circuit at the bias point $\phi_{\text{ext}} = k$ for integer k is also being explored, referred to as an **integer fluxonium qubit** [100].

in Fig. 2.9(b,d), respectively.

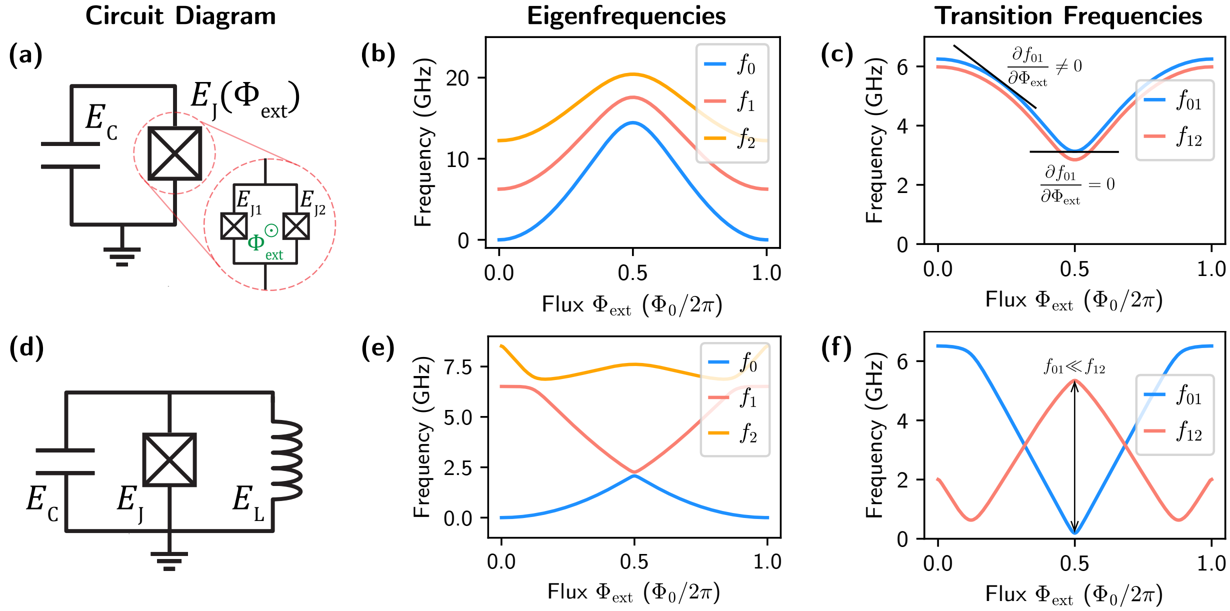

Figure 2.9: **Transmon and fluxonium circuits and energy levels.** **(a)** Circuit diagram of a transmon comprising a capacitor (charging energy E_C) and Josephson junction (energy E_J) in parallel. The Josephson junction can be replaced by two junctions in parallel (a DC-SQUID) to yield an equivalent circuit with a flux-tunable Josephson energy $E_J(\Phi_{\text{ext}})$ [Eq. (2.93)]. **(b)** The lowest three circuit Hamiltonian eigenfrequencies corresponding to states $|0\rangle$ (blue), $|1\rangle$ (red), and $|2\rangle$ (orange), for the tunable transmon circuit with energies $E_C/h = 240\,\text{MHz}$, $E_{J1}/h = 8\,\text{GHz}$, and $E_{J2}/h = 14\,\text{GHz}$. **(c)** Transition frequencies for $|0\rangle \leftrightarrow |1\rangle$ (blue) and $|1\rangle \leftrightarrow |2\rangle$ (red) for the tunable transmon circuit with parameters as in (b). We highlight the susceptibility of the qubit frequency to external flux by drawing the slope of the spectrum, $\partial f_{01}/\partial\Phi_{\text{ext}}$ at two points on the spectrum. We highlight the susceptibility of the qubit frequency to external flux by drawing the slope of the spectrum, $\partial f_{01}/\partial\Phi_{\text{ext}}$ at two points on the spectrum. **(d)** Circuit diagram of a fluxonium comprising a capacitor (charging energy E_C), Josephson junction (energy E_J), and inductor (inductive energy E_L) in parallel. **(e)** Similar to (b), for the fluxonium circuit with energies $E_C/h = 1.3\,\text{GHz}$, $E_J/h = 5.7\,\text{GHz}$, $E_L/h = 0.5\,\text{GHz}$. **(f)** Similar to (c). We highlight the large anharmonicity, $\alpha/h = f_{12} - f_{01}$, compared to that of the transmon levels in (c).

2.4.5 Key Qubit Features for this Thesis

Here, we highlight two qubit features which are especially relevant for the experimental results of this thesis.

First, we introduce the **anharmonicity**,

$$\alpha \equiv E_{12} - E_{01}, \tag{2.95}$$

which tells us how well-separated the ground and first-excited-state transition energy is from that of the next highest transition. As qubits typically comprise the lowest two energy levels of a circuit, the anharmonicity gives us a limit on the bandwidth of control pulses. Exceeding that limit results in populating higher-lying levels outside of the qubit subspace. For the transmon, $\alpha/2\pi \approx -E_C \sim -200\,\mathrm{MHz}$. This limits the bandwidth of control pulses to approximately $2\pi/\alpha \approx 5\,\mathrm{ns}$ [53, 101]. On the other hand, fluxoniums typically display $\alpha \gtrsim 1\,\mathrm{GHz}$. For the results in Chapter 6, we note that the utilization of a fluxonium enabled the realization of fast gates which were limited by the breakdown of the RWA (pulse time competing with the qubit Larmor period $2\pi/\omega_{01}$) rather than leakage into higher levels (pulse time competing with $2\pi/\alpha$).

Now, we introduce an idea which will become the foundation of the physics we investigate in Chapter 5. The ability to tune qubit frequency with external flux also results in qubits being sensitive to fluctuations in that flux, referred to as **flux noise**. One can elect to utilize fixed-frequency qubits, however, this places a demanding requirement on the fabrication of devices which require specific frequency layouts [102]. Flux-tunable qubits, on the other hand, enable different gate schemes [77, 103] and the dynamic adjustment of frequencies to avoid material defects [90, 104, 105]. The slope of the qubit frequency as a function of flux determines (to first order) the sensitivity of the qubit coherence to flux noise. Points where $\frac{\partial\omega_{01}}{\partial\Phi} = 0$ are known as **sweet-spots**[6]. We will detail the decoherence of qubits from low-frequency flux noise in the next chapter, and investigations elucidating the physics behind flux noise in Chapter 5.

---

[6] Moreover, one can modulate the flux to create effective **dynamical sweet spots** [106].

2.4.6 Dispersive Readout

As the final part of this chapter, we describe the current most common method to perform readout of a superconducting qubit [103, 107]. The method comprises coupling a qubit to a far-detuned resonator (or cavity), described by the famous **Jaynes-Cummings Hamiltonian**

$$H = -\hbar\omega_q \frac{\sigma_z}{2} + \hbar\omega_r a^\dagger a + \hbar g(a^\dagger \sigma_- + a\sigma_+), \tag{2.96}$$

where ω_q is the frequency of the qubit, ω_r is the frequency of the resonator, g is the qubit-cavity coupling, and $\sigma_\pm$ are the qubit raising and lowering operators, defined by

$$\sigma_+ |0\rangle = |1\rangle\,, \quad \sigma_+ |1\rangle = 0 \tag{2.97}$$

$$\sigma_- |1\rangle = |0\rangle\,, \quad \sigma_- |0\rangle = 0. \tag{2.98}$$

We interpret the last terms in the parenthesis of Eq. (2.96) as exchanging excitations between the qubit and resonator[7]. This interaction arises from direct capacitive coupling [89]. In the regime of $|\Delta| = |\omega_q - \omega_r| \gg g$, we can perform a time-independent unitary transformation $U = e^{\lambda(a\sigma_+ - a^\dagger\sigma_-)}$, where $\lambda = g/\Delta \ll 1$, yielding

$$\tilde{H} = UHU^\dagger \tag{2.99}$$

$$= \hbar\left(\omega_q + \frac{g^2}{\Delta}\right)\frac{\sigma_z}{2} + \hbar a^\dagger a\left(\omega_r + \frac{g^2}{\Delta}\sigma_z\right) + \mathcal{O}(\lambda^2). \tag{2.100}$$

The approximation in small $\lambda = g/\Delta$ is known as the **dispersive approximation**, and amounts to operating the qubit and cavity in the far-detuned regime. The first term of Eq. (2.99) corresponds to the qubit, which has inherited a frequency shift $\frac{g^2}{\Delta}$. This is called

---

[7] In general, one will have terms also proportional to simultaneously losing or gaining excitations in both the qubit and resonator, e.g., $a\sigma_-$ or $a^\dagger\sigma_+$. Discarding these terms is also known as the rotating-wave approximation, and it is analogous to the approximation we discussed, now in the context of a fully quantum treatment of qubit-light coupling. In such a treatment, the drive electromagnetic field interacts with the qubit with a Hamiltonian term $(\sigma_- + \sigma_+)(a + a^\dagger)$. Such an interaction arises between the electronic states of an atom and a real-space electromagnetic field.

the **Lamb shift**, and arises from the vacuum fluctuations of the resonator. The second term corresponds to the resonator, which has now inherited a qubit-state-dependent frequency shift $\chi_{01} = \frac{g^2}{\Delta}\sigma_z$. This shift is commonly called the **dispersive shift**, and allows us to determine the qubit state by probing the resonator [89].

A more thorough calculation including more of the original qubit Hilbert space (beyond just the two levels we utilize) yields corrections to the dispersive shift. One approaches this calculation by considering the more complete qubit-resonator Hamiltonian

$$H = -\hbar \sum_i \omega_i \left|i\right\rangle \left\langle i\right| + \hbar\omega_r a^\dagger a + \hbar g \hat{n}(a_r^\dagger \sigma_- + a_r \sigma_+), \tag{2.101}$$

where the first term represents the qubit in its eigenbasis, and $\hat{n}$ is the charge operator for the circuit [78]. By labelling eigenstates as $|n, m\rangle$ where the first index denotes the qubit excitation number and the second denotes the resonator excitation number, the dispersive shift is generally defined as the shift in the resonator frequency depending on the qubit state:

$$2\chi \equiv (\omega_{1,m+1} - \omega_{1,m}) - (\omega_{0,m+1} - \omega_{0,m}). \tag{2.102}$$

Energy level shifts can be computed via **perturbation theory**, see Ref. [78]. We highlight that for qubits such as the transmon, the Hamiltonian eigenstates enable relatively straightforward calculation of the dispersive shift via **selection rules**, i.e., rules reflecting which matrix elements $\left\langle i\right| \hat{n} \left|j\right\rangle$ are zero or non-zero. This calculation is not as analytically straightforward for other qubits, such as the fluxonium.

2.5 Summary

We have now completed the first out of two primary background chapters, congratulations! Before moving on, we emphasize the major ideas covered. First, we introduced some basic aspects of quantum mechanics including the unitary evolution of a system generated by a Hamiltonian operator, and the measurement of a system which modifies its state. We defined mixed states which must be described by a statistical ensemble represented by a density operator. We developed the geometry of qubits via the Bloch-sphere picture, with pure states on the unit sphere and mixed states on the interior, and qubit unitary operations represented by rotations. We then detailed qubit control via resonant, linearly-polarized drives, including their breakdown into co- and counter-rotating components and the rotating-wave approximation for weak, resonant drives. We then highlighted that a qubit irradiated by a drive field will experience two common frequency shifts: the AC Stark shift and the Bloch-Seigert shift. Finally, we described the realization of qubits with superconducting circuits, including the two most common qubits of today, the transmon and fluxonium. In the next chapter, we will introduce models of decoherence, describing what happens when a qubit interacts with uncontrolled external degrees of freedom, otherwise known as noise.

Chapter 3

Noise and Decoherence

In this chapter, we discuss noise and how it degrades the purity of quantum states. We introduce the idea of noise in Section 3.1, how it is modeled in Section 3.2, and how it affects qubits in Section 3.3. We introduce a Hamiltonian description of decoherence with analytical results in the long-time limit in Section 3.4, and present the filter-function formalism of decoherence from qubit frequency noise in Section 3.5. Finally, we introduce the idea of noise spectroscopy (utilizing a qubit to map its noise environment) in Section 3.6.

3.1 Noise Introduction

We begin this chapter by posing a deceptively simple question: what is “noise”?

As it turns out, there is no formal answer (comprising a technical definition) to this question [108]. If you do not believe me, I encourage you to ask a panel of noise experts. This might seem surprising, as scientists use the term frequently and noise comprises a central topic in numerous fields of research.

3.1.1 What is noise?

As there is no formal consensus, we provide a definition which allows the word noise to be used unambiguously in this thesis. We base our definition on two premises: (1) noise is associated with randomness (i.e., unpredictability) in a measured signal, and (2) with full knowledge of a system, there would be no noise, as the evolution of any measured quantity should be deterministic[1].

Definition 3.1: Noise

Noise comprises unpredictable fluctuations in a measured quantity, characterized by a lack of deterministic reproducibility, but often with well-defined statistical properties (defined by averaging over an **ensemble** of nominally identical experiments).

Our definition captures two important aspects of noise. First, noise is defined in association with a quantity under investigation, and is not an intrinsic property of a physical system. Second, noise is associated with our (partial) ignorance of a physical system, assuming that evolution is deterministic. In other words, there would be no noise if we had full predictive power of a physical system, e.g., by knowing the full system state and the equations governing its evolution. This idea is closely related to our ability as experimenters to prepare identical copies of a system for repeated measurements. If we cannot prepare identical copies, due to uncontrolled (or ignored) degrees of freedom, then the system under investigation will certainly be subject to noise.

The ability to create identical preparations of a system and control all relevant degrees of freedom is the foundation on which all experimental science is built. However, we can already appreciate that noise is an unavoidable part of this foundation – it is (effectively) impossible to control all degrees of freedom in a real, material system, and so noise will always accompany experiments. This gives rise to an aesthetic component of experimental science which is the ability to design experiments that isolate phenomena from noise and

---

[1] We comment on measurement in quantum mechanics in the following paragraphs.

extract relevant signals as unambiguously as possible.

We also highlight that one can alternatively view noise as the signal of interest, and study its statistical properties in order to extract information about the physics generating the fluctuations. One of the most prominent historical examples of this is the study of the statistics of indistinguishable particles, elucidating quantum interference phenomena with no classical analogues [109–112]. Another of the most prominent examples is the study of the cosmic microwave background (CMB) radiation [113], comprising a fingerprint of the early universe imprinted on the microwave noise observed when looking at the empty sky. In this thesis, we utilize noise (and the impact of noise on qubit decoherence) as the signal of interest for two of our major results, in Chapter 5 and Chapter 7.

Before continuing, we draw a line in the sand which the reader may or may not agree with. We learned that in quantum systems, measurement outcomes are inherently probabilistic according to Born's rule. This leads to the question, is randomness of measurement outcomes from identical experiments something we should call noise? With our definition, the answer depends on if the probabilistic nature arises from uncontrolled (or perhaps hidden) degrees of freedom. In fact, it is established that the probabilistic nature of quantum measurements cannot be a consequence of hidden **local** degrees of freedom[2] [114]. Barring the existence of nonlocal degrees of freedom (which would violate the principle of **causality**), we argue that quantum measurement outcomes should not be considered noise, even though they do constitute a true source of **randomness** [115]. We choose not to call this randomness "noise" for the following reason: we can construct full knowledge of a quantum state through experiments on an ensemble of identical copies of the system. However, we cannot construct full knowledge of the state of a system containing uncontrolled degrees of freedom which we cannot prepare identically in an ensemble. Indeed, the term **quantum noise** is reserved for a phenomenon distinct from measurement which we will describe in Section 3.2.8.

---

[2] For local degrees of freedom, information can only propagate between them at the speed of light, resulting in the property of **Lorentz-invariance** which is required by the theory of relativity.

3.2 Modelling Noise

In this section, we introduce the mathematics necessary to characterize noise at a level useful for experimental physicists. In broad strokes, the effects of uncontrolled (or ignored) degrees of freedom on a quantity of interest can often be captured by introducing a random variable with the correct coupling and statistical properties[3].

As we stated in our definition, noise is generically unpredictable, but commonly has consistent **statistical** properties, i.e., properties which are defined by averaging over nominally identical experiments (our ensemble). As we will primarily focus on time-domain noise, let us make these ideas concrete by studying a noise process $\eta(t)$, where t represents time, and we will take the units of η to be $[\eta] = \mathrm{V}$. We will treat t as a continuous variable, and note that analogues for all calculations exist for discrete-time processes (which we will use in practice, when we can only take measurements at discrete times). Let us now construct an ensemble of noise processes, i.e., instances of the noise $\eta(t)$ for N different trials of an experiment. Our ensemble is given by $\{\eta_0(t), \eta_1(t), \cdots, \eta_N(t)\}$.

3.2.1 One-point distribution

The most simple properties of noise we can study are the **moments** of its value at a given time, given by a probability distribution function $p(\eta, t)$. As we make our ensemble size larger, we are guaranteed convergence of the sample properties (computed with N trials) to the true properties (determined by $p(\eta, t)$) from the **central-limit theorem**.

The **mean** (average) is given by the first moment,

$$\langle \eta(t) \rangle = \lim_{N\to\infty} \frac{1}{N} \sum_i \eta_i(t) = \int \eta p(\eta, t) d\eta. \tag{3.1}$$

The **variance** (average squared deviation from the mean) is given by the second moment

---

[3] The rigorous description of noise developed by mathematicians is given by the theory of **stochastic processes**, providing the foundation of the results in this section.

about the mean:

$$\langle(\eta(t)-\langle\eta(t)\rangle)^2\rangle = \langle\eta(t)^2\rangle - \langle\eta(t)\rangle^2 \tag{3.2}$$

$$= \lim_{N\to\infty}\left(\frac{1}{N}\sum_i \eta_i(t)^2\right) - \left(\lim_{N\to\infty}\frac{1}{N}\sum_i \eta_i(t)\right)^2 \tag{3.3}$$

$$= \int \eta^2 p(\eta,t)d\eta - \left(\int \eta p(\eta,t)d\eta\right)^2. \tag{3.4}$$

The square root of the variance yields the **standard deviation**, also referred to as the **root-mean-square** (RMS) deviation from the mean: $\sqrt{\langle(\eta(t)-\langle\eta(t)\rangle)^2\rangle}$.

We won't provide expressions for higher moments, but will mention for completeness two more commonly studied properties of the one-point distribution function. The **skewness** (cubed deviation about the mean, normalized by the standard deviation) yields information about the symmetry of the distribution about the mean. The **kurtosis** (deviation about the mean, normalized by the standard deviation, to the fourth power) yields information about the heaviness of the tail of the distribution.

3.2.2 Two-point distribution

The one-point distribution function can tell us much about a noise process, but does not completely specify it. Indeed, $p(\eta,t)$ tells us nothing about how the noise at one time is related to the noise at another, in other words, about the noise dynamics. To this end, we introduce the two-point distribution function, $p(\eta_1,t_1;\eta_2,t_2)$. We can now define the **autocorrelation function**, which tells us how noise at one time is related to noise at another:

$$C_{\eta,\eta}(t_1,t_2) = \langle\eta(t_1)\eta(t_2)\rangle = \int \eta_1\eta_2 p(\eta_1,t_1;\eta_2,t_2)d\eta_2 d\eta_2. \tag{3.5}$$

This is the highest-point characterization needed for our work. Before moving on to simplifying assumptions, we highlight that higher-point distribution functions can completely characterize a noise process which is continuous in the analytical sense [116].

3.2.3 Common Assumptions

Now that we have some statistical quantities which give us a handle on noise processes, we can introduce common, physically-motivated simplifying assumptions which are used in practice. The first assumption we will introduce is that of a **stationary** process.

Definition 3.2: Stationary Noise

A noise process $\eta(t)$ is **strict-sense stationary** if $\eta(t)$ has the same distribution as $\eta(t+\tau)$ for all t and τ. This is equivalent to all finite-point distribution functions being invariant when considering translations in time.

For a stationary noise process, the autocorrelation function (3.5) can be shifted in time such that $t_1 \rightarrow 0$ and $t_2 \rightarrow t_2 - t_1$. In this case, we can write

$$C_\eta(\tau) \equiv C_{\eta,\eta}(0, \tau = t_2 - t_1) = \langle \eta(0)\eta(\tau) \rangle. \tag{3.6}$$

We define the **correlation time** τ_c as the characteristic timescale on which $C_\eta(\tau)$ tends to zero. As it turns out, it is often the case that $C_{\eta,\eta}(t_1, t_2)$ depends only on the time difference τ while the full stationary condition is not satisfied, and so a more commonly used assumption is that of **weak- or wide-sense stationary** noise, for which the second moment is finite at all times and the autocorrelation only depends on the difference in times.

The notion of stationary noise is well-motivated physically for thermal fluctuations of systems in thermodynamic equilibrium. The fluctuations in such systems are described by the physics of equilibrium statistical mechanics: the distribution of state occupancy in a system is determined by the system's microscopic configurations and their associated energies (referred to as the **Boltzmann distribution**). So long as the energies of the states are time-invariant, the thermal fluctuations are stationary.

We now introduce another simplifying assumption, that of **Gaussian noise**, which is characterized by all distribution functions taking on a multivariate Gaussian form. In this case, the mean and autocorrelation functions entirely characterize the noise process. Gaussian noise is extremely common in practice. We can understand this as a consequence of the central limit theorem, which tells us that the amplitude distribution of the mean of independent random variables will have Gaussian fluctuations about the true mean. For example, a large number of independent magnetic moments displaying thermal fluctuations will display an effective net magnetization along a particular axis with Gaussian fluctuations.

3.2.4 Power Spectral Density

The frequency-domain structure of noise can be difficult to appreciate from the autocorrelation function itself. To this end, we now introduce another common noise characterization for stationary noise processes, the **power spectral density (PSD)**. We begin by introducing the windowed Fourier transform of a signal $\eta(t)$,

$$\eta_T(\omega) = \frac{1}{\sqrt{T}} \int_{-T/2}^{T/2} e^{i\omega t} \eta(t) dt. \tag{3.7}$$

The normalization $\sqrt{T}$ can be understood by recognizing that for $T \gg \tau_c$, the integral represents the final position after a random walk with $N = T/\tau_c$ increments of $e^{-i\omega\Delta t}\eta(t+\Delta t)$, which will generically scale as $\sqrt{T}$. The normalization prevents divergence of $\eta_T(\omega)$ in the limit $T \to \infty$. The double-sided power spectral density is simply defined as

$$S_\eta(\omega) \equiv \lim_{T\to\infty} \langle |\eta_T(\omega)|^2 \rangle, \tag{3.8}$$

such that the average (over both time and noise ensemble) power is given by

$$P_\eta = \lim_{T\to\infty} \frac{1}{T} \int_{-T/2}^{T/2} |\eta(t)|^2 dt = \int_{-\infty}^{\infty} S_\eta(\omega) d\omega, \tag{3.9}$$

where the second quality utilized **Parseval's theorem**. In plain words, $S_\eta(\omega)$ is the frequency-density of power. We can re-express $S_\eta(\omega)$ in terms of the autocorrelation function via the **Wiener-Khinchin theorem** as

$$S_\eta(\omega) = \int_{-\infty}^{\infty} e^{i\omega\tau} \langle \eta(\tau)\eta(0) \rangle d\tau. \tag{3.10}$$

Eq. (3.10) is also commonly used to define the PSD. The PSD has units of

$$[S_\eta] = \frac{[\eta]^2}{\text{Hz}}. \tag{3.11}$$

Given a PSD, we can work backwards and derive the autocorrelation,

$$C_\eta(\tau) = \frac{1}{2\pi} \int_{-\infty}^{\infty} e^{-i\omega\tau} S_\eta(\omega) d\omega. \tag{3.12}$$

We are now equipped to appreciate some common examples of noise dynamics.

3.2.5 White Noise

The most simple example is noise in the limit of zero correlation time, with

$$C_{\text{white}}(\tau) = S_0\delta(\tau) \tag{3.13}$$

$$S_{\text{white}}(\omega) = S_0, \tag{3.14}$$

where $\delta(t)$ is the **Dirac delta function**. This noise is known as **white noise**, since it has equal power at all frequencies, analogous to white light comprising all optical frequencies. White noise is a useful toy model for noise which has significantly shorter correlation time than relevant experimental timescales.

3.2.6 Quasistatic Noise

Another simple example is noise in the opposite limit, that of infinite correlation time. Such noise is referred to as **quasistatic noise**, as it is static during any single experiment, but changes experiment-to-experiment. Quasistatic noise is characterized by

$$C_{\mathrm{qs}}(\tau) = \sigma^2 \tag{3.15}$$

$$S_{\mathrm{qs}}(\omega) = 2\pi\sigma^2\delta(\omega). \tag{3.16}$$

This is useful as a toy model for noise with a correlation time much longer than relevant experimental timescales.

3.2.7 Exponentially-Correlated Noise

Another example, which is the one we encounter most in practice, that of noise with exponential correlation (of timescale τ_c),

$$C_{\exp}(\tau) = \sigma^2 e^{-t/\tau_c} \tag{3.17}$$

$$S_{\exp}(\omega) = \frac{2\sigma^2\tau_c}{1+(\omega\tau_c)^2}. \tag{3.18}$$

The PSD of exponentially-correlated noise takes the form of a **Lorentzian function** (also known as a **Cauchy distribution**). At low frequencies ($\omega\tau_c \ll 1$), the PSD resembles that of white noise $S_{\exp}(\omega) \propto$ const., and at high frequencies ($\omega\tau_c \gg 1$), the PSD assumes a power-law decay as $S_{\exp}(\omega) \propto 1/\omega^2$, known as **Brown noise**[4].

A common example of exponentially-correlated noise is the **random-telegraph signal (RTS)**, comprising a variable $\eta(t)$ that randomly toggles between $+\sigma$ and $-\sigma$ with an average rate $\lambda = 1/2\tau_c$. We plot an ensemble of simulated RTSs in Fig. 3.1(a) and the ensemble amplitude distribution in Fig. 3.1(b). Assuming that switching events occur independently, the probability of k switching events occurring in a time interval t is given by the **Poisson**

---

[4] Brown noise takes its name from the random motion (referred to as **Brownian motion**) of particles in a fluid, as first studied by Robert Brown [117] and modelled by Bachelier [118], Einstein [3], and Smoluchowski [119]. The velocity of a particle undergoing Brownian motion is typically modelled as a noise process with exponential correlation, referred to as an **Ornstein-Uhlenbeck process** (which is a stationary **Gauss-Markov process**).

distribution,

$$P(N(t) = k) = \frac{(\lambda t)^k e^{-\lambda t}}{k!}. \tag{3.19}$$

We can calculate the autocorrelation function by noting that the product $\eta(\tau)\eta(0)$ will always have magnitude $|\sigma^2|$, but will have opposite sign if the total number of events is odd or even:

$$\begin{aligned} C_{\mathrm{RTS}}(\tau) &= \sigma^2[P(N(\tau) = \text{even}) - P(N(\tau) = \text{odd})] && (3.20) \\ &= \sigma^2 e^{-2\lambda t} && (3.21) \\ &= \sigma^2 e^{-t/\tau_c}. && (3.22) \end{aligned}$$

We plot $C_{\mathrm{RTS}}(\tau)$, calculated numerically from the simulated RTS ensemble, in Fig. 3.1(c), and plot the corresponding PSD in Fig. 3.1(d). Random-telegraph signals are ubiquitous in real systems. For solid-state technologies in particular, it is common to encounter material defects which have two stable configurations and toggle randomly between them due to thermal fluctuations or quantum tunneling [120–122].

Warning 3.1: Dynamics vs. Amplitude Distribution

Although we have given some commonly encountered autocorrelation functions and PSDs, we emphasize that these do not entirely characterize a noise process unless the Gaussian assumption is made. Specifically, **distinct noises can have identical autocorrelation functions (and PSDs)**. To highlight this, we plot examples of two different noise processes, with identical dynamical properties but differing amplitude distributions, in Fig. 3.1. Solely focusing on the PSD, without paying homage to the amplitude distribution (which mathematician Benoit Mandelbrot referred to as the **geometry of the noise** [123]), was the pitfall of the scientific thrust to find a unifying theory of the infamous noise with $S(\omega) \propto 1/\omega$, which we detail in Chapter 4.

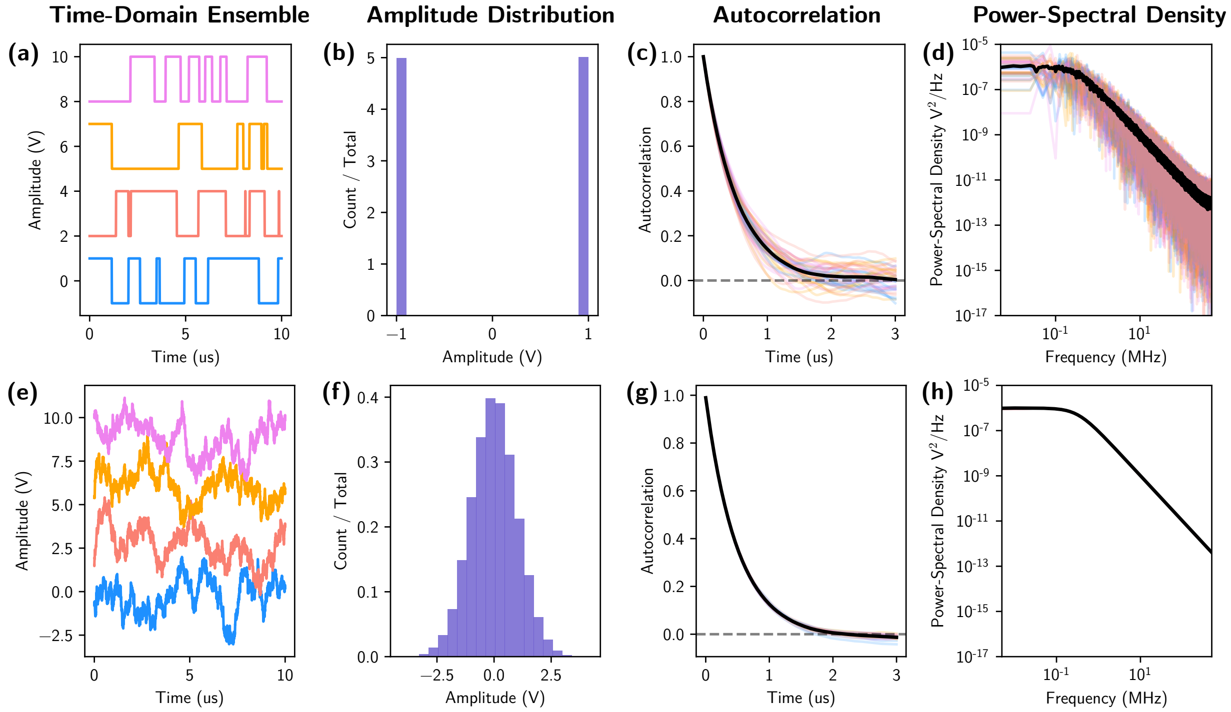
Time-Domain Ensemble

Amplitude Distribution

Autocorrelation

Power-Spectral Density

Figure 3.1: **Examples of noise and noise characterizations.** **(a)** Ensemble comprising noise instances $\{\eta_1(t), \eta_2(t), \cdots\}$ in the time domain, **(b)** the corresponding one-point noise amplitude distribution $p(\eta)$, **(c)** autocorrelation function $\langle \eta(\tau)\eta(0)\rangle$, and **(d)** power-spectral density $S_\eta(\omega)$ for a stationary random-telegraph noise (RTS). **(e-h)** Same as (a-d) for Gaussian-distributed noise. We highlight the distinct impression left by comparing the time-domain ensembles of (a) and (e), despite the identical dynamical characterizations.

3.2.8 Classical vs. Quantum Noise

So far, we have considered real-valued noise processes ($\eta(t) \in \mathbb{R}$). For real-valued noise processes that are stationary, the correlation function is real and symmetric in time: $C_\eta(\tau) = C_\eta(-\tau) \in \mathbb{R}$ (in other words, $C_\eta(\tau)$ is even). As a consequence, the PSD is real and symmetric in frequency[5]:

$$S_\eta(\omega) = \int_{\tau=-\infty}^{\tau=\infty} e^{i\omega\tau} C_\eta(\tau) d\tau \tag{3.23}$$

$$= -\int_{-\tau=\infty}^{-\tau=-\infty} e^{-i\omega\cdot(-\tau)} C_\eta(-\tau) d(-\tau) \tag{3.24}$$

$$= S(-\omega). \tag{3.25}$$

The feature of $\eta(t)$ on which the frequency symmetry of $S_\eta(\omega)$ relies is

$$\langle[\eta(t_1), \eta(t_2)]\rangle = \langle\eta(t_1)\eta(t_2) - \eta(t_2)\eta(t_1)\rangle = 0. \tag{3.26}$$

In words, the noise **commutes** with itself at different times such that for stationary noise, the autocorrelation is symmetric. We will denote noise with this property **classical noise**.

This inspires the following question: what if we consider a noise process which no longer commutes with itself at different times? We will call this **quantum noise**. Since both real and imaginary numbers are commutative, we cannot create this behavior by simply considering complex $\eta(t)$. Instead, we take inspiration from the algebra of conjugate operators in a Hilbert space. As a toy example, we can consider the autocorrelation of σ_x for a qubit,

$$C_{\sigma_x}(\tau) = \langle\sigma_{x,H}(\tau)\sigma_{x,H}(0)\rangle, \tag{3.27}$$

where $\langle\cdot\rangle$ now represents the quantum expectation value, and $\sigma_{x,H}(t)$ represents the σ_x operator in the **Heisenberg picture** of quantum mechanics, defined below.

---

[5] One can also see this from Eq. (3.8), noting that the Fourier transform of a real-valued function will satisfy $\eta(\omega)^* = \eta(-\omega)$ such that $|\eta(\omega)|^2 = \eta(\omega)\eta(\omega)^* = \eta(\omega)\eta(-\omega)$.

Definition 3.3: Heisenberg Picture of Quantum Mechanics

In Chapter 2, we described the dynamics of quantum mechanics with a time-dependent state vector $|\Psi(t)\rangle$ obeying the Schrödinger equation (referred to as the **Schrödinger picture**). An alternative, equivalent formulation is given by utilizing a constant state vector $|\Psi(0)\rangle$ and evolving operators, e.g. A_H, in time according to

$$\frac{dA_H(t)}{dt} = \frac{i}{\hbar}[H_H(t), A_H(t)] + \left(\frac{\partial A_S}{\partial t}\right)_H . \tag{3.28}$$

Operators in the Heisenberg picture are related to those in the Schrödinger picture by $A_H(t) = U(t)^\dagger A_S(t) U(t)$, where $U(t)$ is the time-evolution operator determined by the system Hamiltonian. Operator expectation values are given by

$$\langle A\rangle(t) = \langle\Psi(t)|\, A_S(t)\, |\Psi(t)\rangle = \langle\Psi(0)|\, A_H(t)\, |\Psi(0)\rangle\, . \tag{3.29}$$

We can re-cast the correlator Eq. (3.27) in the more familiar Schrödinger picture as

$$C_{\sigma_x}(\tau) = \langle U^\dagger(\tau)\sigma_x U(\tau)\sigma_x\rangle. \tag{3.30}$$

For a qubit with Hamiltonian $H = -\frac{\hbar\omega}{2}\sigma_z$, we have $U(t) = e^{i\omega\sigma_z t/2}$, and we find

$$C_{\sigma_x}(\tau) = \langle\sigma_x^2\rangle\cos(\omega\tau) + \langle\sigma_x\sigma_y\rangle\sin(\omega\tau) \tag{3.31}$$

The first term is real, as $\sigma_x^2 = I$. However, the second term becomes complex, as $\sigma_x\sigma_y = i\sigma_z$. This term is zero when the qubit is in the maximally mixed state, but non-zero when the qubit has some polarization $\langle\sigma_z\rangle \neq 0$ (i.e., if the qubit displays more population in either the ground or excited states).

To make this concrete, we can calculate the expectation value assuming the qubit is in thermal equilibrium with an environment at temperature T, described by a density matrix from equilibrium statistical mechanics,

$$\rho = \frac{1}{e^{\beta\hbar\omega/2} + e^{-\beta\hbar\omega/2}} \begin{pmatrix} e^{\beta\hbar\omega/2} & 0 \\ 0 & e^{-\beta\hbar\omega/2} \end{pmatrix}, \tag{3.32}$$

where $\beta = 1/k_B T$, and k_B is Boltzmann's constant. Without giving a more formal introduction to statistical mechanics, we can appreciate that this density matrix has some core features: (1) there is no phase coherence, as it is washed away by thermal fluctuations, (2) at infinite temperature ($k_B T/\hbar\omega \to \infty$), we find equal populations in $|0\rangle$ and $|1\rangle$, and (3) at zero temperature ($k_B T/\hbar\omega \to 0$), we find population residing solely in the ground state $|0\rangle$[6]. Calculating Eq. (3.30), we find

$$C^{\mathrm{eq}}_{\sigma_x}(\tau) = \cos(\omega\tau) - i\tanh\left(\frac{\hbar\omega}{2k_B T}\right)\sin(\omega\tau). \tag{3.33}$$

In the infinite-temperature limit, we see $C^{T\to\infty}_{\sigma_x}(\tau) \to \cos(\omega\tau)$, yielding a real, symmetric correlation function, consistent with our notion of "classical" noise. In the zero-temperature limit, we instead see $C^{T\to 0}_{\sigma_x}(\tau) \to e^{-i\omega\tau}$, yielding an imaginary correlation function! The complex nature of $C_{\sigma_x}(\tau)$ will generically yield asymmetry in the power spectral density: $S_{\sigma_x}(\omega) \neq S_{\sigma_x}(-\omega)$.

Aside: Classical Generation of Quantum Noise?

Here, we pose a potentially interesting idea poking at the nature of quantum noise. So far, we have constructed an example of quantum noise which is not quite noise, i.e., it is an autocorrelation function of the transverse dynamics of a qubit Larmor precessing. Let us

---

[6] The probability of finding a system in a state with a particular energy when in thermal equilibrium with a bath is one of the foundational results of statistical mechanics as first described by Ludwig Boltzmann. This so-called **Boltzmann distribution** can be derived by considering the distribution that maximizes entropy, which ties statistical mechanics to information theory.

instead consider two noise processes which can drive σ_x and σ_y independently:

$$\hat{\eta}(t) = \eta_x(t)\sigma_x + \eta_y(t)\sigma_y, \tag{3.34}$$

where $\eta_{x/y}(t)$ are real numbers. The autocorrelation of our operator-valued noise process is given by

$$\begin{aligned}
C_{\hat{\eta}}(\tau) &= \langle \hat{\eta}(\tau)\hat{\eta}(0) \rangle && (3.35)\\
&= \langle (\eta_x(\tau)\sigma_x + \eta_y(\tau)\sigma_y)(\eta_x(0)\sigma_x + \eta_y(0)\sigma_y) \rangle && (3.36)\\
&= \langle [\eta_x(t)\eta_x(0) + \eta_y(t)\eta_y(0)] \cdot I + i[\eta_x(\tau)\eta_y(0) - \eta_y(\tau)\eta_x(0)] \cdot \sigma_z \rangle && (3.37)\\
&= C_{\eta_x}(\tau) + C_{\eta_y}(\tau) + i\langle [\eta_x(\tau)\eta_y(0) - \eta_y(\tau)\eta_x(0)]\sigma_z \rangle && (3.38)
\end{aligned}$$

where we have used $\sigma_i^2 = I$, $\sigma_x\sigma_y = i\sigma_z$, and $\sigma_y\sigma_x = -i\sigma_z$. Assuming that $\eta_{x/y}(\tau)$ are stationary and uncorrelated, the imaginary term vanishes. If instead we consider only $\eta_x(\tau)$ stationary with $\langle \eta_x(\tau) \rangle \neq 0$ and $\langle \eta_y(\tau) \rangle = \lambda\tau$, we can see the imaginary term can be finite. However, we note that the PSD is only well defined for noise which is stationary, and so we have waded into muddy mathematical waters. Regardless, we wonder if playing with the correlations between $\eta_x(\tau)$ and $\eta_y(\tau)$ and introducing non-stationary noise processes might lead to interesting qubit physics.

3.3 Qubit Decoherence from Noise

Now that we are familiar with the idea of noise, we can study its influence on qubits. First, we establish the case of unitary evolution. For a qubit with initial density matrix $\rho(0)$, evolved with unitary time-evolution operator U, the state purity will evolve as

$$\begin{aligned}\mathrm{tr}(\rho(t)^2) &= \mathrm{tr}(U\rho(0)U^\dagger U\rho(0)U^\dagger) && (3.39)\\ &= \mathrm{tr}(U\rho(0)^2U^\dagger) && (3.40)\\ &= \mathrm{tr}(\rho(0)^2), && (3.41)\end{aligned}$$

where we used the cyclic property of the trace for the last equality. The result is simple: unitary evolution preserves the purity of a state. Therefore, decoherence results from non-unitary evolution of the qubit. Effective non-unitary evolution arises when a system interacts with an environment. The study of quantum systems coupled to environments (i.e, **open quantum systems**), has a rich history with significant literature [68, 124].

Our treatment of decoherence will focus on the Hamiltonian

$$H = -\frac{\hbar\omega}{2}\sigma_z + H_\eta(t), \tag{3.42}$$

where $H_\eta(t)$ is a time-dependent noise term of the form

$$\frac{H_\eta(t)}{\hbar} = \frac{1}{2}\left[\eta_x(t)\sigma_x + \eta_y(t)\sigma_y + \eta_z(t)\sigma_z\right]. \tag{3.43}$$

We will refer to the associated PSD of $\eta_\alpha(t)$ as $S_\alpha(\omega)$ for $\alpha \in \{x, y, z\}$. In general, these noise processes correspond to operators acting on degrees of freedom outside of the qubit subspace (the environment), and their statistical properties depend on the environment's structure and dynamics. When the environment is at sufficiently high temperature, the noises can be treated as classical stochastic processes [125].

Although Eq. (3.43) invokes a feeling of symmetry between noise coupled along different Bloch-sphere axes, the symmetry is broken by the quantization axis of the qubit. Due to the qubit Larmor precession, the decays of $\langle\sigma_z\rangle$ (related to eigenstate populations) and $\langle\sigma_{x/y}\rangle$ (related to phase coherence) are distinct.

3.3.1 Population Decay: T_1

The decay of eigenstate populations (ρ_{00} and ρ_{11}) is referred to as **longitudinal relaxation**, as it corresponds to depolarization of the Bloch vector along the $\hat{z}$ axis. The timescale associated with this decay is referred to as T_1. The Bloch sphere gives us an intuitive picture: depolarization along $\hat{z}$ arises from **transverse noise** that couples to the qubit via σ_x or σ_y [Fig. 3.2(a)]. Processes that affect state populations (i.e., T_1 processes) change the expectation value of the state energy $\langle H \rangle = \mathrm{tr}(\rho H)$, and are therefore a consequence of energy exchange between a qubit and its environment.

We can gain further insight by considering the simple scenario of an initial state $|\Psi_0\rangle = |1\rangle$ and noise purely along σ_x ($\eta_y(t) = \eta_z(t) = 0$). Assuming a small noise amplitude relative to the qubit frequency, application of time-dependent perturbation theory yields a rate of population transfer from $|1\rangle \to |0\rangle$ [125–127][7]

$$\Gamma_{\downarrow} = \frac{\partial |\langle 0|\Psi(t)\rangle|^2}{\partial t} = \frac{1}{4} S_x(\omega). \tag{3.44}$$

In deriving Eq. (3.44), no assumption on the commutation of $\eta(t)$ at different times is used, so one must keep careful track of the ordering of $\eta_x(t)$ and $\eta_x(0)$. The same analysis for $|\Psi_0\rangle = |0\rangle$ yields population transfer from $|0\rangle \to |1\rangle$ with rate

$$\Gamma_{\uparrow} = \frac{1}{4} S_x(-\omega). \tag{3.45}$$

Our first insight is that T_1 processes rely on transverse noise power at the qubit frequency. This can be understood geometrically: in the frame co-rotating with the qubit such that the zero-noise dynamics are trivial (the qubit stays still), $|0\rangle \leftrightarrow |1\rangle$ transitions arise from the $\hat{x}$

---

[7] This expression is a simple example of **Fermi's golden rule**, which tells us that the transition rate from an eigenstate i to a state f is given, to first order, by $\Gamma_{i\to f} \propto |\langle f|H_\eta|i\rangle|^2 S_\eta(\omega)$, where H_η is the perturbing Hamiltonian and $S_\eta(\omega = (E_f - E_i)/\hbar)$ is the noise power spectrum at the transition frequency. The environmental (and generally quantum) PSD at a frequency ω is related to the density of environmental states with energy $\hbar\omega$ by the **Lehmann representation**.

and $\hat{y}$ noise components that are static in the rotating frame such that they will not average to zero. A static transverse noise component in the rotating frame oscillates at frequency ω in the lab frame.

Energy Relaxation and Absorption

Our second insight is that Eq. (3.44) and Eq. (3.45) give us an interpretation of the environmental PSD at positive and negative frequencies. Positive frequencies ($S_\eta(\omega > 0)$) correspond to energy flowing from the qubit to the environment, known as **energy relaxation** or **spontaneous emission**, associated with transition $|1\rangle \rightarrow |0\rangle$ and rate $\Gamma_\downarrow$. Negative frequencies ($S_\eta(\omega < 0)$) instead describe energy flowing from the environment to the qubit, known as **absorption** or **heating**, with associated transition $|0\rangle \rightarrow |1\rangle$ and rate $\Gamma_\uparrow$. We highlight that $\Gamma_\uparrow$ and $\Gamma_\downarrow$ need not be equal: if we consider noise defined by a quantum operator $\hat{\eta}(t)$ acting on external bath degrees of freedom, we can encounter asymmetric PSDs ($S_{\hat{\eta}}(\omega) \neq S_{\hat{\eta}}(-\omega)$) as introduced in Section 3.2.8.

The ratio of $\Gamma_\uparrow$ and $\Gamma_\downarrow$ can be determined in thermal equilibrium when qubit populations reach a steady state such that the principle of **detailed balance** is satisfied, yielding

$$0 = \Gamma_\downarrow p_1 - \Gamma_\uparrow p_0. \tag{3.46}$$

For an environment at temperature T, recalling the thermal-equilibrium density matrix Eq. (3.32), solving Eq. (3.46) for the ratio results in

$$\frac{\Gamma_\uparrow}{\Gamma_\downarrow} = e^{-\hbar\omega/k_B T}. \tag{3.47}$$

In the case of zero temperature, $T \rightarrow 0$, we find $\Gamma_\uparrow \rightarrow 0$: the environment acts as a quantum noise source, and the qubit relaxes to its ground state $|0\rangle$. For qubits which operate at frequencies such that $\hbar\omega \gg k_B T$, relaxation to $|0\rangle$ comprises a convenient method for state preparation, commonly used for high-frequency superconducting qubits such as the transmon. In the opposite case of $T \to \infty$, we find $\Gamma_\uparrow = \Gamma_\downarrow$: the environment acts a classical noise source, and the qubit equilibrates to the center of the Bloch sphere. In this limit, the environment can be treated as a classical (real-valued) stochastic process [125].

3.3.2 Phase-Coherence Decay: T_2

The timescale associated with the decay of the coherence amplitude $|\rho_{01}| = \frac{|\langle \sigma_x - i\sigma_y \rangle|}{2}$, corresponding to the XY-plane length of the Bloch vector, is referred to as T_2. Phase-coherence decay is referred to as **transverse relaxation**, and is generated by **longitudinal noise** that couples to the qubit via σ_z [Fig. 3.2(b)], along with T_1 processes. For example, relaxation to the pure state $|0\rangle$ from any initial state with $\rho_{01} \neq 0$ necessarily results in $\rho_{01} \to 0$. In order to distinguish between T_1 and T_2 processes, it is therefore necessary to introduce a new timescale T_φ, referred to as the **pure-dephasing time**, which reflects the decay of $|\rho_{01}|$ in the absence of T_1 processes (i.e., without transversal noise).

Here we develop a geometric understanding of the relevant frequencies of transverse and longitudinal noise for T_2 processes. We will find that, in contrast to T_1 processes, T_2 processes do not just rely on noise at the qubit frequency. For clarity (and without loss of generality), let's consider the relaxation of $\langle \sigma_y \rangle$. The relaxation arises from noise which is static in the co-rotating frame such that it does not average to zero. Since $\hat{z}$ is the same in the lab and rotating frames, the static (and generally low-frequency) component of noise along $\hat{z}$ will cause transverse relaxation. We will study these dynamics in Section 3.5. In contrast, the orthogonal transverse noise (along σ_x) at frequency ω will cause transverse relaxation, as this is the component which is static in the rotating frame.

3.4 Decoherence in the Long-Time Limit

In this section, we will introduce analytical results giving us a more rigorous handle on qubit transverse and longitudinal relaxation from noise. First, we emphasize that there are many

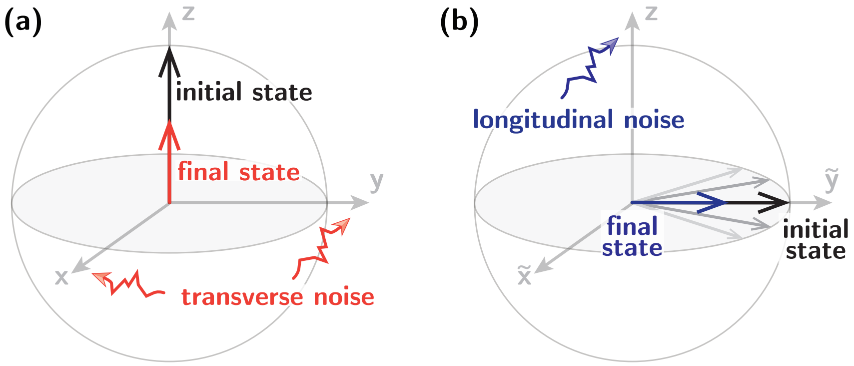

Figure 3.2: **Bloch-sphere picture of decoherence from transverse and longitudinal noise.** Final states represent the result of noise-ensemble-averaged dynamics. **(a)** Transverse noise, coupled to a qubit via σ_x or σ_y, gives rise to relaxation of the Bloch vector along the $\hat{z}$ axis (longitudinal relaxation). The timescale associated with longitudinal relaxation is T_1. **(b)** Longitudinal noise, coupled via σ_z, generates relaxation in the Bloch-sphere XY plane, (transverse relaxation). In this panel, we draw the Bloch sphere in the frame co-rotating with the qubit, enabling visualization of the qubit dynamics without Larmor precession. The timescale associated with transverse relaxation is T_2.

models used to describe qubit decoherence. The most simple description is given by the **Bloch equations** [128], comprising differential equations for each Bloch-vector component. The Bloch equations utilize phenomenological longitudinal and transverse relaxation times T_1 and T_2, respectively. These equations, though historically introduced without a microscopic theory, can be derived from more complete descriptions of qubit reduced-density matrix dynamics (referred to as **quantum master equations** [129]) for systems comprising a qubit coupled to a quantum environment.

To appreciate the results of this thesis (specifically those of Chapter 5 and Chapter 7), it suffices to begin our rigorous understanding of decoherence through the Bloch equations associated with the Hamiltonian Eq. (3.42). Analytical results are straightforward for long times $t \gg \tau_c$ where τ_c is the correlation time for all noise processes $\eta_\alpha(t)$ for $\alpha \in \{x, y, z\}$. In this limit, the dynamics are given by the **Bloch-Wangsness-Redfield theory** (see p. 187 of Ref. [125], or Section 5.11 of Ref. [70]), with

$$\frac{d\langle\vec{\sigma}\rangle}{dt} = -\omega\hat{z} \times \langle\vec{\sigma}\rangle - \frac{1}{T_1}\langle\sigma_z\rangle\hat{z} - \frac{1}{T_{2,x}}\langle\sigma_x\rangle\hat{x} - \frac{1}{T_{2,y}}\langle\sigma_y\rangle\hat{y}, \tag{3.48}$$

where the relaxation rates are given by

$$\frac{1}{T_1} = \frac{1}{4}\sum_{\alpha=x,y}\left[S_\alpha(\omega) + S_\alpha(-\omega)\right] \tag{3.49}$$

$$\frac{1}{T_{2,x}} = \frac{1}{4}\left[S_y(\omega) + S_y(-\omega)\right] + \frac{1}{2}S_z(0) \tag{3.50}$$

$$\frac{1}{T_{2,y}} = \frac{1}{4}\left[S_x(\omega) + S_x(-\omega)\right] + \frac{1}{2}S_z(0). \tag{3.51}$$

This result confirms the geometric intuition we introduced in Section 3.3. Specifically, T_1 processes comprise transverse ($\hat{x}$ and $\hat{y}$) noise at the qubit frequency, and T_2 processes comprise both transverse noise at the qubit frequency and longitudinal ($\hat{z}$) noise at low frequencies (in this case, zero frequency due to the long-time dynamics considered).

In addition, the above equations give us a quantitative handle on the pure-dephasing time T_φ. Letting $\frac{1}{T_2} \equiv \frac{1}{2}\left(\frac{1}{T_{2,x}} + \frac{1}{T_{2,y}}\right)$, we find

$$\frac{1}{T_2} = \frac{1}{2T_1} + \frac{1}{T_\varphi} \tag{3.52}$$

where $\frac{1}{T_\varphi} = \frac{1}{2}S_z(0)$. Eq. (3.52) tells us that, in the absence of longitudinal noise ($S_z(\omega) \to 0$), the characteristic dephasing time is $T_2 = 2T_1$. This is referred to as **T_1-limited** dephasing[8].

Now that we have established an understanding of T_1 and T_2 in the short-correlation-time limit, we will develop a more fine-grained picture of pure dephasing in the case that τ_c is comparable to or longer than the dynamics of interest.

Preview: Anisotropic Transverse Noise

Before moving on, we note that $S_x(\omega)$ and $S_y(\omega)$ need not be equal. For example, superconducting qubit noise sources are often associated with defects that couple to circuits via either charge (e.g., two-level systems with a transition electric-dipole moment [122]) or flux

---

[8] T_1-limited dephasing is routinely achieved with superconducting qubits that are insensitive to external flux or operated at a flux-bias point such that $\frac{\partial\omega(\Phi_{\mathrm{ext}})}{\partial\Phi_{\mathrm{ext}}} = 0$, referred to as a sweetspot [Fig. 2.9].

(e.g., dangling bonds or surface spins with a magnetic moment [121]). Due to the canonically conjugate nature of flux and charge in circuit QED, the corresponding flux and charge operators will always correspond to orthogonal Bloch-sphere axes when considering a qubit subspace. This leads to an interesting possibility: transverse noise may be **anisotropic** (not distributed symmetrically in the Bloch-sphere XY plane).

We explore the dynamical signatures of such anisotropy in the decoherence of superconducting qubits in Chapter 7. Here, we give a small preview by noting that Eq. (3.48) results in the phase-coherence relaxation [70]

$$\frac{d|\rho_{01}|}{dt} = -\frac{|\rho_{01}|}{2}\left(\frac{\cos^2(\omega t+\phi)}{T_{2,x}} + \frac{\sin^2(\omega t+\phi)}{T_{2,y}}\right), \tag{3.53}$$

where ϕ is determined by the initial qubit state. When $S_x(\omega) = S_y(\omega)$, $T_{2,x} = T_{2,y} = T_2$ and Eq. (3.53) simplifies compactly to

$$S_x(\omega) = S_y(\omega) \rightarrow \frac{d|\rho_{01}|}{dt} = -\frac{|\rho_{01}|}{T_2}. \tag{3.54}$$

If instead $S_x(\omega) \neq S_y(\omega)$, we expect decoherence dynamics with an oscillatory component of frequency 2ω. For example, in the limiting case $S_y(\omega) = 0$ ($T_{2,y} \rightarrow \infty$), we find

$$S_y(\omega) = 0 \rightarrow \frac{d|\rho_{01}|}{dt} = -\frac{|\rho_{01}|}{4T_{2,x}}\left(1+\cos[2(\omega t+\phi)]\right). \tag{3.55}$$

Geometrically, we can understand these 2ω dynamics by noting that noise along a particular axis will not affect qubit states that are aligned or anti-aligned with that axis, but will only generate rotations in qubit states orthogonal to that axis. As a consequence, the qubit Larmor precession will lead to decoherence which is modulated every half-Larmor period (the time needed for the Bloch vector to re-align with the noise axis), corresponding to frequency 2ω. We report on the observation of such dynamics and their dependence on the noise PSD, anisotropy, and lab-frame orientation in Chapter 7.

3.5 Filter-Function Formalism for Pure Dephasing

In this section, we introduce the **filter-function formalism** of qubit dephasing, which will give us a rigorous handle on how pure-dephasing noise gives rise to decoherence and how control can be leveraged to mitigate this decoherence. The intuition developed in this section will enable us to appreciate the experimental results of Chapter 5. Specifically, we will derive an expression for the phase-coherence decay of a qubit subject to pure-dephasing noise, corresponding to the bare system Hamiltonian

$$H = \frac{\hbar}{2} \left(\omega_0 + \eta(t) \right) \sigma_z. \tag{3.56}$$

We will study the decay of the coherence amplitude

$$|\rho_{01}| = |\langle \sigma_+ \rangle| = \left| \left\langle \frac{\sigma_x + i\sigma_y}{2} \right\rangle \right|, \tag{3.57}$$

which corresponds to the transverse (XY-plane) length of the Bloch vector. When there is no well-defined relative phase between $|0\rangle$ and $|1\rangle$, we have $|\rho_{01}| = 0$, and in a pure state along the Bloch-sphere equator, we have $|\rho_{01}| = \frac{1}{2}$. In addition to the bare Hamiltonian of Eq. (3.56), we will generalize our calculation to account for deliberately-applied π-pulses, which will enable us to adjust the sensitivity of the qubit to certain bands of noise, in a process known as **dynamical decoupling** [103, 125, 130, 131].

To start the calculation, our goal is to determine an expression for

$$|\rho_{01}(t)| = |\langle \rho_{01,\eta}(t) \rangle|, \tag{3.58}$$

where $\rho_{01,\eta}$ is the coherence element of the density matrix calculated with a particular noise instance, and $\langle \cdot \rangle$ represents the noise-ensemble average. Time-evolution by the Schrödinger equation yields

$$\rho_\eta(t) = U_\eta(t)\rho(0)U_\eta^\dagger(t), \tag{3.59}$$

where $U_\eta(t)$ is the time-evolution operator

$$U_\eta(t) = \exp\left[-\frac{i}{\hbar}\int_0^t H(t')\,dt'\right] \tag{3.60}$$

$$= \exp\left[-\frac{i}{2}\sigma_z\int_0^t [\omega_0 + \eta(t')]\,dt'\right]. \tag{3.61}$$

The coherence decay, Eq. (3.58), can be expressed as

$$|\rho_{01}(t)| = \left|\left\langle \mathrm{tr}\left[\sigma_+ U_\eta(t)\rho(0)U_\eta^\dagger(t)\right]\right\rangle\right|. \tag{3.62}$$

Now, we introduce a critical feature of this calculation: the application of instantaneous π-pulses, which effectively modulate the sign of the phase accrued by the qubit. To make this concrete, we first note that the unitary evolution for a Hamiltonian which is only proportional to σ_z is given by $U(t) = e^{-i\phi(t)\cdot\sigma_z}$ with real-valued phase $\phi(t)$. Considering the evolution for two consecutive time intervals, $0 \leq t \leq t_1$, and $t_1 \leq t \leq t_2$, we can write their respective unitary evolutions as $U^1 = e^{-i\phi_1\sigma_z}$ and $U^2 = e^{-i\phi_2\sigma_z}$. The total evolution from $t = 0$ to $t = t_2$ takes the form

$$U^2U^1 = e^{-i\phi_2\sigma_z}e^{-i\phi_1\sigma_z} = e^{-i(\phi_2+\phi_1)\sigma_z}. \tag{3.63}$$

If we instead interrupt the evolution with a π-pulse instantaneously at t_1, where the unitary evolution of the π-pulse is given by $U_\pi = e^{-i\sigma_x/2\cdot\pi} = -i\sigma_x$, we have

$$U^2U_\pi U^1 = e^{-i\phi_2\sigma_z}(-i\sigma_x)e^{-i\phi_1\sigma_z} = -ie^{-i(\phi_2-\phi_1)\sigma_z}. \tag{3.64}$$

We can see that the total phase accrued by the qubit is now given by the difference $(\phi_2 - \phi_1)$, due to the flipping of the qubit at t_1. In reality, π-pulses cannot be made instantaneous, but this is a good approximation so long as the π-pulse is fast with respect to the noise correlation time[9].

Now, we extend this idea to find the evolution of the qubit under a series of N π-pulses at times $t_1, \cdots, t_N$. It is convenient to define a **modulation function** $s(t)$ which switches between $+1$ and -1 at each t_i to capture the modulation of the phase. Letting U^i be the evolution from t_{i-1} to t_i, $t_0 = 0$, and $t_{N+1} = t$, the qubit evolves with

$$\begin{aligned} U_\eta(t) &= U_\eta^{N+1} U_\pi U_\eta^N \cdots U_\pi U_\eta^1 && (3.65)\\ &= (-i)^N \mathrm{exp}\left[-\frac{i}{2}\sigma_z \sum_{i=0}^{i=N} \int_{t_i}^{t_{i+1}} s(t')[\omega_0 + \eta(t')]\, dt'\right] && (3.66)\\ &= (-i)^N \mathrm{exp}\left[-\frac{i}{2}\sigma_z \int_0^t s(t')[\omega_0 + \eta(t')]\, dt'\right]. && (3.67) \end{aligned}$$

Calculating the coherence amplitude with noise realization $\eta(t)$ then yields

$$\begin{aligned} \rho_{01,\eta}(t) &= \mathrm{tr}\left[\sigma_+ U_\eta(t) \rho(0) U_\eta^\dagger(t)\right] && (3.68)\\ &= \mathrm{tr}\left[U_\eta^\dagger(t) U_\eta^\dagger(t) \sigma_+ \rho(0)\right] && (3.69)\\ &= (-i)^{2N} \mathrm{exp}\left[-i \int_0^t s(t')[\omega_0 + \eta(t')]\, dt'\right] \mathrm{tr}\left[\sigma_+ \rho(0)\right], && (3.70) \end{aligned}$$

where we have used $\sigma_+ e^{-i\phi\sigma_z} = e^{i\phi\sigma_z}\sigma_+$ such that $\sigma_+ U_\eta(t) = U_\eta^\dagger(t)\sigma_+$ for the equality in the second line. Assuming a state prepared on the Bloch-sphere equator, $\mathrm{tr}\left[\sigma_+\rho(0)\right] = \frac{1}{2}$. The bare qubit frequency ω_0 will lead to a phase prefactor which does not depend on the noise. When the magnitude of the noise-averaged coherence is taken, this prefactor, along with the $(-i)^{2N}$, will vanish. With the total accumulated phase

$$X_\eta(t) = \int_0^t s(t')\eta(t')dt', \tag{3.71}$$

---

[9] We further note that during driven evolution (during pulses), qubit coherence becomes particularly sensitive to pure-dephasing noise at the Rabi frequency, although we ignore these effects here [132].

we find that

$$|\rho_{01}(t)| = \frac{1}{2}\left|\left\langle e^{-iX_\eta(t)}\right\rangle\right|. \tag{3.72}$$

In order to proceed in our calculation, we must now make assumptions about the amplitude distribution of $\eta(t)$[10]. This calculation becomes particularly straightforward when assuming Gaussian-distributed noise. As described in Section 3.2.3, we can justify this assumption when $\eta(t)$ comprises the sum over many independent degrees of freedom, thanks to the central-limit theorem [125]. For Gaussian-distributed noise, we find

$$|\rho_{01}(t)| = \frac{1}{2}\left|\left\langle e^{-iX_\eta(t)}\right\rangle\right| = \frac{1}{2}e^{-\frac{1}{2}\left\langle X_\eta(t)^2\right\rangle}. \tag{3.73}$$

Now we introduce the **filter function** which describes the modulation function in the frequency domain,

$$\begin{aligned} F(t,\omega) &= \omega^2 \int_0^t dt' s(t') \int_0^{t'} dt'' s(t'') \cos(\omega(t'-t'')) &(3.74)\\ &= \frac{\omega^2}{2}\left|\int_0^t dt' s(t') e^{i\omega t'}\right|^2. &(3.75)\end{aligned}$$

With $F(t,\omega)$, we arrive at a convenient expression for the normalized coherence decay $W(t)$:

$$\begin{aligned} W(t) &\equiv \frac{|\rho_{01}(t)|}{|\rho_{01}(0)|} = e^{-\chi(t)}, &(3.76)\\ \chi(t) &= \frac{1}{\pi}\int_0^\infty S(\omega)\frac{F(t,\omega)}{\omega^2}\, d\omega. &(3.77)\end{aligned}$$

The central result of this calculation is the **coherence function** $\chi(t)$, which determines the decay envelope for Gaussian-distributed dephasing noise with a power spectrum $S(\omega)$ under a particular control sequence with corresponding filter function $F(t,\omega)$. Dephasing is determined by the frequency-domain overlap of $S(\omega)$ and $F(t,\omega)$.

---

[10] We offer the friendly reminder that assumptions about the amplitude distribution do not determine the dynamics of the noise $C_\eta(\tau)$.

3.5.1 White Noise

Before describing some typical experiments with different filter functions, we note that Eq. (3.77) simplifies greatly in the case of white noise with $S_{\mathrm{white}}(\omega) = S_0$:

$$\begin{aligned}
\chi_{\mathrm{white}}(t) &= \frac{S_0}{\pi}\int_0^\infty \frac{F(t,\omega)}{\omega^2}\, d\omega && (3.78)\\
&= \frac{S_0}{2\pi}\int_0^t dt' s(t') \int_0^t dt'' s(t'') \left[\frac{1}{2}\int_{-\infty}^{\infty} e^{i\omega(t'-t'')}\, d\omega\right] && (3.79)\\
&= \frac{S_0}{2}\int_0^t dt' s(t') \int_0^t dt'' s(t'')\delta(t'-t'') && (3.80)\\
&= \frac{S_0}{2}\int_0^t dt' s(t')^2 && (3.81)\\
&= \frac{S_0 t}{2}. && (3.82)
\end{aligned}$$

For white noise, the coherence decays exponentially in time as $W_{\mathrm{white}}(t) = e^{-\Gamma t}$ where $\Gamma = \frac{S_0}{2}$, no matter which pulse sequence is applied.

3.5.2 Quasistatic Noise

In the opposite limit of only shot-to-shot fluctuations, $S_{\mathrm{qs}}(\omega) = 2\pi\sigma^2\delta(\omega)$, and

$$\begin{aligned}
\chi_{\mathrm{qs}}(t) &= 2\sigma^2 \int_0^t dt' s(t') \int_0^t dt'' s(t'') \left[\frac{1}{2}\int_{-\infty}^{\infty} \delta(\omega) e^{i\omega(t'-t'')}\, d\omega\right] && (3.83)\\
&= \sigma^2 \left[\int_0^t dt' s(t')\right]^2. && (3.84)
\end{aligned}$$

We have uncovered an important feature: the coherence decay depends on the experiment being performed. This is generally the case when qubit dephasing is dominated by low-frequency noise. Now, we will introduce the main experiments performed to probe low-frequency dephasing noise.

3.5.3 Ramsey Experiment

The most simple case is that of no π-pulses, referred to as a **Ramsey** or **free-induction decay** experiment [133]. In this case, we have

$$s_R(t) = 1 \tag{3.85}$$

$$F_R(T,\omega) = 2\sin^2\left(\frac{\omega T}{2}\right). \tag{3.86}$$

We plot the modulation and filter functions in Fig. 3.3(a,b) in blue. For quasistatic noise, Eq. (3.84) simplifies to $W_{\text{R, qs}}(t) = e^{-\sigma^2 t^2}$, comprising a Gaussian decay envelope [Fig. 3.3(c)]. This is a generic feature of the coherence decay when the noise correlation time is much longer than the experiment duration.

3.5.4 Echo Experiment

The next most simple case is that of one π-pulse in the middle of the qubit evolution, referred to as a **Hahn (or spin) echo** [134]. For an experiment of total length T, we have

$$s_E(t) = \begin{cases} 1 & t \leq \frac{T}{2} \\ -1 & t > \frac{T}{2} \end{cases} \tag{3.87}$$

$$F_E(T,\omega) = 8\sin^4\left(\frac{\omega T}{4}\right). \tag{3.88}$$

We plot the modulation and filter functions in Fig. 3.3(a,b) in red. For an Echo experiment, Eq. (3.84) simplifies to $W_{\text{E, qs}}(t) = 1$. This represents another important result: an echo sequence is impervious to zero-frequency noise. However, noise will seldom (if ever) be perfectly quasistatic in practice, and noise with power at intermediate frequencies compared to the experiment duration will lead to decoherence during echo experiments.

3.5.5 Higher-Order Sequences

In general, more π-pulses can be added in equally-spaced intervals, yielding filter functions which are concentrated at higher frequencies. With N total π-pulses and $\tau = T/(2N)$, these sequences typically take the form

$$s_N(t) = \begin{cases} 1 \quad t \leq \tau \\ -1 \quad \tau \leq t < 3\tau \\ 1 \quad 3\tau \leq t < 5\tau \\ \dots \\ (-1)^N \quad (2N-1)\tau < t \end{cases} \tag{3.89}$$

$$F_N(T,\omega) = 2\sin^2\left(\frac{\omega T}{2}\right)\left[1 - \sec^2\left(\frac{\omega T}{2N}\right)\right]. \tag{3.90}$$

We plot an example modulation and filter function for $N = 2$ in Fig. 3.3(a,b) in orange. In practice, nonidealities in the rotation (e.g., from a slightly miscalibrated amplitude or frequency) can be addressed by choosing specific sequences of rotating about $\hat{x}$ or $\hat{y}$ such as the Carr-Purcell-Meiboom-Gill (CPMG) sequence [135] (initial and final $\pi/2$ pulses about $\hat{x}$ with all π-pulses about $\hat{y}$), or XY sequences (initial and final $\pi/2$ pulses about $\hat{x}$ with π-pulses alternating between $\hat{x}$ and $\hat{y}$).

We plot modulation, filter, and coherence decay functions for a few different experiments and noise power spectra in Fig. 3.3.

3.5.6 Dynamical Decoupling

From the prior subsections, we can conclude that adding π-pulses can decouple a qubit from low-frequency noise [103, 125, 130, 131]. This idea can be leveraged when the dephasing-noise correlation time is longer than an experiment duration, and represents an important technique when utilizing qubits that are especially susceptible to low-frequency dephasing

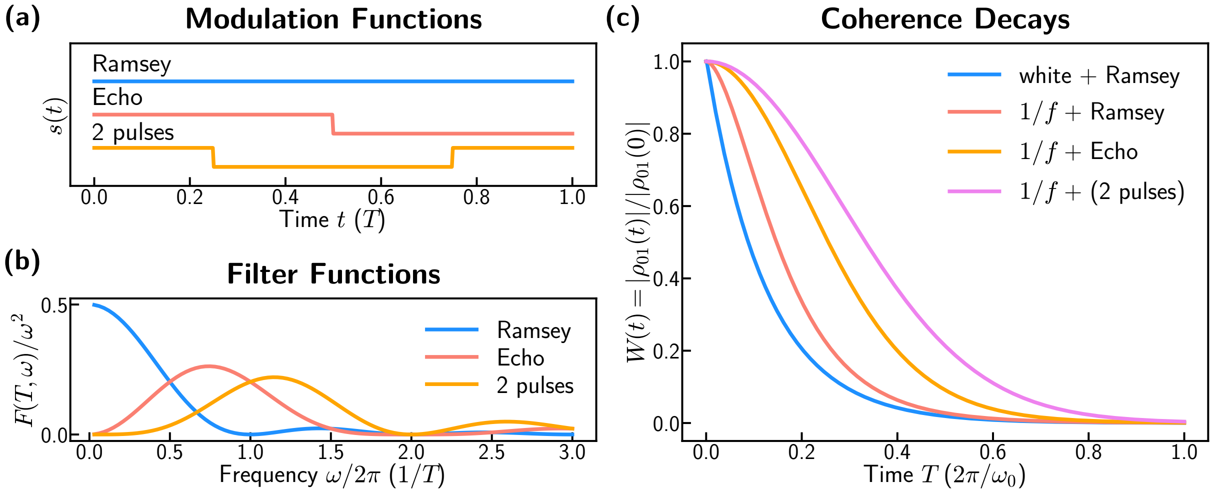

Figure 3.3: **Dephasing from longitudinal noise.** **(a)** Ramsey (free-induction-decay), echo, and 2-pulse modulation functions $s(t)$ over an experiment of duration T, offset for clarity. **(b)** Corresponding filter functions $F(t,\omega)/\omega^2$ for the modulations given in (a). Frequencies on the x axis are given in units of the total experiment time T. The Ramsey filter function is most sensitive to noise at $\omega = 0$, and reaches minima when the period of the noise $2\pi/\omega$ is an integer multiple of the experiment time T. Sequences with more pulses are susceptible (immune) to higher-frequency (lower-frequency) noise. **(c)** Coherence decays for various modulation functions and noise power spectra. For white noise, $S_w(\omega) = \omega_0$, yielding an exponential coherence decay for all pulse sequences. For $1/f$ noise, $S_{1/f}(\omega \geq \omega_0) = \omega_0^2/\omega$ and $S_{1/f}(\omega < \omega_0) = \omega_0$. This low-frequency noise is suppressed by higher-order sequences, which can be seen in the extended coherence of the orange and pink traces.

noise. Such noise is pervasive in experimental platforms, although the details of noise depend on platform-specific physics. We highlight the examples of flux-tunable superconducting qubits [67] and color-center defects surrounded by nuclear- and electron-spin baths [136].

3.6 Noise Spectroscopy

Noise is typically viewed as the enemy of quantum information experiments, as quantum interference effects rely on phase coherence which noise degrades. However, one can embrace the opposite perspective, that of utilizing qubits as sensors of their environment [137]. The field of study based on this perspective is referred to as **quantum sensing**. In this section, we embrace this perspective, and explore the problem of mapping a qubit's noise environment via different qubit-centric experiments. The process of reconstructing the noise power-spectral density is known as **noise spectroscopy**. We emphasize that different noise spectroscopy protocols must be used to reconstruct the PSDs for different types of noise (longitudinal or transverse, in different frequency ranges), and refer to Table 1 of [132] for a helpful summary of various techniques and their applicability. In this section, we introduce some common noise-spectroscopy techniques including those utilized for the results of Chapter 5. For clarity, we refer to the PSD of longitudinal noise as $S_z(\omega)$ and transverse noise as $S_x(\omega)$.

3.6.1 Dynamical Decoupling

As we have seen in Section 3.5, the dephasing of a qubit is dictated by the frequency-domain overlap of the dephasing-noise PSD and a filter function associated with the experiment being conducted, as given by Eq. (3.77). Instead of specifying the experiment and noise statistics to determine the coherence decay, one can also leverage Eq. (3.77) for the reverse problem: given several measured coherence decays for different pulse sequences, reconstruct the dephasing-noise PSD $S_z(\omega)$ [67]. The broad methodology is as follows: (1) perform N-pulse dynamical-decoupling sequences while varying N in order to make the coherence function $\chi(t)$ sensitive to different frequency bands of the noise, and (2) knowing $\chi(t)$ and $F_N(t, \omega)$, solve the inverse equation of Eq. (3.77) for $S_z(\omega)$.

Aside: Dynamical Decoupling as an Anisotropic Noise Probe

Here we propose a potentially interesting extension of dynamical decoupling which might help to measure the anisotropy of lab-frame transverse noise as discussed in Section 3.4 and reported on in Chapter 7. Typically, dynamical decoupling relies on the application of π-pulses which are fast (approximated as instantaneous) with respect to the free-evolution times τ during which noise decoheres a qubit. Dynamical decoupling is typically used to sense pure dephasing (σ_z) noise. Since such noise affects all superposition states equally, having long free-precession times ($\tau \gg \tau_L$ where τ_L is the qubit Larmor period) helps increase the signal, although we note that in this case, the qubit in the lab frame spends equal time in all quadrants of the Bloch-sphere XY plane. The π-pulses only need to be fast with respect to $\tau \gg \tau_L$, and the qubit spending equal time in all parts of the Bloch-sphere XY plane is irrelevant to the dephasing dynamics.

Instead, we propose the following scheme, which utilizes dynamical decoupling pulse sequences with the aim of measuring anisotropic transverse noise. For decoherence to be sensitive to the anisotropy of the noise, we must devise a way to keep the qubit primarily oriented along one Bloch-sphere transverse axis. Our idea is as follows. First, prepare a qubit along a transverse axis of interest. Then, apply fast π-pulses with a center-to-center spacing of $\lesssim \tau_L/4$. Finally, project the qubit back to the $\hat{z}$ axis for readout. By applying the dynamical-decoupling pulses at a spacing $\lesssim \tau_L/4$, the qubit will primarily spend its time oriented along a particular lab-frame axis. We illustrate this proposal in Fig. 3.4. One can then perform this experiment as a function of initial lab-frame state, and explore anisotropy of the lab-frame transverse noise. One major difficulty of this proposed scheme is the realization of control π-pulses which are less than $\tau_L/4$ in duration. This protocol may serve as a lab-frame analog to spin-locking, which we will discuss in Section 3.6.5.

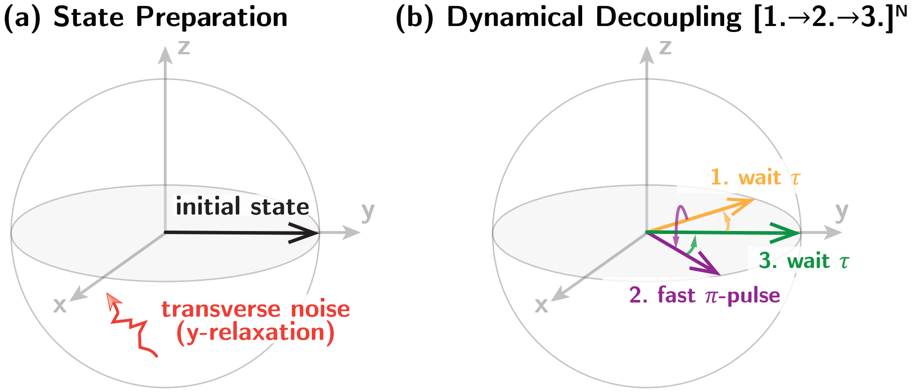

Figure 3.4: **Proposal for fast dynamical decoupling to probe transverse noise anisotropy.** **(a)** An initial qubit state along a Bloch-sphere transverse axis is prepared, and subject to anisotropic transverse noise applied along an orthogonal axis. **(b)** Dynamical decoupling pulses are applied such that the qubit decoheres while mostly oriented within a subsection of the Bloch-sphere XY plane. By varying the initial state, one can then probe the anisotropy of lab-frame transverse noise.

To get a better handle on the required timescale for the control pulses, we can explore a simple metric that will tell us if the qubit spends more time aligned with $\hat{x}$ or $\hat{y}$. We will look at the difference between the integrated, squared component of the Bloch vector along $\hat{x}$ (X^2) and $\hat{y}$ (Y^2). Recalling Eq. (2.25), we find

$$X^2 \equiv \int_{-\tau}^{\tau} \cos^2\left(\frac{4\pi t}{\tau_L}\right) dt = t + \frac{\tau_L}{4\pi} \sin\left(\frac{4\pi\tau}{\tau_L}\right) \tag{3.91}$$

$$Y^2 \equiv \int_{-\tau}^{\tau} \sin^2\left(\frac{4\pi t}{\tau_L}\right) dt = t - \frac{\tau_L}{4\pi} \sin\left(\frac{4\pi\tau}{\tau_L}\right) \tag{3.92}$$

$$X^2 - Y^2 = \frac{\tau_L}{2\pi} \sin\left(\frac{4\pi\tau}{\tau_L}\right). \tag{3.93}$$

This toy model tells us that the anisotropy $|X^2 - Y^2|$ reaches a maximum when

$$\tau = \frac{\tau_L}{8} + \frac{n\tau_L}{4}, \tag{3.94}$$

with integer n. For $n = 0$, this corresponds to the qubit being confined to one quadrant in the Bloch-sphere XY plane, as in Fig. 3.4, requiring π-pulses which are much shorter than the total free precession time of $2\tau = \tau_L/4$. One might be able to achieve anisotropic sampling with slower π-pulses instead by choosing $n > 0$. However, we note that decoherence during the π-pulses will be distinct from the decoherence during free evolution [66], and so simulations or experiments would be required to verify the efficacy of this idea.

3.6.2 Fourier Transform

Through a remarkably direct result only found in 2024 [138], one can show that for a Ramsey sequence with (recalling Eq. (3.86)) $F_R(t, \omega) = 2\sin^2\left(\frac{\omega T}{2}\right)$, the second derivative of the coherence function as defined by Eq. (3.77) is given by

$$\frac{\partial^2 \chi(t)}{\partial t^2} = \frac{1}{\pi} \int_{-\infty}^{\infty} d\omega S_z(\omega) \cos(\omega t) \tag{3.95}$$

such that the Fourier transform of both sides yields

$$S_z(\omega) = \sqrt{2\pi}\mathcal{F}\left[\frac{\partial^2 \chi(t)}{\partial t^2}\right], \tag{3.96}$$

where $\mathcal{F}[\cdot]$ represents the Fourier transform. By conducting Ramsey experiments with finely-sampled durations, one can then directly extract the PSD via a Fourier transform.

3.6.3 Single-Delay Ramseys

Now we detail one of the techniques used in Chapter 5 to map dephasing noise at low frequencies ($\lesssim 10\,\mathrm{Hz}$) [139]. The idea is as follows: by performing a Ramsey sequence with $\pi/2$-pulses of a frequency $f = f_{01} + \Delta$ where Δ is the detuning of the pulse and bare qubit frequencies, measuring along the $\hat{z}$ axis will yield a population of the excited state

$$p(t) = \frac{1 + W(t)\cos(\Delta t)}{2} \tag{3.97}$$

where $W(t)$ is the coherence function capturing the qubit dephasing. The oscillation at frequency Δ arises from the precession of the qubit in the rotating frame defined by the pulse detuning. Taking the derivative with respect to the detuning,

$$\frac{\partial p}{\partial \Delta} = -\frac{tW(t)\sin(\Delta t)}{2}, \tag{3.98}$$

we see that $p(t)$ is maximally sensitive to changes in the detuning at times $\Delta t = \frac{\pi}{4} + n\pi$ for integer n. If we take a sequence of repeated measurements at one of these fixed times, e.g., $\tau = \frac{\pi}{4\Delta}$, we can then measure fluctuations in the probability which correspond to frequency shifts of the qubit $f_{01} \to f_{01} + \eta(t)$:

$$p(\tau) = \frac{1}{2} + \left.\frac{\partial p}{\partial \Delta}\right|_{\tau} \cdot \eta(\tau). \tag{3.99}$$

We note that in practice, qubit measurements will yield either 0 or 1 (a **Bernoulli trial**) with a probability $p(t)$ slightly biased away from 0.5 due to the frequency fluctuations. This Bernoulli-trial sampling leads to an associated white-noise floor of the extracted PSD, which can be mitigated by calculating the PSD from the cross-correlation of interleaved individual measurement outcomes [139].

The frequency range accessible with this method is set by the duration of a single experiment τ due to the **Nyquist-Shannon sampling theorem**, which limits reconstruction of the PSD to frequencies below $1/2\tau$. The experiment duration τ is generally limited by the readout time. Although superconducting qubit readout times on the order $100\,\mathrm{ns} \lesssim \tau \lesssim 1\,\mathrm{us}$ have been achieved, this technique is sensitive to long-time transients in the qubit population (e.g., from relaxation of quasiparticles or measurement-induced transitions), and so in practice this technique has only been shown to reconstruct $S_z(f)$ below $f \lesssim 100\,\mathrm{Hz}$. The low-frequency cutoff for PSD reconstruction is set by the total number of experiment repetitions, which can typically be in the tens to hundreds of thousands, leading to $f \gtrsim 1\,\mathrm{mHz}$.

3.6.4 Repeated Ramseys

To probe even lower-frequency noise, one can measure the full time-domain Ramsey oscillation Eq. (3.97) and extract the frequency Δ by fitting the data. Repeating this process yields a time-series of fitted frequencies which can be used to calculate the PSD directly via, e.g., the Welch method. One can alternatively collect the qubit frequency time-series from repeated spectroscopy measurements. The maximum frequency accessible from these measurements is again given by the Nyquist-Shannon sampling theorem as $1/2\tau$ where τ is now the total time of a single Ramsey-trace or spectroscopy acquisition. In practice, this time will seldom be below one second (barring fast frequency-estimation methods such as that in Ref. [140]), resulting in $S_z(f)$ estimation for frequencies $\lesssim 1\,\mathrm{Hz}$.

3.6.5 Spin Locking

Here we introduce a technique to measure $S_z(\omega)$ at frequencies in the megahertz range [66] (which is used in Chapter 5). The technique, referred to as **spin locking** [141], comprises preparing a qubit on the Bloch-sphere equator, let us assume along the rotating-frame axis $\hat{\tilde{x}}$ without loss of generality. Then, the qubit is subject to a resonant drive along the same axis $\hat{\tilde{x}}$, and finally rotated back to the $\hat{z}$ axis for readout.

We can understand the dynamics most easily in the rotating frame. The Rabi drive of strength Ω acts as a new effective quantization axis along $\hat{\tilde{x}}$ (which is static in the rotating frame), giving rise to an effective pseudospin of frequency Ω. Depolarization along $\hat{\tilde{x}}$ will then occur with a timescale $T_{1\rho}$, and can be interpreted as longitudinal relaxation of the pseudospin arising from its transverse noise, which is the bare qubit's σ_z noise. The relevant noise frequency for the $T_{1\rho}$ process is the pseudospin frequency, so we find

$$\frac{1}{T_{1\rho}} = \frac{1}{2T_1} + \frac{1}{T_\varphi}, \tag{3.100}$$

where $\frac{1}{T_\varphi} = \frac{1}{2}S_z(\Omega)$. By measuring the depolarization of the pseudospin as a function of the Rabi frequency Ω, one can then map the lab-frame longitudinal noise spectrum $S_z(\Omega)$ with typical Rabi frequencies in the range $1\,\mathrm{MHz} \lesssim \Omega/2\pi \lesssim 200\,\mathrm{MHz}$. However, heating induced by strong Rabi drives limits the straightforward application of this technique for high-frequency noise spectroscopy.

3.6.6 T_1 Relaxometry

Beyond longitudinal noise spectroscopy, transverse noise spectroscopy (that is, reconstructing the PSD of σ_x or σ_y noise) can be performed by taking advantage of Fermi's golden rule [94, 142]. Specifically, one can measure transition rates from $|1\rangle \to |0\rangle$ and $|0\rangle \to |1\rangle$, and map those to a transverse-noise PSD via Eq. (3.44) and Eq. (3.45). This technique cannot distinguish between different transverse noise sources along $\hat{x}$ and $\hat{y}$, and only gives access to noise at the qubit frequency ω. However, frequency-tunable qubits can be leveraged to map transverse noise in an accessible range of qubit frequencies. For superconducting qubits, this range is typically $100\,\mathrm{MHz} \lesssim \omega/2\pi \lesssim 5\,\mathrm{GHz}$.

3.7 Summary

Here, we briefly summarize the major takeaways of this chapter. We introduced the idea of noise which arises from uncontrolled degrees of freedom in an experiment. Noise is characterized by its statistical properties rather than individual measurements. We linked noise to qubit decoherence, focusing on the geometric Bloch-sphere picture: relaxation along $\sigma_{x/y}$ (σ_z) arises from noise coupled to $\sigma_{x/y/z}$ ($\sigma_{x/y}$). We developed the filter-function formalism for pure-dephasing (σ_z) noise, which told us that a qubit's dephasing relies on the frequency-space overlap of the noise PSD and the filter function determined by the particular pulse sequence applied to the qubit. As a consequence, one can leverage control to decouple the qubit from pure-dephasing noise which has a structured PSD (dynamical decoupling). Finally, we discussed several techniques for noise spectroscopy: the problem of mapping a qubit's noise environment with different protocols.

This chapter completes our introduction of background material required to appreciate the upcoming experimental results of Chapter 5, Chapter 6, and Chapter 7. We offer one additional primer on $1/f$ noises in Chapter 4 which helps to contextualize the results of Chapter 5, although it is not strictly necessary to understand the results themselves.

Chapter 4

$1/f$ Noise Primer

> . . . I am thinking [of] noises that become stripped of everything deemed inessential and labeled as having $1/f$ spectrum. The concision of this description seemed admirable, but turned out to be a drawback. Whatever contribution I managed to bring to this study came from forsaking concision and paying respect to the reputedly inessential geometry. For example, arrange for $1/f$ noises from different sources to be traced on an oscilloscope. Even the untrained observer will notice deep geometric differences that turn out to be symptoms of deep physical differences. . . . I think that a unique physical explanation for all $1/f$ noises is hopeless. . . . the identification of a $1/f$ spectrum is never enough.
>
> *Benoit Mandelbrot* [123]

In this chapter, we introduce a topic that has a long and rich history beginning almost exactly one century ago [143], which to this day remains controversial. The topic is noises with power spectral densities (PSDs) following a frequency dependence of roughly $1/f$. A noise with this property is referred to broadly as $1/f$ noise, flicker noise, excess noise, pink noise, fractional noise, or fractal noise. We immediately note that the term "$1/f$ noise" as referring to a singular noise lends itself to the misconception that such noise is distinct and refers to one physical phenomenon. This is an unfortunate consequence of the terminology, and we will attempt to rectify this by generically using the plural term “$1/f$ noises" to address the broad nature of all things called “$1/f$” (but yes, we have kept this term in the title in order to attract those who might benefit from this primer).

Noises characterized by this PSD frequency dependence have been observed in physical systems including but not limited to electronics, mechanics, biology, geology, astronomy, psychology, language [42], music [43], economics [144], traffic flows both on the road [145] and in your ethernet cable [146], and even the concentration of oxygen in your brain right now [40, 147]. Given the ubiquity of the $1/f$ PSD in such diverse contexts together with its scale-invariant property (that the integrated noise power in any decade you choose is the same as in any other decade, or more intuitively – if one plays a recording of such noise at different speeds, it will always sound the same [148]), it is no surprise that physicists and applied mathematicians searched tirelessly for a universal explanation, i.e., a broadly applicable model which generates such noise. One tantalizing thread is the generation of such noise from fractional noises, characterized by the self-similarity of their statistics and therefore the mathematics of fractals [149, 150].

The consensus today (and for the past several decades) is that $1/f$ noises should not be attributed to a universal model, but rather can be described in specific contexts with detailed microscopic models [41, 148, 151, 152]. Despite this null result, $1/f$ noises remain curious phenomena, with a persisting relevance due to their ubiquity in systems where low-frequency fluctuations are sought to be understood. In particular, we can see this renewed interest in the context of current-day quantum information experiments, where $1/f$ noises in solid-state platforms remain a leading source of qubit decoherence [153].

This chapter is structured as follows. In Section 4.1, we begin with a historical overview of $1/f$ noise from its first discovery, focusing on its place in condensed matter physics. In Section 4.2, we present some phenomenological models of $1/f$ noises. In Section 4.3, we detail this noise in superconducting circuits, and introduce magnetic flux noise in Section 4.4.

4.1 A Brief History of $1/f$ Noise

In 1918, Walter Schottkey [154] coined the term "small-shot effect" to describe current fluctuations created by the discrete nature of charge carriers, which he predicted to have a frequency-independent PSD (white noise). The first experimental attempt to verify this noise by Hartman in 1921 failed [155], but technical improvements led to J.B. Johnson's historic vacuum-tube experiment soon after in 1925 [143]. Johnson observed the predicted white noise at high frequencies, but an unexpected excess of noise diverging as $1/f$ at low frequencies. He hypothesized that this effect was independent of the small-shot effect, and was due to fluctuations (or "flickering") in the surface properties of his samples (starting the rich tradition of speculation about $1/f$ noise and disordered surfaces which continues today). In 1926, just one year after its discovery, Schottkey was quick to provide a theory for this so-called "flicker effect," [156] setting off the next century of research on the topic.[1]

By the 1940s-1950s, noise with a similar frequency dependence was observed in a number of semiconductor devices [159, 160], and by the 1960s-1970s the noise was also observed in tunnel-junctions, superconducting films [161], and even biological systems [162] and music [43]. An abundance of microscopic models accompanied these early observations [151, 161].

At this time, during the late 1960s, a beautiful idea from two mathematicians Benoit B. Mandelbrot and John W. Van Ness appeared. The idea was of time-domain random processes which are self-similar (exhibiting invariance under changes in the timescale) [149], with the tantalizing property that their PSD obeys a power-law scaling in frequency, much like the mysterious $1/f$ noises by then found commonly in solid-state systems. Noise of this type was called "fractional Brownian motion," which was a generalization of Brownian motion, but with a fractional (rather than integer) derivative. In the years following, related ideas were

---

[1] For historical context, just a few years later in 1928, another white noise arising from the thermal fluctuation of charge carriers was measured and explained in electronic circuits by Johnson [157] and Nyquist [158] in back-to-back papers in *Physical Review*, to become known as Johnson-Nyquist noise.

developed and turned into Mandelbrot's celebrated fractal geometry (infinitely self-similar shapes) [163] – which described shapes ever present in nature, and seemingly the power-law PSDs ever present in timeseries [150, 164]. In the decades after the first development of fractional noises, the physical interpretation of such processes was explored [165]. The beauty and ubiquity of fractals in nature along with the coincident knowledge of $1/f$ noise in such diverse contexts [43, 163] led to a rush of excitement for this potential universal model of the noise, however after some time even Mandelbrot himself had a change of heart, and offered a word of caution which is included as an epigraph to this chapter [123].

Aside from fractional noises, there have been explorations of $1/f$ noise in physical systems with fractal properties, specifically in resistor networks and spin glasses. Studies of resistance noise in fractal and random percolating resistor networks began in the 1980s. The frequency dependence of resistance noise in such systems arises from anomalous diffusion [166–168], and does not yield a universal $1/f$ frequency dependence. Confusingly, many theoretical investigations have been conducted on the scaling of an *assumed* $1/f$ noise amplitude (rather than the frequency dependence) in these systems, with the unfortunate effect of correlating the terms $1/f$ noise and "fractal" without providing a fractal origin for the noise. Experimental investigations of such networks have however measured $1/f$ noise [169, 170]. We conclude that one should not mistake the fractal property of some percolating resistor networks as the origin of their $1/f$ noise. Also in the 1980s, another fractal-related $1/f$ noise exploration began in the context of spin-glass systems. The free energy surface of spin glasses exhibits fractal properties which give rise to a wide distribution of relaxation times [171]. Considering the logarithmic relaxation of remnant magnetization in a spin glass, $1/f$ noise can be derived as a direct consequence of the fluctuation-dissipation theorem [172].

The plethora of models for $1/f$ noise and their varying success in different contexts led to the apparent consensus that such noise is not universal, but explained well by microscopic models in specific contexts. However, work on $1/f$ noise as a property of general stochastic models has persisted, and gives the impression of progress towards a more general understanding of the phenomenon in the context of applied mathematics [173–175]. Curiously, a simple search for discussions of these general ideas in the context of condensed matter physics does not appear in the popular reviews of [148, 151, 153] – although these ideas were surely perceived [176]. Given the immense amount of literature about $1/f$ noise, we are left to wonder...is this missing connection simply an oversight of the field, or of the author?

In conclusion, we have poured through (some of) the history of $1/f$ noises, and now provide our outlook. $1/f$ noises, although interesting and relevant phenomena, should not be considered one of the great mysteries of condensed-matter physics. The initial hope for a universal explanation has been dismissed for decades [123, 148, 151], but even today, this sentiment does not seem pervasive. The term $1/f$ *noise* is used broadly and generously for *noises* $1/f^{\alpha}$ where the exponent α can fall in a range as wide as 0.5 to 1.5. The ambiguity in what are called $1/f$ noises may contribute to some lack of clarity in the field, and has typically been explained away by modifying specific model assumptions in *ad-hoc* ways [151, 161]. In addition, the appearance of these noises spanning broadly unrelated fields has led to an overwhelming amount of literature, making the topic difficult to assess. As a final point, a noise PSD in isolation is a limited piece of data (for non-Gaussian processes, the PSD does not uniquely characterize the noise), and the difficulty of experimentally probing microscopic models in many contexts (e.g., in material systems, where one cannot arbitrarily change system parameters at will) often prevents scientists from verifying the underlying physics. As a consequence, $1/f$ noise has unfortunately remained a controversial and confused topic, and we warn the reader to approach it carefully. On a more optimistic note, there is no denying that noises with this PSD are present and relevant as ever. The origin of $1/f$ noises in any given system is not necessarily a solved problem, and remains in many active areas of research and engineering today.

4.2 Phenomenological Descriptions

Here we provide an overview of the physics for some phenomenological models of $1/f$ noises. We emphasize that this is not an exhaustive list, but includes the two most common models in condensed matter physics (an ensemble of exponentially relaxing processes and diffusion), as well as a more recent thermodynamics-based model.

4.2.1 Exponential Relaxation Processes

The most common phenomenological model for a $1/f$ noise in the context of solid-state devices involves a collection of random variables $\eta(t)$, each of which has an exponential autocorrelation with characteristic decay time τ_c. Considering one such random variable, the autocorrelation in time and PSD (previously introduced in Chapter 3.2) are given by

$$\langle \eta(\tau)\eta(0)\rangle = \sigma^2 e^{-\tau/\tau_c}, \tag{4.1}$$

$$S_\tau(\omega) = \frac{2\sigma^2\tau_c}{1+(\omega\tau_c)^2}. \tag{4.2}$$

With an appropriate distribution of relaxation times $p(\tau_c) \propto 1/\tau_c$ for $\tau_1 \lesssim \tau_c \lesssim \tau_2$, we find

$$S(\omega) = \int_{\tau_1}^{\tau_2} S_\tau(\omega)\, p(\tau_c)\, d\tau_c \propto \frac{\sigma^2}{\omega}. \tag{4.3}$$

In Figure 4.1, we plot the PSD of an exponentially correlated process and the emergent $1/f$ spectrum from a log-uniform distribution of such processes.

One such noise process yielding an appropriate autocorrelation function is the random telegraph signal (RTS), which jumps between two discrete values with an average rate (e.g., an electron spin flipping due to thermal excitation, or an atom, group of atoms, or electron which tunnels between two favorable spatial configurations with a transition dipole moment). For this reason, this model of a $1/f$ noise is sometimes referred to as the RTS model. To

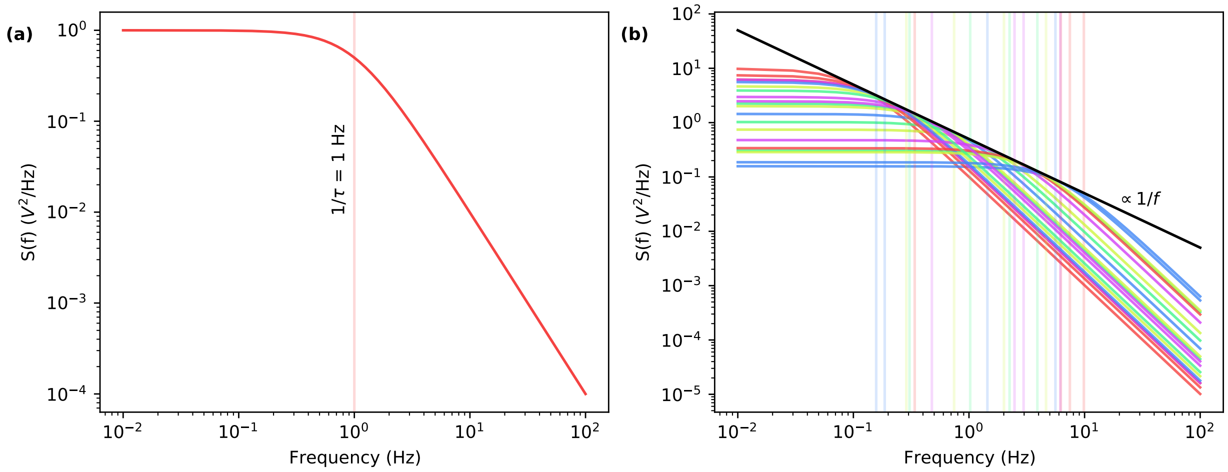

Figure 4.1: **Noise from exponential relaxation processes.** **(a)** Noise from a single exponential relaxation process (Eq. 4.1) with timescale $\tau_c = 1\,\mathrm{s}$. **(b)** Emergent $1/f$ noise from a collection of 20 exponential relaxation processes with τ_c drawn from a log-uniform distribution with minimum value $\tau_1 = 0.1\,\mathrm{s}$ and maximum value $\tau_2 = 10\,\mathrm{s}$.

motivate the distribution of flip rates, we can consider the relation $\tau_c \propto e^{\lambda}$ where λ is uniformly distributed, leading to $p(\tau_c) \propto 1/\tau_c$ (log-uniformly distributed). This is the case when τ_c represents the tunneling time in a double-well potential, where λ is proportional to the well separation.

4.2.2 Diffusion Models

Another popular theme among $1/f$ noise theories is stochastic processes. Before considering the case of noise from a generic random driving term, we introduce Brownian motion in position and velocity spaces to get intuition for the frequency scalings of the emergent noises, roughly following [41].

Let's start with Brownian motion of a coordinate $x(t)$ in 1D governed by the Weiner process, $dx/dt = \zeta(t)$, where $\zeta(t)$ is a random driving term which is a Gaussian-distributed white noise. By looking at the Fourier transform $i\omega\tilde{x}(\omega) = \tilde{\zeta}(\omega)$, one finds the PSDs of $x(t)$ and $\zeta(t)$ are related by $S_x(\omega) = S_\zeta/\omega^2 \propto 1/\omega^2$. For this reason, noise scaling with frequency as $1/f^2$ is referred to as a Brownian noise or "Brown noise."

Let's instead consider Brownian motion of the particle's velocity governed by the Langevin equation, $dv/dt = -\gamma v(t) + \zeta(t)$. In Fourier space, we have $\tilde{v}(\omega) = \tilde{\zeta}(\omega)/(\gamma + i\omega)$. Therefore, the PSDs of $v(t)$ and $x(t)$ are related by $S_v(\omega) = S_\zeta/(\gamma^2 + \omega^2) \propto 1/(\gamma^2 + \omega^2)$. Finally, using the relation $dx/dt = v(t)$, we have $S_x(\omega) \propto 1/(\gamma^2 + \omega^2) \cdot 1/\omega^2$. We can see that the PSD of this noise has a faster fall-off than $1/f$ in all frequency ranges.

In order to find the frequency dependence we desire between white noise and Brownian noise, the approach of the condensed-matter $1/f$-noise community has been to consider a general diffusion equation with a generic driving term (for completeness, here we acknowledge the seemingly relevant idea of fractional noises [149] as mentioned in Section 4.1 which, to our knowledge, has not found its way to the condensed-matter community). Consider $M(t)$ which depends on a random variable $f(x,t)$ which obeys a diffusion equation,

$$M(t) = \int g(x)\, f(x,t)\, dx, \tag{4.4}$$

$$\frac{\partial f}{\partial t} = D\nabla^2 f + \zeta(x,t). \tag{4.5}$$

Here, $\zeta(x,t)$ is a random driving term and $g(x)$ describes a geometry-dependent coupling strength. We note that this generalizes straightforwardly to the case when $g(x)$ and $f(x,t)$ are vectors. Transforming into Fourier space and calculating the PSD of $M(t)$, we have

$$\tilde{f}(k,\omega) = \frac{\tilde{\zeta}(k,\omega)}{i\omega + Dk^2}, \tag{4.6}$$

$$S(\omega) \propto \int |\tilde{g}(k)|^2 \, \frac{\langle |\tilde{f}(k,\omega)|^2 \rangle}{\omega^2 + (Dk^2)^2}\, dk. \tag{4.7}$$

As a minimal example, consider a coupling $g(x)$ that is constant in a region and vanishes elsewhere, and a driving force which yields $\langle |\tilde{f}(k,\omega)|^2 \rangle \propto k^2$. We show the spectrum from a numerical integration of equation 4.7 with these conditions in Figure 4.2. We can motivate physical examples of this in condensed matter systems by considering critical dynamics near a second-order phase transition, where one finds correlation functions satisfying

$\langle f(x,t)f(x',t')\rangle \propto \nabla^2\delta(x-x')\delta(t-t')$ [177]. There have been multiple investigations of creating $1/f$ noises from Eq. 4.7 in the context of superconducting qubit flux noise [178, 179]. In conclusion, the free parameters in Eq. 4.7 allow one to derive a $1/f$ spectra readily, but do not give the impression of uniqueness in such models [41, 151].

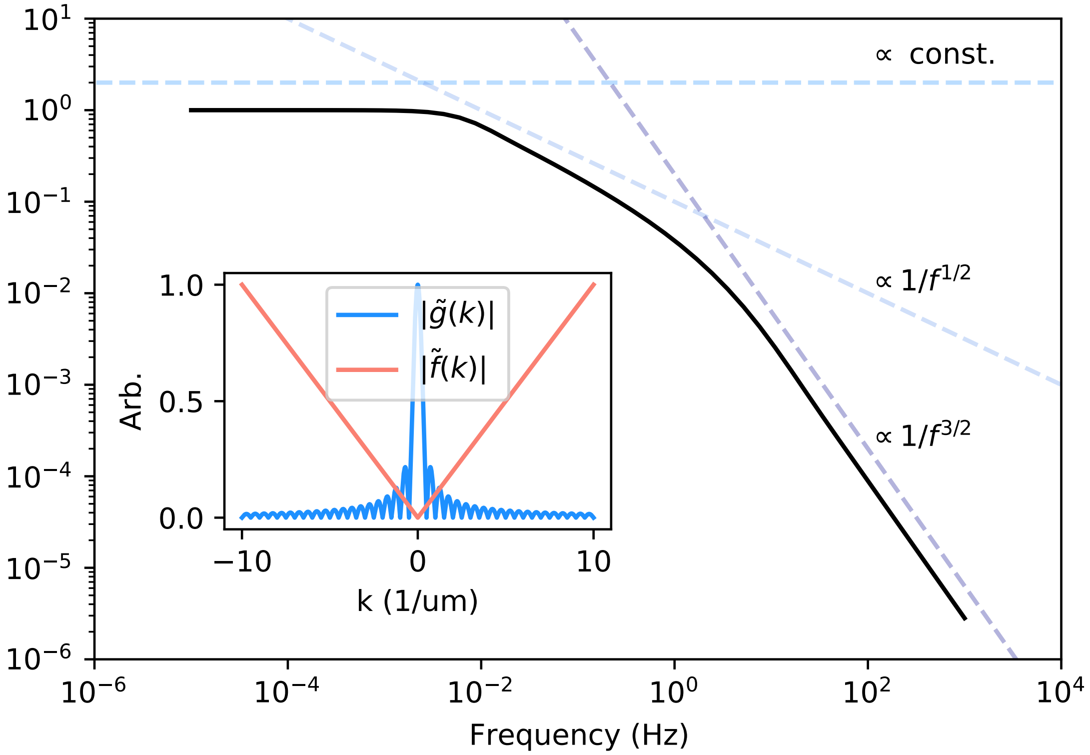

Figure 4.2: **Noise from a diffusion process.** We plot $S(f)$, normalized to its maximum value, obtained with a numerical integration of equation 4.7 for $D = 100\,\mathrm{um}^2/\mathrm{s}$ and a coupling $g(x) = 1\,\mathrm{V}$ for $|x| \leq 1\,\mathrm{um}$, and $g(x) = 0$ elsewhere. We assume the dependence $\langle|\tilde{f}(k,\omega)|^2\rangle \propto k^2$. We observe three distinct regions: 1. white noise below $1\times10^{-2}\,\mathrm{Hz}$, 2. $S(f) \propto 1/f^{1/2}$ for $1\times10^{-2}\,\mathrm{Hz} \lesssim f \lesssim 1\,\mathrm{Hz}$, and 3. $S(f) \propto 1/f^{3/2}$ above $1\,\mathrm{Hz}$. Inset shows the Fourier-space values of $\tilde{g}(k)$ and $\tilde{f}(k)$.

4.2.3 Nanothermodynamics

Here we detail an especially appealing recent model for a $1/f$ noise arising from the conservation of entropy in small systems coupled to similarly small baths, the fluctuations of which are described by the theory of nanothermodynamics [180, 181]. This model requires no assumptions about the microscopic physics of the system other than the existence of a collection of indistinguishable binary degrees of freedom (e.g., electron spins) in contact with a similarly-sized bath. We detail the physics of this model below, following Ref. [181].

Consider a system with N binary degrees of freedom, $s_i \in \{+1, -1\}$, where the net alignment $m = \sum_i s_i$ is known. Let us also define the alignment entropy of a macrostate m, $S_m = k_B \ln(\Omega_m)$ where Ω_m is the multiplicity of the alignment configuration. For example, when $m = 0$ (half of the spins are up, the other half down) the alignment multiplicity and entropy are at a maximum with $\Omega_0 = \binom{N}{N/2}$, $S_0 = k_B \ln(\Omega_0)$. When $m = \pm N$ (all spins aligned), the alignment multiplicity and entropy are at a minimum with $\Omega_N = 1$, $S_{\pm N} = 0$. In order for the entire system to maintain maximum entropy during equilibrium fluctuations, we assume the existence of a number of bath states that depends on the alignment state, $\Omega_B(m)$, such that the total entropy remains constant at $S = S_0$ (i.e., $\Omega_0 = \Omega_B(m) + \Omega_m$). This is the crucial ingredient leading to slow fluctuation dynamics and $1/f$ noise – when the system is in a macrostate with high alignment ($m \approx \pm N$), the alignment multiplicity is low so the system will spend a long time exploring the large number of bath states.

The dynamics of this system are modelled by a matrix M where each row (column) corresponds to a macrostate (microstate) of the system, yielding $N + 1$ rows ($\Omega_0 = \binom{N}{N/2}$ columns). In each row, we will place $+1$ (-1) with a multiplicity corresponding to the probability that the alignment can shift by $+1$ (-1) when flipping a random spin at random. For simplicity, considering $N = 4$ spins, we have the following matrix:

$$M = \begin{bmatrix} -1 & 0 & 0 & 0 & 0 & 0 \\ 1 & -1 & -1 & -1 & 0 & 0 \\ 1 & 1 & 1 & -1 & -1 & -1 \\ 1 & 1 & 1 & -1 & 0 & 0 \\ 1 & 0 & 0 & 0 & 0 & 0 \end{bmatrix}. \tag{4.8}$$

To simulate the dynamics of the alignment in time $m(t_i)$, let's start in the row k corresponding to state $m(t_0)$. We proceed by picking an element in that row at random, $M_{k,j}$ where j is randomly chosen from $\{1, 2, ..., \Omega_0 = 6\}$, and updating the state of the system by the following rules. If $M_{k,j} = +1(-1)$, the state of the system shifts from row k to row $k+1$ $(k-1)$. If $M_{k,j} = 0$, the system stays in row k. Iteratively updating the state yields a timeseries corresponding to the macrostate evolution of the system $\{k_0, k_1, ...\}$, from which the alignment timeseries $\{m(t_0), m(t_1), ...\}$ can be calculated directly. We simulate the dynamics for $N = 20$ spins and calculate the alignment PSD in Fig. 4.3.

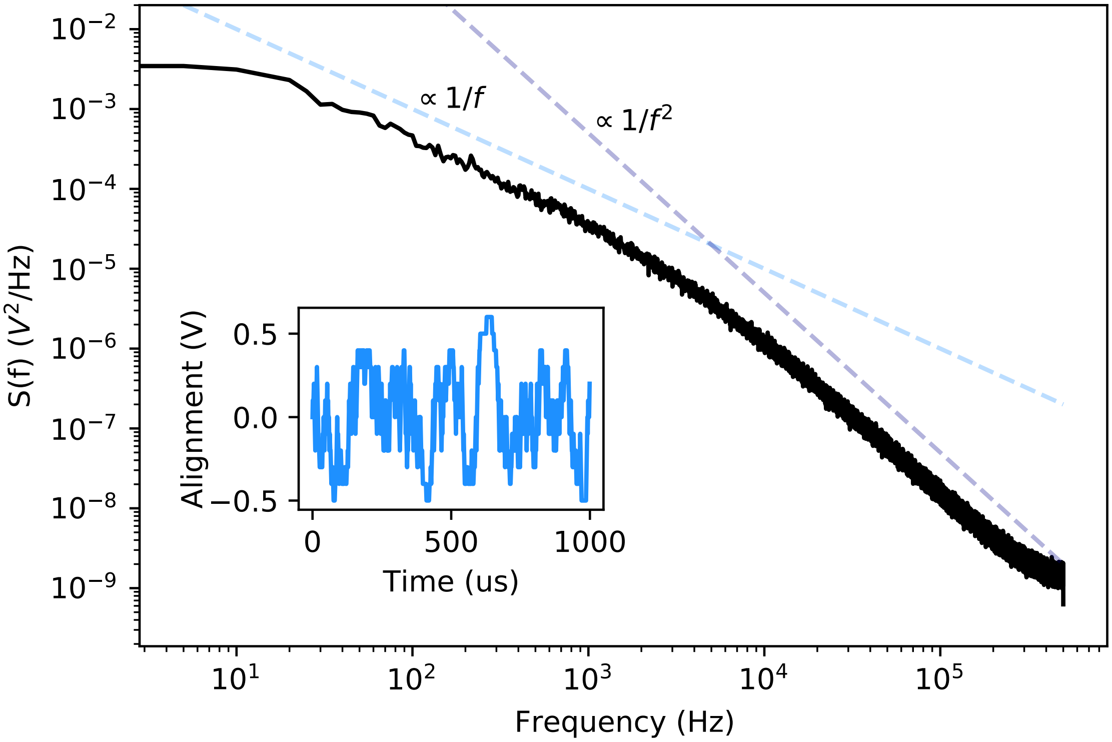

Figure 4.3: **Noise from nanothermodynamics.** We plot $S(f)$ from a system of $N = 20$ indistinguishable spins, calculated from a simulated timeseries with 10^7 steps with the Welch method (using a bin size 2×10^5). We observe four distinct regions: 1. white noise at low frequencies, 2. $S(f) \propto 1/f$ for $1 \times 10^{-1}\,\mathrm{Hz} \lesssim f \lesssim 1 \times 10^4\,\mathrm{Hz}$, 3. $S(f) \propto 1/f^2$ for $1 \times 10^4\,\mathrm{Hz} \lesssim f \lesssim 2 \times 10^5\,\mathrm{Hz}$, and the beginning of a white noise plateau at higher frequencies. Inset shows the simulated alignment in the time domain.

4.3 $1/f$ Noise in Superconducting Qubits

To end this chapter, we introduce $1/f$ noises in the context of superconducting circuits, and develop a Hamiltonian-level model for the noise of interest in Chapter 5: magnetic-flux noise.

The first superconducting qubits were realized in the late 1990s [38, 79, 92], and the discussion of their coherence-limiting noise was quick to follow [182–184]. As we learned in Chapter 3, fluctuations in any parameter $\eta(t)$ coupled to a qubit with operator $\hat{O}$ will provide a source of dephasing when the qubit frequency ω depends on the parameter or a source of relaxation and dephasing when the parameter couples the qubit states and has non-zero noise power at the qubit frequency ($\langle 0| \hat{O} |1\rangle \neq 0$ and $S_\eta(\omega) \neq 0$).

Now, we introduce the main intrinsic noises that limit superconducting qubits[2]. Environmental fluctuations that couple to circuits via the charge operator $\hat{n}$ are broadly referred to as **charge noise** [186]. Such noise is generically blamed on the ubiquitous **two-level system (TLS)** model of defects in amorphous materials which can couple to qubits via their transition electric dipole moments [187–189], and typically displays a $1/f$ PSD [186, 190, 191]. Fluctuations that couple via the flux operator $\hat{\phi}$ are broadly referred to as **flux noise**, and also display a $1/f$ PSD [44]. Flux noise is associated with defects with magnetic moments near the device Josephson-junction loop [192]. Earlier generations of superconducting qubits were also limited by **critical-current noise** of the Josephson junctions in the circuit [183, 184], again with a $1/f$ PSD [193].

4.4 Magnetic Flux Noise

In this section, we introduce a specific $1/f$ noise generated by defects with fluctuating magnetic moments (e.g., spins) coupled to the Josephson-junction (JJ) loop of a superconducting

---

[2] It is often the case that noise can be traced back to imperfections in experimental setups (e.g., from thermal radiation, spurious modes, or signal crosstalk from nonideal signal conditioning, sample design, or package design [103]), although state-of-the-art superconducting qubits routinely achieve decoherence limited by noise intrinsic to the materials comprising the devices [185].

circuit. We will develop a Hamiltonian-level model of such noise.

4.4.1 Spin-SQUID Coupling

Consider a magnetic defect with moment $\vec{\mu}$ (describing the strength and orientation of the magnet) . We can model the defect as a small current loop with area A_d and current I_d such that $\vec{\mu} = I_d \vec{A}_d$. When the defect is near another current loop s, the magnetic flux coupled into s from the defect will be $\Phi_s = MI_d$, where M is the mutual inductance between the defect loop and s.

Similarly, the flux coupled into the defect will be $\Phi_d = MI_s$, and will also be equal to the magnetic field created by the current loop s at the location of the defect, dotted with the area of the defect current loop,

$$\Phi_d = \vec{B}_s \cdot \vec{A}_d \tag{4.9}$$

$$= \vec{B}_s \cdot \vec{\mu}/I_d \tag{4.10}$$

$$= MI_s \tag{4.11}$$

Using the last two lines to solve for M, we can plug this into the expression for Φ_s,

$$\Phi_s = MI_d \tag{4.12}$$

$$= \frac{\vec{B}_s \cdot \vec{\mu}/I_d}{I_s} \cdot I_d \tag{4.13}$$

$$= \frac{\vec{\mu} \cdot \vec{B}_s}{I_s}. \tag{4.14}$$

Generally, the magnetic field produced by a current will be linear in the current, so $\vec{B}_s/I_s$ will take the form of a vector that depends solely on the geometry and position of the defect $\vec{x}$. We can then write the flux coupled into the loop, with $\vec{\tau}$ as the Pauli operator vector for the defect, as

$$\hat{\Phi}_s = \vec{g}_\Phi(\vec{x}) \cdot \vec{\tau}, \tag{4.15}$$

where we have upgraded the flux to a quantum operator to reflect the quantum nature of the defect spins. As an order of magnitude, $\boldsymbol{g}_\Phi \approx 2-4$ nΦ_0 [192]. We can perform an order-of-magnitude estimate of Φ_s by assuming the current density for a thin superconducting sheet $J(x) \propto 1/\sqrt{1-(2x/W)^2}$, then considering an infinitesimal Amperian loop around the sheet. Calculating $\Phi_s = \mu_B B(x)/I$ with $I = \int J(x)dx$, we find $\Phi_s \approx 2\text{n}\Phi_0$.

Considering an ensemble of spins coupled to a JJ loop, the net flux is given by

$$\hat{\Phi}_{\text{spins}} = \sum_i \vec{g}_\Phi(\vec{x}_i) \cdot \vec{\tau}_i, \tag{4.16}$$

where $\vec{\tau}_i$ is the Pauli matrix vector and $\vec{g}_\Phi(\vec{x}_i)$ is the flux coupling to the JJ loop associated with defect i at position $\vec{x}_i$. Noise in $\hat{\Phi}_{\text{spins}}$ is determined by its quantum autocorrelation function as discussed in Chapter 3.2.8. However, due to the low frequency of $\hat{\Phi}_{\text{spins}}$ noise relevant for quantum circuits, it often suffices to treat $\hat{\Phi}_{\text{spins}}$ in the classical (high-temperature) limit such that the PSD,

$$S_\Phi(\omega) = \int_{-\infty}^{\infty} e^{i\omega\tau} \langle \hat{\Phi}_{\text{spins}}(\tau) \hat{\Phi}_{\text{spins}}(0) \rangle d\tau, \tag{4.17}$$

is symmetric in frequency. For more thorough analytical explorations of this noise, we refer Refs. [192, 194].

4.4.2 Spin Noise for a Flux-Tunable Qubit

In this subsection, we link flux noise to frequency noise of a qubit defined by Hamiltonian

$$H = \hbar\omega\left(\Phi_B + \Phi_{\text{spins}}\right)\frac{\sigma_z}{2}, \tag{4.18}$$

where $\omega(\Phi_{\text{ext}})$ represents the flux-dependent qubit frequency. For small fluctuations about $\Phi_{\text{ext}} = \Phi_B$, we can expand the frequency to first order in Φ_{spins}, finding

$$H \approx \hbar[\omega(\Phi_B) + \omega'(\Phi_B)\Phi_{\text{spins}}]\frac{\sigma_z}{2}. \tag{4.19}$$

First, we note that the susceptibility of the qubit to flux noise is given by $\omega'(\Phi_B)$. This leads to the preferable operation of qubits where $\omega'(\Phi_B) = 0$. Recalling the expression for Φ_{spins} given by Eq. (4.16), we find that spins couple to the qubit via $\sigma_z\tau_x$, $\sigma_z\tau_y$, and $\sigma_z\tau_z$ terms. In general, one might also have coupling terms $\sigma_{x/y}\tau_{x/y}$. However, for far-detuned spins we expect these terms to become effectively longitudinal and lead to renormalization of the qubit frequency (similar to the dispersive regime explored in Chapter 2.4.6). The coupling strength and dominant term for a particular spin depends on the defect position and geometry of the JJ loop.

Aside: Suppression of Flux Noise for Elongated JJ Loops

Here, we introduce a potentially interesting experiment which can serve to validate our microscopic understanding of flux noise in superconducting circuits. The idea relies on the feature that, for a polarized spin, fluctuations can be suppressed along the axis of polarization [192]. Specifically, a spin that is polarized parallel or anti-parallel to $\vec{g}$ (e.g., by a strong applied magnetic field) will have no fluctuations along that axis since it will be frozen in its ground state. The spin will instead have maximal fluctuations along the axes orthogonal to $\vec{g}$. However, recalling Eq. (4.16), the qubit is insensitive to such fluctuations! By creating an elongated rectangular JJ loop, one would then expect to observe anisotropy of the qubit flux-noise-limited dephasing time by orienting an applied field along either the short or long axes of the rectangle.

4.5 Conclusion

In this chapter, we have given a brief historical overview of $1/f$ noises, and introduced a few toy models with power-law frequency dependence of their PSDs. We hope that this primer has helped orient the interested reader who seeks clarity about $1/f$ noises. We then introduced magnetic flux noise, which commonly displays a $1/f$ frequency dependence, and is the central topic of Chapter 5. Flux noise also serves as an example of anisotropic transverse noise for low-frequency superconducting qubits which is the central topic of Chapter 7.

Congratulations on having completed all the background material for this thesis! Now, we hope you enjoy the novel experimental results presented in the following chapters.

Chapter 5

Evolution of $1/f$ Flux Noise in Weak Magnetic Fields

As discussed in the previous chapter, the microscopic description of $1/f$ magnetic flux noise in superconducting circuits has remained an open question for several decades despite extensive experimental and theoretical investigation. However, recent progress in superconducting devices for quantum information has highlighted the need to mitigate sources of qubit decoherence, driving a renewed interest in understanding the underlying noise mechanism(s). Though a consensus has emerged attributing flux noise to surface spins, their identity and interaction mechanisms remain unclear, prompting further study. In this chapter, we detail experimental investigations probing the response of $1/f$ flux noise to weak in-plane magnetic fields (where the Zeeman splitting of surface spins lies below the device temperature), utilizing a capacitively-shunted flux qubit. We study the flux-noise-limited qubit dephasing, revealing previously unexplored trends that may shed light on the dynamics behind the emergent $1/f$ noise. Notably, we observe an enhancement (suppression) of the spin-echo (Ramsey) pure dephasing time in fields up to $B = 100\,\mathrm{G}$. With direct noise spectroscopy, we further observe a transition from a $1/f$ to approximately Lorentzian frequency dependence below $10\,\mathrm{Hz}$ and a reduction of the noise above $1\,\mathrm{MHz}$ with increasing magnetic field. We suggest that these trends are qualitatively consistent with an increase of spin cluster sizes with magnetic field. These results should help to inform a complete microscopic theory of $1/f$ flux noise in superconducting circuits.

5.1 Background

The experimental progress towards building quantum processors with superconducting qubits has advanced significantly in recent years. However, environmental noise and material quality limit qubit coherence, which constrains the ability to scale to larger devices and utilize different qubit architectures [195–197]. One major limitation to qubit coherence is the ubiquitous low-frequency magnetic-flux noise which displays a $1/f$ power spectral density [121, 198]. This noise often limits the dephasing time of frequency-tunable qubits [67, 199–202] and the fidelity of flux-activated gates [203]. Removing the source of $1/f$ flux noise would greatly expand the design space for next-generation quantum hardware, yet the origin of the noise has remained an open question for decades.

Several microscopic theories of magnetic defects in superconducting circuits with emergent $1/f$ flux noise spectra have been proposed [121, 122, 194, 204, 205]. However, there is a lack of consensus in the community on both the nature and source of the spins and the spin physics which gives rise to the noise. Nonetheless, several experimental constraints for microscopic flux noise models have been established, including an emergent $1/f^{\alpha}$ noise power spectral density from 10^{-4} Hz to 10^{8} Hz with $\alpha \lesssim 1$ [94, 142], anticorrelation of the noise in loops sharing a boundary [206], perimeter scaling of the noise amplitude [207, 208], pivoting of the noise spectrum with temperature about a fixed frequency [209], non-vanishing flux-inductance noise cross-correlation [210], paramagnetic temperature dependence of the spin bath susceptibility [211], and asymmetry of the noise spectrum [142]. Several of these features point to the likely relevance of spin-spin interactions [211, 212] and emergent phenomena including spin diffusion [48, 49] and clustering [48, 209, 210, 213, 214]. In addition to providing low-frequency dephasing noise, magnetic defects may also play a role in broadband flux noise which contributes to high-frequency energy relaxation processes [67, 94, 142], or give rise to other decoherence mechanisms [215, 216].

Despite the extensive experimental and theoretical efforts to understand and mitigate $1/f$ flux noise, one critical characterization has remained absent: the response of the flux-noise spectrum to magnetic fields. Such characterization proves experimentally challenging due to the interplay of magnetic fields with superconducting devices (often Al or Nb metallizations on Si or sapphire substrates) and the isolation of flux noise from other noise sources [216–225].

In this chapter, we investigate $1/f$ flux noise as a function of applied magnetic fields up to $B = 100\,\mathrm{G}$ with a superconducting flux qubit, where the field is oriented in the plane of the device. At low frequencies ($\lesssim 10\,\mathrm{Hz}$), we observe a $1/f$ to approximately Lorentzian transition in the noise spectrum accompanied by an increase of the Ramsey pure-dephasing rate with applied field. Surprisingly, at high frequencies ($\gtrsim 1\,\mathrm{MHz}$) we observe a suppression of the flux noise and an increase in the $1/f^{\alpha}$ noise exponent α with applied field. These results provide the first study to date of flux-noise-limited qubit dephasing and $1/f$ flux noise evolution in magnetic fields, which can serve as a new experimental reference for future microscopic theories of flux noise.

5.2 Experimental Setup

5.2.1 Overview

We measured capacitively-shunted flux qubit samples comprising Al metalizations with Al/AlOx/Al Josephson junctions (JJs) on a Si substrate at the base temperature of a dilution refrigerator with $T \lesssim 40\,\mathrm{mK}$. The samples were mounted on a cold finger with superconducting magnets in a Helmholtz coil geometry providing an approximately in-plane magnetic field (where we estimate the out-of-plane component to be $\approx 0.2\%$ of the total applied field).

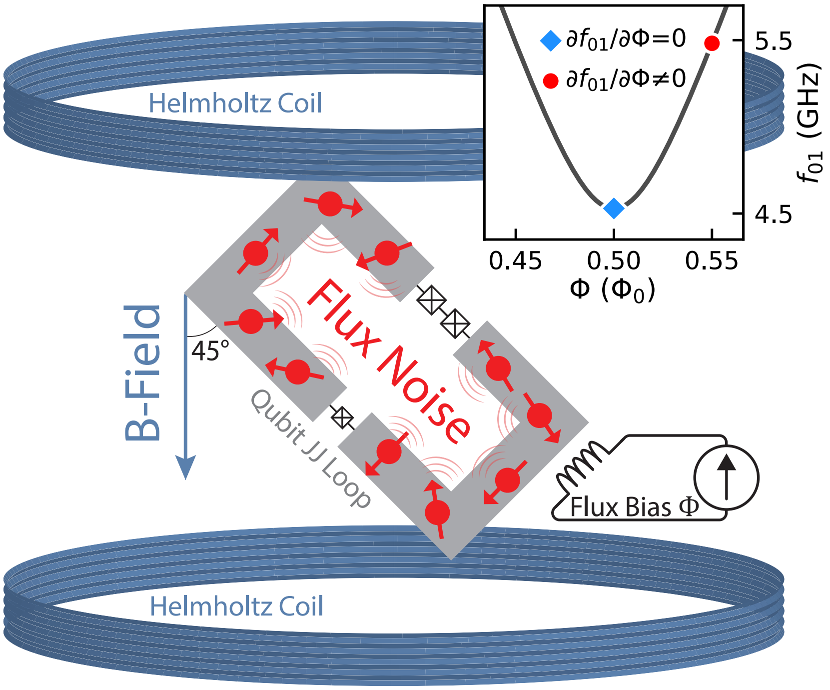

Figure 5.1: **Flux qubit in a magnetic field.** A simplified schematic of the experimental setup. The Josephson-junction (JJ) loop (gray) of a flux qubit is placed in a uniform magnetic field provided by Helmholtz coils (blue). The field is oriented in the plane of the device, and the device is tilted at a 45° in-plane angle relative to the field. Surface spins (red) in proximity to the loop generate flux noise which dephases the qubit. The inset shows an example flux qubit spectrum, with frequency f_{01} as a function of an independent flux bias Φ. The blue diamond indicates the point of first-order flux insensitivity (the so-called "sweet spot"). The red circle highlights an example operating point where the qubit displays flux-noise-limited dephasing.

The sample was rotated 45° relative to the field direction in order to ensure the qubit was sensitive to spin fluctuations both along and transverse to the direction of the field. We further detail this choice in a following subsection. A cartoon of the experimental setup and a representative qubit frequency spectrum are shown in Fig. 5.1.

5.2.2 Cryostat and Control Electronics

The experiment was conducted in a Leiden CF-650 dilution refrigerator (DR) operating at a base temperature of 30-40 mK. The sample was mounted on a cold finger with the magnet, both inside a superconducting Aluminum magnetic shield. A Mu-metal encasing around the

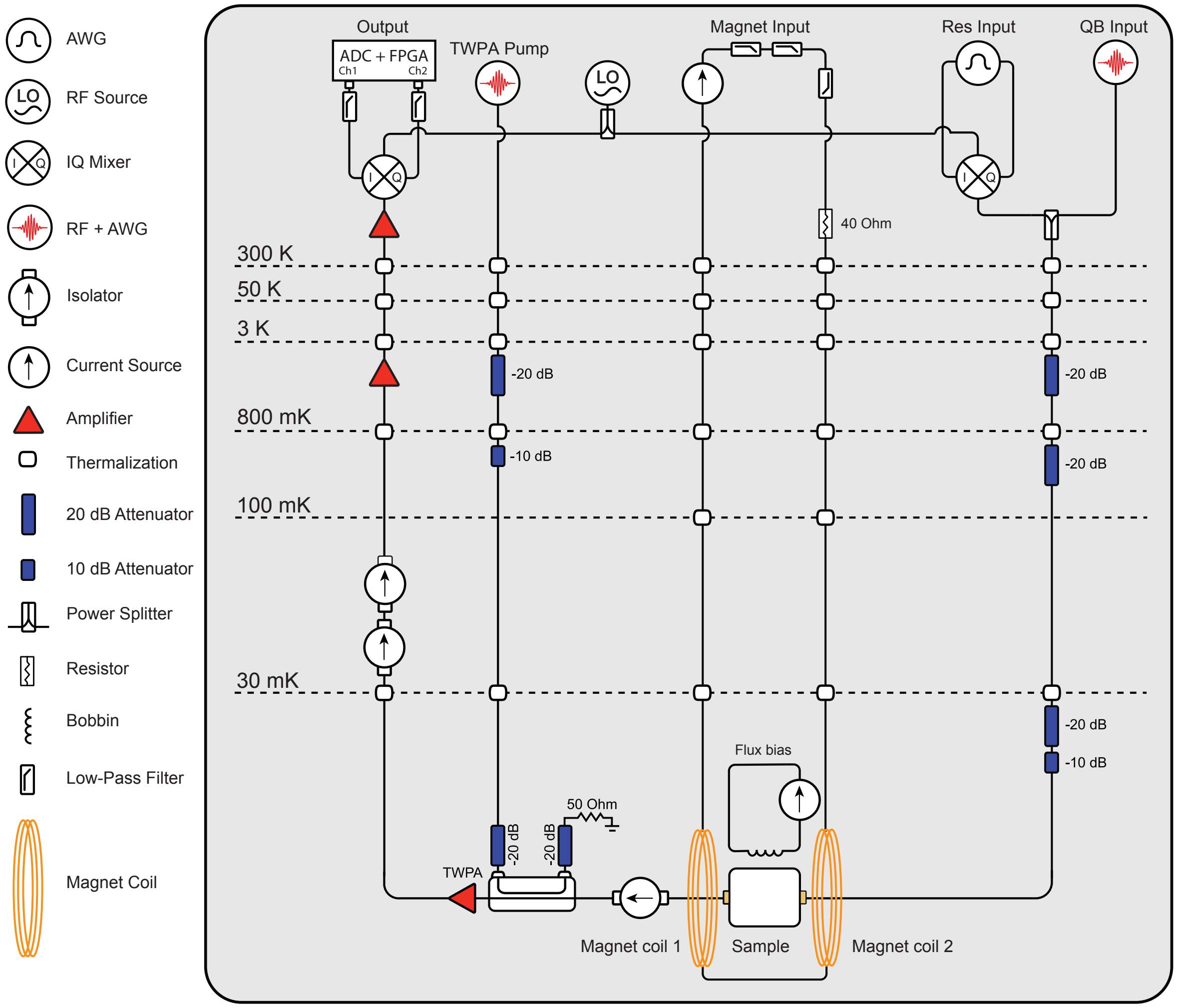

Figure 5.2: Experimental setup.

base stage provided a second layer of magnetic shielding. An explicit wiring diagram is shown in Fig. 5.2, and the specific control electronics utilized are listed in Table 5.1. A common DC flux bias for tuning the qubit frequency was provided to the whole chip using a 500-turn bobbin attached to the package lid, biased by a QDevil QDAC. Input signals providing qubit control and readout pulses were generated by arbitrary waveform generators (AWGs, one Keysight M3202A for qubit signals and another for resonator signals) and RF sources (Rohde & Schwarz SGS100 for the qubit, Agilent E8257C for the resonator), upconverted with IQ mixers, and sent into the DR. Output signals were downconverted and digitized with an ADC (Keysight M3102A). A Keysight M9019A chassis was used to synchronize and trigger the AWGs and ADC.

Component	Manufacturer	Model
Dilution Fridge	Leiden	CF-650
RF Source (Qubit)	Rohde & Schwarz	SGS100
RF Source (Readout)	Agilent	E8257C
DC Source (Qubit)	QDevil	QDAC
DC Source (Magnet)	Yokogawa	GS200
Control Chassis	Keysight	M9019A
AWG	Keysight	M3202A
ADC	Keysight	M3102A

Table 5.1: **Summary of control equipment.** The manufacturers and model numbers of the control equipment used for the experiment.

5.2.3 Sample

The sample, originally characterized in [208], comprises 10 uncoupled Al flux qubits with individual dispersively coupled resonators for control and readout, all multiplexed to a single transmission line. SQUID loop parameters were varied across the chip; the measured qubit had a rectangular SQUID with inner dimensions $18.32\,\mu\mathrm{m} \times 90.51\,\mu\mathrm{m}$ and wire width of $1\,\mu\mathrm{m}$. The flux noise amplitude in the experimental setup at $B = 0$ G was measured to be $A_\Phi \approx (4.95\,\mu\Phi_0)^2$ with the method of [208], within 10% of the value measured in the previous experiment which was conducted in a different dilution refrigerator with different control electronics over one year ago at the time of submission. This supports the hypothesis of intrinsic flux noise limited dephasing for the device, rather than extrinsic flux noise limitations from the setup.

The sample was rotated such that the SQUID loop was aligned at 45° relative to the applied field so that spins on all arms coupled to the SQUID via fluctuations both along and transverse to the applied field [192]. Specifically, assuming the applied field is the dominant field seen by a defect spin, the spin's quantization axis will be aligned with the applied field. In that case, spin flips (fluctuations parallel to the field) maximally couple to the SQUID for spins on arms orthogonal to the field, and are decoupled for spins on arms parallel to the field. Similarly, Larmor precession of spins, in the transverse direction to the applied field, maximally couples to the SQUID for spins on arms parallel to the field and decouples for spins on arms orthogonal to the field. Therefore, in the case that the applied field set the quantization axis of the spins, we elected to position the SQUID at a 45° angle relative to the chip such that spins on all arms of the SQUID would couple via both spin fluctuations along the field (spin flips) and transverse to it (e.g. Larmor precession). This geometry was chosen to accommodate sample SQUIDs which had varying aspect ratios, although the underlying assumption (that the applied field sets the quantization axis of spins) has not yet been tested with, e.g., an investigation of the field orientation dependence of the noise.

5.2.4 Magnet

Two NbTi superconducting coils in a Helmholtz geometry (hand-wound, 868 turns for each coil) provided in-plane fields of up to $B = 100\,\mathrm{G}$ at an always-on bias current of $520\,\mathrm{mA}$, supplied by four Yokogawa GS200 DC sources in a parallel current-source configuration. The magnet constant (field per current at the location of the sample) was analytically calculated from the geometry of the coils and verified with a Lakeshore F71 Teslameter at room temperature to be $c = 0.192(2)$ Gauss/mA. Room-temperature filtering on the current bias lines ensured that noise coming from the power supply did not dominate the qubit flux noise (see Section 5.2.6). Due to field misalignment, a slight out-of-plane component $B_\perp$ provided an additional flux offset to the qubits. From measuring the periodicity of 5 separate qubit spectra on the same chip with respect to the applied field, we estimated the field misalignment to be $\epsilon \approx 0.2 \pm 0.05\%$ (where $B_\perp = \epsilon B$). Specifically, with magnet bias current I providing an out-of-plane flux $\Phi_\perp$ through a SQUID loop of area A, we have $\Delta I = \Delta\Phi_\perp / c_\perp \cdot 1/A$, where $c_\perp$ is the out-of-plane magnet constant ($B_\perp = c_\perp I$). We measured ΔI corresponding to one flux quantum ($\Delta\Phi_\perp = \Phi_0$) for five separate qubits and extracted the misalignment ratio $\epsilon = c_\perp / c$ from a linear fit the data $(1/A_i, \Delta I_i)$. When sweeping the magnetic field, the qubit spectrum and flux noise susceptibility $\partial f_{01}/\partial\Phi$ was recalibrated with the separate global bobbin flux bias.

5.2.5 Evolution of Qubit Spectrum and Susceptibility to Applied Field Noise

We first note the response of the qubit sweet spot frequency to the in-plane field. Placing a Josephson junction in a magnetic field results in the suppression of the critical current I_c, which follows a Fraunhofer pattern as a function of the applied field. This phenomena has been observed to affect both the intended junctions as well as the large-area parasitic junctions resulting from shadow evaporation processes in device fabrication [218]. We observe this effect and present the measured sweetspot frequency as a function of field in Fig. 5.3a.

We then note that, at specific magnetic fields, there are divergences in the sweet spot frequency indicating a heightened susceptibility of the qubit frequency to noise in the applied field, even at the sweet spot. We display the gradient computed for fit values of the sweet spot frequency as a function of field in Fig. 5.3b. We note that at the working point of $B = 40\,\mathrm{G}$, the qubit sweet spot frequency is highly susceptible to noise in the applied field. This provides a likely explanation for the heightened dephasing noise observed at the sweet spot at $B = 40\,\mathrm{G}$ in the data of Fig. 2. In addition, we probe the sensitivity of the qubit frequency to the applied field while moving off of the sweet spot in Fig. 5.3c, and observe the highest sensitivity at $B = 40\,\mathrm{G}$. This heightened susceptibility to applied field provides a likely explanation for the outlier dephasing rates observed off the sweet spot at $B = 40\,\mathrm{G}$ in Fig. 2.

5.2.6 Applied Field Noise

In order to guarantee that observed trends in the qubit flux noise are not artifacts from changes in the applied magnetic field noise, we directly measured fluctuations of the magnet bias current I at both zero field and the highest field, shown in Fig. 5.4. The current noise

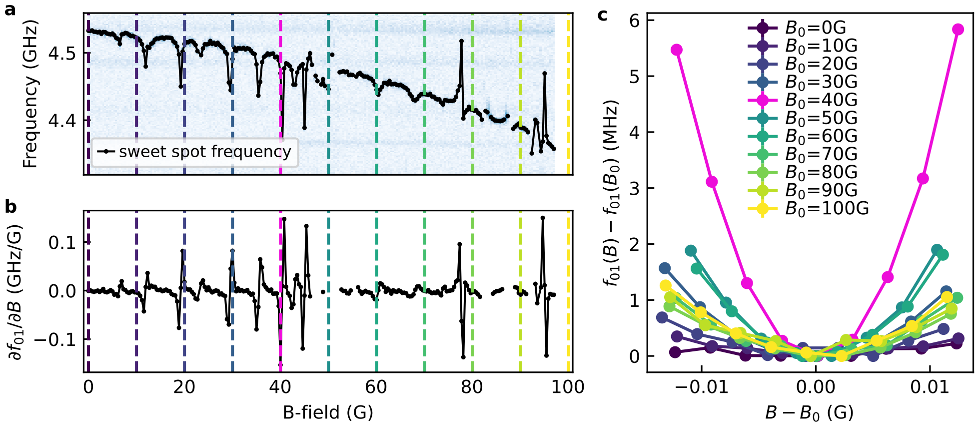

Figure 5.3: **Evolution of the Qubit Spectrum and Susceptibility to Field Noise. (a)** Flux qubit sweet spot frequency vs in-plane field. At each magnetic field, the external flux is set to $\Phi = 0.5\,\Phi_0$. **(b)** Gradient of the sweet spot frequency vs in-plane field, indicating the susceptibility of the qubit frequency to in-plane field fluctuations while operating at the sweet spot. **(c)** Qubit spectroscopy around the sweet spot as a function of in-plane field. At each field B_0, the qubit is moved to the sweet spot $\Phi = 0.5\,\Phi_0$ with an additional flux control. The in-plane field is then swept in a small range around B_0. Each trace is artificially offset to $f_{01}(B_0) = 0$. The slope of the spectrum indicates the sensitivity of the qubit frequency $f_{01}(B)$ to in-plane field fluctuations, with the highest susceptibility at fields closest to $B_0 = 40\,\mathrm{G}$.

PSD $S_I(f)$ is converted to units of flux noise by

$$S_\Phi(f) = \left(\frac{\partial f_{01}}{\partial \Phi}\right)^{-2} \left(\frac{\partial f_{01}}{\partial I}\right)^{2} S_I(f), \tag{5.1}$$

where we measure $\partial f_{01}/\partial I$ at identical points on the qubit spectrum $\partial f_{01}/\partial \Phi = 25.0\,\mathrm{GHz}/\Phi_0$ for low and high fields separately. At the frequencies probed by single-shot Ramsey noise spectroscopy ($\lesssim 10\,\mathrm{Hz}$), we observe the magnetic field noise is well below the measured qubit noise at both low and high fields. At higher frequencies ($\gtrsim 10\,\mathrm{kHz}$), the applied field noise decreases below the noise floor of the instrumentation. In this region relevant for spin-locking spectroscopy, we bound the noise with the transfer function $H(f)$ of in-line filters (measured by injecting a known magnitude white voltage noise $S_V^{\mathrm{in}}(f)$ to one end of the filter chain, and measuring the output noise after the filters, $S_V^{\mathrm{out}}(f) = H(f) \cdot S_V^{\mathrm{in}}(f)$), which places the projected applied field noise $S_\Phi^{\mathrm{projected}}(f) = H(f) \cdot S_\Phi^{\mathrm{unfiltered}}(f)$ several orders of magnitude below the measured qubit flux noise at $B = 0\,\mathrm{G}$, where $S_\Phi^{\mathrm{unfiltered}}(f)$ corresponds to the measured field noise without the in-line filters. We were unable to measure the transfer function of the in-line filters while applying the bias current required for $B = 100\,\mathrm{G}$, but we observe that the current noise measurement floor corresponds to $\lesssim 7\%$ of the lowest measured qubit noise at all fields ($S_\Phi(8.3\,\mathrm{MHz}) \approx 4.7 \times 10^{-17}\,\Phi_0^2/\mathrm{Hz}$ at $B = 20\,\mathrm{G}$). We note that in the configuration used to measure qubit flux noise, the total transfer function including the wiring of the fridge and inductance of the magnet would necessarily strengthen the bound given by the instrumentation floor, as there are only passive components in the magnet wiring. We also note that for all frequencies, the measured applied field noise increases with field, which is opposite to the observed qubit flux noise decreasing with field in the frequency domain relevant for spin-locking spectroscopy and spin echo pure dephasing. This further supports the independence of the observed qubit flux noise trends from the applied field noise.

5.3 Methods

5.3.1 Coherence

To probe broad flux-noise trends with applied magnetic field, we first performed standard qubit coherence measurements of the energy-relaxation rate $\Gamma_1 = 1/T_1$ and pure-dephasing rates from Ramsey (Γ_ϕ^R) and spin-echo (Γ_ϕ^E) protocols.

At each working point, the qubit lifetime $T_1 = 1/\Gamma_1$ was measured by preparing the qubit in the excited state and fitting the decay with an exponential function $p(t) = A\exp(-\Gamma_1 t) + C$. The Ramsey and spin-echo coherences were then measured to extract the pure dephasing rates $\Gamma_\phi^{R(E)}$. At the sweet spot ($\partial f_{01}/\partial\Phi = 0$), we observed exponential decays of the Ramsey (spin-echo) coherence for all magnetic fields and extracted the pure dephasing rate by fitting the decay to

$$p(t) = A\exp[-(\Gamma_\phi^{R(E)} + \Gamma_1/2)t] \cdot f_{R(E)}(t) + C \tag{5.2}$$

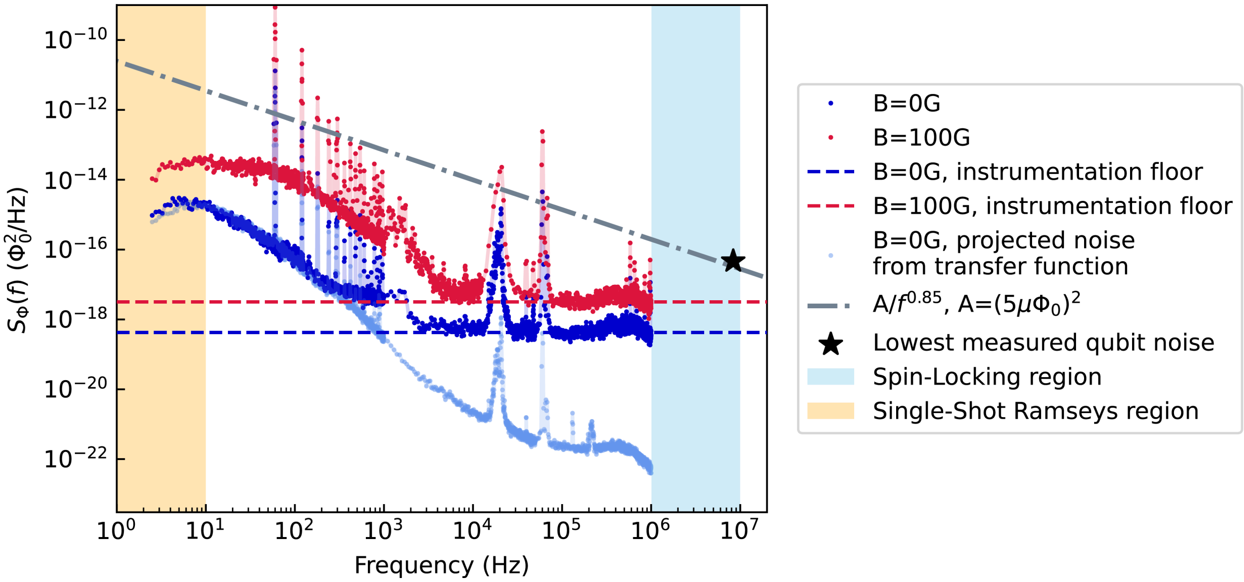

Figure 5.4: **Applied magnetic field noise.** Measured field noise at the lowest ($B = 0\,\mathrm{G}$) and highest ($B = 100\,\mathrm{G}$) fields is shown. The instrumentation noise floor is shown for both fields (dotted horizontal lines). We measure the transfer function of the in-line filters with zero bias current (corresponding to $B = 0\,\mathrm{G}$), and use this to project the applied field noise below the instrumentation noise floor (light blue). We show an estimate of the qubit flux noise (gray dash-dotted line), as well as the lowest measured flux noise ($S_\Phi(8.3\,\mathrm{MHz}) \approx 4.7 \times 10^{-17}\,\Phi_0^2/\mathrm{Hz}$ at $B = 20\,\mathrm{G}$, black star). Colored regions on the plot correspond to the frequency ranges of measured noise spectra via single-shot Ramseys (light orange) and spin-locking (light blue).

where Γ_1 is a fixed parameter determined by the preceding relaxation measurement, $f_E(t) = 1$ and $f_R(t) = \sin(2\pi f t + \delta)$, where f is an oscillation frequency equal to the detuning of the qubit and the applied pulse frequencies.

At the operating point $\partial f_{01}/\partial\Phi = 26.0\,\mathrm{GHz}/\Phi_0$, we assume $1/f$ noise limited dephasing which leads to Gaussian decay envelopes for both Ramsey and spin-echo experiments. For Ramsey experiments at all fields, we detune our qubit drive to create oscillations for ease of fitting the decay envelope.

Due to calibration drifts and jumps in the middle of magnetic field sweeps, a criteria for rejecting data collected with faulty calibration was used. The criteria was independent of magnetic field, and consisted of checking that the data fit with the appropriate fit function yielded a coefficient of determination $R^2 > 0.9$.

5.3.2 Low-Frequency ($\lesssim 10\,\mathrm{Hz}$) Noise Spectroscopy

For low-frequency noise spectroscopy, we measured $S_{f_{01}}(f)$ with the single-shot Ramsey method detailed in [139] which utilizes a time series of repeated single-shot qubit-state measurements following a fixed-time free induction decay in the presence of dephasing noise. The single-shot readout voltages were classified with a state discriminator to obtain a binary time series and converted to flux noise by a calibrated scale factor, utilizing a cross-correlation calculation to remove statistical sampling noise [139].

We attribute the white noise floor to readout infidelity, modeled by uncorrelated errors in the qubit state readout with a probability $(1-F)/2$, yielding a voltage white noise floor [226]

$$S_V^{\mathrm{ro}}(f) = (1 - F^2)\Delta t \cdot d^2, \tag{5.3}$$

where Δt is the repetition time of single-shot measurements, and d is the voltage separation of the ground and excited state cluster means. For all measured PSDs, the measured noise floor yields $F \gtrsim 85\%$ which is consistent to within 20% of the separation fidelity F estimated by a 2-state Gaussian mixture model applied to the single-shot data for all datasets.

All presented PSDs are comprised of an average of 10 sequentially measured PSDs and smoothed with a rolling window of 7 points in the frequency domain. To measure $S_\Phi(f)$, we choose an operating bias slope of $22.0\,\mathrm{GHz}/\Phi_0$ ($21.0\,\mathrm{GHz}/\Phi_0$ at $B = 100\,\mathrm{G}$) to obtain high sensitivity to frequency noise while maintaining reasonable readout SNR at high fields. To confirm that the measured noise spectra off the sweet spot and their magnetic field dependence are dominated by flux noise, we measure $S_{f_{01}}(f)$ at the sweet spot and show that it is both field-independent and well below the PSD at the flux-sensitive point for all magnetic fields in the frequency range $f \lesssim 10\,\mathrm{Hz}$ (Fig. 5.8a).

Fit functions and resulting parameters for the data of Fig. 3a are presented in Table 5.2.

Fit Function	B (G)	Fit Parameters
$S_\Phi(f) = A/f^\alpha + C$	0	$A = 1.650(2)\,\mu\Phi_0^2$, $\alpha = 0.987(4)$, $C = 1.205(6)\,\mu\Phi_0^2/\mathrm{Hz}$
$S_\Phi(f) = \frac{A}{(1+(2f/\Gamma)^2)} + C$	20	$\Gamma = 0.438(3)\,1/\mathrm{s}$, $A = 97.1(5)\,\mu\Phi_0^2/\mathrm{Hz}$, $C = 1.41(2)\,\mu\Phi_0^2/\mathrm{Hz}$
	50	$\Gamma = 0.890(6)\,1/\mathrm{s}$, $A = 239(1)\,\mu\Phi_0^2/\mathrm{Hz}$, $C = 2.24(7)\,\mu\Phi_0^2/\mathrm{Hz}$
	80	$\Gamma = 1.301(9)\,1/\mathrm{s}$, $A = 309(2)\,\mu\Phi_0^2/\mathrm{Hz}$, $C = 1.8(1)\,\mu\Phi_0^2/\mathrm{Hz}$
	100	$\Gamma = 0.631(3)\,1/\mathrm{s}$, $A = 219.5(9)\,\mu\Phi_0^2/\mathrm{Hz}$, $C = 1.78(3)\,\mu\Phi_0^2/\mathrm{Hz}$

Table 5.2: **Summary of fit functions and parameters for Fig. 3a .**

5.3.3 High-Frequency ($\gtrsim 1\,\mathrm{MHz}$) Noise Spectroscopy

For high-frequency noise spectroscopy, we use the spin-locking method detailed in [132], with interleaved SL-5a, SL-5b, and T_1 pulses. In order to average away time-dependent fluctuations in the noise environment, we avoid taking frequency data sequentially, instead taking frequency points in 10 interleaved sequences. To obtain the PSD of the qubit pure dephasing noise at a frequency f, we apply the SL-5a and SL-5b pulse sequences with Rabi frequency $f_R = f$, and fit the resulting averaged trace to an exponential decay with rate $\Gamma_{1\rho} = \Gamma_\nu + \Gamma_1/2$, where we obtain Γ_1 from the interleaved T_1 sequence. The resulting decay rate Γ_ν is related to qubit frequency noise PSD (corresponding to noise along the undriven qubit quantization axis) by $\Gamma_\nu = 1/2 \cdot S_{f_{01}}(f = f_R)$.

5.4 Experimental Results

5.4.1 Coherence

We characterized the qubit coherence both at the flux degeneracy point (where the qubit is first-order insensitive to flux noise, i.e. $\partial f_{01}/\partial\Phi = 0$, hereafter referred to as the "sweet spot"), and at a flux bias where dephasing was dominated by flux noise ($|\partial f_{01}/\partial\Phi| = 26.0\,\mathrm{GHz}/\Phi_0$, calibrated at each field with an independent flux control) [Fig. 5.5]. In order to extract the pure dephasing trends, we first isolated the field dependence of Γ_1 [Fig. 5.5a]. We found that Γ_1 varies non-monotonically, but generally increases with field. These observations may be due to the softening of the Al superconducting gap at higher fields and an associated elevated population of quasiparticles (QPs), or the effects of vortices penetrating the thin-film aluminum of our device [217, 219, 227]. We also observed a slight difference in Γ_1 at the two different working points, which is accounted for in the analysis of the qubit pure dephasing.

We extracted the Ramsey and spin-echo pure dephasing rates as proxies for the low- and high-frequency flux-noise power. Off the sweet spot, the Ramsey and spin-echo decay envelopes were approximately Gaussian and therefore consistent with $1/f$-limited dephasing [208]. We fit the decays to the product of an exponential envelope from energy relaxation and a Gaussian envelope from pure dephasing, with the relaxation rate fixed from an immediately preceding measurement. With increasing field, we observed an increase in the quasistatic noise power probed by Γ_ϕ^R [Fig. 5.5b] accompanied by a decrease in the $\gtrsim$ MHz noise probed by Γ_ϕ^E [Fig. 5.5c]. At the sweet spot, Ramsey and spin-echo traces followed exponential decays and were therefore not $1/f$ limited. We observed relaxation-limited spin-echo dephasing ($\Gamma_\phi^E \lesssim \Gamma_1/2$) and Ramsey dephasing of the same order as the relaxation rate ($\Gamma_\phi^R \sim \Gamma_1$). All coherence data were taken in nine separate runs, during each of which the field was first swept from $B = 0\,\mathrm{G}$ to $B = 100\,\mathrm{G}$ and then reversed. No hysteretic behavior was observed in $\Gamma_\phi^{R/E}$.

Anomalous Beating at Intermediate Fields

Surprisingly, in the range of magnetic fields from $B \approx 50\,\mathrm{G}$ to $B \approx 90\,\mathrm{G}$ we observe beating in the oscillations which are best fit with three oscillatory components. Some representative Ramsey decay traces are displayed in Fig. 5.6. In particular, we extract the pure dephasing rate $\Gamma_\phi^{R(E)}$ by fitting the Ramsey (spin-echo) decay to

$$p(t) = A \exp[-\Gamma_1 t/2 - (\Gamma_\phi^{R(E)} t)^2] \cdot f_{R(E)}(t) + C \tag{5.4}$$

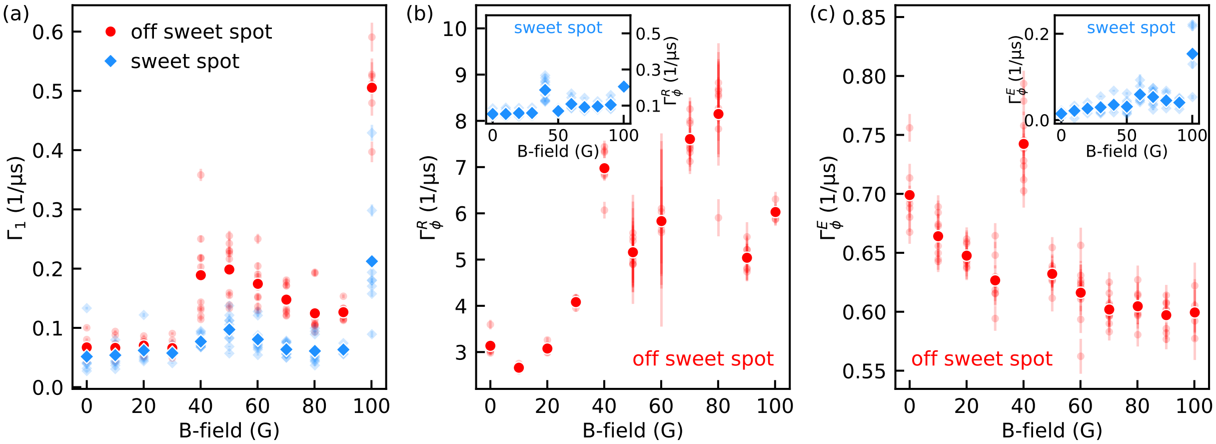

Figure 5.5: **Evolution of qubit coherence with an in-plane magnetic field.** Data taken at the sweet spot ($\partial f_{01}/\partial\Phi = 0$, blue diamonds) and off the sweet spot ($|\partial f_{01}/\partial\Phi| = 26.0\,\mathrm{GHz}/\Phi_0$, red circles). **(a)** Energy relaxation rate Γ_1. **(b)** Ramsey pure-dephasing rate Γ_ϕ^R. **(c)** Spin-echo pure dephasing rate Γ_ϕ^E. Insets in **(b)**, **(c)** show dephasing rates at the sweet spot. Data was taken during nine field sweeps, with Γ_1, Γ_ϕ^R, and Γ_ϕ^E measured consecutively at each bias point and field. Individual rate measurements are presented as partially transparent small markers with error bars given by the fit uncertainty. Average rates at each field are presented as large opaque markers. The outlier dephasing at $B = 40\,\mathrm{G}$ is likely dominated by noise in the applied field (see Section 5.2.6 for details).

where for spin-echo traces $f_E(t) = 1$ for all fields and for Ramsey traces $f_R(t) = \sin(2\pi f t + \delta)$ for fields outside of the interval $B = 50\,\mathrm{G}$ to $B = 90\,\mathrm{G}$, and $f_R(t) = \sin(2\pi f_1 t + \delta_1) + \sin(2\pi f_2 t + \delta_2) + \sin(2\pi f_3 t + \delta_3)$ for $50\,\mathrm{G} \leq B \leq 90\,\mathrm{G}$. For all fits, Γ_1 is a fixed parameter determined by a preceding T_1 measurement.

5.4.2 Noise Spectroscopy

To gain further insight into the nature of the flux noise trends, we measured the noise power spectral density (PSD) as a function of magnetic field. We observed an increase in the low-frequency noise along with a $1/f$ ($B = 0\,\mathrm{G}$) to approximately Lorentzian ($B \gtrsim 20\,\mathrm{G}$) transition in the PSD [Fig. 5.7a]. We emphasize that, in contrast to the general noise increase, the noise appears to decrease from $B = 80\,\mathrm{G}$ to $B = 100\,\mathrm{G}$, which is also present in the Γ_ϕ^R trend. Surprisingly, we also observed beating in Ramsey decays at intermediate fields $50\,\mathrm{G} \lesssim B \lesssim 90\,\mathrm{G}$ (shown in Fig. 5.6) which may be consistent with telegraphic noise

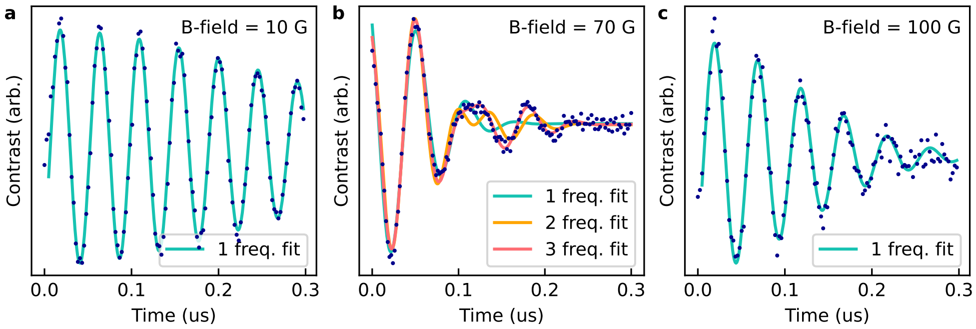

Figure 5.6: **Ramsey beating in a magnetic field.** Representative Ramsey decay traces at **(a)** $B = 10\,\mathrm{G}$, **(b)** $B = 70\,\mathrm{G}$, and **(c)** $B = 100\,\mathrm{G}$. All data is truncated at a time of $0.3\,\mu\mathrm{s}$. The Ramsey decays for magnetic fields from $B = 50\,\mathrm{G}$ to $B = 90\,\mathrm{G}$ displayed beating and were best fit by decay functions with three oscillatory components, detailed in Supplemental Material 5.3.1.

processes giving rise to the corresponding Lorentzian-like spectra; we leave a confirmation of the consistency between these observations to follow-up studies. At high frequencies, we observed a suppression of the flux noise in fields up to $B = 30\,\mathrm{G}$ [Fig. 5.7b] (past this field, high-fidelity calibration for spin-locking spectroscopy became difficult due to the excess low-frequency noise). Both low- and high-frequency PSD trends were reproduced with a second qubit on the same chip. We note that both noise spectroscopy methods measure the symmetrized PSD of qubit frequency fluctuations, $S_{f_{01}}(f)$, and when operating away from the sweet spot, we utilized the conversion between frequency- and flux-noise PSDs

$$S_{f_{01}}(f) = (\partial f_{01}/\partial\Phi)^2 S_\Phi(f). \tag{5.5}$$

To validate this conversion, we confirmed the echo dephasing rate varied linearly with the flux noise susceptibility $\partial f_{01}/\partial\Phi$ (as in [208]) at multiple magnetic fields.

Sweetspot Measurements and Hysteresis

To confirm that flux noise was responsible for the observed trends, we measured qubit frequency noise at the sweet spot and found it primarily magnetic-field-independent and well below the off-sweet-spot noise in the frequency ranges of interest, being approximately T_1

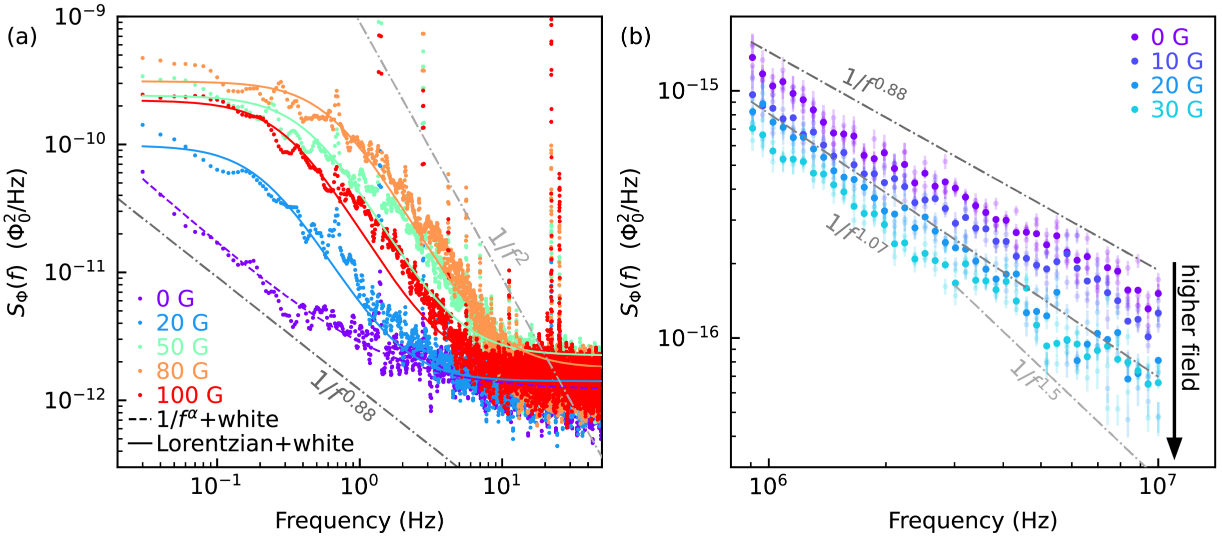

Figure 5.7: **Evolution of flux noise with an in-plane magnetic field.** **(a)** Low-frequency noise spectroscopy taken with single-shot Ramsey measurements. Data for $B < 100\,\text{G}$ were taken in one upwards sweep with $|\partial f_{01}/\partial\Phi| = 22.0\,\text{GHz}/\Phi_0$, and data at $B = 100\,\text{G}$ was taken in a separate upwards sweep with $|\partial f_{01}/\partial\Phi| = 21.0\,\text{GHz}/\Phi_0$. Gray dash-dotted lines serve as guides to the eye displaying power laws $1/f^{0.88}$ (bottom) and $1/f^2$ (top, characteristic of a Lorentzian roll-off). The $B = 0\,\text{G}$ data is fit to a $1/f$ + white noise model (purple, dashed line), and data at each non-zero field is fit to a Lorentzian + white noise model (solid line, color of corresponding data). We attribute the white noise floor to readout infidelity (see Section 5.3.2). **(b)** Spin-locking noise spectroscopy. Data was taken in four separate field sweeps with $|\partial f_{01}/\partial\Phi| = 30.0\,\text{GHz}/\Phi_0$ for $B \lesssim 10\,\text{G}$ and $|\partial f_{01}/\partial\Phi| = 31.0\,\text{GHz}/\Phi_0$ for $B \gtrsim 20\,\text{G}$. Individual measurements are presented as partially transparent small markers with error bars given by the spin-locking decay fit uncertainty. Averages at each field are presented with opaque markers. Gray dash-dotted lines serve as guides to the eye displaying the power laws $1/f^\alpha$ with $\alpha = 0.88 \pm 0.02$ (top, α from fit to $B = 0\,\text{G}$ data), $\alpha = 1.07 \pm 0.02$ (middle, from fit to $B = 20\,\text{G}$ data), and $\alpha = 1.5$ (bottom, characteristic of the asymptotic behavior of spin-diffusion noise). At higher fields, we note a suppression of the measured flux noise, denoted by an annotated black arrow.

limited ($T_{1\rho} \gtrsim T_1$) [Fig. 5.8(a,c)]. We also observed slight hysteretic behavior of the flux noise PSD at low frequencies [Fig. 5.8(b)] but not at high frequencies [Fig. 5.8(d)].

5.5 Interpretations of the Data

We now discuss possible physical mechanisms that could explain our observations. We first explore the relevance of spin polarization with the applied field, which depends on temper-

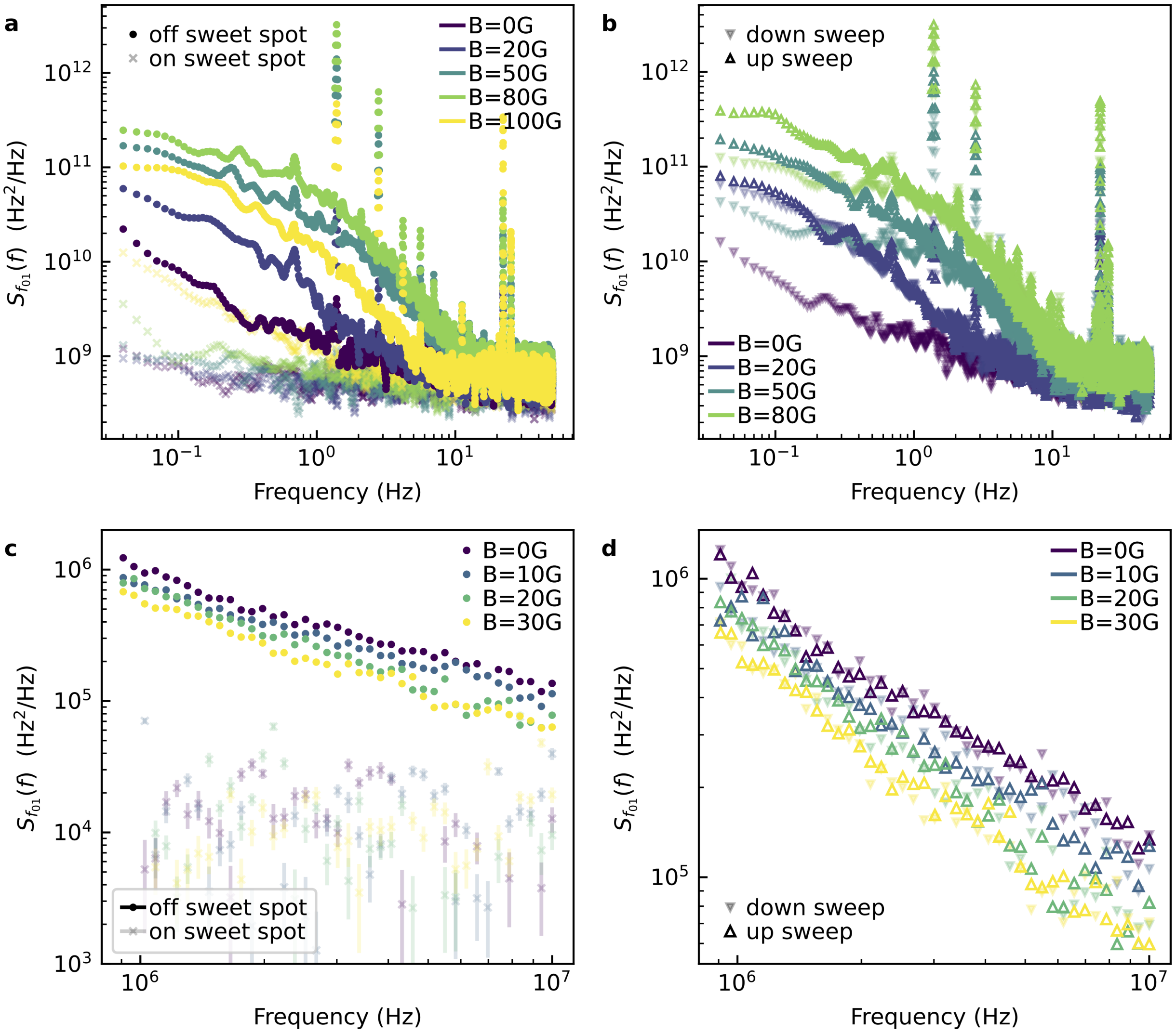

Figure 5.8: **Noise spectroscopy at the sweet spot and hysteretic effects.** PSDs are presented here in units of frequency noise, and for off sweet spot data are related to flux noise spectra by $S_{f_{01}}(f) = (\partial f_{01}/\partial\Phi)^2 S_\Phi(f)$. Off sweet spot data in **a,c** are the same as those presented in Fig. 3, and sweet spot data were collected in separate upwards field sweeps. **(a)** Low frequency noise spectroscopy on and off the sweet spot as a function of magnetic field. **(b)** Hysteresis of the low frequency noise spectra. All data was taken with $\partial f_{01}/\partial\Phi = 22.0\,\mathrm{GHz}/\Phi_0$. The field was first lowered from $B = 80\,\mathrm{G}$ to $B = 0\,\mathrm{G}$ (partially transparent downwards triangle markers), then raised back up to $B = 80\,\mathrm{G}$ (faceless triangle markers). **(c)** High frequency noise spectroscopy on and off the sweet spot as a function of magnetic field. **(d)** Hysteresis of the high frequency noise spectra. Data was taken with $\partial f_{01}/\partial\Phi = 30.0\,\mathrm{GHz}/\Phi_0$ for $B \lesssim 10\,\mathrm{G}$ and $\partial f_{01}/\partial\Phi = 31.0\,\mathrm{GHz}/\Phi_0$ for $B \gtrsim 20\,\mathrm{G}$. The field was first raised from $B = 0\,\mathrm{G}$ to $B = 30\,\mathrm{G}$ (faceless triangle markers), then lowered back down to $B = 0\,\mathrm{G}$ (partially transparent downwards triangle markers).

ature and is expected to reduce total SQUID flux noise power [192]. Similar experiments have observed evidence for the low-frequency ($hf \ll k_B T_{\text{eff}}$) environment of the spin bath being in thermal equilibrium at an effective temperature T_{eff} close to but above that of the mixing-chamber plate [142]. Studies of the native surface spin bath of Al_2O_3 observed signatures consistent with a population of $g = 2$, $S = 1/2$ electron spins [212] at a density matching that of the surface spins producing the ubiquitous $1/f$ flux noise in SQUIDs [211]. We expect saturation of noise suppression from spin freezing to occur in the regime

$$800\,\text{MHz} \ll k_B T_{\text{eff}}/h \lesssim \frac{\gamma_e}{2\pi} B, \tag{5.6}$$

where $\gamma_e/2\pi \approx 2.8\,\text{MHz/G}$ is the free-electron gyromagnetic ratio and the lower bound of T_{eff} is set by the measured mixing-chamber plate temperature in our experiment ($\approx 40\,\text{mK}$). Our largest applied field ($B_{\text{max}} = 100\,\text{G}$) corresponds to a free electron Zeeman energy of $\frac{\gamma_e}{2\pi} B_{\text{max}} \approx 280\,\text{MHz}$ which is below the thermal energy scale of $\approx 800\,\text{MHz}$. Given the non-monotonic behavior of the low-frequency flux noise and the saturation of the high-frequency spin-echo dephasing, we suggest that thermal polarization alone cannot explain the observed trends.

One plausible interpretation of the data is an increase in surface spin cluster size with magnetic field, where a cluster refers to a group of interacting spins. In this paragraph, we justify clustering as a relevant phenomenon in superconducting qubit surface spin baths. Clustering is a known behavior of spin ensembles in proximity to a phase transition [47], with the cluster-size distribution depending on temperature [47] and field [228]. Multiple experiments on similar superconducting quantum circuits have observed evidence of native surface spin baths being near a magnetic phase transition while at standard operating conditions (i.e. millikelvin temperatures and nominally zero applied field) [48, 211]. Increasing cluster size has been previously hypothesized as a source of the spectral pivoting of $1/f$ noise with decreasing temperature [209]. We note that experimental and theoretical studies have suggested that high-frequency $1/f$ flux noise emerges from spin diffusion dynamics [46–49], while a distinct mechanism is responsible for the low-frequency flux noise, such as longer-time fluctuations of the net magnetization of clusters [47, 48].

We now discuss the low frequency ($\lesssim 10\,\mathrm{Hz}$) flux noise spectrum [Fig. 5.7a]. It has been suggested that clusters of spins may act as “macrospins" with effective magnetic moments and relaxation processes, which produce an ensemble of telegraphic noise processes giving rise to $1/f$ noise [47, 213, 214]. Assuming the effective relaxation rate of a cluster rapidly decreases with the number of spins in the cluster [47], an increasing size with applied field would be consistent with the rise in low-frequency flux noise. The transition from $1/f$ to approximately Lorentzian noise suggests a narrowing of the distribution of cluster relaxation rates, which may reflect clusters becoming more homogeneous in size with applied field as a result of, e.g., fewer total clusters or size saturation due to the finite dimension of the superconducting wire. We note that the Lorentzian cut-off frequency does not saturate with magnetic field, but appears highest at $B \approx 80\,\mathrm{G}$. This non-monotonic behavior may be due to the field dependence of system parameters such as individual spin relaxation times, the effective spin diffusion constant, cluster sizes, etc.

We now proceed to the high frequency ($\gtrsim 1\,\mathrm{MHz}$) flux noise spectrum [Fig. 5.7b]. We present two potential mechanisms for the suppression of spin diffusion that would lead to the lowering of flux noise in the MHz range: (1) spin clustering, and (2) inhomogeneous broadening of the spin bath. The growth of spin clusters (and corresponding reduction of their flip-rate [47]) would reduce the number of smaller clusters contributing to high-frequency noise [209]. Beyond this generic trend, we consider the case of ferromagnetic or random clusters. In the case of ferromagnetic clusters, growth would inhibit flip-flop processes contributing to spin diffusion by decreasing the number of participating antiparallel spin pairs. In the case of random clusters (in which spins are oriented randomly), growth would inhibit diffusion processes past a critical timescale $f_c^{-1} \propto L^2/D$, where D is the effective spin diffusion coefficient and L is the spatial extent of a cluster which determines how far excitations can freely diffuse before running into a boundary—at frequencies above f_c, the noise PSD asymptotically approaches $S(f > f_c) \sim 1/f^{1.5}$ [48, 49]. In addition to a reduction of the noise level, our data displays an increasing noise exponent α with applied field which is consistent with an increase in L. We note that in an earlier cooldown we observed $\alpha \approx 1.5$ at magnetic fields $B \gtrsim 12\,\mathrm{G}$ in multiple datasets, although this behavior was not observed during the subsequent cooldown. We also note the apparent saturation of Γ_ϕ^E, which may suggest a saturation of spin cluster sizes complementing the $1/f$ to Lorentzian transition in the low-frequency noise.

Another possible mechanism for the suppression of spin diffusion (i.e. spin flip-flops) is inhomogeneous broadening of the spin bath from local variations in the applied field [229, 230], which would reduce the effective diffusion constant D [231]. Spin flip-flops are possible between resonant spins (detuned less than their interaction strength) with antiparallel orientations. Since the saturation of Γ_ϕ^E occurs at lower field than would be expected from polarization (reorientation) of the surface spins, we suggest that inhomogeneous broadening provides a more consistent explanation for both the qubit coherence and noise spectroscopy data. A number of mechanisms may lead to inhomogeneous broadening such as spatially inhomogeneous Meissner screening, or a statistical distribution of the effective gyromagnetic ratios of magnetic defects. Attributing the saturation of Γ_ϕ^E entirely to such broadening, we place a rough bound on the spin-spin interaction strength assuming the spin energy is given approximately by the applied field Zeeman splitting—a spin experiencing the bare field would have a frequency $\approx \frac{\gamma_e}{2\pi}B$, and a nearby spin experiencing no applied field (i.e. on an adjacent face of the wire which is entirely shielded) would have a frequency ≈ 0. Flip-flop processes would be inhibited between these spins if their coupling strength J satisfies

$$J < h\frac{\gamma_e}{2\pi}(B - 0). \tag{5.7}$$

With a saturation field $B_{\mathrm{sat}} \approx 50\,\mathrm{G}$, we have $J/h \lesssim 150$ MHz.

5.6 Outlook

In summary, our results provide the first characterization of flux-noise-limited dephasing in superconducting qubits as a function of applied magnetic field. Our data reveals a distinct $1/f$ to approximately Lorentzian transition of the noise spectrum below 10 Hz as well as a suppression of noise above 1 MHz. The observed trends are consistent with increasing spin cluster sizes with applied field, although more experimental and theoretical investigation is required to validate this interpretation. Further insight can be obtained by mapping the flux noise response at higher fields using magnetic-field-resilient devices (e.g. niobium or thinner aluminum metallizations), or by probing the noise response to applied fields while varying device materials or field angle. In addition, searching for resonant peaks in the flux noise spectra at higher frequency ($\gtrsim$ 10 MHz) as a function of magnetic field may provide valuable clues about the electronic and chemical configuration of the magnetic defects comprising the spin bath. Such signatures of coherent fluctuators in flux noise spectra have already been observed, albeit at nominally zero field, and without consistent reproducibility [132]. Already, we anticipate that our results can provide a new experimental constraint for future flux noise models incorporating magnetic field dependence [232], which may bring us one step closer to solving the decades-long open question of the microscopic origin of $1/f$ flux noise in superconducting circuits.

Chapter 6

Fast Gates with Fluxonium Qubits

Qubit decoherence unavoidably degrades the fidelity of quantum logic gates. Accordingly, realizing gates that are as fast as possible is a guiding principle for qubit control, necessitating protocols for mitigating error channels that become significant as gate time is decreased. One such error channel arises from the counter-rotating component of strong, linearly polarized drives. This error channel is particularly important when gate times approach the qubit Larmor period and represents the dominant source of infidelity for sufficiently fast single-qubit gates with low-frequency qubits such as fluxonium. In this work, we develop and demonstrate two complementary protocols for mitigating this error channel. The first protocol realizes circularly polarized driving in circuit quantum electrodynamics (QED) through simultaneous charge and flux control. The second protocol—commensurate pulses—leverages the coherent and periodic nature of counter-rotating fields to regularize their contributions to gates, enabling single-qubit gate fidelities reliably exceeding 99.997%. This protocol is platform independent and requires no additional calibration overhead. This work establishes straightforward strategies for mitigating counter-rotating effects from strong drives in circuit QED and other platforms, which we expect to be helpful in the effort to realize high-fidelity control for fault-tolerant quantum computing.

6.1 Introduction

Superconducting qubits have emerged as a leading contender for performing quantum computation [233], with steadily increasing circuit sizes and rising gate fidelities approaching the levels required to begin scaling error correcting codes [39, 54, 234–236]. However, gate fidelities must improve further to realize useful quantum computations, e.g., by surpassing code thresholds to yield algorithmically-relevant logical error rates [31, 236–238].

Decoherence poses a significant challenge to the realization of high-fidelity gates, contributing an error proportional to t_g/T_{coh}, where t_g represents the duration of a gate operation and T_{coh} the relevant coherence timescale. For superconducting qubits, decoherence often limits the fidelity of state-of-the-art gates. Consequently, to build useful quantum hardware, we aim to increase system coherence and decrease gate times as much as possible.

The speed of quantum logic gates is generally limited by effects that become significant as gate times approach relevant system timescales. As a primary example, leakage to non-computational states becomes significant when gate times approach the timescale set by the qubit anharmonicity [53, 239]. This example is especially relevant for transmon qubits [54, 240], for which low anharmonicities of typically $|\alpha|/2\pi \sim 200\,\text{MHz}$ limit gate times to $(|\alpha|/2\pi)^{-1} \sim 5\,\text{ns}$ [101, 241]. As another example, linear drives [52] for gates with durations approaching the qubit Larmor period ($t_g/\tau_L \to 1$) give rise to significant undesirable counter-rotating dynamics, resulting from the breakdown of the rotating-wave approximation (RWA) [242–245]. These effects are typically negligible for transmons due to their high transition frequency ($t_g/\tau_L \gtrsim 5\,\text{ns} \cdot 4\,\text{GHz} = 20$).

Both the intrinsic control limitations and coherence properties of a particular qubit are dictated by its Hamiltonian. The interplay between qubit anharmonicity, sensitivity to noise, and circuit simplicity for superconducting qubits has been elucidated over the past several decades [39, 55, 246–252], leading to the transmon as the current workhorse superconducting qubit. However, the limitations imposed by its low anharmonicity and unprotected computational states [96] have motivated further investigation of circuits with more favorable coherence and control properties. The fluxonium [55] is one such qubit, featuring a transition frequency typically less than 1 GHz, with state-of-the-art coherence times and single- and two-qubit gate fidelities [99, 253–256]. One beneficial property of the fluxonium is its high anharmonicity, typically several gigahertz, when operated at a flux bias of a half magnetic flux quantum $\Phi_0/2$. This property mitigates leakage during fast single-qubit gates, enabling the exploration of new dominant error channels and strategies to mitigate them. In particular, fast, resonant control of fluxonium naturally places one in the regime $t_g/\tau_L \lesssim 5\,\mathrm{ns} \cdot 1\,\mathrm{GHz} = 5$, where errors due to counter-rotating effects start to become severe.

In this work, we explore fast single-qubit gates based on the resonant control of a fluxonium qubit in the regime of few-cycle pulses ($1 \lesssim t_g/\tau_L \lesssim 5$), where errors from counter-rotating dynamics are significant. We develop two complementary strategies for mitigating these errors. Our first strategy takes inspiration from circularly polarized free-space electromagnetic fields and realizes tunable-polarization drives [257] with simultaneous charge and flux control. We demonstrate the tunability of drive polarization and the calibration of co-rotating drives for gates. Our second strategy, enabling fidelities exceeding 99.997% with only a linear drive, involves leveraging the time-periodicity of the counter-rotating fields to regularize their contributions to all pulses [258]. This approach, hereafter referred to as commensurate pulses, eliminates the coherent error channel posed by counter-rotating effects with no additional calibration overhead and can be implemented straightforwardly to mitigate these effects in any platform where fast resonant control is desired. We utilized both approaches to implement single-qubit gates, exploring different drive schemes—charge, flux, and circularly polarized drives—and the resulting fidelity dependence on the gate duration. Finally, we developed an error budget for our gates and investigated their stability, finding that our best gates were coherence limited, and the performance remained stable (error per gate fluctuations $\lesssim 1.13 \times 10^{-5}$) for the entire measurement duration of 34 hours after an initial calibration.

6.2 Device and Theory

In this section, we detail the device, our two complementary protocols for mitigating counter-rotating errors for fast gates, and our single-qubit gate implementation.

6.2.1 Fluxonium Device

Our device comprises a two-dimensional differential fluxonium qubit capacitively coupled to a charge line and inductively coupled to a flux line as shown in Fig. 6.1(a). Modeling just the fluxonium qubit and the two drive lines, our device obeys the system Hamiltonian

$$\hat{H} = \hat{H}_0 + \hbar\Omega_c \cos(\omega_d t)\hat{n} + \hbar\Omega_f \cos(\omega_d t - \Delta\varphi)\hat{\phi}, \tag{6.1}$$

where $\hat{H}_0$ is the bare fluxonium Hamiltonian

$$\hat{H}_0 = 4E_C\hat{n}^2 + \frac{1}{2}E_L\hat{\phi}^2 - E_J\cos(\hat{\phi} - \phi_{\mathrm{dc}}). \tag{6.2}$$

This Hamiltonian is written in the lab frame, where Ω_c (Ω_f) describes the amplitude of a cosinusoidal charge (flux) drive with frequency ω_d and phase difference $\Delta\varphi$ between the two drives. In the fluxonium Hamiltonian, $\hat{n}$ and $\hat{\phi}$ represent the charge and phase operators, $E_C/h = 1.30\,\mathrm{GHz}$, $E_L/h = 0.59\,\mathrm{GHz}$, and $E_J/h = 5.71\,\mathrm{GHz}$ are the charging-, inductive-, and Josephson energy, respectively, and ϕ_{dc} is a phase offset resulting from a static external magnetic flux $\Phi_{\mathrm{dc}}/\Phi_0 = \phi_{\mathrm{dc}}/2\pi$ supplied by a superconducting coil inductively coupled to the fluxonium loop. The sample qubit was a subsystem of a device comprising two fluxonium qubits with a capacitively-coupled transmon coupler (refer to device A, fluxonium 2 of Ref. [255]). We note that the linear flux drive arises from the allocation of time-dependent flux inside the inductor term, which has recently been theoretically and experimentally verified [259, 260].

Our experiments were performed at $\Phi_{\mathrm{dc}} = 0.5\Phi_0$, where the qubit had a frequency

$\omega_{01}/2\pi \approx 243\,\text{MHz}$ (Larmor period $\tau_L \approx 4.1\,\text{ns}$) and coherence times generally between $200\,\mu\text{s} \lesssim T_1, T_{2E} \lesssim 500\,\mu\text{s}$. Dispersive readout was performed with a capacitively-coupled resonator at frequency $\omega_r/2\pi = 7.08\,\text{GHz}$, with linewidth $\kappa/2\pi \approx 1.5\,\text{MHz}$ and dispersive shift $\chi/2\pi \approx 1\,\text{MHz}$ [89]. We herald the desired initial state with a preceding projective measurement, with a buffer time of $2\,\mu\text{s}$ before applying qubit pulses to avoid photon-shot-noise dephasing. All charge and flux control pulses were directly synthesized on a high-bandwidth arbitrary waveform generator (see Appendix 6.3 for details).

We emphasize the relevance of fluxonium qubits for our experiments exploring counter-rotating dynamics, as their typically low qubit frequency and high anharmonicity cause counter-rotating effects to manifest before leakage into non-computational states is observed when performing Rabi-based single-qubit gates.

6.2.2 Circularly Polarized Driving

In this subsection, we detail the ability to tune qubit drive polarization by controlling the relative phase $\Delta\varphi$ of simultaneous charge and flux drives [Fig. 6.1(b)]. In particular, we show that for particular values of the relative phase, drives consisting of purely linear, co-, or counter-rotating components can be generated. We also derive an expression for the Rabi frequency (within the RWA) as a function of the relative phase between simultaneous charge and flux drives, enabling us to determine the relative phase offset in our setup and consequently generate drives with desired polarizations.

We begin by simplifying the system Hamiltonian Eq. (6.1). Truncating to the ground and first excited state manifold, with $\hat{H}\left|0\right\rangle = 0$, the two-level Hamiltonian terms take the following form

$$\begin{aligned} \hat{H}_0 &\to \hbar\omega_{01} \left|1\right\rangle\left\langle 1\right|, \\ \hat{n} &\to i(\left|0\right\rangle\left\langle 1\right| - \left|1\right\rangle\left\langle 0\right|), \\ \hat{\phi} &\to \left|0\right\rangle\left\langle 1\right| + \left|1\right\rangle\left\langle 0\right|. \end{aligned}$$

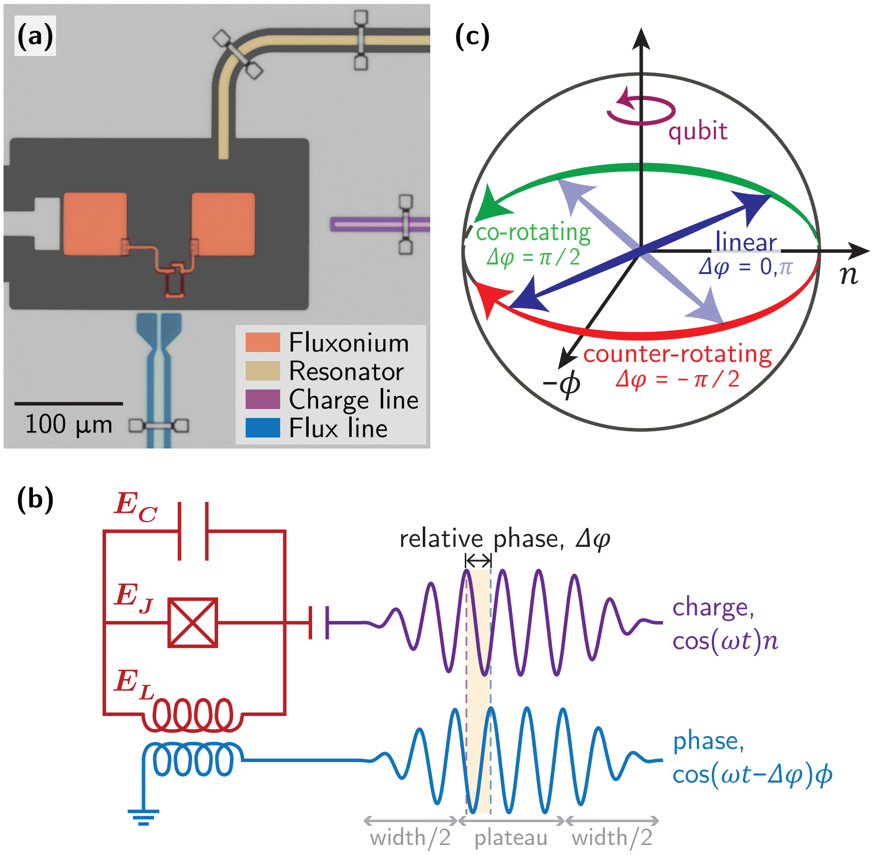

Figure 6.1: **Device and concept.** **(a)** False-colored optical micrograph of the fluxonium qubit (orange) with a coupled charge (purple) and flux line (blue). **(b)** Diagram illustrating how all drives are performed in this experiment. All drives comprise a phase-sensitive linear combination of a charge and flux drive, parameterized by a cosine-shaped rise-fall and a flat top. **(b)** Bloch sphere representation of a qubit with the trajectory of various drive polarization vectors drawn. A co-rotating (green) drive has a polarization vector rotating with the same orientation as the qubit, a counter-rotating (red) drive has a polarization vector rotating in the opposite direction as the qubit, and a linear (blue) drive has a polarization vector which traces out a line.

Considering charge and flux drives of the same strength ($\Omega_c|\langle 0|\,\hat{n}\,|1\rangle| = \Omega_f|\langle 0|\,\hat{\phi}\,|1\rangle| \equiv \Omega/2$), we arrive at the two-level Hamiltonian

$$\begin{aligned}\frac{\hat{H}}{\hbar} = {} & \omega_{01}\,|1\rangle\,\langle 1| \\ & - i\frac{\Omega}{4}\cos(\omega_d t)(|0\rangle\,\langle 1| - |1\rangle\,\langle 0|) \\ & + \frac{\Omega}{4}\cos(\omega_d t - \Delta\varphi)(|0\rangle\,\langle 1| + |1\rangle\,\langle 0|).\end{aligned} \tag{6.3}$$

Inspecting the above equation, we find that the two drive terms act along orthogonal axes of the Bloch sphere in the lab frame. We can see this simply by expressing the operators with Pauli matrices: $\hat{\phi} \propto \sigma_x$ and $\hat{n} \propto \sigma_y$. This is a consequence of the canonically conjugate nature of the charge and flux operators, and it enables the effective field polarization to be tuned by the relative phase of the charge and flux drives. This may be contrasted with the polarization of free-space electromagnetic fields, where polarization is defined by the relation of real-space field components.

Linear drives

Setting the relative phase to $\Delta\varphi = 0$ (π) [Fig. 6.1(c), blue] yields a linearly polarized drive with drive operator $\hat{n} + \hat{\phi}$ ($\hat{n} - \hat{\phi}$). One can also trivially generate linear drives by applying an individual charge or flux drive (oscillating only along the n or ϕ axes respectively).

Co-rotating drives

Applying a rotating frame transformation to Eq. (6.3),

$$\hat{\tilde{H}} = \hat{U}\hat{H}\hat{U}^{-1} + i\hbar \frac{\partial \hat{U}}{\partial t}\hat{U}^{-1}, \tag{6.4}$$

at a frequency ω_d co-rotating with the qubit, $\hat{U}_{\mathrm{rf}}(t) = e^{i\omega_d t |1\rangle\langle 1|}$ gives

$$\begin{aligned} \frac{\hat{\tilde{H}}}{\hbar} = &\, (\omega_{01} - \omega_d) \left|1\right\rangle \left\langle 1\right| \\ & - i\frac{\Omega}{4}\left[1 + ie^{-i\Delta\varphi} + e^{-2i\omega_d t}(1 + ie^{i\Delta\varphi})\right] \left|0\right\rangle \left\langle 1\right| + \mathrm{h.c.} \end{aligned} \tag{6.5}$$

For $\Delta\varphi = \pi/2$ [Fig. 6.1(c) green], the fast-oscillating terms exactly cancel, and the Hamiltonian simplifies to a qubit with a static drive field (without needing the RWA),

$$\frac{\hat{\tilde{H}}_{\mathrm{co}}}{\hbar} = (\omega_{01} - \omega_d) \left|1\right\rangle \left\langle 1\right| - i\frac{\Omega}{2}(\left|0\right\rangle \left\langle 1\right| - \left|1\right\rangle \left\langle 0\right|). \tag{6.6}$$

In the lab-frame Bloch sphere picture, the net drive field travels along the equator in the same direction as the qubit Larmor precession [Fig. 6.1(c) purple].

Counter-rotating drives

Alternatively, for $\Delta\varphi = -\pi/2$ [Fig. 6.1(c), red], the drive field travels along the equator but opposite to the qubit Larmor precession. In a frame counter-rotating relative to the qubit at frequency ω_d, $\hat{U}_{\mathrm{rf}}(t) = e^{-i\omega_d t |1\rangle\langle 1|}$, we likewise find a time-independent Hamiltonian without making the RWA,

$$\frac{\hat{\tilde{H}}_{\mathrm{counter}}}{\hbar} = (\omega_{01} + \omega_d)\,|1\rangle\,\langle 1| - i\frac{\Omega}{2}\left(|0\rangle\,\langle 1| - |1\rangle\,\langle 0|\right). \tag{6.7}$$

Considering resonant drives ($\omega_d = \omega_{01}$), turning on such a counter-rotating field diabatically will have the effect of inducing small oscillations of the qubit population at a frequency $\approx 2\omega_{01} + \Omega^2/4\omega_{01}^2$, as the system eigenstates dressed with the counter-rotating drive comprise an admixture of the bare qubit eigenstates. Oscillations around $2\omega_{01}$ under strong resonant driving is a hallmark of counter-rotating effects, signifying a breakdown of the RWA as $\Omega \to \omega_{01}$.

Rabi Oscillations with Simultaneous Drives of Arbitrary Relative Phase

With resonant drives ($\omega_d = \omega_{01}$), the rotating frame Hamiltonian Eq. (6.5) only retains the coupling term

$$\frac{\hat{\tilde{H}}}{\hbar} = -i\frac{\Omega}{4}(1 + ie^{-i\Delta\varphi} + e^{-2i\omega_d t}(1 + ie^{i\Delta\varphi}))\,|0\rangle\,\langle 1| + \mathrm{h.c.} \tag{6.8}$$

For weak drives ($\Omega \ll \omega_{01}$), we can perform the RWA (discard terms oscillating at $2\omega_d$) and the qubit will display generalized Rabi oscillations at a frequency

$$\begin{aligned}\tilde{\Omega} &= \frac{\Omega}{4}|1 + ie^{-i\Delta\varphi}| && (6.9)\\ &= \frac{\Omega}{2}|\cos((\Delta\varphi - \pi/2)/2)| && (6.10)\\ &= \frac{\Omega}{2}\sqrt{\frac{1+\cos(\Delta\varphi - \pi/2)}{2}}. && (6.11)\end{aligned}$$

To determine the relative phase offset of the charge and flux drives, we applied simultaneous drives of the same strength while sweeping the relative phase and fit the observed oscillation frequencies to Eq. (6.11).

To conclude this subsection, we emphasize that the ability to realize circularly polarized electromagnetic fields with superconducting qubit drives ultimately relies on the charge and flux drive operators being linearly independent and on the equatorial plane of the qubit Bloch sphere.

Can we generate circular drives with only one control line?

The requirement for distinct charge and flux drives raises a question: for a linear drive, the rotation axis of a gate defined in the rotating frame can be adjusted via the drive phase, so is it possible to create a circularly polarized drive with phase-shifted tones applied on the same control line?

The answer is no – simultaneous pulses on the same control line have the same lab-frame polarization, and the counter-rotating components from both pulses cannot completely destructively interfere unless the net drive tone is zero.

From another perspective, if one tries to determine which phase-shifted pulses to apply, it also becomes apparent that this is impossible: perpendicular rotations in the rotating frame are implemented with one control line by adding a 90° relative phase, and further phase-shifting the tones in order to create a circularly polarized drive requires another 90°

relative phase, leading to either 0 or 180° total relative phase. The resulting net drive is linearly polarized in either case.

6.2.3 Commensurate Pulses: Regularizing Coherent Errors from Counter-Rotating Terms

In this section, we detail a complementary method for mitigating counter-rotating errors even when employing a linear drive. For clarity, we explore resonant drives in this section, but provide analysis for the general case of off-resonant drives in Appendix B. In contrast to the implementation of co-rotating drives, this method relies solely on restricting pulse application times according to the qubit frequency, i.e., no additional calibration overhead is required relative to conventional Rabi gates. In addition to regularizing counter-rotating effects, this approach also regularizes other sources of error, e.g., AC Stark shifts or transients which depend on pulse profiles, and can be straightforwardly implemented in parallel with typical gate calibration methods.

We introduce this method by considering a qubit subjected to a resonant, linearly polarized pulse of duration t_g applied at a start time t_0

$$\frac{\hat{H}}{\hbar} = \omega_{01} \left|1\right\rangle \left\langle 1\right| + \Omega(t - t_0) \cos(\omega_{01} t + \varphi) \left(\left|0\right\rangle \left\langle 1\right| + \left|1\right\rangle \left\langle 0\right|\right), \tag{6.12}$$

where $\Omega(t' = t - t_0)$ denotes the envelope of the pulse such that $\Omega(t') = 0$ for $t' < 0$ and $t' > t_g$. Rewriting the Hamiltonian in terms of t' and in a frame co-rotating with the qubit at frequency ω_{01},

$$\frac{\hat{\tilde{H}}}{\hbar} = \frac{e^{i\varphi}\Omega(t')}{2} \left[1 + e^{-2i(\omega_{01}(t'+t_0)+\varphi)}\right] \left|0\right\rangle \left\langle 1\right| + \text{h.c.}, \tag{6.13}$$

and the time-evolution operator generated by the pulse is given by

$$\hat{\tilde{U}}(t' = t_g, t' = 0) = \exp\left[-\frac{i}{\hbar}\int_0^{t_g} \hat{\tilde{H}}(t', t_0)\, dt'\right]. \tag{6.14}$$

By inspecting the counter-rotating field—the second term in the square brackets of Eq. (6.13)—we can interpret the pulse start time t_0 as effectively setting a phase offset of the counter-rotating field. When working within the RWA (neglecting the counter-rotating term), the rotating-frame Hamiltonian and resulting unitary given by Eq. (6.14) become invariant with respect to t_0. In contrast, when applying strong linear drives with $1/t_g$ approaching $\omega_{01}/2\pi$, the counter-rotating field cannot be neglected and the unitary remains a function of t_0. In other words, counter-rotating effects cause the qubit rotation to depend on when the pulse is applied [1].

However, noting that this effect is coherent and deterministic, we can make the contribution from counter-rotating fields uniform for all pulses by utilizing their time periodicity. In particular, the exponential in Eq. (6.13) has a period of $\tau = \pi/\omega_{01} = \tau_L/2$. So, restricting the times at which we apply pulses to $t_0 = n\tau_L/2 + \delta t_0$ with integer n and arbitrary constant time-offset δt_0 leads to the same unitary dynamics for every pulse of a fixed φ. We set $\delta t_0 = 0$ as this time offset is equivalent to an absolute carrier-phase offset $\varphi \to \varphi - \omega_{01}\delta t_0$. As a result of regularizing the pulse unitary, any calibration that can correct for a systematic rotation error automatically mitigates the counter-rotating contribution. We refer to gates performed with this approach as commensurate, since pulses are locked to a lattice defined by $\tau_L/2$.

We refer to gates not following this restriction as incommensurate and highlight their susceptibility to the coherent error generated by the non-uniform sampling of counter-rotating fields for pulses applied at different times. We further note that when performing pulse sequences composed of a large number of incommensurate pulses, each pulse contributes a

---

[1] An analogous example of physics that depends on the stability of the relative phase between the carrier and envelope of few-cycle pulses can be found in ultrafast optics [261, 262].

different counter-rotating error, reducing fidelity and rendering a global shift of the carrier phase φ to all pulses indiscernable. In contrast, a pulse sequence employing commensurate pulses will generally be sensitive to such a global offset in φ.

To form a gate set with X and Y rotations (i.e. with phases $\varphi \in \{0, \pi/2\}$), we can regularize the counter-rotating dynamics for both phases simultaneously by applying X gates at times $t_0^X = n\tau_L/2$ and Y gates at $t_0^Y = (n + 1/2)\tau_L/2$ [263]. Pragmatically, this can be implemented by defining X gates to have a duration that is a multiple of $\tau_L/2$ and forming Y gates by padding X gates before and after with duration $\tau_L/4$ identity gates. These identity gates can be compiled away for consecutive Y gates to reduce the total sequence duration. In practice, we found the benefit from this compilation to be minimal and did not utilize it for data presented in this chapter.

To conclude this subsection, we highlight that commensurate gates offer the ability to regularize and thereby eliminate coherent errors from the counter-rotating component of strong linear drives with no additional calibration overhead. This stands in contrast to co-rotating drives, which natively do not include a counter-rotating component but require extra calibration. In practice, we still found that co-rotating gates with durations approaching τ_L benefited from adhering to the commensurate condition—we attribute this to the regularization of AC Stark shifts arising from the off-resonant driving of transitions beyond $0 - 1$. The AC Stark shift magnitude is dependent on when co-rotating pulses are applied due to the varying relative value of charge and flux drive components, which couple the non-target levels with different matrix elements. This effect also grows with increasing drive strength, and its mitigation highlights another distinct benefit of commensurate gates. We further emphasize that this approach does not rely on any specific details of the qubit. In other words, this approach can be applied to mitigate counter-rotating effects in any platform where strong linear drives are desired. The small price to pay for applying commensurate gates is in coherence—by requiring X and Y gates to be applied at times belonging to lattices shifted by $\tau_L/4$ relative to each other, the target qubit accrues decoherence during the $\tau_L/4$

waiting times between applying X then Y or Y then X gates. For our qubit, this amounted to 2.05 ns for every such occasion.

6.2.4 Single-Qubit Gate Implementation

In this subsection, we detail the implementation of our single-qubit gates. We performed gates with three driving schemes: circularly polarized, purely charge [254, 255], and purely flux [264].

Calibrating the $\pi/2$ pulse.

For all drive schemes, a $\pi/2$ rotation was explicitly calibrated with Rabi driving and pulse train techniques. Circularly polarized drives underwent additional calibration steps to ensure (1) equal drive strengths between the two drives, (2) a relative drive phase corresponding to a co-rotating circular polarization, and (3) simultaneity of the charge and flux pulse arrivals at the qubit. Following the commensurate restriction required no additional calibration relative to conventional Rabi gates. We include full details on the pulse calibration in Chapter 6.4.

Forming a gate set

With a fully calibrated $\pi/2$ rotation, we defined our X (Y) gate as having no phase shift (90° phase shift) of the carrier. π-pulses were implemented by playing two $\pi/2$-pulses back to back, and Z gates were implemented as virtual-Z gates [265]. All microwave pulses used a pure-cosine envelope, with a 0.1 ns gap between adjacent pulses. We generated the single-qubit Clifford group with the gate set $\mathcal{G} = \{I, \pm X_{\pi/2}, \pm Y_{\pi/2}\}$, which yields on average $53/24 \approx 2.208$ non-identity gates per Clifford. We used this decomposition as it comprises the native gates in our experiment and allows direct comparison with other recent works [60, 101] demonstrating state-of-the-art single-qubit gates.

6.2.5 Gate Benchmarking

Both standard and interleaved Clifford randomized benchmarking were performed to assess the quality of our gates [266, 267]. To quantify the proportion of incoherent and coherent error in our gates, we performed purity randomized benchmarking (RB) [268, 269]. Our implementation of the purity RB pulse sequence included a recovery gate as in standard Clifford RB, followed by single-qubit state tomography. This enabled us to extract both the total and incoherent error per gate by analyzing $\langle \sigma_z \rangle$ and the purity $P = \langle \sigma_x \rangle^2 + \langle \sigma_y \rangle^2 + \langle \sigma_z \rangle^2$ from the same dataset, respectively. All fidelities were reported with uncertainties representing the standard error of the mean.

RB analysis

The total error per Clifford ϵ was extracted by fitting the excited state population p_e by

$$\langle p_e \rangle = A + B u^m, \tag{6.15}$$

where $\langle \cdot \rangle$ denotes the average over a collection of random sequences of m Cliffords, $u = 1 - 2\epsilon$, and A and B are constants determined by state preparation and measurement (SPAM) errors. The error per gate was then calculated by $\epsilon_g = \epsilon / N$, where $N = 53/24 \approx 2.2083$ was the number of gates per Clifford given our native gateset $\mathcal{G} = \{I, \pm X_{\pi/2}, \pm Y_{\pi/2}\}$.

Purity RB analysis

The incoherent error per Clifford ϵ_{in} was extracted by fitting the average state purity

$$\langle P \rangle = A' + B' u'^m, \tag{6.16}$$

where

$$P = \langle \sigma_z \rangle^2 + \langle \sigma_z \rangle^2 + \langle \sigma_z \rangle^2 \tag{6.17}$$

is the state purity, shifted and rescaled to lie in the interval $[0, 1]$, extracted by tomography after the m-Clifford RB sequence, $u' = (1 - 2\epsilon_{\text{in}})^2$, and similarly A' and B' are determined by SPAM errors. The incoherent error per gate was given by $\epsilon_{g,\text{in}} = \epsilon_{\text{in}}/N$.

6.3 Experimental Setup

All experiments were conducted in a Bluefors XLD600 dilution refrigerator maintaining a base temperature stabilized at $\sim 22\,\text{mK}$. Flux biases were provided by a small superconducting solenoid mounted to the lid of the sample package. We specify the equipment used for qubit biasing, control, and readout in Table. 6.1, and detail the experimental wiring in Fig. 6.2.

Table 6.1: **Summary of control equipment.**

Component	Manufacturer	Model
Dilution Refrigerator	Bluefors	XLD600
RF Source	Rohde and Schwarz	SGS100A
DC Source	QDevil	QDAC I
Control Chassis	Keysight	M9019A
AWG (readout pulses)	Keysight	M3202A
AWG (qubit pulses)	Keysight	M8195A
ADC	Keysight	M3102A

6.4 Single-Qubit Gate Calibration

In this section, we detail the full routine used for our single-qubit gate calibration. All gates in this work were made of $\pi/2$-pulses (e.g. π-pulses utilized two sequential $\pi/2$-pulses) with cosine envelopes and performed at $\Phi_{\text{ext}} = 0.5\Phi_0$, referred to as the “sweet spot." A pulse

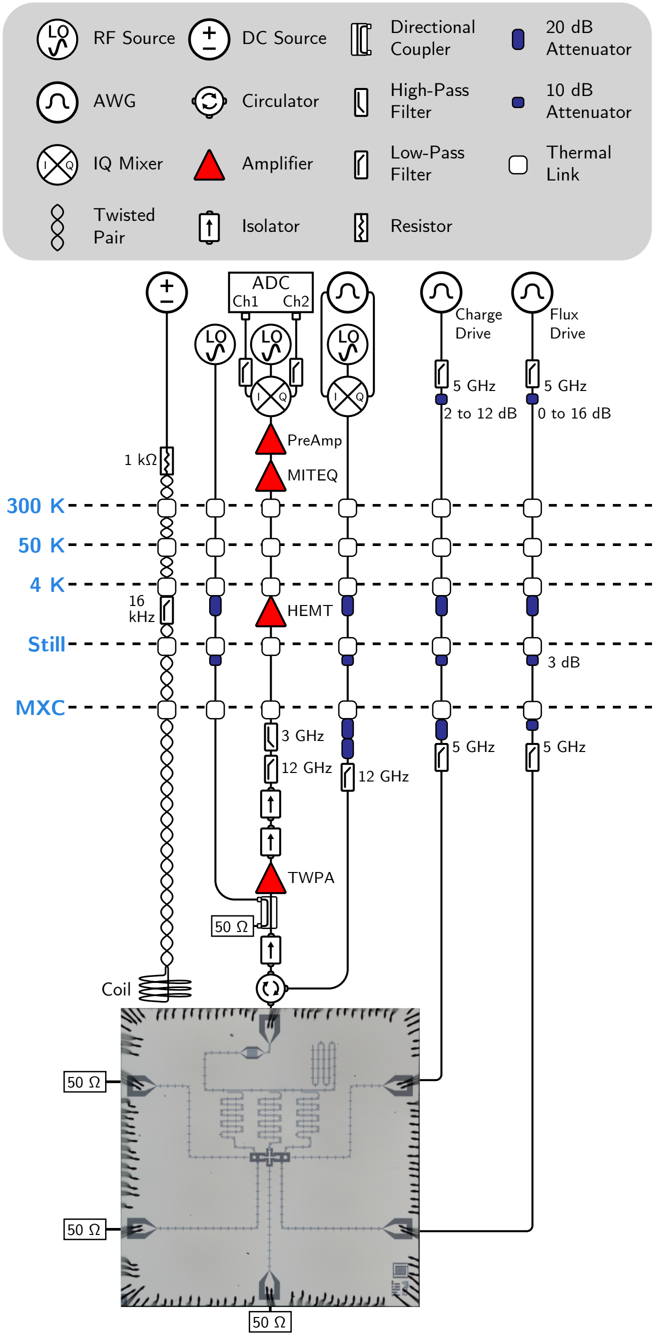

Figure 6.2: **Wiring schematic of the experimental setup.**

starting at time t_0 with duration t_g was implemented with the waveform $w(t)$,

$$w(t) = A(t)\cos[\omega_{01}t - \delta(t - t_0) + \phi]$$

$$A(t) = \begin{cases} \frac{A_0}{2}(1 - \cos[2\pi\frac{(t-t_0)}{t_g}]), & t_0 \leq t \leq t_0 + t_g \\ 0, & \text{otherwise} \end{cases}$$

where $\omega_{01}/2\pi$ is the undriven qubit frequency, δ is the pulse detuning, and ϕ is the phase of the carrier defining the axis of the qubit rotation. We emphasize that no pulse predistortion was used in this experiment, giving an avenue for potential future improvement.

Before precise gate calibration, we performed rough calibrations of the flux bias, qubit frequency, and a slow (≥ 30 ns) charge $\pi/2$-pulse for precise flux bias and frequency calibrations. The following preliminary calibrations were performed before gate tune-up.

1. **Precise flux bias calibration.** Ramsey oscillations were measured with a fixed pulse frequency (slightly detuned below the qubit frequency at the sweet spot) as a function of flux bias. The oscillation frequencies vs flux were fit to a parabola, with a minimum oscillation frequency at the flux sweet spot. For details, we refer to [255].

2. **Single-shot readout calibration.** We collected single-shot voltage measurements with no initialization of the qubit, and trained a Gaussian mixture model on the resulting dataset in the IQ plane.

3. **Precise qubit frequency calibration.** Ramsey oscillations were measured for 10 µs with an applied detuning of −800 kHz and fit with a cosine function. The difference between the fit oscillation frequency and the applied detuning was then used to calculate the precise qubit frequency.

6.4.1 Gates with Linear Drives

Linear drive gates for a given $\pi/2$-pulse duration were calibrated roughly following the procedure of [255], with minor adjustments. We detail the exact procedure below.

1. **Rough π-pulse amplitude calibration.** A train of two Rabi pulses was applied to the qubit while sweeping the amplitude of their cosine envelopes. The resulting population of the excited state was fit with a cosine function, yielding the rough amplitude corresponding to two sequential $\pi/2$ pulses.

2. **Pulse detuning.** A train of $\pi/2$ pulses with alternating signs (e.g. $[X_{\pi/2} + X_{-\pi/2}]^n$) was applied while sweeping the number of pulses and a detuning modulation of the envelope of each pulse given by $e^{-i\delta(t-t_0)}$, where t_0 was the start time of each pulse. The optimal value of δ was chosen such that the oscillation between $|0\rangle$ and $|1\rangle$ was minimized. Interestingly, for commensurate gates, we found that the particular pulse used for this calibration (e.g. X or Y) was important – for gate durations $t_X = n\tau_L$ ($t_X = (n+1/2)\tau_L$), $n \in \mathbb{N}$, we found that this pulse sequence behaved as expected when using Y (X) rotations. Recall that for our commensurate implementation, Y gates have a duration $\tau_L/2$ longer than X gates. This results in, for $t_X = n\tau_L$ ($t_X = (n+1/2)\tau_L$), alternating Y (X) pulse trains with identical waveforms for all gates (in contrast, the equivalent same-sign pulse trains correspond to the waveform for each subsequent gate being flipped). We hypothesize that, due to sequential pulses implementing rotations in opposite directions having the same waveform, long-time transients were suppressed rather than amplified in this calibration by the choice of X vs Y rotations.

3. **Precise amplitude calibration.** We used a pulse train looping over the set $\{X_{\pi/2}, Y_{\pi/2}, X_{-\pi/2}, Y_{-\pi/2}\}$ measuring only trains with a multiple of 3 pulses (e.g. $n_{\text{tot}} = 3n$, $n \in \mathbb{N}$). This sequence implements a pseudo-identity gate (only an identity with perfect control) that is sensitive to the pulse amplitude. We also note that this sequence was sensitive to the pulse detuning. However, the pulse detuning was calibrated immediately preceding and no effective change was seen by changing this calibration to the more usual X_π^n train. This specific pulse sequence was chosen in order to treat X and Y pulses equally and mitigate any skewing of the optimal amplitude from e.g. unwanted amplification of transients from a homogeneous pulse train.

6.4.2 Gates with Circular (Co-Rotating) Drives

For circular gates, three additional calibrations were performed to determine 1) the relative phase offset, 2) the relative pulse delay, and 3) the precise relative amplitude between the charge and flux drives. The exact procedure is outlined below.

1. **Rough π-pulse amplitude calibration for charge and flux.** We applied a sequence $X_\pi + X_\pi$ while sweeping the pulse amplitude and fit the resulting population of $|1\rangle$ to a cosine function. The optimal π-pulse amplitude was then calculated as half the amplitude for the max population.

2. **Relative phase offset calibration.** We applied simultaneous charge and flux drives of equal strength (with relative amplitude set by the previous measurement) and measured Rabi oscillations while sweeping the relative phase. The offset phase was determined by fitting the data to Eq. (6.9).

3. **Relative pulse delay calibration.** We applied an alternating X_π pulse train of nominally simultaneous charge and flux gates while sweeping the relative drive delay and the total number of pulses (constraining it to be odd) and setting $\Delta\varphi = 0$. The resulting interference pattern yielded maximal population of $|1\rangle$ when the pulse trains for charge and flux arrived at the qubit simultaneously.

4. **Pulse detuning calibration (coarse).** The optimal pulse detuning parameter for circular gates was found with the same routine as for linear gates, with the relative phase set to $\Delta\varphi = \pi/2$ and enforcing $\delta = \delta_{\text{charge}} = \delta_{\text{flux}}$.

5. **Relative amplitude calibration.** We applied a nominally counter-rotating Rabi drive ($\Delta\varphi = -\pi/2$) with a plateau equal to 3 times the pulse width as a function of the flux pulse amplitude (while keeping the charge amplitude fixed), resulting in minimal excited state occupation when the Rabi strengths of charge and flux were balanced.

6. **Pulse detuning calibration (fine).** As described in step 4.

7. **Precise amplitude calibration.** As described in the linear gate calibration, step 3.

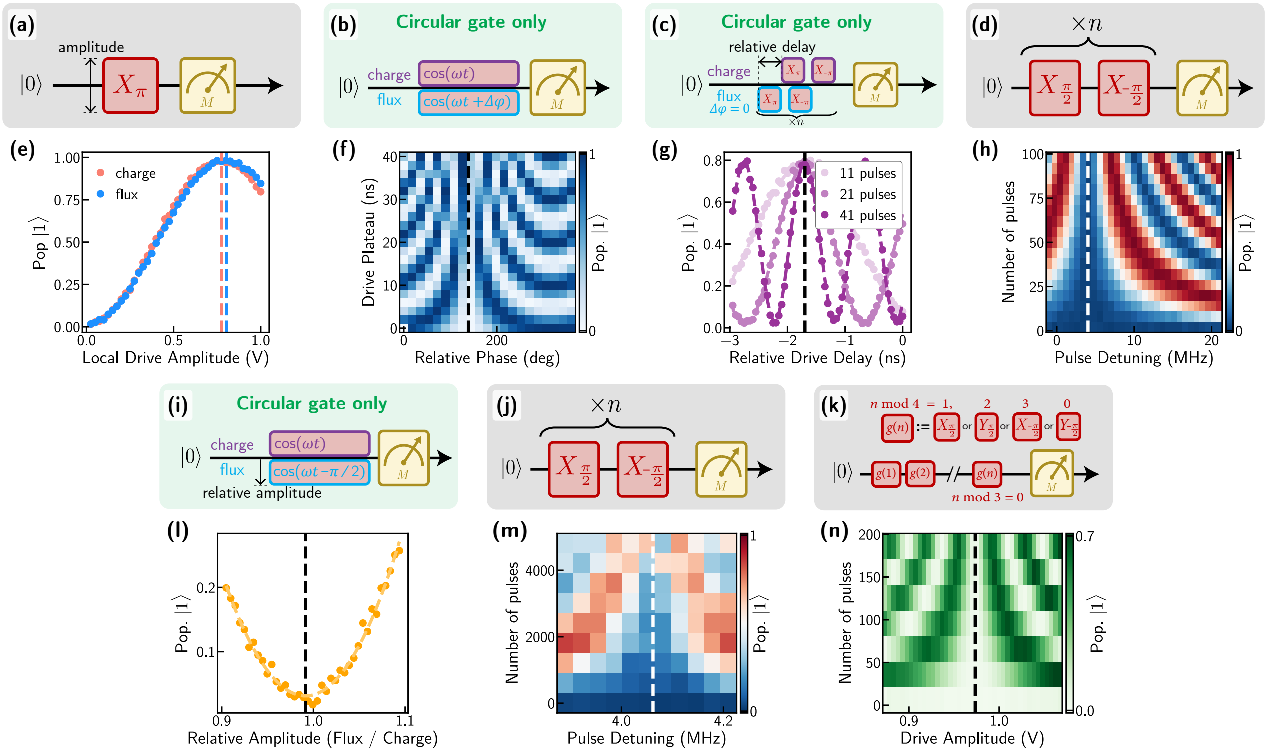

Figure 6.3: **Measurement pulse sequences for single-qubit gate calibration. (a-d),(i-k)** Measurement pulse sequences for **(e-h)**,**(l-n)**, respectively. **(e)** Rough pulse amplitude calibration. **(f)** Circular-only calibration for the relative phase between charge and flux drives. Marked in black is the counter-rotating relative phase. All circular gates were performed with the co-rotating phase (180° offset from the counter-rotating phase). **(g)** Circular-only calibration for the relative delay between charge and flux pulses, to ensure pulses sent down both control lines arrived simultaneously at the qubit. **(h)** Rough pulse detuning calibration, primarily compensating for AC Stark shifts. **(l)** Circular-only fine calibration to balance the charge and flux drive strengths. **(m)** Fine pulse detuning calibration. **(n)** Fine pulse amplitude calibration.

6.4.3 Gaussian Fitting of Calibration Scans: Gaussian Function as an Infinite Product

For multiple pulse parameters, optimal values were determined by fitting the product of pulse-train dataset line-cuts to a Gaussian function (in other words, multiplying the horizontal rows of a dataset which looks like Fig. 6.3(h), and fitting the resulting line). In this subsection, we justify this methodology and provide an infinite product expression of the Gaussian function $e^{-x^2/2\sigma^2}$. We provide a rigorous derivation and extended results in

Appendix A.

For a pulse parameter x, we assume that at the optimal value x_{opt} applying a pseudo-identity gate comprised of a pulse train with n repetitions (e.g. $(X_\pi + X_{-\pi})^n$) leaves the qubit in its initial state. However, a slightly offset value of x will lead to an over- or under-rotation of the qubit by an amount $n\Delta\theta = nk(x - x_{\text{opt}})$ and a corresponding population of the excited state of $p^n_{|0\rangle} = \frac{1}{2}(1 + \cos(n\Delta\theta))$, where k is a constant of proportionality depending on the details of how the parameter x affects the qubit rotation. In our experiment, x corresponded to the pulse detuning or amplitude, but we note that this argument can be generalized to other parameters which effect the qubit rotation angle similarly.

In order to determine the optimal value x_{opt}, we took datasets measuring the excited state probability $p^n_{|1\rangle}$ after pseudo-identity gates as a function of the number of repetitions n and the pulse parameter x. We then took the product for all different n, resulting in the signal $s(x)$,

$$\begin{aligned} s(x) &= \prod_{n=0}^{N} \frac{1}{2}(1 + \cos(n\Delta\theta)) && (6.18) \\ &= \left(\prod_{n=0}^{N} \cos(n\Delta\theta) \right)^2 . && (6.19) \end{aligned}$$

In the limit as $N \to \infty$, one can show that such an infinite product converges exactly to a Gaussian when the cosine frequencies are weighted correctly,

$$\lim_{N\to\infty} \prod_{n=0}^{N} \cos\left(\frac{n}{N^{3/2}} \Delta\theta \right) = e^{-\Delta\theta^2/6}. \tag{6.20}$$

Even for small N (in our datasets, $N \leq 5$), the above expression is easily fit to a Gaussian, giving an efficient and robust way to fit datasets such as Fig. 6.3(g,h,m,n).

6.5 Experimental Results

In this section, we describe our three main results: (1) the demonstration of tunable-polarization drives, (2) the mitigation of counter-rotating errors for linearly polarized drives with commensurate gates, and (3) the optimization of gate duration for different drive schemes.

6.5.1 Arbitrarily Polarized Drives

As our first experiment, we demonstrated the generation of arbitrarily polarized microwave drives. To ensure equal drive strengths for the charge and flux components, we first calibrated the charge and flux drive amplitudes to individually produce the same Rabi frequency. Then, time-domain Rabi oscillations were measured with the relative phase $\Delta\varphi$ of the two simultaneous drives swept between 0° and 360° [Fig. 6.4(a)]. In this plot, the drive is shown to continuously vary between a completely co-rotating drive ($\Delta\varphi = 90°$) and a completely counter-rotating drive ($\Delta\varphi = 270°$). In between, at $\Delta\varphi = 0°$ and $\Delta\varphi = 180°$, the drive is completely linearly polarized, but along a diagonal axis in the Bloch sphere equatorial plane [Fig. 6.1(c), blue arrows]. The counter-rotating dynamics are visibly apparent as fast oscillations on top of the slower Rabi flopping away from $\Delta\varphi = 90°$. The Rabi frequency of the simultaneous drive (within the RWA) depends on the relative phase, and is given by Eq. 6.9.

To fairly compare the dynamics for Rabi drives of different polarizations, we then separately calibrated Rabi drives of the same strength for a mostly counter-rotating drive [Fig. 6.4(b)], a linear drive with equal charge and flux components [Fig. 6.4(c)], and a co-rotating drive [Fig. 6.4(d)]. The associated Bloch sphere trajectories measured with state tomography are shown in panels Fig. 6.4(e-g) respectively.

In both simulation and experiment, we found that a slow rise and fall of the pulse envelope could dampen the effects of the counter-rotating terms by allowing the Hamiltonian to change

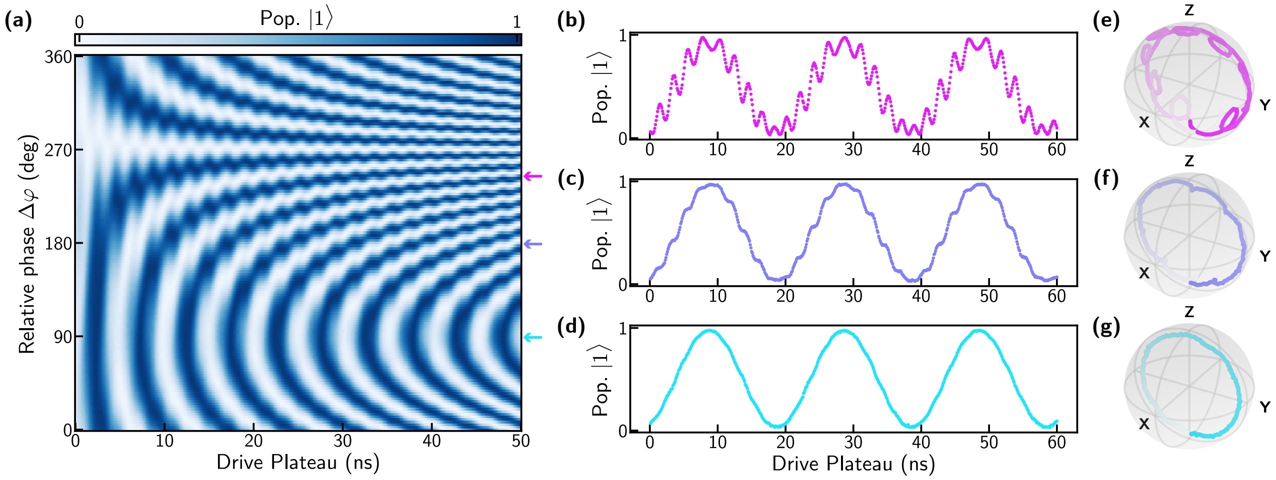

Figure 6.4: **Rabi oscillations with tunable drive polarization.** **(a)** Time-domain Rabi oscillations as the relative phase between the charge and flux drives is varied. The relative strength of the individual charge and flux drives were calibrated to be equal, and kept constant throughout the plot. All oscillations use a 1 ns rise-fall time. **(b-d)** Similar data taken for three different polarizations, calibrated to each have the same Rabi frequency, all using a 2.5 ns rise-fall time. **(b)** Nearly completely counter-rotating ($\Delta\varphi = 245°$) Rabi oscillations of the fluxonium qubit. The counter-rotating oscillations are visible on top of the slower co-rotating oscillation. **(c)** Linearly polarized drive ($\Delta\varphi = 180°$) with equal contributions from charge and flux. **(d)** Completely co-rotating drive ($\Delta\varphi = 90°$) illustrating elimination of counter-rotating effects. The remaining small distortions are a result of the fast rise-time of the pulse. **(e-f)** Bloch-sphere trajectories of the corresponding oscillations (truncated to the first Rabi flop) of the data in (b-d). Opaque color corresponds to the start time, and transparent corresponds to the end time.

adiabatically relative to the counter-rotating drive contribution [244]. Here, to magnify the counter-rotating oscillations, we used pulses with a total rise and fall time of 1 ns for the data in Fig. 6.4(a) and 2.5 ns for the data in Fig. 6.4(b-g).

The apparent tuning of the counter-rotating drive strength as a function of $\Delta\varphi$ confirms both our circuit QED analogy to optical polarization and that our two drive lines truly couple to the qubit through canonically conjugate operators; if the two drives coupled through the same operator, the Rabi frequency would still be observed to tune from a local maximum to zero as in Fig. 6.4(a), but no increase in counter-rotating dynamics would be observed near $\Delta\varphi = 270°$. Our technique also simplifies further research involving counter-rotating dynamics by enabling direct access to purely counter-rotating drives.

6.5.2 Incommensurate Linear and Circular Gate Characterization

Here we present randomized benchmarking data comparing linear and circular driving schemes for incommensurate gates [Fig. 6.5]. To represent linear drives, we utilized the best linear driving scheme comprised of a purely flux drive. Since incommensurate gates were found to be worse than commensurate gates for all driving schemes, we only present data for two separate gate durations, $t_g = 1.2\tau_L \approx 4.9\,\text{ns}$ and $t_g = 1.7\tau_L \approx 7.0\,\text{ns}$, and provide a more thorough fidelity dependence on gate duration for commensurate gates in the following sections. For $t_g = 1.2\tau_L$, we observe no benefit from circular driving over flux driving, suggesting the relevance of error channels beyond counter-rotating effects as $t_g \to \tau_L$, e.g., coherent leakage or the non-uniformity of AC Stark shifts. In contrast, for $t_g = 1.7\tau_L$, we observe that circular driving outperforms flux driving, signaling the benefit of circular driving for incommensurate single-qubit gates when counter-rotating errors dominate.

6.5.3 Commensurate Gates

In this subsection, we highlight the coherent error channel posed by the non-uniform sampling of counter-rotating fields for resonant pulses applied at different times relative to the carrier phase and the mitigation of this error channel with commensurate gates.

To establish this error channel, we simulated a two-level system subjected to an X pulse applied at different start times Fig. 6.6(a). We plot the the polar angle traversal of the ground state Bloch vector after application of the pulse (with duration $t_g = 0.84\tau_L$) as a function of the pulse start time in Fig. 6.6(b). Shifting the pulse start by $0.5\tau_L$ corresponds to a π phase shift of the carrier at the start of the pulse (leading to a rotation of the same amount, but in the opposite direction), resulting in a $0.5\tau_L$ periodicity of the effective rotation angle. We then simulated this effect as a function of the pulse duration [Fig. 6.6(c)], plotting the rotation range as a proxy for the coherent error. It is apparent that, as pulse durations approach τ_L, this error channel grows significantly.

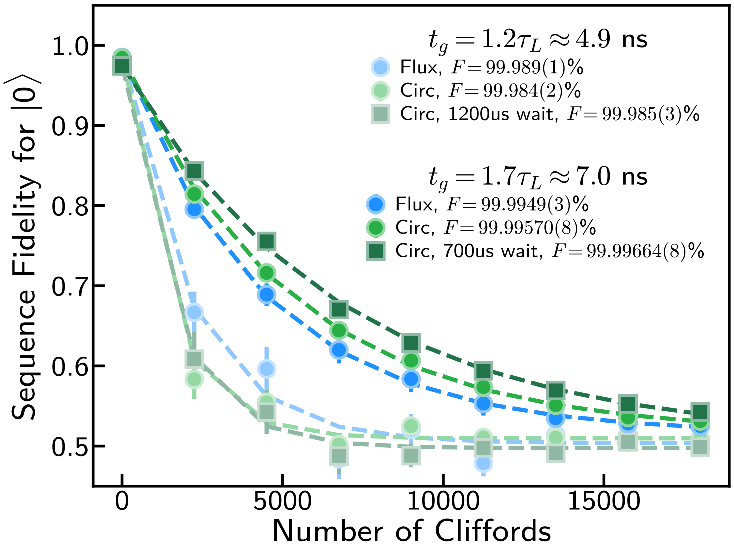

Figure 6.5: **Comparison of incommensurate gates with linear and circular drives.** RB data for incommensurate gates utilizing a linearly polarized flux drive and a circularly polarized co-rotating drive is shown for two gate durations, $t_g = 1.2\tau_L \approx 4.9\,\mathrm{ns}$ and $t_g = 1.7\tau_L \approx 7.0\,\mathrm{ns}$. We include data for circular drives with (square marker) and without (circular marker) additional wait times as defined in Fig. 6.10 in order to elucidate the efficacy of circular driving for suppressing counter-rotating errors while mitigating heating effects associated with the charge drive. For $t_g = 1.2\tau_L$, we observed no benefit from circular driving. For $t_g = 1.7\tau_L$, circularly polarized driving both with and without an additional wait time benefited gate performance relative to flux driving, which showed no benefit from an equivalent wait time.

In order to mitigate this error channel, we adopted the commensurate approach detailed in Section 6.2.3. This approach entailed applying pulses at times constrained to a lattice of spacing $\tau_L/2$ for X gates (and the corresponding lattice shifted by $\tau_L/4$ for Y gates, which we implemented by padding Y gates before and after with $\tau_L/4$ wait times such that Y gates had durations $\tau_L/2$ longer than those of X gates). Intuitively, this amounts to sampling only a single point in Fig. 6.6(b). We draw a simple single-qubit circuit and waveforms implementing it in Fig. 6.7(a,b) with both incommensurate pulses of duration $t_g = 1.2\tau_L$ and commensurate pulses of duration $t_X = \tau_L$ ($t_Y = 1.5\tau_L$).

We implemented both commensurate and incommensurate single-qubit gates and characterized their performance with Clifford randomized benchmarking [Fig. 6.7(c)]. For commensurate gates, we additionally optimized the absolute carrier phase offset, which effectively

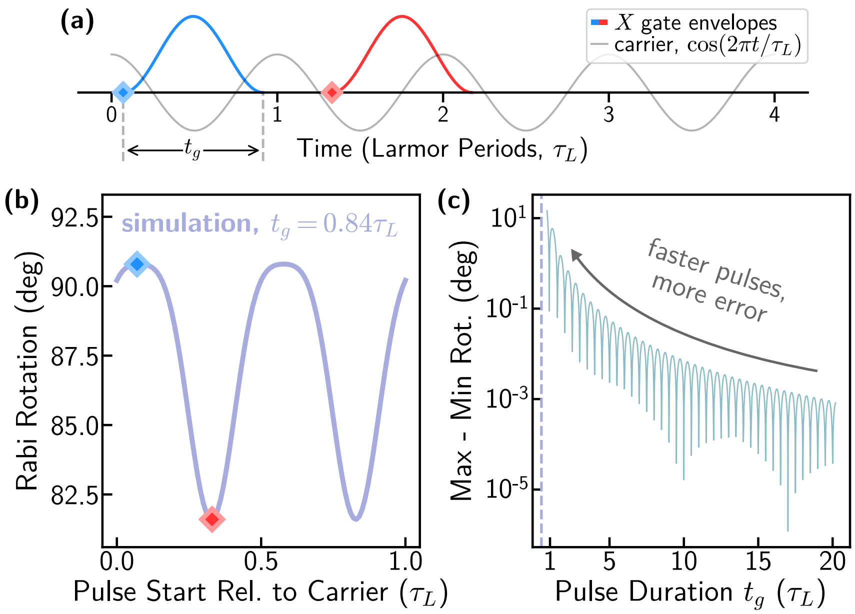

Figure 6.6: **Counter-rotating errors from linear drives.** **(a)** Time-domain depiction of two resonant linearly polarized X-pulse envelopes (red and blue), starting at different times relative to the carrier ($\cos(2\pi t/\tau_L)$, grey), where τ_L is the qubit Larmor period. **(b)** Rabi rotation angle (polar angle of the Bloch vector) of an ideal two-level system starting in the ground state subject to an X pulse of duration $t_g = 0.84\tau_L$ as a function of the pulse start time modulo τ_L. The rotations from the pulses in (a) are highlighted as points on the plot. The qubit rotation depends strongly on the pulse start time due to the time dependence of the counter-rotating drive component. **(c)** Rotation angle range versus pulse duration, showing the divergence of this effect for short pulse times. The dotted line represents the pulse duration used in (b). The y-axis serves as a proxy for the coherent error magnitude of this effect for gates.

determines the shape of the regularized waveform. The dependence of the fidelity on this phase was larger for shorter gates, with a most extreme variation of 5×10^{-5}. We attribute this dependence to the compensation of, e.g., transients or a slight offset of the qubit flux bias, which would affect the qubit trajectory through the 0-1 avoided crossing. Notably, commensurate gates with durations as low as τ_L were characterized by fidelities well in excess of 99.997%, in contrast to incommensurate pulses at similar times which were characterized by fidelities as low as 99.985%. As expected, the benefit from commensurate pulses was more significant for faster gates.

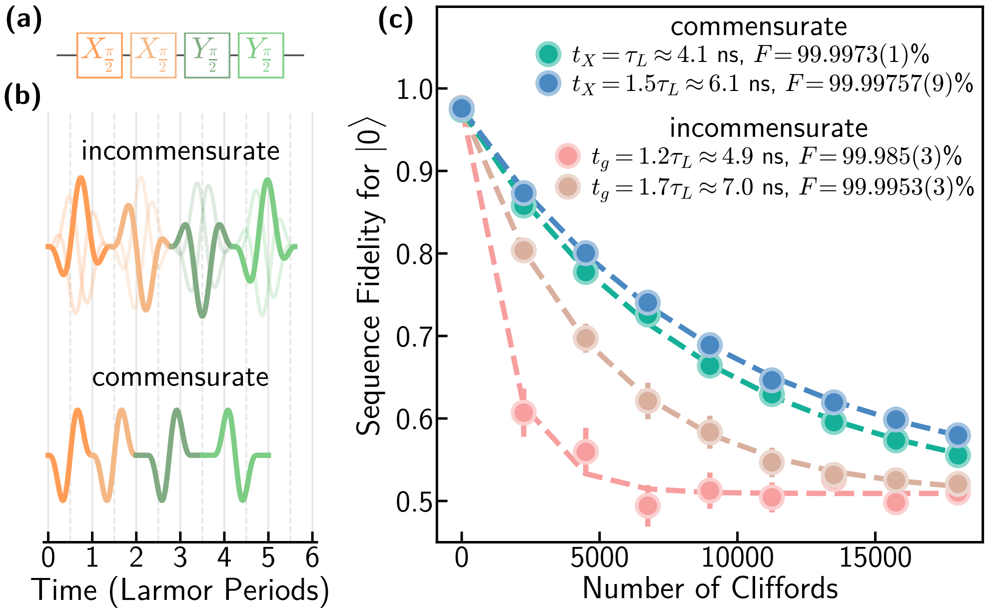

Figure 6.7: **Commensurate gates: alleviating counter-rotating errors for linear drives.** **(a)** Example single-qubit circuit. **(b)** Cartoon waveforms for two different implementations of the circuit drawn in (d). Top: incommensurate pulses ($t_g = 1.2\tau_L$), which suffer from the coherent error channel depicted in panel (b). Bottom: commensurate pulses ($t_X = \tau_L$, $t_Y = 1.5\tau_L$), which regularize the counter-rotating fields during each pulse. This turns the coherent errors which were previously different for each pulse into a systematic coherent rotation which is corrected for automatically in our other calibrations. For the reasons described in Section 6.2.3, commensurate Y pulses require $\tau_L/4$ identity-gate padding before and after each pulse. **(c)** Clifford randomized benchmarking (RB) of single-qubit gates performed with flux pulses, comparing commensurate and incommensurate implementations. All curves were averaged over 40 random seeds. We include data from two incommensurate pulse durations ($t_g = 1.2\tau_L \approx 4.92\,\text{ns}$ and $t_g = 1.7\tau_L \approx 6.97\,\text{ns}$), and two commensurate implementations ($t_X = 1.0\tau_L \approx 4.1\,\text{ns}$ and $t_X = 1.5\tau_L \approx 6.15\,\text{ns}$). At these gates times, we see a significant increase in fidelity by using commensurate pulses. This highlights the ability to mitigate coherent errors from counter-rotating terms for strong linear drives by adopting straightforward pulse-timing constraints.

6.5.4 Commensurate Linear and Circular Gate Characterization

In this subsection, we report the results of empirically optimizing the duration of our commensurate gates by measuring the average single-qubit gate fidelity as a function of the gate duration for three driving schemes: charge, flux, and co-rotating drives [Fig. 6.8(a)]. Coherence bounds were calculated using the average gate time $t_g = (t_X + t_Y)/2 = t_X + \tau_L/4$. We found all drive schemes were optimal near $t_X = 2\tau_L \approx 8.2\,\text{ns}$, with fidelities $> 99.994\%$

for charge, $> 99.996\%$ for circular co-rotating, and $> 99.997\%$ for flux drives. Linear flux (charge) drives resulted in our best (worst) gates, with circular drives performing better than charge but worse than flux. We separately performed interleaved randomized benchmarking using the $t_X = 2\tau_L$ flux pulses for each gate in our gate set [Fig. 6.8(b)]. We further explored the distribution of errors and gate stability in Chapter 6.5.5. We present additional data comparing incommensurate linear and circular gates in Chapter 6.5.2, demonstrating that circular drives can benefit incommensurate gates, but do not outperform flux-driven commensurate gates.

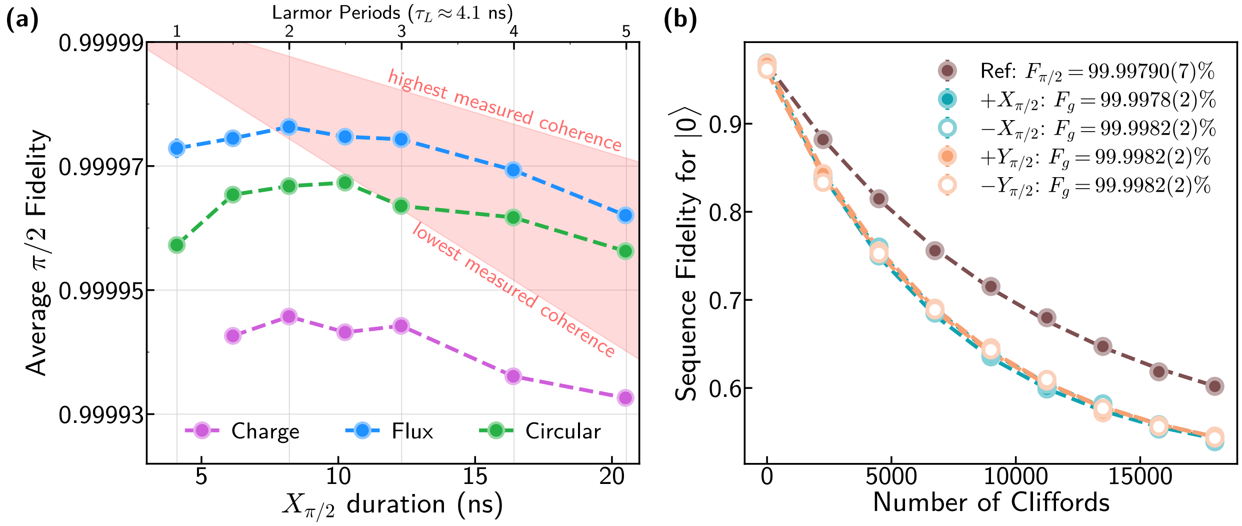

Figure 6.8: **Commensurate single-qubit gates with linear and circularly polarized drives. (a)** Gate fidelity measured with Clifford randomized benchmarking as a function of the $\pi/2$-pulse width for a pure charge drive (purple), pure flux drive (blue), and a co-rotating circularly polarized drive (green). In order to mitigate the effect of coherence fluctuations, data was collected over a span of two weeks with intermittent breaks taken when the qubit coherence fluctuated to low values. The lowest and highest measured coherences during this window ($300\,\mu s \lesssim T_1 \lesssim 500\,\mu s$, $200\,\mu s \lesssim T_{2E} \lesssim 500\,\mu s$) were used to calculate fidelity bounds (red). **(b)** Clifford interleaved randomized benchmarking for a calibrated linearly polarized flux drive with an $X_{\pi/2}$ duration of $t_X = 2\tau_L$. The reference trace has an average single-qubit gate error of $(2.10 \pm 0.07) \times 10^{-5}$. All randomized benchmarking traces were averaged over 25 random seeds.

6.5.5 Coherent and Incoherent Errors

We constructed an error budget for several commensurate charge and flux gates by measuring their total and incoherent errors as detailed in Chapter 6.2.5 and quantifying the proportion of incoherent error from T_1 and T_{2E} [Fig. 6.9]. Flux gates at times $t_X \gtrsim 8\,\mathrm{ns}$ were limited by incoherent errors, which could be attributed entirely (within uncertainty) to qubit decoherence. We note that for this dataset, the flux gate set with $t_X = 2\tau_L$ represents our highest measured fidelity with a value of 99.99807(7)%. For our fastest flux gate ($t_X = \tau_L \approx 4\,\mathrm{ns}$), coherent errors were found to play a more significant role, suggesting the breakdown of our calibration. Charge gates at all times were limited by incoherent errors, and the value could not be entirely accounted for by undriven qubit decoherence.

To probe the role of heating (from, e.g., power dissipated on the chip or in-line attenuators immediately before the device) on charge gate performance, we utilized a two-readout-pulse heralding scheme and swept the wait time between the readout pulses [Fig. 6.10]. At long wait times, we expect the relevant components to be in thermal equilibrium with the environment at the start of every qubit pulse sequence and provide no excess decoherence to the qubit. At short wait times, we expect the elements to heat during an experiment and provide a more severe source of qubit decoherence, which would contribute to incoherent error. The maximum wait time of 1600 µs represents a duration of over 5x the longest pulse sequence used in the RB measurements. The $t_X = 2\tau_L$ commensurate charge gate error displays an improvement until $\approx 500\,\mu\mathrm{s}$ and then plateaus, with a maximum error reduction of $\sim 20-30\%$. The measured coherence times remained approximately constant over the duration of the experiment, supporting our interpretation that the total error trend originated from mitigating system heating. At the longest wait time (least heating), we still find that our measured decoherence only accounts for at most $\approx 45\%$ of the total error. We hypothesize that the remaining incoherent error for charge gates is due to leakage, enabled by the large charge matrix elements to higher levels (relative to that of the $|0\rangle \leftrightarrow |1\rangle$ transition).

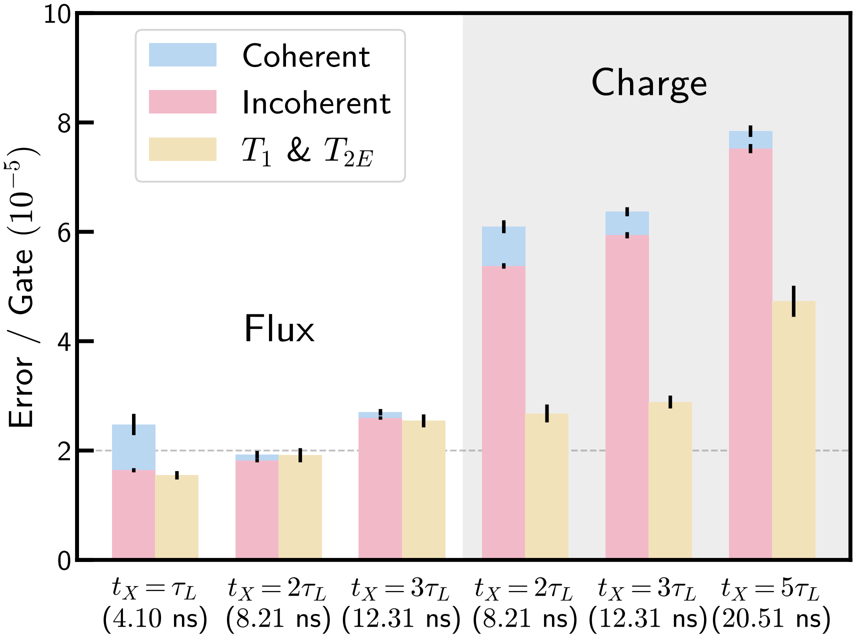

Figure 6.9: **Error budget for commensurate charge and flux gates.** The total and incoherent error were measured through RB and purity RB, extracted from the same dataset for each gate as described in Appendix 6.2.5. The estimated incoherent error from decoherence was also extracted from T_1 and T_{2E} measurements taken immediately after each RB dataset. The coherent error budget item was determined by the difference between the total and incoherent errors. Black lines denote the uncertainty from parameter fits, with the error bar at the top of the coherent budget item corresponding to the total error uncertainty (extracted from the RB fit). Flux gates (white background) for times $t_X \gtrsim 8\,\mathrm{ns}$ were limited by qubit coherence, whereas charge gates (grey background) were largely limited by incoherent errors beyond undriven qubit decoherence.

6.5.6 Stability

To investigate the stability of our system and gate parameters, we measured the total and incoherent error for a commensurate flux gate set with $t_X = 2\tau_L \approx 8.2\,\mathrm{ns}$ (with interleaved T_1 and T_{2E} measurements) as a function of time after an initial calibration [Fig. 6.11]. Over a span of 34 hours after the initial calibration, the total error per gate fluctuated by less than 1.13×10^{-5}, and displayed no significant degradation.

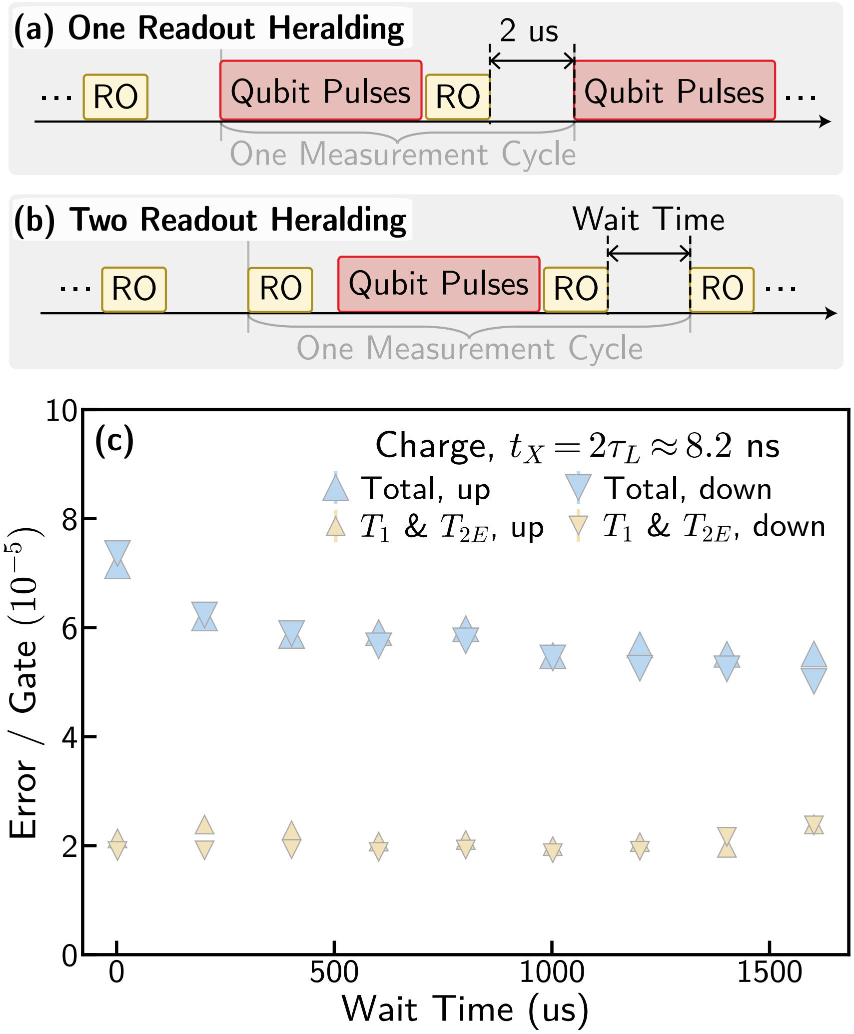

Figure 6.10: **Charge gate heating characterization.** **(a)** One-readout-pulse heralding scheme, as used for all other data in this work. **(b)** Two-readout-pulse heralding scheme, as used for the experiment in this figure. The time between qubit pulses and the preceding readout pulse was kept 2 µs. The time between readout pulses was swept in order to investigate the impact of heating on gate performance. **(c)** Total and $T_1 + T_{2E}$ error for a commensurate charge gate with $t_X = 2\tau_L \approx 8.2$ ns as a function of the wait time between readout pulses, using the pulse sequence of (b). The total error (blue) was measured through RB, and the $T_1 + T_{2E}$ error (yellow) was extracted from T_1 and T_{2E} measurements taken immediately after each RB dataset. Data is displayed from back-to-back sweeps of the wait time from 0 to 1600 µs (upwards triangles) and then 1600 µs to 0 (downwards triangles). The total error improved by $20-30\%$ for wait times above 500 µs, while the measured qubit coherence remained approximately constant.

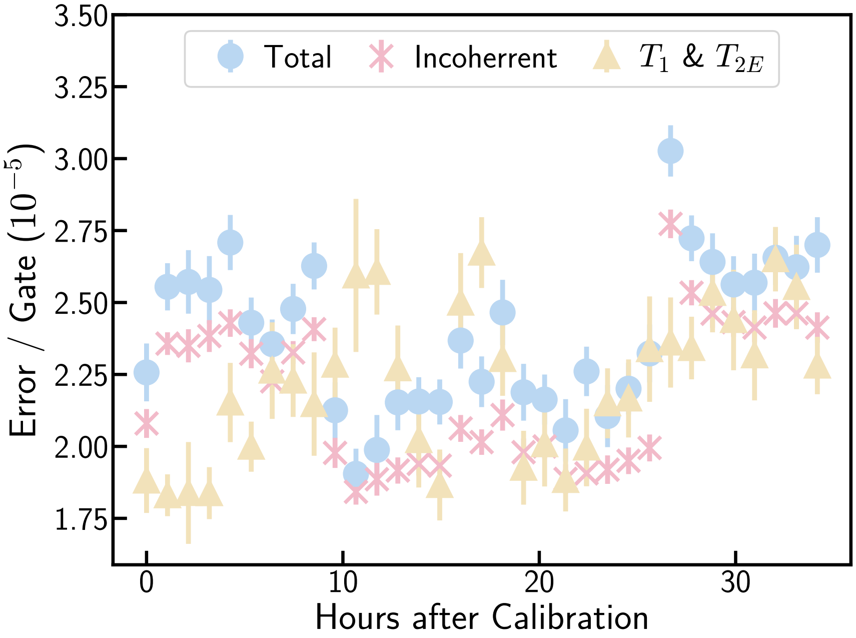

Figure 6.11: **Stability for commensurate flux gates ($t_X = 2\tau_L \approx 8.2\,\mathrm{ns}$).** The total and incoherent error per gate were measured through RB and purity RB, extracted from the same dataset as described in Appendix 6.2.5. No significant drift or degredation of gate performance was observed.

6.6 Outlook

The effect of counter-rotating dynamics on gate operations has long been an understudied aspect of Rabi-oscillation-based gates. With the growing popularity of fluxonium and other low-frequency qubits as well as the ongoing development of control strategies to mitigate other dominant error channels [101], counter-rotating effects have become increasingly relevant for calibrating fast, high-fidelity microwave gates. We introduced and demonstrated two complementary approaches for mitigating these effects.

Our first protocol uses independently controlled linear charge and flux drives, representing two independent quadratures in circuit QED. This control enables the ability to change the polarization angle of the total effective drive, giving a controllable means to study counter-rotating dynamics and the trade-offs between different linear drives. Using such control, we demonstrated the ability to create a circularly polarized drive—natively lacking a counter-rotating component, independent of the drive amplitude—for use in gates.

Our second protocol, commensurate pulses, leverages the coherent and time-periodic nature of counter-rotating fields to regularize their contributions to all control pulses, thereby eliminating the counter-rotating error channel for linear drives. This protocol relies on the application of gates at periodically discrete times determined by the qubit Larmor period, is platform independent, and requires no additional calibration overhead for Rabi-based gates. We established the efficacy of this protocol for gates as short as one Larmor period, finding almost an order of magnitude improvement in fidelity over incommensurate pulses of a similar duration.

We note that our commensurate pulse technique shares close resemblance with those used for Landau-Zener-based single-qubit gates [56, 263]. In both schemes, the exact specification of the waveform, including its timing, is crucial for the fidelity of the gate. However, these gates are often viewed from a different perspective; commensurate pulses are readily modeled in a rotating frame, whereas Landau-Zener gates are not. In the lab frame, the natural qubit precession supports $Z_{\phi(t)}$ gates by idling for a time t. Identity gates that are not exact multiples of the Larmor period must then be performed by modulating the qubit frequency [270]. Likewise, identity gates of arbitrary duration cannot be performed in the rotating frame without relaxing the commensurate pulse conditions, and Z gates are implemented via a combination of idling and phase shifting the next drive pulse so that it is once again commensurate. The main advantage of commensurate pulses is the ability to use a stable underlying carrier frequency in hardware (e.g. with a dedicated RF source). With this in place, errors in envelope timing only translate into small errors in the polar rotation angle [Fig. 6.6(c)], whereas without, errors in timing freely rotate the equatorial axis of the gate. This advantage is more pronounced when the qubit frequency is higher. While the language to describe these operations is often different, both pairs of gates rely on the same underlying physics of the natural qubit precession to perform I- and Z-gates.

We demonstrated state-of-the-art single-qubit gates with three separate drive schemes on the same qubit (pure charge, pure flux, and circularly polarized), and found that flux pulses performed the best. We attribute this to extra decoherence from system heating associated with the charge drive (see Chapter 6.5.5) and the matrix element structure of the fluxonium at half-flux (featuring larger charge matrix elements for transitions to states outside the computational subspace). We hypothesize that, if leakage transitions and heating were mitigated for charge drives, circularly polarized drives may potentially benefit Rabi-based gates for even more aggressive gate times. Furthermore, a circularly polarized drive remains an attractive tool when optimizing single-qubit gates in even lower-frequency qubits [56, 263, 271, 272] and for other low-frequency microwave interactions such as cross-resonance [273], iSWAP [256], or bSWAP gates [274].

We expect commensurate pulses, being platform-independent and requiring no additional calibration overhead, to benefit any platform where fast, resonant control is desired and counter-rotating dynamics are problematic. Although our demonstration only included one qubit, we note the straightforward extension of commensurate pulses to a multi-qubit processor based on resonant single-qubit control. Each qubit i will have an associated Larmor period τ_L^i, and so control pulses for each qubit will follow their individual lattices as defined in 6.2.3. Any multi-qubit gate then simply needs to allocate a requisite number of Larmor periods from each qubit to accommodate the duration of the added gate. Aside from the short idling times this requires, the compilation of commensurate pulses with multiple qubits needs no other special consideration.

Note: While preparing this manuscript, we became aware of a related work [275]

Chapter 7

Qubit-State Purity Oscillations from Anisotropic Transverse Noise

In this chapter, we explore the dynamics of qubit-state purity in the presence of transverse noise that is anisotropically distributed in the Bloch-sphere XY plane. We perform Ramsey experiments with noise injected along a fixed laboratory-frame axis and observe oscillations in the purity at twice the qubit frequency arising from the intrinsic qubit Larmor precession. We probe the oscillation dependence on the noise anisotropy, orientation, and power spectral density, using a low-frequency fluxonium qubit. Our results elucidate the impact of transverse noise anisotropy on qubit decoherence and may be useful to disentangle charge and flux noise in superconducting quantum circuits.

7.1 Introduction

Quantum systems experience decoherence in the presence of uncontrolled environmental degrees of freedom. When engineering quantum systems for applications such as computing [25, 30] or metrology [276], decoherence poses a significant challenge to conducting high-precision experiments. Consequently, understanding the structure of coherence-limiting noise and corresponding decoherence dynamics is of both high interest and value. Although significant effort has been put into the development of qubit decoherence models [129, 189, 277, 278] and noise spectral estimation [279–282], signatures of the anisotropy of transverse noise (i.e., noise that is not isotropically distributed in the Bloch-sphere XY plane) in qubit decoherence [72, 283–285] remains relatively underexplored[1], with the notable exception of squeezed light inducing anisotropic rotating-frame transverse relaxation times [287–289]. These prior studies focused on squeezed light in a narrow bandwidth around the qubit frequency, resulting in dynamics consistent with the rotating-wave approximation (RWA), given by the optical Gardiner-Bloch equations [71, 287].

We instead ask the following question: when exposed to large-bandwidth, off-resonant noise resulting in physics beyond the RWA [290, 291], are there distinct signatures of transverse noise anisotropy in qubit decoherence? Such signatures may inform a method to disentangle noise sources coupled to distinct transverse axes [292], e.g., charge and flux noise in circuit quantum electrodynamics. We focus on classical rather than quantum noise [293], and utilize linear polarization of the noise (rather than squeezing) to probe transverse noise anisotropy. Our approach, leveraging injected classical noise [294, 295], bypasses the bandwidth limitations and experimental complexity of engineered squeezed light sources [296, 297].

We now introduce the central theoretical idea of this work [Fig. 7.3(a)]. Consider a qubit described by density matrix ρ, which experiences noise that is coupled to a transverse axis in the lab frame (e.g. $H_{\mathrm{noise}}/\hbar = \eta_y(t)\sigma_y$ where $\eta_y(t)$ is real-valued and referred to as linearly polarized, since the noise field couples to a single Bloch-sphere axis). Starting in a superposition state, the state purity $\mathrm{tr}\,(\rho^2)$—indicating the degree of decoherence or disorder—will display an oscillatory component at twice the qubit frequency. We can understand this behavior by considering the qubit Larmor precession: when aligned with (perpendicular to) the noise

---

[1] Although such noise is a feature of the extensively-studied spin-boson model in the regime of zero bias [189, 286] (see, e.g., Section IIIB of Ref. [189]), prior work primarily focused on dynamics of the spin polarization along one axis rather than that of the state purity. In the weak-coupling limit, the polarization dynamics are those of the damped harmonic oscillator (see Eq. 3.10 of Ref. [189]), displaying no features at twice the qubit frequency. By studying state purity, we elucidate dynamics related to decoherence, unobscured by Larmor motion.

axis, the qubit state will be insensitive (sensitive) to rotations generated by the noise field. Consequently, as the qubit precesses, the susceptibility of the state to the noise will oscillate at twice the qubit frequency. Qubit purity oscillations [285, 295] do not typically appear in conventional descriptions of decoherence, such as through isotropic transverse noise [283] or coupling to a (squeezed) electromagnetic field within the RWA [72, 287, 288]. However, such oscillations should arise from noise in transversely-coupled qubit-control electronics, such as those used for charge or flux drives in superconducting circuits [89], or for laser-amplitude modulation in neutral atom experiments [69].

In this chapter, we directly measure time-domain purity oscillations in the state of a superconducting fluxonium qubit via injected-noise experiments. We establish that anisotropic transverse noise generates periodic behavior in qubit purity. For noise with a short correlation time (Markovian noise), we observe a step-wise monotonic decay in purity, whereas longer noise correlation times result in purity revivals. We probe the noise-axis dependence of the oscillations, finding a period-doubling behavior for noise approaching the quasistatic limit (where noise is constant during a single experiment, but changes shot-to-shot).

7.2 Analytical results

Before presenting our experimental results, in this section we provide analytical calculations for the purity decay of a qubit subject to anisotropic transverse noise in the quasistatic and Markovian limits.

7.2.1 Anisotropic Quasistatic Noise

In this subsection, we derive expressions for the purity $\gamma = \mathrm{tr}\left(\rho^2\right)$ of a qubit prepared in a superposition state $|\Psi_0\rangle = (|0\rangle + |1\rangle)/\sqrt{2}$ and evolved under the influence of a static noise field $\eta \in \mathbb{R}$ coupled to an axis at angle θ with the Bloch-sphere $\hat{x}$ axis. The Hamiltonian is given by

$$\frac{H_\eta}{\hbar} = -\omega\frac{\sigma_z}{2} + \eta(\cos(\theta)\sigma_x + \sin(\theta)\sigma_y). \tag{7.1}$$

Here, $\eta \ll \omega$ is a random variable representing noise that is constant during a single run of the experiment (shot) but different shot-to-shot. We refer to such noise as "quasistatic." For a single instance of noise η, the qubit state at time t will be given by $|\Psi_\eta(t)\rangle = U_\eta(t)\,|\Psi_0\rangle$, where $U_\eta(t)$ is the time-evolution operator for H_η.

We compute the noise-averaged purity from the density matrix $\rho_\eta = |\Psi_\eta\rangle\,\langle\Psi_\eta|$ as $\rho = \langle\rho_\eta\rangle$, where $\langle\cdot\rangle$ represents the noise ensemble average [295]. In the frame co-rotating with the qubit and keeping only terms up to $(\eta/\omega)^2$, we find

$$\tilde{\rho}_\eta^{00} = \frac{1}{2} + \frac{\eta}{\omega}\left(\cos(\theta + \omega t) - \cos(\theta)\right) \tag{7.2}$$

$$\tilde{\rho}_\eta^{11} = \frac{1}{2} - \frac{\eta}{\omega}\left(\cos(\theta + \omega t) - \cos(\theta)\right) \tag{7.3}$$

$$\tilde{\rho}_\eta^{01} = \frac{1}{2} - \frac{\eta^2}{\omega^2}\left[1 - i\omega t - e^{-i(2\theta+\omega t)}(1 + e^{2i\theta} - \cos(\omega t))\right] \tag{7.4}$$

$$\tilde{\rho}_\eta^{10} = (\tilde{\rho}_\eta^{01})^*, \tag{7.5}$$

and note that $\mathrm{tr}(\tilde{\rho}_\eta^2) = \mathrm{tr}(\rho_\eta^2) = 1$ up to terms of order $(\eta/\omega)^4$. For zero-mean noise processes ($\langle\eta\rangle = 0$, as was the case for all experiments and simulations in this work), we find

$$\mathrm{tr}\left(\rho^2\right) = 1 - \frac{2\langle\eta^2\rangle}{\omega^2}(\cos\theta - \cos(\omega t + \theta))^2 + \mathcal{O}(\langle\eta^4\rangle/\omega^4). \tag{7.6}$$

By expanding the squared second term, we find two time-dependent oscillations: (1) $\cos^2(\omega t + \theta)$ and (2) $\cos\theta\cos(\omega t + \theta)$. When the noise axis is perpendicular to the initial qubit state ($\theta = \pi/2 + \pi n$ for integer n), the second oscillation vanishes and the remaining oscillation has a period of $\tau = \pi/\omega = \tau_L/2$. In contrast, when the noise axis is aligned or anti-aligned with the initial qubit state ($\theta = n\pi$), both oscillations remain and the period is determined by the slowest oscillation with $\tau = 2\pi/\omega = \tau_L$. In summary, we expect to find a period-doubling behavior for purity oscillations for noise in the quasistatic limit.

7.2.2 Anisotropic White Noise

In this subsection, we derive expressions for purity decays in the case of transversely-coupled high-frequency white noise by modelling the qubit as an open quantum system for which the noise acts as a Markovian bath. Notably, the Markovian model for linearly-polarized (maximally anisotropic) white noise leads both to an exponential decay of purity – characteristic of dissipative dynamics in open quantum systems – as well as oscillations in purity at twice the qubit frequency.

In experiments, we realize high-frequency white noise with the Hamiltonian

$$\frac{H_\eta}{\hbar} = -\omega\frac{\sigma_z}{2} + \eta(t)\left(\cos(\theta)\sigma_x + \sin(\theta)\sigma_y\right), \tag{7.7}$$

where $\eta(t)$ comprises a noise process, with a white power spectral density extending to frequencies above the qubit frequency ω [Fig. 7.2(e,f)], and θ indicates the polarization axis of the noise with respect to the $\hat{x}$ axis of the Bloch sphere. In this section, however, we model the evolution of the qubit as Markovian by using a Lindblad master equation for the qubit density matrix [298, 299],

$$\dot{\rho} = -i\left[\frac{H}{\hbar}, \rho\right] + \sum_i \Gamma_i\left(L_i\rho L_i^\dagger - \frac{1}{2}\left\{L_i^\dagger L_i, \rho\right\}\right), \tag{7.8}$$

where the L_i are a set of jump operators describing the Markovian dynamics of the noise, and the $\Gamma_i \geq 0$ is a dissipation rate characterizing the strength of the coupling between the white noise and the qubit. The qubit's evolution becomes Markovian if the qubit and the noise bath remain roughly unentangled and uncorrelated over the course of the qubit's evolution. See, for example, Ref. [300].

For transversely-polarized noise, we use the simple model of a single jump operator

$$L = \cos(\theta)\sigma_x + \sin(\theta)\sigma_y, \tag{7.9}$$

and a single corresponding dissipation rate Γ. This choice represents a coupling of the qubit to a stochastic noise field along the $(\cos(\theta)\,\hat{x}+\sin(\theta)\,\hat{y})$ axis of the Bloch sphere [72, 301]. The density matrix equation of motion is given by

$$\dot{\rho}=\begin{pmatrix}\Gamma(\rho_{11}-\rho_{00}) & (i\omega-\Gamma)\rho_{01}+e^{-2i\theta}\Gamma\rho_{10}\\ -(i\omega+\Gamma)\rho_{10}+e^{2i\theta}\Gamma\rho_{01} & \Gamma(\rho_{00}-\rho_{11})\end{pmatrix}. \tag{7.10}$$

We can gain some insight by looking at the resulting Bloch equations for such single-axis noise, taking $\theta=0$ without loss of generality,

$$\frac{\partial\langle\sigma_x\rangle}{\partial t}=\omega\langle\sigma_y\rangle \tag{7.11}$$

$$\frac{\partial\langle\sigma_y\rangle}{\partial t}=-\omega\langle\sigma_x\rangle-2\Gamma\langle\sigma_y\rangle \tag{7.12}$$

$$\frac{\partial\langle\sigma_z\rangle}{\partial t}=-2\Gamma\langle\sigma_z\rangle. \tag{7.13}$$

We find relaxation of the transverse polarization solely along $\hat{y}$ and not $\hat{x}$ (see Ref. [283], Section 5.12 for an alternative derivation). These equations are identical to those describing the infinite-temperature, zero-bias spin-boson model in the weak-coupling limit, see Ref. [189], Section IIIB, Eq. 3.9 (with our spin quantized along $\hat{z}$ rather than $\hat{x}$, and noise along $\hat{x}$ rather than $\hat{z}$). We note the well-established result that the transverse polarization dynamics, e.g. $\langle\sigma_x\rangle(t)$, are equivalent to those of a damped harmonic oscillator with bare frequency ω. However, time-domain decoherence signatures of the noise anisotropy at frequency 2ω are uncovered by studying the state purity. Starting with a qubit prepared in the state $|\Psi_0\rangle=(|0\rangle+|1\rangle)/\sqrt{2}$, we solve Eq. (7.10), finding

$$\mathrm{tr}\left(\rho^2\right)=1-\Gamma t-\frac{\Gamma}{2\omega}\left(\sin(2\theta)-\sin(2\theta+2\omega t)\right)+\mathcal{O}(\Gamma^2), \tag{7.14}$$

which exhibits oscillations at twice the qubit frequency and a periodicity in the noise axis of $\Delta\theta=\pi$. We find that the purity decay for high-frequency white noise is monotonic:

$\partial\gamma/\partial t \le 0$. The derivative has oscillation amplitude $0 \le |\partial\gamma/\partial t| \le 2\Gamma$.

We note that for isotropic (unpolarized) noise, qubit purity decays exponentially with no oscillations. For example, choosing $\Gamma_1 = \Gamma_2 = \Gamma$ and $(L_1, L_2) = (\sigma^+,\ \sigma^-)$ or $(L_1, L_2) = \left(\sigma_x/\sqrt{2},\ \sigma_y/\sqrt{2}\right)$, we find $\mathrm{tr}\,(\rho^2) = (1 + e^{-2\Gamma t})/2$. This result qualitatively captures the behavior we will observe later in Section 7.4 [Fig. 7.4]. However, we note that the noise used for the experiments in that figure did not approach the Markovian limit.

7.3 Experimental Setup

Our experimental platform comprises a superconducting fluxonium qubit [55] of transition frequency $f_{01} = \omega_{01}/2\pi \approx 243.7\,\mathrm{MHz}$ (Larmor period $\tau_L = f_{01}^{-1} \approx 4.1\,\mathrm{ns}$) with individual charge and flux control. Qubit states were measured using a dispersively-coupled readout resonator [89], and initial qubit states are heralded with prior readout pulses [255]. The fluxonium qubit obeys the system Hamiltonian

$$\hat{H} = \hat{H}_0 + \hbar\Omega_{\hat{n}}(t)\hat{n} + \hbar\Omega_{\hat{\phi}}(t)\hat{\phi}, \tag{7.15}$$

where $\Omega_{\hat{n}}(t)$ and $\Omega_{\hat{\phi}}(t)$ are the charge and flux drives respectively (comprising both coherent control pulses and injected noise), and $\hat{H}_0$ is the bare fluxonium Hamiltonian

$$\hat{H}_0 = 4E_C\hat{n}^2 + \frac{1}{2}E_L(\hat{\phi} - \phi_{\mathrm{dc}})^2 - E_J\cos(\hat{\phi}). \tag{7.16}$$

In the fluxonium Hamiltonian, $\hat{n}$ and $\hat{\phi}$ represent the charge and phase operators; $E_C/h = 1.30\,\mathrm{GHz}$, $E_L/h = 0.59\,\mathrm{GHz}$, and $E_J/h = 5.71\,\mathrm{GHz}$ are the charging, inductive, and Josephson energies, respectively; and ϕ_{dc} is a phase offset resulting from a static external magnetic flux $\Phi_{\mathrm{dc}}/\Phi_0 = \phi_{\mathrm{dc}}/2\pi$ supplied by a superconducting coil mounted to the lid of the sample package, inductively coupled to the fluxonium loop. All experiments were performed with $\Phi_{\mathrm{dc}} = 0.5\Phi_0$, referred to as the degeneracy point. The sample qubit was a subsystem of a device comprising two fluxonium qubits with a capacitively-coupled transmon coupler (refer to device A, fluxonium 2 of Ref. [255]).

Considering a qubit comprising the lowest two eigenstates of Eq. (7.15) we realize the effective system Hamiltonian (written in matrix form with Pauli matrices σ_i),

$$\frac{H}{\hbar} = \omega_{01}\frac{\sigma_z}{2} + \eta_x(t)\sigma_x + \eta_y(t)\sigma_y. \tag{7.17}$$

The transverse driving terms originate from charge ($\hat{n} \propto \sigma_y$) and flux ($\hat{\phi} \propto \sigma_x$) control.

7.3.1 Wiring and Control Equipment

All experiments were conducted in a Bluefors XLD600 dilution refrigerator maintaining a base temperature stabilized at $\sim 22\,\mathrm{mK}$. We specify the equipment used for qubit biasing, coherent control pulses, injected noise generation, and readout in Table. 7.1, and we detail the experimental wiring in Fig. 7.1.

Table 7.1: **Summary of control equipment.**

Component	Manufacturer + Model
Dilution Refrigerator	Bluefors XLD600
RF Source	Rohde & Schwarz SGS100A
DC Source	QDevil QDAC I
Control Chassis	Keysight M9019A
AWG (readout pulses)	Keysight M3202A
AWG (qubit pulses)	Keysight M8195A
AWG (noise gating)	Keysight M8195A
ADC	Keysight M3102A
100 MHz white noise	Agilent 33250A
1 GHz white noise	(Mini-Circuits ZFL-500LN+)x3
Noise 2 MHz LPF	Mini-Circuits SLP-1.9+
Noise Mixer	Mini-Circuits ZFM-2-S+
Noise Combiner	Mini-Circuits ZFRSC-42-S+

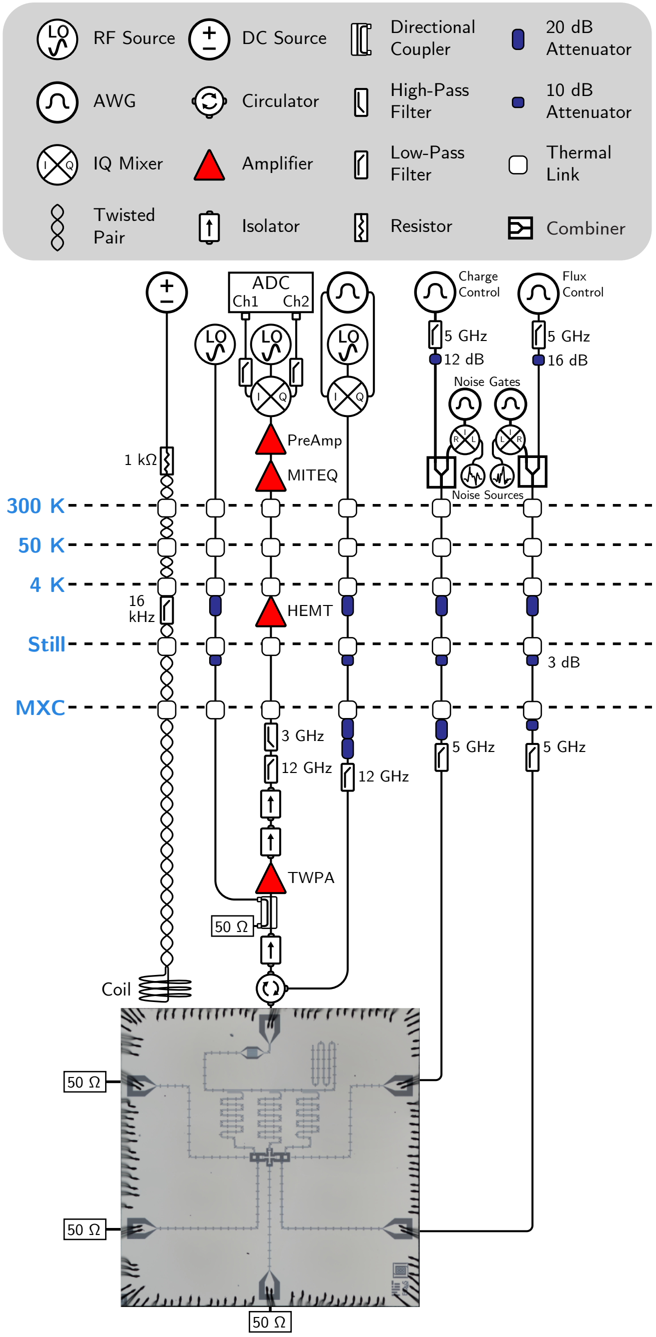

Figure 7.1: **Wiring schematic of the experimental setup.**

7.3.2 Injected Noise Characterization

In this subsection, we present characterization of the injected noise used in our experiments.

To characterize the injected noise, we measured noise after the combiner as in the wiring diagram [Fig. 6.2 and Fig. 7.3(b)] in the time domain with a high-bandwidth oscilloscope for the three noise configurations used in this work: (1) white noise up to $\sim 100\,\mathrm{MHz}$ [Fig. 7.2(a,b)] generated with an Agilent 33250A, (2) 2 MHz low-pass filtered noise [Fig. 7.2(c,d)] generated by filtering the output of the Agilent 33250A before mixing with the noise gate, and (3) white noise up to 1 GHz [Fig. 7.2(e,f)] generated by daisy-chaining three amplifiers with a passive 50 Ohm input. For each type of noise, we computed the PSD of measured time-domain traces, and averaged the resulting PSDs over several noise instances. The PSD for each timeseries was computed as

$$S_{\eta\eta}(f) = \frac{|\mathrm{FFT}\{\eta(t)\}|^2 \delta t}{N}, \tag{7.18}$$

where $\eta(t)$ is the noise process, sampled at rate $1/\delta t$ yielding a time-series with N total samples. We converted the units of the time series from voltage to frequency by scaling the measured traces by the ratio of the analytical $\pi/2$ amplitude for our 80 ns cosine pulse (in MHz) to the measured $\pi/2$ pulse amplitude (in volts). We report the measured PSDs and amplitude distributions in Fig. 7.2.

The 100 MHz white noise amplitude distribution most closely resembled an ideal bimodal distribution, and the 2 MHz low-pass filtered and 1 GHz white noise configurations contained an additional significant proportion of the amplitude distribution centered around zero. We attribute the sharp cutoff of the noise amplitude distribution to saturation of the mixer used for gating the noise. We emphasize that in simulations, we found no dependence of the presence of purity oscillations on the specific noise amplitude distribution (e.g., bimodal, Gaussian, or uniform) for a given noise power spectral density. Our analytical treatment of purity decays suggests that higher-order moments of the noise distribution would add small effects on the order of $(\eta/\omega)^n \sim (10\%)^n$ for $n > 2$.

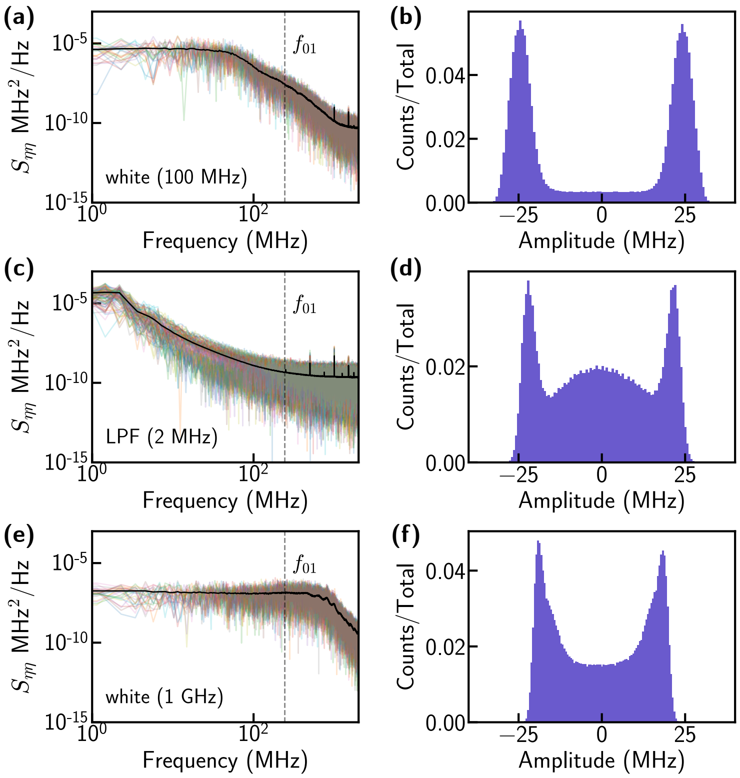

Figure 7.2: **Injected noise characterization.** To most directly characterize the noise sent to the qubit, all data presented were measured with an oscilloscope after the noise gating and combination with the coherent control line. **(a)** Noise power-spectral density (PSD) and **(b)** noise amplitude distribution for the $\sim 100\,\mathrm{MHz}$ white noise configuration. **(c,d)** Similar to (a,b), for 2 MHz low-pass filtered noise. **(e,f)** Similar to (a,b), for 1 GHz white noise.

7.4 Experimental Results

The primary experiment performed in this work is a Ramsey experiment with injected noise [Fig. 7.3(a,b)]. Starting from the ground state, we prepare the qubit on the Bloch-sphere equator with a resonant $\pi/2$ pulse. We then let the qubit evolve for a total free-precession time $\tau = 2\tau_b + \tau_n$, where τ_n is the injected-noise duration and $\tau_b \geq 5\,\mathrm{ns}$ is a buffer time before and after the noise injection, used to minimize interference with the coherent control pulses. Unless specified, we set $\tau_b = 10\,\mathrm{ns}$. The noise is turned on diabatically with rise and fall times of 0.5 ns such that the initial qubit state is approximately unchanged when turning the noise on and off. Finally, the qubit state is transferred to the $\hat{z}$ axis with a second resonant $\pi/2$ pulse. We ensure that the initial and final $\pi/2$ pulses are about the same axis in the frame co-rotating with the qubit such that the Bloch vector is aligned with the $\hat{z}$ axis at the end of the sequence. This enables us to probe the purity $\gamma \equiv \mathrm{tr}\left(\rho^2\right)$ with only one measurement of the qubit along σ_z as

$$\gamma = \frac{\langle\sigma_x\rangle^2 + \langle\sigma_y\rangle^2 + \langle\sigma_z\rangle^2}{2} + \frac{1}{2} \to \gamma_{\text{approx}} \equiv \frac{\langle\sigma_z\rangle^2}{2} + \frac{1}{2} \tag{7.19}$$

in the limit $\langle\sigma_x\rangle^2 + \langle\sigma_y\rangle^2 \to 0$. We later justify the correspondence of γ_{approx} and γ for all experiments in Section 7.4.5. Noise injection is performed by gating a noise source with a double-balanced mixer and connecting it to the charge and/or flux drive line of the qubit [Fig. 7.3(c)]. We begin data collection after a minimum noise duration of approximately 20 ns in order to mitigate transients from the rapid toggling of the noise field.

7.4.1 Purity Oscillations from Anisotropic Transverse Noise

To demonstrate the appearance of purity oscillations from anisotropic noise, we performed Ramsey experiments with noise injected along σ_y. We utilized three noise configurations: (1) noise off, (2) low-frequency white noise up to $100\,\text{MHz} < f_{01}$, and (3) broadband white noise up to $1\,\text{GHz} > f_{01}$ [Fig. 7.3(d)] (refer to Section 7.3.2 for details about the noise sources). We plot the purity decays in Fig. 7.3(e). With noise off, we observe nearly constant purity due to the long coherence of our qubit relative to the measured free-precession times. With white noise below the qubit frequency, we observe oscillations in the purity at a frequency $2f_{01}$. With white noise over a range that includes the qubit frequency, we observe the purity decay in small steps. We observe oscillations present in the derivative of the signal in Fig. 7.3(e), inset. For this high-frequency noise, the lack of purity revivals ($\partial\gamma/\partial t \leq 0$) is consistent with the short correlation time of the broadband noise relative to the qubit dynamics, which emulates a Markovian bath. Our observations confirm our expectation of dynamics at twice the qubit frequency developed in Chapter 3.4, and are consistent with the analytical result

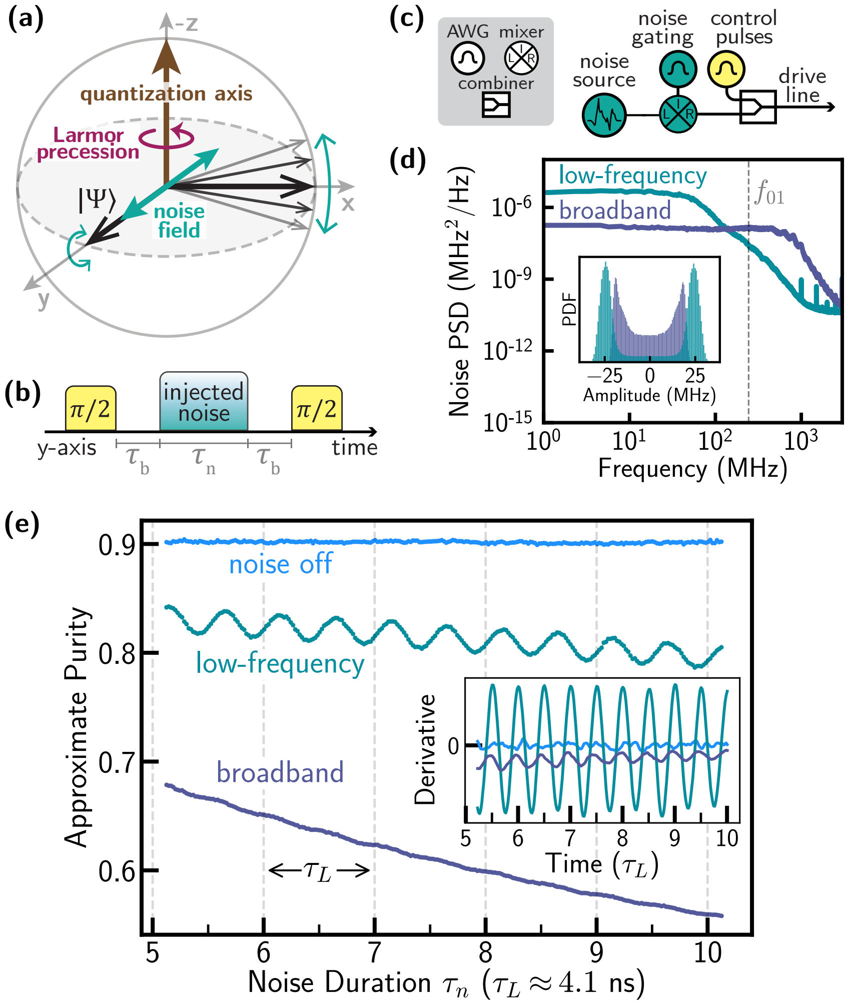

Figure 7.3: **Purity oscillations in Ramsey experiments with anisotropic noise.** **(a)** Bloch-sphere representation of a qubit in the lab frame undergoing Larmor precession (purple) under the influence of linearly polarized transverse noise (turquoise). When the qubit state is aligned with (perpendicular to) the noise axis, the state is insensitive (sensitive) to the noise, resulting in purity oscillations at twice the qubit frequency due to the Larmor precession. **(b)** Pulse sequence. A superposition state is prepared, and noise is turned on after a buffer time τ_b. The noise is kept on for a duration τ_n. **(c)** Experimental setup for noise injection. Noise is generated, gated with a mixer, and combined with coherent control pulses on the device charge or flux line. **(d)** Injected noise power spectral densities for two noise configurations: (1) low-frequency white noise up to $100\,\text{MHz} < f_{01}$, and (2) broadband white noise up to $1\,\text{GHz} > f_{01}$. Inset: noise amplitude distributions. We attribute the bimodal nature of the noise to saturation of the mixer used for noise gating. **(e)** Approximate purity, $\gamma_{\text{approx}} \equiv \langle\sigma_z\rangle^2/2 + 1/2$, for Ramsey experiments with injected charge noise ($\hat{n} \propto \sigma_y$) in three configurations: noise off (light blue), white noise up to $100\,\text{MHz} < f_{01}$ (turquoise), and white noise up to $1\,\text{GHz} > f_{01}$ (dark blue). Insert: time derivatives of the approximate purity data, smoothed with a triangular window function of size $0.22\tau_L$ to clarify the signal.

derived with the Lindblad master equation in Section 7.2.2 given by Eq. (7.14):

$$\mathrm{tr}\left(\rho^2\right) = 1 - \Gamma t - \frac{\Gamma}{2\omega}\left(\sin(2\theta) - \sin(2\theta + 2\omega t)\right) + \mathcal{O}(\Gamma^2), \tag{7.20}$$

From the experimental data in Fig. 7.3(e) for broadband white noise, fitting the decay envelope to an exponential function yields $\Gamma_{\text{from envelope}} = 6.4 \pm 0.5\,\text{MHz}$. We corroborate the analytical result by inspecting the initial fringe contrast of the derivative in Fig. 7.3(e), inset, yielding $\Gamma_{\text{from derivative}} \sim 5\,\text{MHz}$. Due to noisiness of the signal, we only emphasize that both estimates of Γ yield order-of-magnitude agreement.

7.4.2 Varying Noise Anisotropy

As our next main result, we validated that the purity oscillations are related to noise anisotropy by measuring the purity dynamics while varying the noise distribution anisotropy between three configurations: (1) anisotropic, (2) Z_4-symmetric (symmetric under 90° rotations), and (3) isotropic. Anisotropic noise (1) comprised perfectly correlated noise along the $\hat{x}$ (flux) and $\hat{y}$ (charge) axes [Fig. 7.4(a)], yielding noise along $\hat{x} + \hat{y}$. Z_4-symmetric noise (2) comprised uncorrelated, equal-amplitude noise sources connected to $\hat{x}$ and $\hat{y}$ [Fig. 7.4(b)]. The Z_4 symmetry resulted from the bimodal nature of the noise amplitude distribution (uncorrelated Gaussian noise sources would instead produce isotropic noise). Isotropic noise (3) comprised Z_4-symmetric noise averaged over 19 qubit initial states equally spaced along the Bloch-sphere equator, yielding an effective isotropic noise distribution in the XY plane for the ensemble-averaged dynamics [295]. Two-dimensional noise amplitude distributions are presented in Fig. 7.4(c). With the anisotropic noise, we observe pronounced oscillations in the time-domain purity trace [Fig. 7.4(d)]. We observe nearly complete extinction of the oscillations with the Z_4-symmetric noise and complete extinction for the isotropic noise [Fig. 7.4(e)]. We note that for the isotropic noise, the isotropy is a consequence of ensemble averaging over qubit-state preparations equally spaced along the Bloch-sphere equator [295]

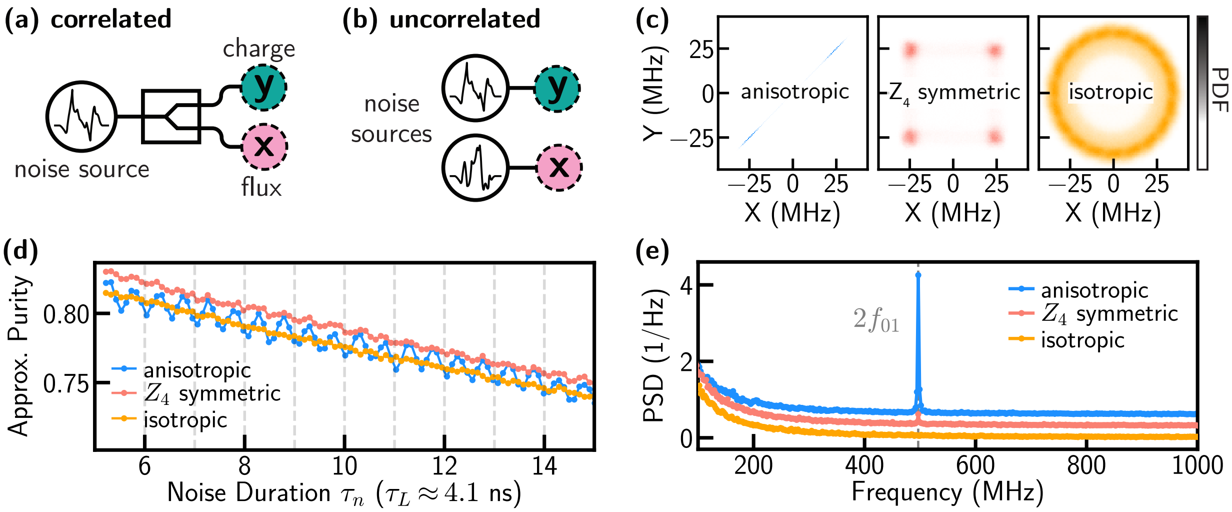

Figure 7.4: **Varying the anisotropy of injected noise.** All experiments in this figure utilized the low-frequency white noise source (noise power up to 100 MHz $< f_{01}$) with a bimodal amplitude distribution [Fig. 7.3d]. **(a)** Correlated (one source split to σ_x and σ_y) and **(b)** uncorrelated (separate sources for σ_x and σ_y) noise source configurations. **(c)** Noise-amplitude distributions from noise traces measured on an oscilloscope, reflecting noise in the Bloch-sphere XY plane, for three configurations: (1) anisotropic, comprising the correlated configuration in (a), (2) Z_4-symmetric, comprising the uncorrelated configuration in (b), and (3) isotropic, comprising the Z_4-symmetric noise averaged over 19 equally-spaced rotations about the $\hat{z}$ axis. **(d)** Time-domain traces of the approximate purity, $\langle\sigma_z\rangle^2/2 + 1/2$, during a Ramsey sequence with the injected noise configurations in (c). In order to visualize the oscillations, we plot a subset of the full data (1001 points between $5.12\tau_L \leq \tau_n \leq 105.12\tau_L$). **(e)** Power spectral densities (PSDs) of the full time-domain data taken for (d), offset for clarity. We attribute the small $2f_{01}$ feature in the Z_4-symmetric trace to a slight imbalance of the calibrated charge and flux noise amplitudes.

rather than reflecting the noise symmetry during individual shots. We emphasize that the qualitative purity-decay behavior (smooth decay with no oscillations) matches that from numerical simulations with shot-to-shot isotropically distributed noise. We attribute the remaining oscillatory component in the Z_4-symmetric trace to imperfect balancing of the noise amplitudes, which were experimentally calibrated by measuring the charge/flux π-pulse amplitudes individually.

7.4.3 Varying Noise Correlation Time and Noise Axis

As our next main result, we probed the noise-axis dependence of purity oscillations for two anisotropic noise configurations: (1) white noise up to 100 MHz [Fig. 7.5(a,b,c)], and (2) 2 MHz low-pass-filtered noise [Fig. 7.5(e,f,g)]. We elected to sweep the initial superposition phase φ rather than the noise axis directly, which allowed us to calibrate the qubit frequency with the noise-induced AC Stark shift only once at the beginning of the experiment. For noise configuration (1), we observed purity oscillations at twice the qubit frequency with a phase periodicity of $\Delta\varphi = 180°$, consistent with identical purity decays for a shift in the noise axis of 180°. We can understand the oscillation frequency in the Bloch-sphere picture: as the qubit precesses along the equator, the noise susceptibility oscillates with a period of $\tau_L/2$ [Fig. 7.5(d)]. For noise configuration (2), the correlation time of the noise $\tau_c \sim 100\,\mathrm{ns}$ exceeds the free-precession time, approaching the quasistatic noise limit in which noise is constant during a single experiment, but differs shot-to-shot. We observed purity oscillations with a frequency dependent on the noise axis relative to the initial state, with the same phase periodicity of $\Delta\varphi = 180°$. We can understand the doubling of the period in the Bloch-sphere picture by considering shot-to-shot fluctuations of the qubit quantization axis [Fig. 7.5(h)]. Our observations are consistent with the analytical result developed in Section 7.2.1 and given by Eq. (7.6) for noise with variance $\langle\eta^2\rangle$ (now with the angle of the noise axis $\theta = \pi/2 - \varphi$ to match the notation used in Fig. 7.5):

$$\mathrm{tr}\left(\rho^2\right) = 1 - \frac{2\langle\eta^2\rangle}{\omega^2}(\sin\varphi + \sin(\omega t - \varphi))^2 + \mathcal{O}\left(\frac{\langle\eta^4\rangle}{\omega^4}\right). \tag{7.21}$$

The purity decay for isotropic quasistatic noise is obtained by averaging Eq. (7.21) over $\varphi \in [0, 2\pi)$, yielding purity oscillations at the qubit frequency ω. Unlike the oscillations at 2ω, these oscillations are not a consequence of the noise anisotropy; starting in a consistent state on the zero-noise Bloch-sphere equator, tilting the quantization axis in any direction will always leave the starting state as a fixed point of the Larmor orbit [294].

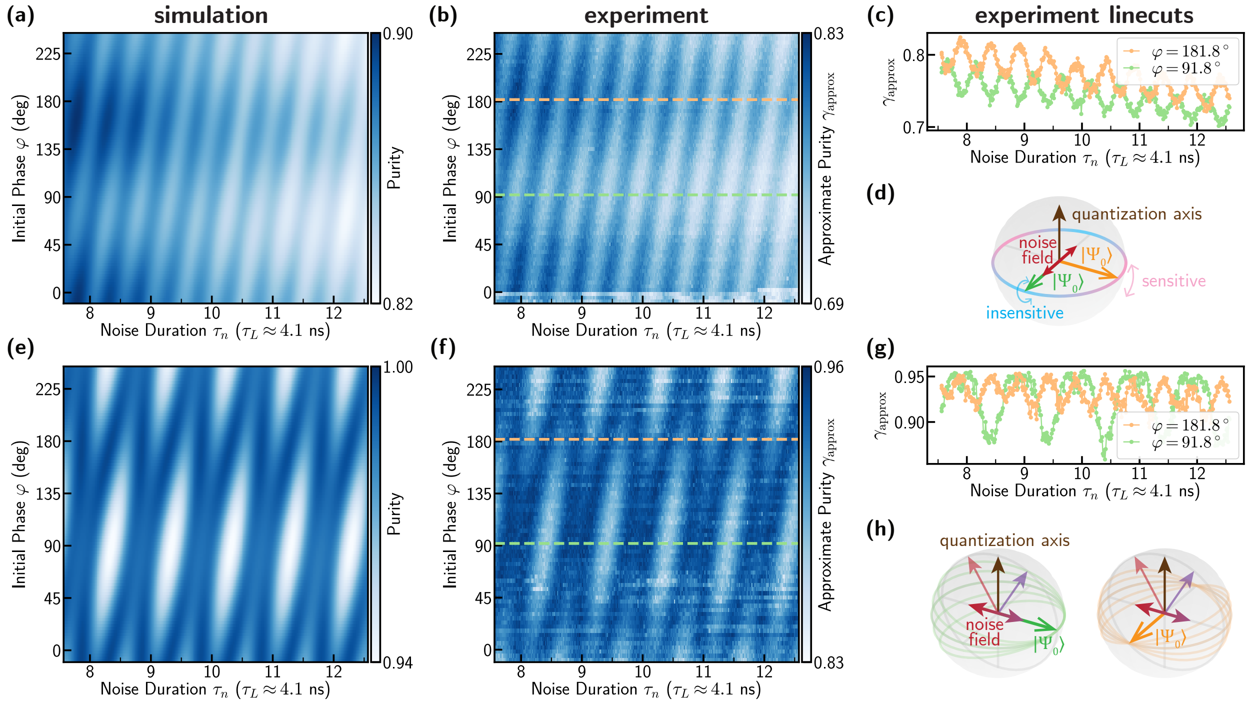

Figure 7.5: **Noise axis and power spectrum dependence of purity oscillations.** All data comprise Ramsey experiments with injected charge noise ($\hat{n} \propto \sigma_y$) as a function of noise duration and initial superposition phase φ, $|\Psi_0\rangle = (|0\rangle + e^{i\varphi}|1\rangle)/\sqrt{2}$, with $\tau_b = 5\,\mathrm{ns}$. We elected to sweep the phase φ rather than the noise axis for experimental ease, noting that the resulting physics is identical. Simulated 100 MHz white (2 MHz low-pass filtered) noise comprises a random telegraph signal with amplitude $\approx \pm 24\,\mathrm{MHz}$ ($\approx \pm 23\,\mathrm{MHz}$) and average switching rate $\approx 96\,\mathrm{MHz}$ ($\approx 4.4\,\mathrm{MHz}$). **(a)** Simulation, **(b)** experiment, and **(c)** experimental linecuts for 100 MHz white noise. **(d)** Bloch sphere cartoon illustrating the insensitivity (sensitivity) of the qubit state to rotations induced by the noise when the qubit is parallel (perpendicular) to the noise axis, resulting in purity oscillations at frequency $2f_{01}$. **(e,f,g)** Similar to (a,b,c), respectively, for 2 MHz low-pass-filtered noise, which approaches the quasistatic limit where noise is constant during a single run of the experiment (shot), but changes shot-to-shot. **(h)** Bloch sphere cartoon for quasistatic noise. In the quasistatic limit, when noise is constant during the Larmor precession but changing shot-to-shot, the effective quantization axis is affected. Left (right): When the qubit state is initially aligned with (perpendicular to) the noise axis, all Larmor orbits have one (two) fixed point(s). This results in maximal purity when the qubit is aligned (aligned or anti-aligned) with its starting state, characterized by purity oscillations of frequency f_{01} ($2f_{01}$).

7.4.4 Relaxation Experiments

In this section, we explore the affect of anisotropic (linearly polarized) noise on relaxation experiments where the qubit is initially prepared in $|\Psi_0\rangle = |1\rangle$ and then subject to noise injected on the charge line ($\hat{n} \propto \sigma_y$): $H_{\text{noise}} = \eta_y(t)\sigma_y$. We perform relaxation experiments with injected noise in the low-frequency and quasistatic limits [Fig. 7.6]. Interestingly, we observe pronounced purity oscillations for experiments with noise approaching the quasistatic limit. Through further numerical simulations and analytical results, we establish that these oscillations do not depend on the axis of the noise and do not depend sensitively on the distribution of noise amplitudes (e.g., Gaussian or bimodal).

Here we give intuition for these purity oscillations for relaxation experiments with classical transverse noise in the quasistatic limit. Consider a qubit initially prepared in $|1\rangle$, and subject to time-evolution governed by the system Hamiltonian Eq. (7.1). The Bloch vector, starting at the pole, will precess around the new effective quantization axis with a period $\omega_\eta = \sqrt{\omega^2 + 4\eta^2} \approx \omega + 2\eta^2/\omega$. For any η, the Larmor orbit will always pass through the pole of the zero-noise Bloch sphere resulting in maximum purity. Oscillations in the purity will be pronounced until the orbits for different η diverge enough to average incoherently. We can estimate the damping time for these oscillations by considering how long it takes for π phase difference to accumulate between orbits for noise of strength η and no noise: $\Delta T = \pi/|\omega - \omega_\eta| \approx \pi\omega/2\eta^2 = f_{01}/4(\eta/2\pi)^2$. For the simulated quasistatic noise used in Fig. 7.6, we calculate $\Delta T \approx 29\tau_L$, which is consistent with the $1/e$ decay time of the oscillation amplitude to within 15%.

We can understand the oscillations analytically by repeating the analysis for quasistatic noise presented in Section 7.2.1, with the modification that $|\Psi_0\rangle = |1\rangle$. For a noise value η, the density matrix in the frame co-rotating with the qubit is given by

$$\tilde{\rho}_\eta^{00} = \frac{2\eta^2}{\omega^2}(1 - \cos(\omega t)) \tag{7.22}$$

$$\tilde{\rho}_\eta^{11} = 1 - \tilde{\rho}_\eta^{00} \tag{7.23}$$

$$\tilde{\rho}_\eta^{01} = \frac{\eta}{\omega} e^{-i\theta}(-1 + e^{-i\omega t}) \tag{7.24}$$

$$\tilde{\rho}_\eta^{10} = (\tilde{\rho}_\eta^{01})^*, \tag{7.25}$$

with $\mathrm{tr}(\rho_\eta^2) = 1$ up to terms of order $(\eta/\omega)^4$. For zero-mean noises ($\langle\eta\rangle = 0$), we find

$$\mathrm{tr}\left(\rho^2\right) = 1 - \frac{4\langle\eta^2\rangle}{\omega^2}(1 - \cos(\omega t)) + \mathcal{O}(\langle\eta^4\rangle/\omega^4). \tag{7.26}$$

We note that there is no θ dependence, i.e., these purity oscillations have no dependence on the noise axis. From the experimental data of Fig. 7.6(a) with fringe contrast $\sim 4.3\%$ and $\omega/2\pi \approx 243.7\,\mathrm{MHz}$, we estimate $\sqrt{\langle\eta^2\rangle} \approx 19\,\mathrm{MHz}$, consistent with the measured injected noise standard deviation of $\sqrt{\langle\eta^2_{\mathrm{meas}}\rangle} \approx 16\,\mathrm{MHz}$.

We emphasize that the result for relaxation experiments stands in contrast to our result for Ramsey experiments, for which purity oscillations have a noise-axis-dependent period [Fig. 7.5(e,f,g)]. We confirmed the lack of noise-axis dependence for relaxation experiments with quasistatic noise in further numerical simulations. We also find that for polarized Markovian noise treated with the Lindblad equation as in Section 7.2.2 with $|\Psi_0\rangle = |1\rangle$, relaxation experiments result in purely exponential purity decays with no noise axis dependence.

7.4.5 Validation of Approximate Purity

In this section, we justify the correspondence of approximate and exact purity for all experiments presented. First, we experimentally confirmed the correspondence of γ_{approx} and γ by performing state tomography after Ramsey experiments with and without injected charge noise of the highest amplitude used in this work [Fig. 7.7]. We found that $|\gamma - \gamma_{\mathrm{approx}}| \leq 1.5\%$ (relative error bounded by 2.1%) for free precession times up to $12.6\,\tau_{\mathrm{L}}$, validating that γ_{approx} can act as a reliable proxy for γ.

We further justify the use of γ_{approx} analytically. In an ideal Ramsey experiment with the qubit initially in its ground state, the first $\pi/2$ pulse (about the $\hat{y}$ axis, without loss of generality) transfers the qubit state to the $\hat{x}$ axis of the Bloch sphere. Subsequently, the Bloch vector rotates about the $\hat{z}$ axis as the qubit undergoes Larmor precession in the

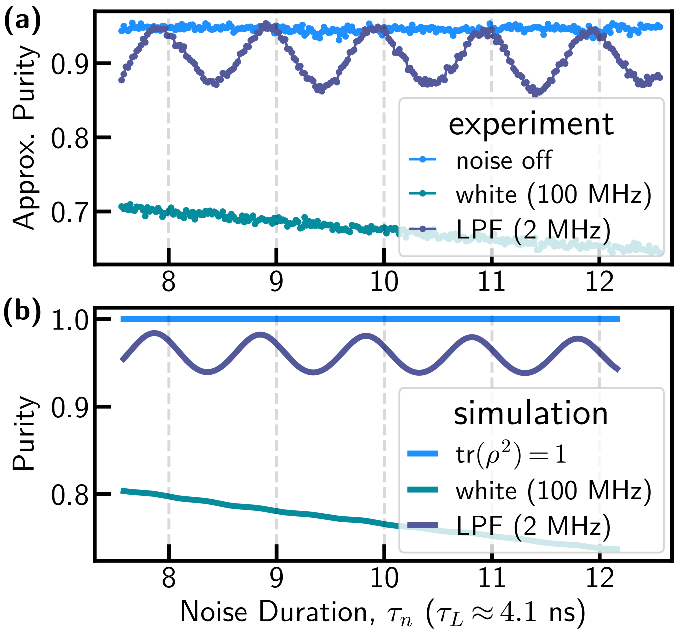

Figure 7.6: **Purity oscillations in relaxation experiments. (a)** Experiment and **(b)** simulation for relaxation experiments with $|\Psi_0\rangle = |1\rangle$ and injected noise along σ_y, $\tau_b = 5\,\mathrm{ns}$. Traces are shown for the case of zero noise (light blue), white noise up to 100 MHz (green), and 2 MHz low-pass filtered noise (dark blue). Low-pass filtered noise perturbs the quantization axis of the qubit, leading to purity oscillations at frequency f_{01} from the modified Larmor precession.

laboratory frame. In the frame co-rotating with the qubit, the qubit remains stationary and along the $\hat{x}$ axis. After waiting a set phase accumulation time, a second $\pi/2$ pulse (about the same rotating-frame axis as the first) transfers the qubit state to the $\hat{z}$ axis. Assuming that the qubit maintains constant frequency during the phase accumulation time, the length of the Bloch vector at the end of the sequence is given entirely by the expectation value $\langle\sigma_z\rangle$:

$$\gamma = \frac{\langle\sigma_z\rangle^2}{2} + \frac{1}{2} = \gamma_{\mathrm{approx}}. \tag{7.27}$$

If the qubit is instead subject to a frequency shift during the evolution time, the Bloch vector immediately before the final $\pi/2$ pulse will be slightly misaligned from the $\hat{x}$ axis by an angle θ. In this case, the approximate purity deviates from the exact purity:

$$|\gamma - \gamma_{\mathrm{approx}}| = \frac{r^2 \sin^2(\theta)}{2}, \tag{7.28}$$

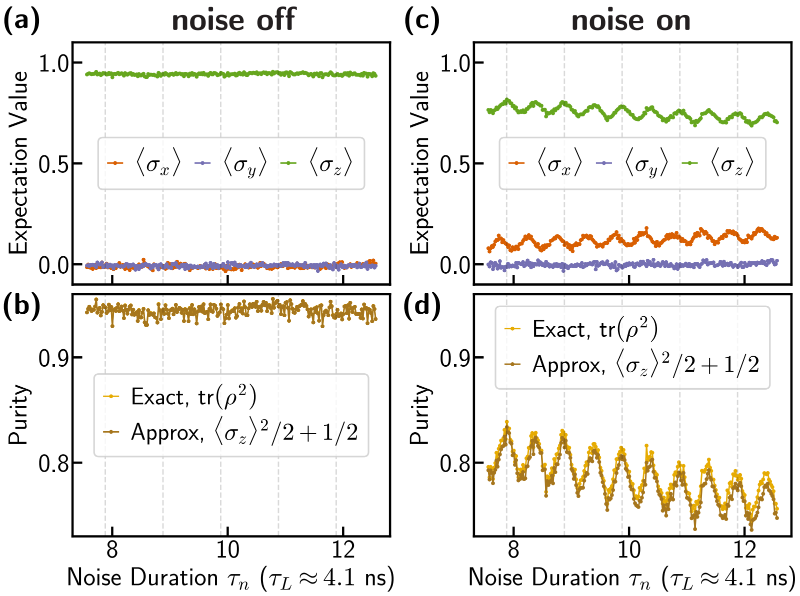

Figure 7.7: **Approximate and exact purity.** All data shown are for free-induction-decay experiments with injected 100 MHz white noise along $\hat{n} \propto \sigma_y$ and buffer time $\tau_b = 5\,\text{ns}$. **(a)** State tomography and extracted **(b)** exact purity, $(\langle\sigma_x\rangle^2 + \langle\sigma_y\rangle^2 + \langle\sigma_z\rangle^2)/2 + 1/2$, and approximate purity, $\langle\sigma_z\rangle^2/2 + 1/2$, with noise amplitude set to zero. **(c,d)** Similar to (a,b), for non-zero noise amplitude.

where $0 \le r \le 1$ is the length of the Bloch vector.

We measured the qubit frequency shift from injected charge noise of the highest amplitude used in this experiment, finding $|f_{01}^{\text{bare}} - f_{01}^{\text{noise}}| \lesssim 0.54\,\text{MHz}$. For such noise (as used in Fig. 7.3, Fig. 7.5, Fig. 7.7, and Fig. 7.6) with durations up to $\tau_n \lesssim 12.56\tau_L$, we expect misalignments from the frequency shift of $\theta \lesssim 10°$ and resulting errors in the approximate purity bounded by $|\gamma - \gamma_{\text{approx}}| \le 1.5\%$, consistent with measured data.

We found that injected flux noise significantly modified the qubit frequency. For the configuration used in Fig. 7.4 with simultaneously injected charge and flux noise, we measured a frequency shift of $|f_{01}^{\text{bare}} - f_{01}^{\text{noise}}| \approx 4.6 \pm 0.015\,\text{MHz}$. Accordingly, we adjusted the final $\pi/2$-pulse phase for the experiments in Fig. 7.4 to account for the measured detuning. The frequency uncertainty from the fit leads to an error bound of the approximate purity of $< 10^{-4}$ for noise durations up to $15\tau_L$.

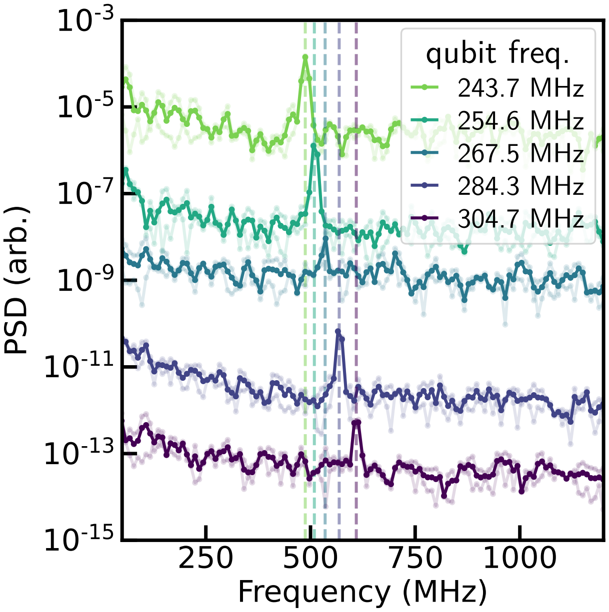

Figure 7.8: **Purity oscillations vs. qubit frequency.** Each trace corresponds to a different flux bias, and represents a PSD calculated with Welch's method for a free-induction decay experiment with injected 100 MHz white noise along $\hat{n} \propto \sigma_y$ and $\tau_b = 5\,\mathrm{ns}$. Traces are artificially offset for clarity. Dashed lines correspond to $2f_{01}$.

7.4.6 Frequency Dependence of Purity Oscillations

In order to validate that the frequency of the purity oscillations was determined by the twice the qubit frequency, we measured purity oscillations from injected charge noise as a function of external flux bias in a small window around $\Phi_{\mathrm{ext}} = 0.5\Phi_0$ corresponding to qubit frequencies $243.7\,\mathrm{MHz} \leq f_{01} \leq 304.7\,\mathrm{MHz}$ [Fig. 7.8]. At each external flux bias, readout pointers, the qubit frequency, and the $\pi/2$-pulse amplitude was recalibrated. We observed the purity oscillation frequency matched $2f_{01}$ at all measured biases, consistent with the oscillations being generated by the anisotropic noise.

7.4.7 Simulations of Experiments

Before detailing our simulations, we first emphasize that at the level of qualitative behavior (e.g., presence or absence of purity oscillations), all simulated signals did not depend sensitively on the noise distribution (bimodal, Gaussian, or uniform) or on the high-frequency limit of the noise PSD ($1/f^2$ or $1/f^4$), consistent with the analytical results of Section 7.2.1 and Section 7.2.2.

To simulate our experimental results, we first extracted the correlation time of the measured injected noise for each configuration. We then modelled the noise as an ideal random telegraph signal (RTS) with average switching rate determined by the correlation time, and amplitude determined by the cutoff values (defined as the center of the peaks at the edges of the distributions in Fig. 7.2). For each simulated experiment, we generated several instances of noise $\eta(t)$ and calculated the noise-averaged purity as $\mathrm{tr}\left(\rho^2\right)$, where $\rho = \langle \rho_{\eta(t)} \rangle$ and $\langle \cdot \rangle$ represents the noise-ensemble average. We plot simulated experiments corresponding to Fig. 7.3 and Fig. 7.4 in Fig. 7.9. We find agreement of the qualitative behavior between simulation and experiment; anisotropic noise leads to purity oscillations at twice the qubit frequency, with revivals (monotonic decay) generated by noise with a long (short) correlation time [Fig. 7.9(a)], and extinction of the oscillations for noise which is isotropically distributed in the Bloch-sphere XY plane [Fig. 7.9(b)]. We find quantitative order-of-magnitude agreement of the oscillation fringe contrast and decay magnitudes between simulation and experiment. We note that differences can arise from a variety of sources including state preparation and measurement (SPAM) errors, differences between the simulated (ideal RTS) and experimentally realized noise, and discrepancies between the approximate purity (reported for experiments) and true purity (reported for simulations).

7.5 Discussion

We now discuss our results in the context of quantum information applications, where understanding and mitigating noise [45, 73, 302] and further exploring dynamics beyond the RWA [61, 72, 275] are of high interest due to, e.g., advancing metrology and quantum error correction experiments. For superconducting qubits in particular, decoherence mechanisms are associated with microscopic models that couple to either the charge or flux degrees of

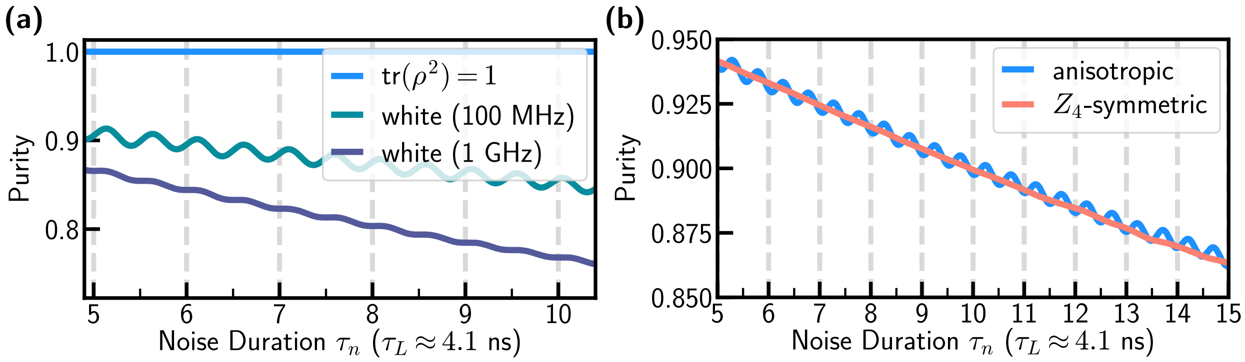

Figure 7.9: **Simulations of Fig. 7.3 and Fig. 7.4.** The simulation methodology is described in Section 7.3.2. **(a)** Simulated Ramsey experiments as in Fig. 7.3, with injected σ_y noise in three configurations: (1) no noise, represented by a pure state with $\mathrm{tr}\,(\rho^2) = 1$ (light blue), (2) low-frequency white noise up to 100 MHz $< f_{01}$ (turquoise), and (3) broadband white noise up to 1 GHz $> f_{01}$ (dark blue). **(b)** Simulated Ramsey experiments as in Fig. 7.4, with Z_4-symmetric noise (uncorrelated equal-amplitude noise along σ_x and σ_y, red), and anisotropic noise (correlated equal-amplitude noise along σ_x and σ_y, blue).

freedom of a circuit [89]. The time-domain signatures explored in this work can potentially be used to determine if decoherence is due to noise that is anisotropic (i.e., primarily coupled to either charge or flux), and whether the noise dynamics approach either the Markovian or quasistatic limits. In this experiment, utilizing a low-frequency fluxonium qubit, no purity oscillations were observed in the case of no injected noise; this may be due to the weakness of the native noise resulting in an oscillation too small to detect, or the low-frequency nature of the qubit which results in decoherence from both $1/f$ flux noise and dielectric loss [303, 304]. For high-frequency qubits such as conventional transmons or fluxonium qubits operated far from the degeneracy point, the dominant transverse loss mechanism may be anisotropic due to, e.g., dominance of the charge or phase matrix element [54, 303], or different quantum-to-classical crossover frequencies of charge- and flux-noise spectra [305, 306]. However, finer time resolution would be required to observe the oscillations due to shorter qubit Larmor periods. In general, the signatures explored in this work may be used to validate the understanding of qubit decoherence in other platforms. One potential difficulty of observing such signatures from the native coherence-limiting noise is state preparation: if the noise is present during state preparation, differing initial states shot-to-shot may obfuscate oscillations. For superconducting qubits, this difficulty may be circumvented by preparing initial states at at a low-noise point (e.g., where the charge or flux matrix element is suppressed), and leveraging fast-flux control to probe decoherence where transverse noise is expected to be anisotropic.

7.6 Conclusion

In summary, we investigated qubit decoherence under the effect of transverse noise that is anisotropic (linearly polarized) in the lab frame. We have established that, when initially prepared in a superposition state, the state purity $\mathrm{tr}\,(\rho^2)$ displays an oscillatory component at twice the qubit frequency [72]; when the qubit is aligned with (perpendicular to) the noise, the qubit state is insensitive (sensitive) to noise-induced rotations. We verified that the oscillations are mitigated for noise that is isotropically distributed in the Bloch sphere XY plane and explored the oscillation dependence on the noise axis and power spectral density. We further elucidated our results with analytical models for purity decay in the presence of noise in the quasistatic and Markovian limits. Our results establish the impact of transverse noise anisotropy on qubit decoherence, providing a new time-domain signature for probing the anisotropy of coherence-limiting noise in experiments.

Chapter 8

Conclusion

In this thesis, we presented three novel results: (1) the characterization of low-frequency flux noise in superconducting qubits as a function of applied magnetic field, (2) the suppression of counter-rotating errors for fast gates with low-frequency qubits, and (3) the observation of qubit-state purity oscillations from anisotropic transverse noise. In this chapter, we offer a broad outlook for this work.

Our first result, presented in Chapter 5, primarily offers a new experimental benchmark for microscopic theories of flux noise. Qualitatively, our results are consistent with the suppression of spin-diffusion processes which are generically blamed for high-frequency flux noise. The low-frequency $1/f$ to approximately Lorentzian transition of the PSD below 1 Hz may indicate changing spin-cluster sizes with field. Further experiments are required to validate these interpretations. The $1/f$ to Lorentzian transition in particular was reproduced theoretically with no notion of spin-spin interactions or clustering [232]. Despite this model's feature of a similar lineshape transition with applied field, it does not predict a net increase in the low-frequency noise amplitude or the suppression of higher-frequency flux noise with increasing field, both of which were observed in our experiment. This motivates the need for further flux-noise models which accommodate applied magnetic fields.

Our second result, presented in Chapter 6, opens the door to Rabi gates as fast as one

Larmor period. For low-frequency qubits, our techniques enable fast, high-fidelity single-qubit gates which do not suffer from counter-rotating errors. Our commensurate technique in particular does not require any additional hardware resources or calibration overhead relative to conventional Rabi gates, and can be utilized in any platform. We expect this technique to be immediately beneficial for fluxonium-based quantum processors. Such processors are currently of high interest due to several recent promising results displaying state-of-the-art single- and two-qubit gate fidelities [56, 59, 255]. Our result, comprising record single-qubit gate fidelity for the superconducting qubit platform, further increases the attractiveness fluxonium-based quantum computing. In addition, our single-qubit gate fidelities begin to approach those of the trapped ion platform [64, 307].

Beyond fluxonium single-qubit gates, our commensurate gate technique may be suitable for the control of low-frequency composite qubits with applications as erasure qubits with favorable error-correction properties [308, 309], or to benefit other low-frequency microwave interactions including parametric gates between transmon qubits [310]. Our circular driving method may also inspire solutions to measurement-induced state transitions (MIST) [275], which represents a significant barrier to scaling error-correcting codes. Beyond superconducting qubits, our methods may also benefit ultrafast gates in semiconductor spin qubits, which have displayed Rabi rates comparable to the Larmor frequency [311–313]. We also note that the experimental capability to perform commensurate pulses in the optical domain is already present and comprises an important experimental technique, referred to as carrier-envelope phase stabilization for few-cycle optical pulses [261, 262].

Our third result, presented in Chapter 7, we hope will be used to characterize native (rather than injected) coherence-limiting noise across experimental platforms. In particular, the observation of such oscillations should be feasible for low-frequency qubits with experimental access to Larmor-scale dynamics, which are realized with physically distinct noise sources coupled to different Bloch-sphere axes. This arises naturally for low-frequency superconducting qubits such as the fluxonium. However, high-coherence samples, such as the one used in our experiment, would yield extremely small oscillations. Purity oscillations are likely to be observed in much lower-coherence samples. As an estimate, we can (very roughly) approximate a purity decay under Markovian noise as N purity steps of equal amplitude in a total time $\Delta T = N\tau_L/2$ where τ_L is the Larmor period. For a low-frequency qubit which equilibrates to the maximally mixed state, starting along the z axis would result in a purity decay step size of $0.5/N = 0.25\tau_L/\Delta T$. For the step size to be 1%, we would need the total decay time to be $25\tau_L$. This estimate is not encouraging, but we hypothesize this signature might be found in extremely low-frequency qubits with transverse noise bias [314].

Appendix A

Infinite Product Expression for the Gaussian Function

In this appendix, we provide a derivation and extended results for the infinite product expression used in the fitting of calibration data as in Chapter 6.4.3. Motivated by the surprisingly effective Gaussian fitting of the data, the contents of this appendix blossomed from a quick and fruitful collaboration with my mathematically-oriented colleagues Samuel C. Alipour-Fard and David C. Newsome. Our main result is an infinite-product expression for the Gaussian function,

$$\lim_{N\to\infty}\prod_{n=1}^{N}\cos\left(\frac{n}{N^{1+p}}\,x\right)=\begin{cases}\chi_0(x) & \text{if } 0<p<1/2,\\ e^{-x^2/6}, & \text{if } p=1/2,\\ 1, & \text{if } p>1/2,\end{cases}\tag{A.1}$$

where $\chi_0(x) = 1$ if $x = 0$, 0 if $x \neq 0$. We plot Eq. (A.1) in Fig. A.1(a).

Our second main result is the extension of Eq. (A.1) for a general infinitely differentiable function $f(x)$ satisfying $f(0) = 1$ and with $k > 0$ the smallest integer such that $f^{(k)}(0) \neq 0$,

$$\lim_{N\to\infty} \prod_{n=1}^{N} f\left(\frac{n}{N^{1+\frac{1}{k}}} x\right) = \exp\left(\frac{f^{(k)}(0)}{(k+1)!} x^k\right). \tag{A.2}$$

As an example, we plot Eq. (A.2) with $f(x) = 1 - \sin(x)$, where $k = 1$ and $f^1(0) = -1$ in Fig. A.1(b).

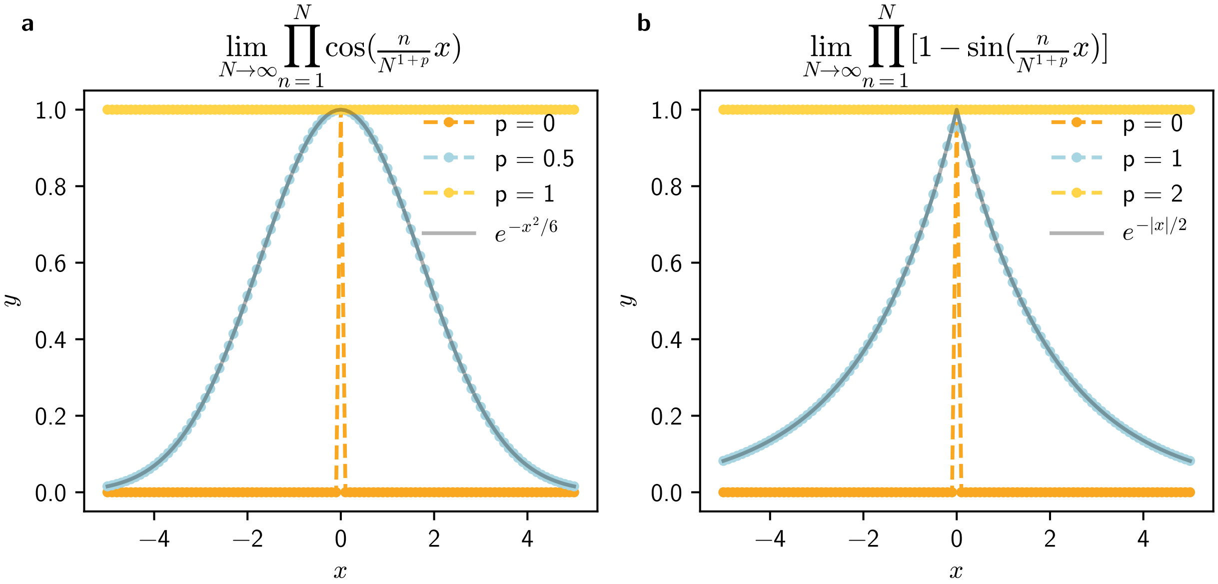

Figure A.1: **(a)** Plots of Eq. (A.1). **(b)** Plots of Eq. (A.2) for $f(x) = 1 - \sin(x)$. For both panels, $N = 10^6$.

A.1 Proof of Eq. (A.1)

Fix $p > 0$. For $N \in \mathbb{N}$, let

$$f_N(x) \coloneqq \prod_{n=1}^{N} \cos\left(\frac{n}{N^{1+p}} x\right).$$

Define the function f as the pointwise limit

$$f(x) \coloneqq \lim_{N\to\infty} f_N(x).$$

We aim to prove the following theorem:

Theorem 1. *For every $x \in \mathbb{R}$, $f(x)$ exists and specifically,*

$$f(x) = \begin{cases} \chi_0, & \text{if } 0 < p < 1/2, \\ e^{-x^2/6}, & \text{if } p = 1/2, \\ 1, & \text{if } p > 1/2, \end{cases} \tag{A.3}$$

where χ_0 is the indicator function defined by

$$\chi_0(x) \coloneqq \begin{cases} 1, & x = 0, \\ 0, & x \neq 0. \end{cases}$$

Proof

It is immediately clear that $f(0) = 1$ for any p, thus we focus on $x \neq 0$. Given that f_N is even for all N, it suffices to demonstrate the result for $x > 0$. Fix $x > 0$.

The proof strategy relies on the equality

$$f(x) = \exp\left(\lim_{N\to\infty} \log(f_N(x))\right), \tag{A.4}$$

which is a consequence of the continuity of the exponential function. Rewrite the limit as

$$\lim_{N\to\infty} \log(f_N(x)) = \lim_{N\to\infty} N \cdot g_N(z_N),$$

where

$$z_N \coloneqq \frac{x}{N^p},$$
$$g_N(z) \coloneqq \sum_{n=1}^{N} \frac{1}{N} \log\left(\cos\left(\frac{n}{N} z\right)\right).$$

Note that for sufficiently large N, $0 \leq z_N \leq 1$.

Step 1

First, we establish that

$$\lim_{N\to\infty} N \cdot g_N(z_N) = \lim_{N\to\infty} N \cdot I(z_N), \tag{A.5}$$

where

$$I(z) \coloneqq \int_0^1 \log(\cos(uz))\,\mathrm{d}u.$$

To demonstrate this, note that $g_N(z)$ acts as a right Riemann sum for the integral $I(z)$. Thus, we can express

$$g_N(z) = I(z) + E_N(z),$$

where $E_N(z)$ is an error term bounded by

$$|E_N(z)| \leq \frac{1}{2N} \max_{0\leq u\leq 1} \left| \frac{\mathrm{d}}{\mathrm{d}u} \log(\cos(uz)) \right| = \frac{\tan(z)z}{2N},$$

which holds for $0 \leq z \leq 1$. Therefore,

$$\lim_{N\to\infty} N \cdot g_N(z_N) = \lim_{N\to\infty} N \cdot I(z_N) + \lim_{N\to\infty} N \cdot E_N(z_N).$$

The desired result follows from observing that

$$\left| \lim_{N\to\infty} N \cdot E_N(z_N) \right| \leq \lim_{N\to\infty} |N \cdot E_N(z_N)| \leq \lim_{N\to\infty} \frac{\tan(z_N)z_N}{2} = 0.$$

Step 2

Next, we evaluate the limit

$$\lim_{N\to\infty} N \cdot I(z_N).$$

Expressing this as

$$N \cdot I(z_N) = N \int_0^1 \log(\cos(uz))\,\mathrm{d}u = \frac{N}{z_N} \int_0^{z_N} \log(\cos(u))\,\mathrm{d}u.$$

By Taylor's theorem, for $u \in [0, 1]$,

$$\log(\cos(u)) = -\frac{1}{2}u^2 + h(u)u^4,$$

where $h(u)$ is continuous and satisfies

$$\lim_{u \to 0} h(u) = 0.$$

Thus,

$$N \cdot I(z_N) = -\frac{N z_N^2}{6}(1 + H_N),$$

where H_N is defined as

$$H_N \coloneqq -\frac{6}{z_N^3} \int_0^{z_N} h(u)u^4\,\mathrm{d}u.$$

The bound on H_N is

$$|H_N| \le \frac{6}{z_N^3} \max_{0 \le u \le z_N} |h(u)| \int_0^{z_N} u^4\,\mathrm{d}u = \frac{6}{5} z_N^2 \max_{0 \le u \le z_N} |h(u)|.$$

It follows that $H_N \to 0$ as $N \to \infty$, leading to

$$\lim_{N \to \infty} N \cdot I(z_N) = \lim_{N \to \infty} -\frac{N z_N^2}{6}(1 + H_N) = \lim_{N \to \infty} -\frac{N z_N^2}{6} = -\frac{x^2}{6} N^{1-2p}.$$

Step 3

We have established that

$$\lim_{N\to\infty} \log(f_N(x)) = -\frac{x^2}{6}N^{1-2p} = \begin{cases} -\infty, & 0 < p < 1/2, \\ -x^2/6, & p = 1/2, \\ 0, & p > 1/2, \end{cases}$$

from which the theorem follows. $\square$

Proposition 1. *Let* f $\mathbb{R}\mathbb{R}$ *be a infinitely differentiable function such that* $f(0) = 1$. *Let* $k > 0$ *be the smallest integer such that*

$$f^{(k)}(0) \neq 0.$$

Then we have

$$\lim_{N\to\infty} \prod_{n=1}^{N} f\left(\frac{n}{N^{1+\frac{1}{k}}}x\right) = \exp\left(\frac{f^{(k)}(0)}{(k+1)!}x^k\right)$$

Appendix B

Commensurate Condition for Off-Resonant Pulses

In this appendix, we derive more general commensurate conditions, which ensure the uniformity of the qubit rotation for different pulse start times, polychromatic drives, and off-resonant drives.

Consider a qubit subjected to a linearly-polarized polychromatic pulse of duration t_g with carrier frequencies $\omega_i = \omega_{01} + \delta_i$ applied at a variable start time t_0

$$\frac{\hat{H}}{\hbar} = \omega_{01} \left|1\right\rangle \left\langle 1\right| + \sum_i \Omega_i(t - t_0) \cos(\omega_i t + \varphi) \left|0\right\rangle \left\langle 1\right| + h.c. \tag{B.1}$$

where $\Omega_i(t' = t - t_0)$ denotes the pulse envelope of the i-th frequency component such that $\Omega_i(t') = 0$ for $t' < 0$ and $t' > t_g$ for all i. Rewriting the Hamiltonian in terms of t' and performing the standard rotating-frame transformation co-rotating with the qubit at frequency ω_{01}, we obtain

$$\frac{\hat{\tilde{H}}}{\hbar} = \sum_i \frac{\Omega_i(t')}{2} \left[e^{i(\delta_i t + \varphi)} + e^{-i(\omega_{\Sigma,i} t + \varphi)}\right] \left|0\right\rangle \left\langle 1\right| + h.c. \tag{B.2}$$

$$= e^{i\varphi} \sum_i \frac{e^{i\delta_i t_0} \Omega_i(t')}{2} \left[e^{i\delta_i t'} + e^{-i(\omega_{\Sigma,i} t' + 2\omega_i t_0 + 2\varphi)}\right] \left|0\right\rangle \left\langle 1\right| + h.c., \tag{B.3}$$

with $\omega_{\Sigma,i} \equiv \omega_i + \omega_{01}$ and $\delta_i = \omega_i - \omega_{01}$. The unitary generated by the pulse is given by

$$\hat{\tilde{U}}(t' = t_g, t' = 0) = \exp\left[-\frac{i}{\hbar}\int_0^{t_g} \hat{\tilde{H}}(t', t_0)\, dt'\right]. \tag{B.4}$$

We now derive the constraints on t_0 such that all pulses will implement the same rotation given by Eq. (B.4), in a few cases of interest.

B.1 Monochromatic, resonant drive.

In this case, $\delta = 0$ and Eq. (B.3) reduces to Eq. (6.13). To regularize the unitary for all pulse start times t_0 of a given φ, we require

$$t_0 \in \{n\tau_L/2,\, n \in \mathbb{N}\}. \tag{B.5}$$

B.2 Monochromatic, off-resonant drive.

In this case, $\delta \neq 0$ and Eq. (B.3) reduces to

$$\frac{\hat{\tilde{H}}}{\hbar} = e^{i(\varphi + \delta t_0)} \frac{\Omega(t')}{2}\left[e^{i\delta t'} + e^{-i(\omega_\Sigma t' + 2\omega_d t_0 + 2\varphi)}\right] |0\rangle \langle 1| + h.c.$$

In contrast to the resonant case, we now have an additional t_0 dependence in the phase prefactor which affects the axis of rotation. However, this prefactor is a constant with respect to the t' integration of Eq. (B.4). To regularize the unitary for all pulse start times t_0, it suffices to regularize the counter-rotating term with

$$t_0 \in \{n\tau_d/2,\, n \in \mathbb{N}\}, \tag{B.6}$$

where $\tau_d = 2\pi/\omega_d$ is the drive period. The axis of rotation can be corrected for with a subsequent Z rotation.

B.3 Polychromatic, off-resonant drive.

In this case, we now have a collection of non-zero δ_i. In contrast to the previous case, the prefactors $e^{i\delta_i t_0} = e^{i(\omega_i - \omega_{01})t_0}$ for all terms of the sum in Eq. (B.3) give rise to interference of the drive tones[1]. For this interference to be consistent, we require

$$t_0 \in \{2n_i\tau_i/2,\, n_i \in \mathbb{N}\ \forall i\} \cup \{(2n_i+1)\tau_i/2,\, n_i \in \mathbb{N}\ \forall i\}, \tag{B.7}$$

where $\tau_i = 2\pi/\omega_i$. These two sets correspond to the pulse unitary having an additional Z rotation of 0 or π, respectively. This condition also ensures invariance of the counter-rotating terms.

---

[1] The $e^{-i\omega_{01}t_0}$ phase applies to all terms consistently, and can be factored out and interpreted as a shift of the axis of rotation.

References

[1] Richard Feynman. *The Character of Physical Law*. Cambridge, Massachusetts: MIT Press, Jan. 1, 2001.

[2] Max Planck. “Ueber das Gesetz der Energieverteilung im Normalspectrum”. *Annalen der Physik* 309.3 (1901), pp. 553–563.

[3] A. Einstein. “Über einen die Erzeugung und Verwandlung des Lichtes betreffenden heuristischen Gesichtspunkt”. *Annalen der Physik* 322.6 (1905), pp. 132–148.

[4] N. Bohr. “The Structure of the Atom”. *Nature* 112.2801 (July 1923), pp. 29–44.

[5] Paul Adrien Maurice Dirac. *The Principles of Quantum Mechanics*. Clarendon Press, 1981.

[6] P. W. Anderson. “More Is Different”. *Science* 177.4047 (Aug. 4, 1972), pp. 393–396.

[7] J. G. Bednorz and K. A. Müller. “Possible highTc superconductivity in the BaLaCuO system”. *Zeitschrift für Physik B Condensed Matter* 64.2 (June 1, 1986), pp. 189–193.

[8] Henrik Bruus and Karsten Flensberg. *Many-body quantum theory in condensed matter physics: An Introduction*. Aug. 15, 2002.

[9] D. J. Thouless. *The Quantum Mechanics of Many-Body Systems: Second Edition*. Courier Corporation, Dec. 3, 2013.

[10] Román Orús. “A practical introduction to tensor networks: Matrix product states and projected entangled pair states”. *Annals of Physics* 349 (Oct. 1, 2014), pp. 117–158.

[11] Justus A. Calvin, Chong Peng, Varun Rishi, Ashutosh Kumar, and Edward F. Valeev. “Many-Body Quantum Chemistry on Massively Parallel Computers”. *Chemical Reviews* 121.3 (Feb. 10, 2021), pp. 1203–1231.

[12] Yuri Manin. *Computable and uncomputable*. Sovetskoye Radio, Moscow, 1980.

[13] Richard P. Feynman. “Simulating physics with computers”. *International Journal of Theoretical Physics* 21.6 (June 1, 1982), pp. 467–488.

[14] David P. DiVincenzo. “The Physical Implementation of Quantum Computation”. *Fortschritte der Physik* 48.9 (2000), pp. 771–783.

[15] I. M. Georgescu, S. Ashhab, and Franco Nori. “Quantum simulation”. *Reviews of Modern Physics* 86.1 (Mar. 10, 2014), pp. 153–185.

[16] Michael A. Nielsen and Isaac L. Chuang. *Quantum computation and quantum information*. 10th anniversary ed. Cambridge ; New York: Cambridge University Press, 2010.

[17] A. Morvan et al. “Phase transitions in random circuit sampling”. *Nature* 634.8033 (Oct. 2024), pp. 328–333.

[18] Peter W. Shor. “Polynomial-Time Algorithms for Prime Factorization and Discrete Logarithms on a Quantum Computer”. *SIAM Journal on Computing* 26.5 (Oct. 1997), pp. 1484–1509.

[19] R. L. Rivest, A. Shamir, and L. Adleman. “A method for obtaining digital signatures and public-key cryptosystems”. *Commun. ACM* 21.2 (Feb. 1, 1978), pp. 120–126.

[20] Alexander M. Dalzell et al. *Quantum algorithms: A survey of applications and end-to-end complexities*. Oct. 4, 2023.

[21] Thomas Schuster, Chao Yin, Xun Gao, and Norman Y. Yao. *A polynomial-time classical algorithm for noisy quantum circuits*. July 17, 2024.

[22] Peter W. Shor. "Scheme for reducing decoherence in quantum computer memory". *Physical Review A* 52.4 (Oct. 1, 1995), R2493–R2496.

[23] A. Yu Kitaev. *Fault-tolerant quantum computation by anyons*. July 9, 1997.

[24] *A Quantum Engineer's Guide to Superconducting Qubits: Applied Physics Reviews: Vol 6, No 2*. https://aip.scitation.org/doi/10.1063/1.5089550.

[25] Dolev Bluvstein et al. "Logical Quantum Processor Based on Reconfigurable Atom Arrays". *Nature* 626.7997 (Feb. 2024), pp. 58–65.

[26] Colin D. Bruzewicz, John Chiaverini, Robert McConnell, and Jeremy M. Sage. "Trapped-ion quantum computing: Progress and challenges". *Applied Physics Reviews* 6.2 (May 29, 2019), p. 021314.

[27] Sergei Slussarenko and Geoff J. Pryde. "Photonic quantum information processing: A concise review". *Applied Physics Reviews* 6.4 (Oct. 14, 2019), p. 041303.

[28] J. R. Weber, W. F. Koehl, J. B. Varley, A. Janotti, B. B. Buckley, C. G. Van de Walle, and D. D. Awschalom. "Quantum computing with defects". *Proceedings of the National Academy of Sciences* 107.19 (May 11, 2010), pp. 8513–8518.

[29] Guido Burkard, Thaddeus D. Ladd, Andrew Pan, John M. Nichol, and Jason R. Petta. "Semiconductor spin qubits". *Reviews of Modern Physics* 95.2 (June 14, 2023), p. 025003.

[30] Google Quantum AI. "Quantum Error Correction below the Surface Code Threshold". *arXiv:2408.13687 [quant-ph]* (Aug. 2024).

[31] M. P. da Silva et al. "Demonstration of logical qubits and repeated error correction with better-than-physical error rates". *arXiv:2404.02280 [quant-ph]* (2024).

[32] A. G. Radnaev et al. *A universal neutral-atom quantum computer with individual optical addressing and non-destructive readout.* Aug. 20, 2024.

[33] Aaron J. Weinstein et al. “Universal logic with encoded spin qubits in silicon”. *Nature* 615.7954 (Mar. 2023), pp. 817–822.

[34] Héctor Bombín. “Single-Shot Fault-Tolerant Quantum Error Correction”. *Physical Review X* 5.3 (Sept. 28, 2015), p. 031043.

[35] Nikolas P. Breuckmann and Jens Niklas Eberhardt. “Quantum Low-Density Parity-Check Codes”. *PRX Quantum* 2.4 (Oct. 11, 2021), p. 040101.

[36] Hengyun Zhou, Chen Zhao, Madelyn Cain, Dolev Bluvstein, Casey Duckering, Hong-Ye Hu, Sheng-Tao Wang, Aleksander Kubica, and Mikhail D. Lukin. *Algorithmic Fault Tolerance for Fast Quantum Computing.* June 25, 2024.

[37] John M. Martinis, Michel H. Devoret, and John Clarke. “Energy-Level Quantization in the Zero-Voltage State of a Current-Biased Josephson Junction”. *Physical Review Letters* 55.15 (Oct. 7, 1985), pp. 1543–1546.

[38] V. Bouchiat, D. Vion, P. Joyez, D. Esteve, and M. H. Devoret. “Quantum coherence with a single Cooper pair”. *Physica Scripta* 1998 (T76 Jan. 1, 1998), p. 165.

[39] Yu Nakamura, Yu A Pashkin, and Jaw Shen Tsai. “Coherent control of macroscopic quantum states in a single-Cooper-pair box”. *Nature* 398.6730 (1999), pp. 786–788.

[40] Qingguang Zhang, Kyle W. Gheres, and Patrick J. Drew. “Origins of 1/f-like tissue oxygenation fluctuations in the murine cortex”. *PLoS Biology* 19.7 (July 15, 2021), e3001298.

[41] Edoardo Milotti. *1/f noise: a pedagogical review.* Apr. 12, 2002.

[42] Dietrich Wolf. “1/f-Noise”. In: *Noise in Physical Systems.* Ed. by Dietrich Wolf. Springer Series in Electrophysics. Berlin, Heidelberg: Springer, 1978, pp. 122–133.

[43] Richard F. Voss and John Clarke. "'1/fnoise' in music and speech". *Nature* 258.5533 (Nov. 1975), pp. 317–318.

[44] Frederick C. Wellstood, Cristian Urbina, and John Clarke. "Low-frequency noise in dc superconducting quantum interference devices below 1 K". *Applied Physics Letters* 50.12 (Mar. 23, 1987), pp. 772–774.

[45] E. Paladino, Y. M. Galperin, G. Falci, and B. L. Altshuler. "1/f Noise: Implications for Solid-State Quantum Information". *Reviews of Modern Physics* 86.2 (Apr. 2014), pp. 361–418.

[46] Lara Faoro and Lev B. Ioffe. "Microscopic Origin of Low-Frequency Flux Noise in Josephson Circuits". *Physical Review Letters* 100.22 (June 2008), p. 227005.

[47] Juan Atalaya, John Clarke, Gerd Schön, and Alexander Shnirman. "Flux 1/f$^{\alpha}$ noise in two-dimensional Heisenberg spin glasses: Effects of weak anisotropic interactions". *Physical Review B* 90.1 (July 2014), p. 014206.

[48] T. Lanting, M. H. Amin, C. Baron, M. Babcock, J. Boschee, S. Boixo, V. N. Smelyanskiy, M. Foygel, and A. G. Petukhov. "Probing Environmental Spin Polarization with Superconducting Flux Qubits" (Apr. 2020).

[49] T. Lanting, M. H. Amin, A. J. Berkley, C. Rich, S.-F. Chen, S. LaForest, and Rogério de Sousa. "Evidence for Temperature-Dependent Spin Diffusion as a Mechanism of Intrinsic Flux Noise in SQUIDs". *Physical Review B* 89.1 (Jan. 2014), p. 014503.

[50] José Alberto Nava Aquino and Rogério de Sousa. *Model for 1/f Flux noise in Superconducting Aluminum Devices: Impact of External Magnetic Fields*. Feb. 23, 2023.

[51] I. I. Rabi. "Space Quantization in a Gyrating Magnetic Field". *Physical Review* 51.8 (Apr. 15, 1937), pp. 652–654.

[52] F. Bloch and A. Siegert. “Magnetic Resonance for Nonrotating Fields”. *Phys. Rev.* 57.6 (Mar. 1940), pp. 522–527.

[53] F. Motzoi, J. M. Gambetta, P. Rebentrost, and F. K. Wilhelm. “Simple Pulses for Elimination of Leakage in Weakly Nonlinear Qubits”. *Phys. Rev. Lett.* 103 (11 Sept. 2009), p. 110501.

[54] Jens Koch, Terri M. Yu, Jay Gambetta, A. A. Houck, D. I. Schuster, J. Majer, Alexandre Blais, M. H. Devoret, S. M. Girvin, and R. J. Schoelkopf. “Charge-insensitive qubit design derived from the Cooper pair box”. *Phys. Rev. A* 76 (4 Oct. 2007), p. 042319.

[55] Vladimir E Manucharyan, Jens Koch, Leonid I Glazman, and Michel H Devoret. “Fluxonium: Single cooper-pair circuit free of charge offsets”. *Science* 326.5949 (2009), pp. 113–116.

[56] Helin Zhang, Srivatsan Chakram, Tanay Roy, Nathan Earnest, Yao Lu, Ziwen Huang, D. K. Weiss, Jens Koch, and David I. Schuster. “Universal Fast-Flux Control of a Coherent, Low-Frequency Qubit”. *Phys. Rev. X* 11 (1 Jan. 2021), p. 011010.

[57] Long B. Nguyen et al. “Blueprint for a High-Performance Fluxonium Quantum Processor”. *PRX Quantum* 3 (3 Aug. 2022), p. 037001.

[58] Leon Ding et al. “High-Fidelity, Frequency-Flexible Two-Qubit Fluxonium Gates with a Transmon Coupler”. *Physical Review X* 13.3 (Sept. 2023), p. 031035.

[59] Wei-Ju Lin, Hyunheung Cho, Yinqi Chen, Maxim G. Vavilov, Chen Wang, and Vladimir E. Manucharyan. *24 days-stable CNOT-gate on fluxonium qubits with over 99.9% fidelity.* July 22, 2024.

[60] Zhiyuan Li et al. “Error per Single-Qubit Gate below 10-4 in a Superconducting Qubit”. *npj Quantum Information* 9.1 (Nov. 2023), pp. 1–6.

[61] David A. Rower et al. “Suppressing Counter-Rotating Errors for Fast Single-Qubit Gates with Fluxonium”. *arXiv:2406.08295 [quant-ph]* (June 2024).

[62] Cheng Sheng, Xiaodong He, Peng Xu, Ruijun Guo, Kunpeng Wang, Zongyuan Xiong, Min Liu, Jin Wang, and Mingsheng Zhan. “High-Fidelity Single-Qubit Gates on Neutral Atoms in a Two-Dimensional Magic-Intensity Optical Dipole Trap Array”. *Physical Review Letters* 121.24 (Dec. 10, 2018), p. 240501.

[63] W. I. L. Lawrie, M. Rimbach-Russ, F. van Riggelen, N. W. Hendrickx, S. L. de Snoo, A. Sammak, G. Scappucci, J. Helsen, and M. Veldhorst. “Simultaneous single-qubit driving of semiconductor spin qubits at the fault-tolerant threshold”. *Nature Communications* 14.1 (June 19, 2023), p. 3617.

[64] T. P. Harty, D. T. C. Allcock, C. J. Ballance, L. Guidoni, H. A. Janacek, N. M. Linke, D. N. Stacey, and D. M. Lucas. “High-Fidelity Preparation, Gates, Memory, and Readout of a Trapped-Ion Quantum Bit”. *Physical Review Letters* 113.22 (Nov. 24, 2014), p. 220501.

[65] Fei Yan et al. “Distinguishing Coherent and Thermal Photon Noise in a Circuit Quantum Electrodynamical System”. *Physical Review Letters* 120.26 (June 29, 2018), p. 260504.

[66] Fei Yan, Simon Gustavsson, Jonas Bylander, Xiaoyue Jin, Fumiki Yoshihara, David G. Cory, Yasunobu Nakamura, Terry P. Orlando, and William D. Oliver. “Rotating-frame relaxation as a noise spectrum analyser of a superconducting qubit undergoing driven evolution”. *Nature Communications* 4.1 (Aug. 15, 2013), p. 2337.

[67] Jonas Bylander, Simon Gustavsson, Fei Yan, Fumiki Yoshihara, Khalil Harrabi, George Fitch, David G. Cory, Yasunobu Nakamura, Jaw-Shen Tsai, and William D. Oliver. “Noise Spectroscopy through Dynamical Decoupling with a Superconducting Flux Qubit”. *Nature Physics* 7.7 (July 2011), pp. 565–570.

[68] Peter Zoller and C. W. Gardiner. *Quantum Noise in Quantum Optics: the Stochastic Schr\"odinger Equation.* Feb. 12, 1997.

[69] Harry Levine, Dolev Bluvstein, Alexander Keesling, Tout T. Wang, Sepehr Ebadi, Giulia Semeghini, Ahmed Omran, Markus Greiner, Vladan Vuletić, and Mikhail D. Lukin. "Dispersive Optical Systems for Scalable Raman Driving of Hyperfine Qubits". *Physical Review A* 105.3 (Mar. 2022), p. 032618.

[70] Charles P. Slichter. *Principles of Magnetic Resonance.* Red. by Manuel Cardona, Peter Fulde, Klaus von Klitzing, Hans-Joachim Queisser, and Helmut K. V. Lotsch. Vol. 1. Springer Series in Solid-State Sciences. Berlin, Heidelberg: Springer Berlin Heidelberg, 1990.

[71] C. W. Gardiner and M. J. Collett. "Input and Output in Damped Quantum Systems: Quantum Stochastic Differential Equations and the Master Equation". *Physical Review A* 31.6 (June 1985), pp. 3761–3774.

[72] Bassano Vacchini, Heinz-Peter Breuer, and Angelo Bassi, eds. *Advances in Open Systems and Fundamental Tests of Quantum Mechanics: Proceedings of the 684. WE-Heraeus-Seminar, Bad Honnef, Germany, 2–5 December 2018.* Vol. 237. Springer Proceedings in Physics. Cham: Springer International Publishing, 2019.

[73] David A. Rower et al. "Evolution of $1/f$ Flux Noise in Superconducting Qubits with Weak Magnetic Fields". *Physical Review Letters* 130.22 (May 2023), p. 220602.

[74] David A. Rower et al. *Qubit-State Purity Oscillations from Anisotropic Transverse Noise.* Sept. 18, 2024.

[75] David Isaac Schuster. "Circuit quantum electrodynamics". PhD thesis. Jan. 1, 2007.

[76] Amy Greene. "Calibration and Utilization of High-Fidelity Two-Qubit Operations". Thesis. Massachusetts Institute of Technology, Feb. 2023.

[77] Youngkyu Sung. "High-fidelity Two-qubit Gates and Noise Spectroscopy with Superconducting Qubits". Thesis. Massachusetts Institute of Technology, May 2022.

[78] Leon Ding. “Novel Gates with Superconducting Fluxonium Qubits”. Thesis. Massachusetts Institute of Technology, June 2023.

[79] Y. Nakamura, Yu A. Pashkin, and J. S. Tsai. “Coherent control of macroscopic quantum states in a single-Cooper-pair box”. *Nature* 398.6730 (Apr. 1999), pp. 786–788.

[80] Uri Vool and Michel H. Devoret. “Introduction to Quantum Electromagnetic Circuits”. *International Journal of Circuit Theory and Applications* 45.7 (July 2017), pp. 897–934.

[81] J. B. Johnson. “Thermal Agitation of Electricity in Conductors”. *Nature* 119.2984 (Jan. 1927), pp. 50–51.

[82] S. E. Rasmussen, K. S. Christensen, S. P. Pedersen, L. B. Kristensen, T. Bækkegaard, N. J. S. Loft, and N. T. Zinner. “The superconducting circuit companion – an introduction with worked examples”. *PRX Quantum* 2.4 (Dec. 14, 2021), p. 040204.

[83] Ulrik L. Andersen, Tobias Gehring, Christoph Marquardt, and Gerd Leuchs. “30 years of squeezed light generation”. *Physica Scripta* 91.5 (Apr. 2016), p. 053001.

[84] Jack Y. Qiu et al. “Broadband squeezed microwaves and amplification with a Josephson travelling-wave parametric amplifier”. *Nature Physics* 19.5 (May 2023), pp. 706–713.

[85] Dennis Willsch et al. “Observation of Josephson harmonics in tunnel junctions”. *Nature Physics* 20.5 (May 2024), pp. 815–821.

[86] John Clarke and Frank K. Wilhelm. “Superconducting quantum bits”. *Nature* 453.7198 (June 2008), pp. 1031–1042.

[87] S. M. Girvin, M. H. Devoret, and R. J. Schoelkopf. “Circuit QED and engineering charge-based superconducting qubits”. *Physica Scripta* 2009 (T137 Dec. 2009), p. 014012.

[88] Xiu Gu, Anton Frisk Kockum, Adam Miranowicz, Yu-xi Liu, and Franco Nori. "Microwave photonics with superconducting quantum circuits". *Physics Reports*. Microwave photonics with superconducting quantum circuits 718-719 (Nov. 30, 2017), pp. 1–102.

[89] P. Krantz, M. Kjaergaard, F. Yan, T. P. Orlando, S. Gustavsson, and W. D. Oliver. "A Quantum Engineer's Guide to Superconducting Qubits". *Applied Physics Reviews* 6.2 (June 2019), p. 021318.

[90] Rajeev Acharya et al. "Suppressing quantum errors by scaling a surface code logical qubit". *Nature* 614.7949 (Feb. 2023), pp. 676–681.

[91] Jens Koch, Terri M. Yu, Jay Gambetta, A. A. Houck, D. I. Schuster, J. Majer, Alexandre Blais, M. H. Devoret, S. M. Girvin, and R. J. Schoelkopf. "Charge insensitive qubit design derived from the Cooper pair box". *Physical Review A* 76.4 (Oct. 12, 2007), p. 042319.

[92] T. P. Orlando, J. E. Mooij, Lin Tian, Caspar H. van der Wal, L. S. Levitov, Seth Lloyd, and J. J. Mazo. "Superconducting persistent-current qubit". *Physical Review B* 60.22 (Dec. 1, 1999), pp. 15398–15413.

[93] J. E. Mooij, T. P. Orlando, L. Levitov, Lin Tian, Caspar H. van der Wal, and Seth Lloyd. "Josephson Persistent-Current Qubit". *Science* 285.5430 (Aug. 13, 1999), pp. 1036–1039.

[94] Fei Yan et al. "The Flux Qubit Revisited to Enhance Coherence and Reproducibility". *Nature Communications* 7.1 (Nov. 2016), p. 12964.

[95] Fei Yan, Youngkyu Sung, Philip Krantz, Archana Kamal, David K. Kim, Jonilyn L. Yoder, Terry P. Orlando, Simon Gustavsson, and William D. Oliver. *Engineering Framework for Optimizing Superconducting Qubit Designs*. June 7, 2020.

[96] András Gyenis, Agustin Di Paolo, Jens Koch, Alexandre Blais, Andrew A. Houck, and David I. Schuster. “Moving beyond the Transmon: Noise-Protected Superconducting Quantum Circuits”. *PRX Quantum* 2.3 (Sept. 2021), p. 030101.

[97] Matilda Peruzzo, Farid Hassani, Gregory Szep, Andrea Trioni, Elena Redchenko, Martin Žemlička, and Johannes M. Fink. “Geometric Superinductance Qubits: Controlling Phase Delocalization across a Single Josephson Junction”. *PRX Quantum* 2.4 (Nov. 24, 2021), p. 040341.

[98] N. Earnest et al. “Realization of a $\mathrm{\ensuremath{\Lambda}}$ System with Metastable States of a Capacitively Shunted Fluxonium”. *Physical Review Letters* 120.15 (Apr. 13, 2018), p. 150504.

[99] Long B Nguyen, Yen-Hsiang Lin, Aaron Somoroff, Raymond Mencia, Nicholas Grabon, and Vladimir E Manucharyan. “High-coherence fluxonium qubit”. *Phys. Rev. X* 9.4 (2019), p. 041041.

[100] Raymond A. Mencia, Wei-Ju Lin, Hyunheung Cho, Maxim G. Vavilov, and Vladimir E. Manucharyan. *Integer Fluxonium Qubit*. Mar. 25, 2024.

[101] Eric Hyyppä et al. “Reducing Leakage of Single-Qubit Gates for Superconducting Quantum Processors Using Analytical Control Pulse Envelopes”. *arXiv:2402.17757 [quant-ph]* (2024). preprint.

[102] Jared B. Hertzberg et al. “Laser-annealing Josephson junctions for yielding scaled-up superconducting quantum processors”. *npj Quantum Information* 7.1 (Aug. 19, 2021), pp. 1–8.

[103] Philip Krantz, Morten Kjaergaard, Fei Yan, Terry P. Orlando, Simon Gustavsson, and William D. Oliver. “A Quantum Engineer’s Guide to Superconducting Qubits”. *Applied Physics Reviews* 6.2 (June 2019), p. 021318.

[104] Jurgen Lisenfeld, Alexander Bilmes, Anthony Megrant, Rami Barends, Paul Klimov, Georg Weiss, John M Martinis, and Alexey V Ustinov. “Electric Field Spectroscopy of Material Defects in Transmon Qubits Supplementary Material”, p. 9.

[105] P. V. Klimov et al. “Fluctuations of Energy-Relaxation Times in Superconducting Qubits”. *Physical Review Letters* 121.9 (Aug. 31, 2018), p. 090502.

[106] Joseph A. Valery, Shoumik Chowdhury, Glenn Jones, and Nicolas Didier. “Dynamical Sweet Spot Engineering via Two-Tone Flux Modulation of Superconducting Qubits”. *PRX Quantum* 3.2 (May 18, 2022), p. 020337.

[107] Maxime Boissonneault, J. M. Gambetta, and Alexandre Blais. “Dispersive regime of circuit QED: Photon-dependent qubit dephasing and relaxation rates”. *Physical Review A* 79.1 (Jan. 23, 2009), p. 013819.

[108] Joe Rowland Adams, Julian Newman, and Aneta Stefanovska. “Distinguishing between deterministic oscillations and noise”. *The European Physical Journal Special Topics* 232.20 (Dec. 1, 2023), pp. 3435–3457.

[109] R. Hanbury Brown and R.Q. Twiss. “LXXIV. A new type of interferometer for use in radio astronomy”. *The London, Edinburgh, and Dublin Philosophical Magazine and Journal of Science* 45.366 (July 1, 1954), pp. 663–682.

[110] H. J. Kimble, M. Dagenais, and L. Mandel. “Photon Antibunching in Resonance Fluorescence”. *Physical Review Letters* 39.11 (Sept. 12, 1977), pp. 691–695.

[111] Gerson Goldhaber, William B. Fowler, Sulamith Goldhaber, T. F. Hoang, Theodore E. Kalogeropoulos, and Wilson M. Powell. “Pion-Pion Correlations in Antiproton Annihilation Events”. *Physical Review Letters* 3.4 (Aug. 15, 1959), pp. 181–183.

[112] William D. Oliver, Jungsang Kim, Robert C. Liu, and Yoshihisa Yamamoto. “Hanbury Brown and Twiss-Type Experiment with Electrons”. *Science* 284.5412 (Apr. 9, 1999), pp. 299–301.

[113] A. A. Penzias and R. W. Wilson. “A Measurement of Excess Antenna Temperature at 4080 Mc/s.” *The Astrophysical Journal* 142 (July 1, 1965), pp. 419–421.

[114] J. S. Bell. “On the Einstein Podolsky Rosen paradox”. *Physics Physique Fizika* 1.3 (Nov. 1, 1964), pp. 195–200.

[115] Xiao Yuan, Hongyi Zhou, Zhu Cao, and Xiongfeng Ma. “Intrinsic randomness as a measure of quantum coherence”. *Physical Review A* 92.2 (Aug. 27, 2015), p. 022124.

[116] John K. Hunter. *Lecture Notes on Applied Mathematics.* https://www.math.ucdavis.edu/~hunter/m280_09/ch.pdf. June 2009.

[117] Robert Brown. “XXVII. A brief account of microscopical observations made in the months of June, July and August 1827, on the particles contained in the pollen of plants; and on the general existence of active molecules in organic and inorganic bodies”. *The Philosophical Magazine* 4.21 (Sept. 1, 1828), pp. 161–173.

[118] L. Bachelier. “Théorie de la spéculation”. *Annales scientifiques de l’École normale supérieure* 17 (1900), pp. 21–86.

[119] M. von Smoluchowski. “Zur kinetischen Theorie der Brownschen Molekularbewegung und der Suspensionen”. *Annalen der Physik* 326.14 (1906), pp. 756–780.

[120] Anthony J. Leggett and Dervis C. Vural. ““Tunneling Two-Level Systems” Model of the Low-Temperature Properties of Glasses: Are “Smoking-Gun” Tests Possible?” *The Journal of Physical Chemistry B* 117.42 (Oct. 24, 2013), pp. 12966–12971.

[121] E. Paladino, Y. M. Galperin, G. Falci, and B. L. Altshuler. “1 / f Noise: Implications for Solid-State Quantum Information”. *Reviews of Modern Physics* 86.2 (Apr. 2014), pp. 361–418.

[122] Clemens Müller, Jared H Cole, and Jürgen Lisenfeld. “Towards Understanding Two-Level-Systems in Amorphous Solids: Insights from Quantum Circuits”. *Reports on Progress in Physics* 82.12 (Dec. 2019), p. 124501.

[123] Benoit B. Mandelbrot. *Multifractals and 1/f Noise*. New York, NY: Springer New York, 1999.

[124] Crispin Gardiner and Peter Zoller. *Quantum Noise: A Handbook of Markovian and Non-Markovian Quantum Stochastic Methods with Applications to Quantum Optics*. Springer Science & Business Media, Aug. 27, 2004.

[125] Marco Fanciulli, ed. *Electron Spin Resonance and Related Phenomena in Low-Dimensional Structures*. Red. by Claus E. Ascheron and Adelheid H. Duhm. Vol. 115. Topics in Applied Physics. Berlin, Heidelberg: Springer Berlin Heidelberg, 2009.

[126] A. A. Clerk, M. H. Devoret, S. M. Girvin, Florian Marquardt, and R. J. Schoelkopf. “Introduction to quantum noise, measurement, and amplification”. *Reviews of Modern Physics* 82.2 (Apr. 15, 2010), pp. 1155–1208.

[127] R. J. Schoelkopf, A. A. Clerk, S. M. Girvin, K. W. Lehnert, and M. H. Devoret. *Qubits as Spectrometers of Quantum Noise*. Oct. 10, 2002.

[128] F. Bloch. “Nuclear Induction”. *Physical Review* 70.7 (Oct. 1, 1946), pp. 460–474.

[129] A. G. Redfield. “On the Theory of Relaxation Processes”. *IBM Journal of Research and Development* 1.1 (1957), pp. 19–31.

[130] Łukasz Cywiński, Roman M. Lutchyn, Cody P. Nave, and S. Das Sarma. “How to Enhance Dephasing Time in Superconducting Qubits”. *Physical Review B* 77.17 (May 2008), p. 174509.

[131] J. L. Skinner and D. Hsu. “Pure dephasing of a two-level system”. *The Journal of Physical Chemistry* 90.21 (Oct. 1986), pp. 4931–4938.

[132] Fei Yan, Simon Gustavsson, Jonas Bylander, Xiaoyue Jin, Fumiki Yoshihara, David G. Cory, Yasunobu Nakamura, Terry P. Orlando, and William D. Oliver. “Rotating-Frame Relaxation as a Noise Spectrum Analyser of a Superconducting

Qubit Undergoing Driven Evolution". *Nature Communications* 4.1 (Aug. 2013), p. 2337.

[133] Norman F. Ramsey. "A Molecular Beam Resonance Method with Separated Oscillating Fields". *Physical Review* 78.6 (June 15, 1950), pp. 695–699.

[134] E. L. Hahn. "Spin Echoes". *Physical Review* 80.4 (Nov. 15, 1950), pp. 580–594.

[135] S. Meiboom and D. Gill. "Modified Spin-Echo Method for Measuring Nuclear Relaxation Times". *Review of Scientific Instruments* 29.8 (Aug. 1, 1958), pp. 688–691.

[136] Dolev Bluvstein, Zhiran Zhang, Claire A. McLellan, Nicolas R. Williams, and Ania C. Bleszynski Jayich. "Extending the Quantum Coherence of a Near-Surface Qubit by Coherently Driving the Paramagnetic Surface Environment". *Physical Review Letters* 123.14 (Oct. 2019), p. 146804.

[137] C. L. Degen, F. Reinhard, and P. Cappellaro. "Quantum Sensing". *Reviews of Modern Physics* 89.3 (July 2017), p. 035002.

[138] Arian Vezvaee, Nanako Shitara, Shuo Sun, and Andrés Montoya-Castillo. "Fourier transform noise spectroscopy". *npj Quantum Information* 10.1 (May 17, 2024), pp. 1–12.

[139] Fei Yan, Jonas Bylander, Simon Gustavsson, Fumiki Yoshihara, Khalil Harrabi, David G. Cory, Terry P. Orlando, Yasunobu Nakamura, Jaw-Shen Tsai, and William D. Oliver. "Spectroscopy of Low-Frequency Noise and Its Temperature Dependence in a Superconducting Qubit". *Physical Review B* 85.17 (May 2012), p. 174521.

[140] Antti Vepsäläinen et al. "Improving Qubit Coherence Using Closed-Loop Feedback". *arXiv:2105.01107 [quant-ph]* (May 2021).

[141] Alfred G. Redfield. "Nuclear Magnetic Resonance Saturation and Rotary Saturation in Solids". *Physical Review* 98.6 (June 15, 1955), pp. 1787–1809.

[142] C M Quintana et al. "Observation of Classical-Quantum Crossover of $1/f$ Flux Noise and Its Paramagnetic Temperature Dependence". *Physical Review Letters* 118.5 (2017), p. 057702.

[143] J. B. Johnson. "The Schottky Effect in Low Frequency Circuits". *Physical Review* 26.1 (July 1, 1925), pp. 71–85.

[144] Giovanni Bonanno, Fabrizio Lillo, and Rosario N. Mantegna. "1/f and 1/f2 noise in financial time series". In: *Noise in Physical Systems and 1/F Fluctuations*. WORLD SCIENTIFIC, Aug. 2001, pp. 791–796.

[145] Misako Takayasu and Hideki Takayasu. "1/f NOISE IN A TRAFFIC MODEL". *Fractals* 01.4 (Dec. 1993), pp. 860–866.

[146] I. Csabai. "1/f noise in computer network traffic". *Journal of Physics A: Mathematical and General* 27.12 (June 1994), p. L417.

[147] Michael D. Fox and Marcus E. Raichle. "Spontaneous fluctuations in brain activity observed with functional magnetic resonance imaging". *Nature Reviews Neuroscience* 8.9 (Sept. 2007), pp. 700–711.

[148] M. B. Weissman. "1 f noise and other slow, nonexponential kinetics in condensed matter". *Reviews of Modern Physics* 60.2 (Apr. 1, 1988), pp. 537–571.

[149] Benoit B. Mandelbrot and John W. Van Ness. "Fractional Brownian Motions, Fractional Noises and Applications". *SIAM Review* 10.4 (Oct. 1968), pp. 422–437.

[150] Richard F Voss. "Characterization and Measurement of Random Fractals". *Physica Scripta* T13 (Jan. 1, 1986), pp. 27–32.

[151] P. Dutta and P. M. Horn. "Low-frequency fluctuations in solids: $\frac{1}{f}$ noise". *Reviews of Modern Physics* 53.3 (July 1, 1981), pp. 497–516.

[152] Sh. Kogan. *Electronic Noise and Fluctuations in Solids*. Cambridge: Cambridge University Press, 1996.

[153] E. Paladino, Y. M. Galperin, G. Falci, and B. L. Altshuler. “$\mathbsf{1}/\mathbsfit{f}$ noise: Implications for solid-state quantum information”. *Reviews of Modern Physics* 86.2 (Apr. 3, 2014), pp. 361–418.

[154] W. Schottky. “Über spontane Stromschwankungen in verschiedenen Elektrizitätsleitern”. *Annalen der Physik* 362.23 (1918), pp. 541–567.

[155] C. A. Hartmann. “Über die Bestimmung des elektrischen Elementarquantums aus dem Schroteffekt”. *Annalen der Physik* 370.9 (1921), pp. 51–78.

[156] W. Schottky. “Small-Shot Effect and Flicker Effect”. *Physical Review* 28.1 (July 1, 1926), pp. 74–103.

[157] J. B. Johnson. “Thermal Agitation of Electricity in Conductors”. *Physical Review* 32.1 (July 1, 1928), pp. 97–109.

[158] H. Nyquist. “Thermal Agitation of Electric Charge in Conductors”. *Physical Review* 32.1 (July 1, 1928), pp. 110–113.

[159] A. Van Der Ziel. “On the noise spectra of semi-conductor noise and of flicker effect”. *Physica* 16.4 (Apr. 1, 1950), pp. 359–372.

[160] G. G. MacFarlane. “A theory of flicker noise in valves and impurity semi-conductors”. *Proceedings of the Physical Society* 59.3 (May 1947), p. 366.

[161] A. Van Der Ziel. “Flicker Noise in Electronic Devices”. In: *Advances in Electronics and Electron Physics*. Ed. by L. Marton and C. Marton. Vol. 49. Academic Press, Jan. 1, 1979, pp. 225–297.

[162] F. N. Hooge. “1/f noise”. *Physica B+C* 83.1 (May 1, 1976), pp. 14–23.

[163] Benoit B. Mandelbrot. *The Fractal Geometry of Nature*. Henry Holt and Company, 1983.

[164] T. Higuchi. “Relationship between the fractal dimension and the power law index for a time series: A numerical investigation”. *Physica D: Nonlinear Phenomena* 46.2 (Nov. 1, 1990), pp. 254–264.

[165] M. Moshrefi-Torbati and J. K. Hammond. “Physical and geometrical interpretation of fractional operators”. *Journal of the Franklin Institute* 335.6 (Aug. 1, 1998), pp. 1077–1086.

[166] M. J. Stephen. “Noise in percolating systems”. *Journal of Physics C: Solid State Physics* 11.24 (Dec. 1978), p. L965.

[167] R. Rammal. “Noise excess on fractals and percolating systems”. *Journal de Physique Lettres* 45.21 (1984), pp. 1007–1014.

[168] B. Fourcade and A.-M. S. Tremblay. “Diffusion noise of fractal networks and percolation clusters”. *Physical Review B* 34.11 (Dec. 1, 1986), pp. 7802–7812.

[169] G. A. Garfunkel and M. B. Weissman. “Noise scaling in continuum percolating films”. *Physical Review Letters* 55.3 (July 15, 1985), pp. 296–299.

[170] R. H. Koch, R. B. Laibowitz, E. I. Alessandrini, and J. M. Viggiano. “Resistivity-noise measurements in thin gold films near the percolation threshold”. *Physical Review B* 32.10 (Nov. 15, 1985), pp. 6932–6935.

[171] V S Dotsenko. “Fractal dynamics of spin glasses”. *Journal of Physics C: Solid State Physics* 18.32 (Nov. 20, 1985), pp. 6023–6031.

[172] Sh. M Kogan. “1f noise in spin glasses and in the disordered kinetic ising model”. *Solid State Communications* 38.11 (June 1, 1981), pp. 1015–1018.

[173] Bronislovas Kaulakys, Julius Ruseckas, Vygintas Gontis, and Miglius Alaburda. “Nonlinear stochastic models of 1/f noise and power-law distributions”. *Physica A: Statistical Mechanics and its Applications*. Fundamental Problems of Modern Statistical Mechanics 365.1 (June 1, 2006), pp. 217–221.

[174] Sveinung Erland and Priscilla E. Greenwood. “Constructing 1 / ω α noise from reversible Markov chains”. *Physical Review E* 76.3 (Sept. 12, 2007), p. 031114.

[175] Ming Li and Wei Zhao. “On 1 / f Noise”. *Mathematical Problems in Engineering* 2012 (2012), pp. 1–23.

[176] D. A. Bell. “A survey of 1/f noise in electrical conductors”. *Journal of Physics C: Solid State Physics* 13.24 (Aug. 1980), p. 4425.

[177] P. M. Chaikin and T. C. Lubensky. *Principles of Condensed Matter Physics*. Cambridge University Press, Sept. 28, 2000.

[178] Lara Faoro and Lev B. Ioffe. “Microscopic Origin of Low-Frequency Flux Noise in Josephson Circuits”. *Physical Review Letters* 100.22 (June 5, 2008), p. 227005.

[179] T. Lanting, M. H. Amin, A. J. Berkley, C. Rich, S.-F. Chen, S. LaForest, and Rogério de Sousa. “Evidence for temperature-dependent spin diffusion as a mechanism of intrinsic flux noise in SQUIDs”. *Physical Review B* 89.1 (Jan. 7, 2014), p. 014503.

[180] Ralph V. Chamberlin. “The Big World of Nanothermodynamics”. *Entropy* 17.1 (Jan. 2015), pp. 52–73.

[181] Ralph V. Chamberlin, Sumiyoshi Abe, Bryce F. Davis, Priscilla E. Greenwood, and Andrew S.H. Shevchuk. “Fluctuation theorems and 1/f noise from a simple matrix”. *The European Physical Journal B* 89.9 (Sept. 5, 2016), p. 185.

[182] E. Paladino, L. Faoro, G. Falci, and Rosario Fazio. “Decoherence and $1/\mathit{f}$ Noise in Josephson Qubits”. *Physical Review Letters* 88.22 (May 20, 2002), p. 228304.

[183] John M. Martinis, S. Nam, J. Aumentado, K. M. Lang, and C. Urbina. “Decoherence of a superconducting qubit due to bias noise”. *Physical Review B* 67.9 (Mar. 25, 2003), p. 094510.

[184] D. J. Van Harlingen, T. L. Robertson, B. L. T. Plourde, P. A. Reichardt, T. A. Crane, and John Clarke. “Decoherence in Josephson-junction qubits due to critical-current fluctuations”. *Physical Review B* 70.6 (Aug. 30, 2004), p. 064517.

[185] William D. Oliver and Paul B. Welander. “Materials in superconducting quantum bits”. *MRS Bulletin* 38.10 (Oct. 2013), pp. 816–825.

[186] Y. Nakamura, Yu. Pashkin, T. Yamamoto, and J. Tsai. “Charge Echo in a Cooper-Pair Box”. *Physical Review Letters* 88.4 (Jan. 2002), p. 047901.

[187] P. w. Anderson, B. I. Halperin, and c. M. Varma. “Anomalous low-temperature thermal properties of glasses and spin glasses”. *The Philosophical Magazine: A Journal of Theoretical Experimental and Applied Physics* 25.1 (Jan. 1, 1972), pp. 1–9.

[188] W. A. Phillips. “Tunneling states in amorphous solids”. *Journal of Low Temperature Physics* 7.3 (May 1, 1972), pp. 351–360.

[189] A. J. Leggett, S. Chakravarty, A. T. Dorsey, Matthew P. A. Fisher, Anupam Garg, and W. Zwerger. “Dynamics of the Dissipative Two-State System”. *Reviews of Modern Physics* 59.1 (Jan. 1987), pp. 1–85.

[190] G. Zimmerli, T. M. Eiles, R. L. Kautz, and John M. Martinis. “Noise in the Coulomb blockade electrometer”. *Applied Physics Letters* 61.2 (July 13, 1992), pp. 237–239.

[191] A. B. Zorin, F.-J. Ahlers, J. Niemeyer, T. Weimann, H. Wolf, V. A. Krupenin, and S. V. Lotkhov. “Background charge noise in metallic single-electron tunneling devices”. *Physical Review B* 53.20 (May 15, 1996), pp. 13682–13687.

[192] S. LaForest and Rogério de Sousa. “Flux-Vector Model of Spin Noise in Superconducting Circuits: Electron versus Nuclear Spins and Role of Phase Transition”. *Physical Review B* 92.5 (Aug. 2015), p. 054502.

[193] Trevis Atherton Crane. “Low -frequency 1/F noise: Low temperature measurements and effect on superconducting qubit dephasing”. PhD thesis. United States – Illinois: University of Illinois at Urbana-Champaign.

[194] José Alberto Nava Aquino and Rogério de Sousa. “Flux Noise in Disordered Spin Systems”. *Physical Review B* 106.14 (Oct. 2022), p. 144506.

[195] Morten Kjaergaard, Mollie E. Schwartz, Jochen Braumüller, Philip Krantz, Joel I.-J. Wang, Simon Gustavsson, and William D. Oliver. “Superconducting Qubits: Current State of Play”. *Annual Review of Condensed Matter Physics* 11.1 (2020), pp. 369–395.

[196] Jay M. Gambetta, Jerry M. Chow, and Matthias Steffen. “Building Logical Qubits in a Superconducting Quantum Computing System”. *npj Quantum Information* 3.1 (Jan. 2017), pp. 1–7.

[197] Irfan Siddiqi. “Engineering High-Coherence Superconducting Qubits”. *Nature Reviews Materials* 6.10 (Oct. 2021), pp. 875–891.

[198] Frederick C. Wellstood, Cristian Urbina, and John Clarke. “Low-frequency Noise in Dc Superconducting Quantum Interference Devices below 1 K”. *Applied Physics Letters* 50.12 (Mar. 1987), pp. 772–774.

[199] F. Yoshihara, K. Harrabi, A. O. Niskanen, Y. Nakamura, and J. S. Tsai. “Decoherence of Flux Qubits Due to 1/f Flux Noise”. *Physical Review Letters* 97.16 (Oct. 2006), p. 167001.

[200] Radoslaw C. Bialczak et al. “1 / f Flux Noise in Josephson Phase Qubits”. *Physical Review Letters* 99.18 (Nov. 2007), p. 187006.

[201] K. Kakuyanagi, T. Meno, S. Saito, H. Nakano, K. Semba, H. Takayanagi, F. Deppe, and A. Shnirman. “Dephasing of a Superconducting Flux Qubit”. *Physical Review Letters* 98.4 (Jan. 2007), p. 047004.

[202] Jens Koch, Terri M. Yu, Jay Gambetta, A. A. Houck, D. I. Schuster, J. Majer, Alexandre Blais, M. H. Devoret, S. M. Girvin, and R. J. Schoelkopf. “Charge Insensitive Qubit Design Derived from the Cooper Pair Box”. *Physical Review A* 76.4 (Oct. 2007), p. 042319.

[203] Trevor McCourt et al. *Learning Noise via Dynamical Decoupling of Entangled Qubits*. Jan. 2022.

[204] S E de Graaf, S Un, A G Shard, and T Lindström. “Chemical and Structural Identification of Material Defects in Superconducting Quantum Circuits”. *Materials for Quantum Technology* 2.3 (Sept. 2022), p. 032001.

[205] Bryce F. Davis and Ralph V. Chamberlin. “1/f noise from a finite entropy bath: comparison with flux noise in SQUIDs”. *Journal of Statistical Mechanics: Theory and Experiment* 2018.10 (Oct. 2018), p. 103206.

[206] Simon Gustavsson, Jonas Bylander, Fei Yan, William D. Oliver, Fumiki Yoshihara, and Yasunobu Nakamura. “Noise Correlations in a Flux Qubit with Tunable Tunnel Coupling”. *Physical Review B* 84.1 (July 2011), p. 014525.

[207] T. Lanting et al. “Geometrical Dependence of the Low-Frequency Noise in Superconducting Flux Qubits”. *Physical Review B* 79.6 (Feb. 2009), 060509(R).

[208] Jochen Braumüller et al. “Characterizing and Optimizing Qubit Coherence Based on SQUID Geometry”. *Physical Review Applied* 13.5 (May 2020), p. 054079.

[209] S. M. Anton et al. “Magnetic Flux Noise in Dc SQUIDs: Temperature and Geometry Dependence”. *Physical Review Letters* 110.14 (Apr. 2013), p. 147002.

[210] S. Sendelbach, D. Hover, M. Mück, and R. McDermott. “Complex Inductance, Excess Noise, and Surface Magnetism in Dc SQUIDs”. *Physical Review Letters* 103.11 (Sept. 2009), p. 117001.

[211] S. Sendelbach, D. Hover, A. Kittel, M. Mück, John M. Martinis, and R. McDermott. “Magnetism in SQUIDs at Millikelvin Temperatures”. *Physical Review Letters* 100.22 (June 2008), p. 227006.

[212] S. E. de Graaf, A. A. Adamyan, T. Lindström, D. Erts, S. E. Kubatkin, A. Ya. Tzalenchuk, and A. V. Danilov. “Direct Identification of Dilute Surface Spins on Al_2O_3: Origin of Flux Noise in Quantum Circuits”. *Physical Review Letters* 118.5 (Jan. 2017), p. 057703.

[213] Amrit De. “Ising-Glauber Spin Cluster Model for Temperature-Dependent Magnetization Noise in SQUIDs”. *Physical Review Letters* 113.21 (Nov. 2014), p. 217002.

[214] Amrit De. “1 / f Flux Noise in Low- T c SQUIDs Due to Superparamagnetic Phase Transitions in Defect Clusters”. *Physical Review B* 99.2 (Jan. 2019), p. 024305.

[215] S E de Graaf, L Faoro, J Burnett, A A Adamyan, A Ya Tzalenchuk, S E Kubatkin, T Lindström, and A V Danilov. “Suppression of Low-Frequency Charge Noise in Superconducting Resonators by Surface Spin Desorption”. *Nature Communications* 9.1 (2018), p. 1143.

[216] S. E. de Graaf, L. Faoro, L. B. Ioffe, S. Mahashabde, J. J. Burnett, T. Lindström, S. E. Kubatkin, A. V. Danilov, and A. Ya. Tzalenchuk. “Two-Level Systems in Superconducting Quantum Devices Due to Trapped Quasiparticles”. *Science Advances* 6.51 (Dec. 2020), eabc5055.

[217] C. Wang et al. “Measurement and Control of Quasiparticle Dynamics in a Superconducting Qubit”. *Nature Communications* 5.1 (Dec. 2014), p. 5836.

[218] Andre Schneider, Tim Wolz, Marco Pfirrmann, Martin Spiecker, Hannes Rotzinger, Alexey V. Ustinov, and Martin Weides. “Transmon Qubit in a Magnetic Field: Evolution of Coherence and Transition Frequency”. *Physical Review Research* 1.2 (Sept. 2019), p. 023003.

[219] F. Luthi et al. “Evolution of Nanowire Transmon Qubits and Their Coherence in a Magnetic Field”. *Physical Review Letters* 120.10 (Mar. 2018), p. 100502.

[220] Patrick Winkel, Kiril Borisov, Lukas Grünhaupt, Dennis Rieger, Martin Spiecker, Francesco Valenti, Alexey V. Ustinov, Wolfgang Wernsdorfer, and Ioan M. Pop. “Implementation of a Transmon Qubit Using Superconducting Granular Aluminum”. *Physical Review X* 10.3 (Aug. 2020), p. 031032.

[221] A. Kringhøj et al. “Magnetic-Field-Compatible Superconducting Transmon Qubit”. *Physical Review Applied* 15.5 (May 2021), p. 054001.

[222] J. Krause, C. Dickel, E. Vaal, M. Vielmetter, J. Feng, R. Bounds, G. Catelani, J. M. Fink, and Yoichi Ando. “Magnetic Field Resilience of Three-Dimensional Transmons with Thin-Film Al/$\mathrm{AlO_x}$/Al Josephson Junctions Approaching 1 T”. *Physical Review Applied* 17.3 (Mar. 2022), p. 034032.

[223] N. Samkharadze, A. Bruno, P. Scarlino, G. Zheng, D. P. DiVincenzo, L. DiCarlo, and L. M. K. Vandersypen. “High-Kinetic-Inductance Superconducting Nanowire Resonators for Circuit QED in a Magnetic Field”. *Physical Review Applied* 5.4 (Apr. 2016), p. 044004.

[224] S. E. de Graaf, A. Ya. Tzalenchuk, and T. Lindström. “1/f Frequency Noise of Superconducting Resonators in Large Magnetic Fields”. *Applied Physics Letters* 113.14 (Oct. 2018), p. 142601.

[225] K. Borisov et al. “Superconducting Granular Aluminum Resonators Resilient to Magnetic Fields up to 1 Tesla”. *Applied Physics Letters* 117.12 (Sept. 2020), p. 120502.

[226] D. Ristè, C. C. Bultink, M. J. Tiggelman, R. N. Schouten, K. W. Lehnert, and L. DiCarlo. “Millisecond Charge-Parity Fluctuations and Induced Decoherence in a Superconducting Transmon Qubit”. *Nature Communications* 4.1 (May 2013), p. 1913.

[227] I. Nsanzineza and B. L. T. Plourde. “Trapping a Single Vortex and Reducing Quasiparticles in a Superconducting Resonator”. *Physical Review Letters* 113.11 (Sept. 2014), p. 117002.

[228] Rogelio Díaz-Méndez and Roberto Mulet. “H - T Phase Diagram of the Two-Dimensional Ising Model with Exchange and Dipolar Interactions”. *Physical Review B* 81.18 (May 2010), p. 184420.

[229] G. P. Berman, B. M. Chernobrod, V. N. Gorshkov, and V. I. Tsifrinovich. “Spin Diffusion and Relaxation in a Nonuniform Magnetic Field”. *Physical Review B* 71.18 (May 2005), p. 184409.

[230] Alexei M. Tyryshkin et al. “Electron Spin Coherence Exceeding Seconds in High-Purity Silicon”. *Nature Materials* 11.2 (Feb. 2012), pp. 143–147.

[231] N. Bloembergen. “On the Interaction of Nuclear Spins in a Crystalline Lattice”. *Physica* 15.3 (May 1949), pp. 386–426.

[232] José Alberto Nava Aquino and Rogério de Sousa. “Model for 1/f flux noise in superconducting aluminum devices: Impact of external magnetic fields”. *Applied Physics Letters* 122.22 (June 1, 2023), p. 224003.

[233] David P. DiVincenzo. “The Physical Implementation of Quantum Computation”. *Fortschritte der Physik* 48.9-11 (2000), pp. 771–783.

[234] Rami Barends, Julian Kelly, Anthony Megrant, Andrzej Veitia, Daniel Sank, Evan Jeffrey, Ted C White, Josh Mutus, Austin G Fowler, Brooks Campbell, et al. “Superconducting quantum circuits at the surface code threshold for fault tolerance”. *Nature* 508.7497 (2014), pp. 500–503.

[235] Frank Arute, Kunal Arya, Ryan Babbush, Dave Bacon, Joseph C Bardin, Rami Barends, Rupak Biswas, Sergio Boixo, Fernando GSL Brandao, David A Buell, et al. “Quantum supremacy using a programmable superconducting processor”. *Nature* 574.7779 (2019), pp. 505–510.

[236] Rajeev Acharya, Igor Aleiner, Richard Allen, Trond I Andersen, Markus Ansmann, Frank Arute, Kunal Arya, Abraham Asfaw, Juan Atalaya, Ryan Babbush, et al. "Suppressing quantum errors by scaling a surface code logical qubit". *Nature* 614.7949 (2023), pp. 676–681.

[237] Austin G. Fowler, Matteo Mariantoni, John M. Martinis, and Andrew N. Cleland. "Surface codes: Towards practical large-scale quantum computation". *Phys. Rev. A* 86.3 (Sept. 2012), p. 032324.

[238] Dolev Bluvstein et al. "Logical quantum processor based on reconfigurable atom arrays". *Nature* 626 (Dec. 2023), pp. 58–65.

[239] Daoquan Zhu, Tuomas Jaako, Qiongyi He, and Peter Rabl. "Quantum Computing with Superconducting Circuits in the Picosecond Regime". *Phys. Rev. Appl.* 16 (1 July 2021), p. 014024.

[240] J. A. Schreier et al. "Suppressing charge noise decoherence in superconducting charge qubits". *Phys. Rev. B* 77 (18 May 2008), p. 180502.

[241] Zijun Chen et al. "Measuring and Suppressing Quantum State Leakage in a Superconducting Qubit". *Phys. Rev. Lett.* 116.2 (Jan. 2016), p. 020501.

[242] G. D. Fuchs, V. V. Dobrovitski, D. M. Toyli, F. J. Heremans, and D. D. Awschalom. "Gigahertz Dynamics of a Strongly Driven Single Quantum Spin". *Science* 326.5959 (2009), pp. 1520–1522.

[243] C. Avinadav, R. Fischer, P. London, and D. Gershoni. "Time-optimal universal control of two-level systems under strong driving". *Phys. Rev. B* 89 (24 June 2014), p. 245311.

[244] Chunqing Deng, Jean-Luc Orgiazzi, Feiruo Shen, Sahel Ashhab, and Adrian Lupascu. "Observation of Floquet States in a Strongly Driven Artificial Atom". *Phys. Rev. Lett.* 115 (13 Sept. 2015), p. 133601.

[245] Daniel Burgarth, Paolo Facchi, Giovanni Gramegna, and Kazuya Yuasa. “One Bound to Rule Them All: From Adiabatic to Zeno”. *Quantum* 6 (June 2022), p. 737.

[246] D. Vion, A. Aassime, A. Cottet, P. Joyez, H. Pothier, C. Urbina, D. Esteve, and M. H. Devoret. “Manipulating the Quantum State of an Electrical Circuit”. *Science* 296.5569 (2002), pp. 886–889.

[247] JE Mooij, TP Orlando, L Levitov, Lin Tian, Caspar H Van der Wal, and Seth Lloyd. “Josephson persistent-current qubit”. *Science* 285.5430 (1999), pp. 1036–1039.

[248] T. P. Orlando, J. E. Mooij, Lin Tian, Caspar H. van der Wal, L. S. Levitov, Seth Lloyd, and J. J. Mazo. “Superconducting persistent-current qubit”. *Phys. Rev. B* 60 (22 Dec. 1999), pp. 15398–15413.

[249] Jonathan R. Friedman, Vijay Patel, W. Chen, S. K. Tolpygo, and J. E. Lukens. “Quantum Superposition of Distinct Macroscopic States”. *Nature* 406.6791 (July 2000), pp. 43–46.

[250] Caspar H. van der Wal, A. C. J. ter Haar, F. K. Wilhelm, R. N. Schouten, C. J. P. M. Harmans, T. P. Orlando, Seth Lloyd, and J. E. Mooij. “Quantum Superposition of Macroscopic Persistent-Current States”. *Science* 290.5492 (2000), pp. 773–777.

[251] Fei Yan, Simon Gustavsson, Archana Kamal, Jeffrey Birenbaum, Adam P Sears, David Hover, Ted J Gudmundsen, Danna Rosenberg, Gabriel Samach, Steven Weber, et al. “The flux qubit revisited to enhance coherence and reproducibility”. *Nat. Commun.* 7.1 (2016), pp. 1–9.

[252] M.A. Yurtalan, J. Shi, G.J.K. Flatt, and A. Lupascu. “Characterization of Multilevel Dynamics and Decoherence in a High-Anharmonicity Capacitively Shunted Flux Circuit”. *Phys. Rev. Appl.* 16 (5 Nov. 2021), p. 054051.

[253] Ioan M Pop, Kurtis Geerlings, Gianluigi Catelani, Robert J Schoelkopf, Leonid I Glazman, and Michel H Devoret. "Coherent suppression of electromagnetic dissipation due to superconducting quasiparticles." *Nature* 508.7496 (2014), pp. 369–72.

[254] Aaron Somoroff, Quentin Ficheux, Raymond A. Mencia, Haonan Xiong, Roman Kuzmin, and Vladimir E. Manucharyan. "Millisecond Coherence in a Superconducting Qubit". *Phys. Rev. Lett.* 130 (26 June 2023), p. 267001.

[255] Leon Ding et al. "High-Fidelity, Frequency-Flexible Two-Qubit Fluxonium Gates with a Transmon Coupler". *Phys. Rev. X* 13 (3 Sept. 2023), p. 031035.

[256] Helin Zhang et al. "Tunable Inductive Coupler for High-Fidelity Gates Between Fluxonium Qubits". *PRX Quantum* 5 (2 May 2024), p. 020326.

[257] P. London, P. Balasubramanian, B. Naydenov, L. P. McGuinness, and F. Jelezko. "Strong driving of a single spin using arbitrarily polarized fields". *Phys. Rev. A* 90 (1 July 2014), p. 012302.

[258] Arne Laucht et al. "Breaking the rotating wave approximation for a strongly driven dressed single-electron spin". *Phys. Rev. B* 94 (16 Oct. 2016), p. 161302.

[259] Xinyuan You, James A Sauls, and Jens Koch. "Circuit quantization in the presence of time-dependent external flux". *Phys. Rev. B* 99.17 (2019), p. 174512.

[260] Jacob Bryon, DK Weiss, Xinyuan You, Sara Sussman, Xanthe Croot, Ziwen Huang, Jens Koch, and Andrew A Houck. "Time-Dependent Magnetic Flux in Devices for Circuit Quantum Electrodynamics". *Phys. Rev. Appl.* 19.3 (2023), p. 034031.

[261] Thomas Brabec and Ferenc Krausz. "Intense Few-Cycle Laser Fields: Frontiers of Nonlinear Optics". *Rev. Mod. Phys.* 72.2 (Apr. 2000), pp. 545–591.

[262] A. Baltuška et al. "Attosecond Control of Electronic Processes by Intense Light Fields". *Nature* 421.6923 (Feb. 2003), pp. 611–615.

[263] Daniel L. Campbell et al. "Universal Nonadiabatic Control of Small-Gap Superconducting Qubits". *Phys. Rev. X* 10 (4 Dec. 2020), p. 041051.

[264] Ilya N Moskalenko, Ilya A Simakov, Nikolay N Abramov, Dmitry O Moskalev, Anastasiya A Pishchimova, Nikita S Smirnov, Evgeniy V Zikiy, Ilya A Rodionov, and Ilya S Besedin. "High fidelity two-qubit gates on fluxoniums using a tunable coupler". *npj Quantum Information* 8.1 (2022).

[265] David C McKay, Christopher J Wood, Sarah Sheldon, Jerry M Chow, and Jay M Gambetta. "Efficient Z gates for quantum computing". *Phys. Rev. A* 96.2 (2017), p. 022330.

[266] Easwar Magesan, Jay M Gambetta, and Joseph Emerson. "Scalable and robust randomized benchmarking of quantum processes". *Phys. Rev. Lett.* 106.18 (2011), p. 180504.

[267] Easwar Magesan et al. "Efficient Measurement of Quantum Gate Error by Interleaved Randomized Benchmarking". *Phys. Rev. Lett.* 109 (8 Aug. 2012), p. 080505.

[268] Joel Wallman, Chris Granade, Robin Harper, and Steven T. Flammia. "Estimating the Coherence of Noise". *New Journal of Physics* 17.11 (Nov. 2015), p. 113020.

[269] Guanru Feng, Joel J. Wallman, Brandon Buonacorsi, Franklin H. Cho, Daniel K. Park, Tao Xin, Dawei Lu, Jonathan Baugh, and Raymond Laflamme. "Estimating the Coherence of Noise in Quantum Control of a Solid-State Qubit". *Phys. Rev. Lett.* 117.26 (Dec. 20, 2016), p. 260501.

[270] D.K. Weiss, Helin Zhang, Chunyang Ding, Yuwei Ma, David I. Schuster, and Jens Koch. "Fast High-Fidelity Gates for Galvanically-Coupled Fluxonium Qubits Using Strong Flux Modulation". *PRX Quantum* 3 (4 Dec. 2022), p. 040336.

[271] N. Earnest et al. "Realization of a Λ System with Metastable States of a Capacitively Shunted Fluxonium". *Phys. Rev. Lett.* 120 (15 Apr. 2018), p. 150504.

[272] Quentin Ficheux, Long B Nguyen, Aaron Somoroff, Haonan Xiong, Konstantin N Nesterov, Maxim G Vavilov, and Vladimir E Manucharyan. "Fast logic with slow qubits: microwave-activated controlled-Z gate on low-frequency fluxoniums". *Phys. Rev. X* 11.2 (2021), p. 021026.

[273] Ebru Dogan, Dario Rosenstock, Loıck Le Guevel, Haonan Xiong, Raymond A. Mencia, Aaron Somoroff, Konstantin N. Nesterov, Maxim G. Vavilov, Vladimir E. Manucharyan, and Chen Wang. "Two-Fluxonium Cross-Resonance Gate". *Phys. Rev. Appl.* 20 (2 Aug. 2023), p. 024011.

[274] Konstantin N. Nesterov, Quentin Ficheux, Vladimir E. Manucharyan, and Maxim G. Vavilov. "Proposal for Entangling Gates on Fluxonium Qubits via a Two-Photon Transition". *PRX Quantum* 2 (2 June 2021), p. 020345.

[275] Daniel Sank, Mostafa Khezri, Sergei Isakov, and Juan Atalaya. "Balanced Coupling in Electromagnetic Circuits". *Private Communication* (2024).

[276] C. L. Degen, F. Reinhard, and P. Cappellaro. "Quantum Sensing". *Reviews of Modern Physics* 89.3 (July 2017), p. 035002.

[277] R. K. Wangsness and F. Bloch. "The Dynamical Theory of Nuclear Induction". *Physical Review* 89.4 (Feb. 1953), pp. 728–739.

[278] Heinz-Peter Breuer and Francesco Petruccione. *The Theory of Open Quantum Systems.* Oxford University Press, 2002.

[279] Jonas Bylander, Simon Gustavsson, Fei Yan, Fumiki Yoshihara, Khalil Harrabi, George Fitch, David G Cory, Yasunobu Nakamura, Jaw-Shen Tsai, and William D Oliver. "Noise spectroscopy through dynamical decoupling with a superconducting flux qubit". *Nature Physics* 7.7 (2011), pp. 565–570.

[280] Fei Yan, Jonas Bylander, Simon Gustavsson, Fumiki Yoshihara, Khalil Harrabi, David G. Cory, Terry P. Orlando, Yasunobu Nakamura, Jaw-Shen Tsai, and William D. Oliver. "Spectroscopy of Low-Frequency Noise and Its Temperature

Dependence in a Superconducting Qubit". *Physical Review B* 85.17 (May 2012), p. 174521.

[281] William Clarke Smith. "Design of protected superconducting qubits". PhD thesis. Yale University, 2019.

[282] Youngkyu Sung et al. "Non-Gaussian Noise Spectroscopy with a Superconducting Qubit Sensor". *Nature Communications* 10.1 (Sept. 2019), p. 3715.

[283] Charles P. Slichter. *Principles of Magnetic Resonance.* Ed. by Manuel Cardona, Peter Fulde, Klaus von Klitzing, Hans-Joachim Queisser, and Helmut K. V. Lotsch. Vol. 1. Springer Series in Solid-State Sciences. Berlin, Heidelberg: Springer Berlin Heidelberg, 1990.

[284] Yujun Choi and Robert Joynt. "Anisotropy with Respect to the Applied Magnetic Field of Spin Qubit Decoherence Times". *npj Quantum Information* 8.1 (June 2022), pp. 1–9.

[285] Hong-Bin Chen. "Effects of Symmetry Breaking of the Structurally-Disordered Hamiltonian Ensembles on the Anisotropic Decoherence of Qubits". *Scientific Reports* 12.1 (Feb. 2022), p. 2869.

[286] Ke Sun, Mingyu Kang, Hanggai Nuomin, George Schwartz, David N. Beratan, Kenneth R. Brown, and Jungsang Kim. "Quantum Simulation of Spin-Boson Models with Structured Bath". *arXiv:2405.14624 [quant-ph]* (June 2024).

[287] C. W. Gardiner. "Inhibition of Atomic Phase Decays by Squeezed Light: A Direct Effect of Squeezing". *Physical Review Letters* 56.18 (May 1986), pp. 1917–1920.

[288] K. W. Murch, S. J. Weber, K. M. Beck, E. Ginossar, and I. Siddiqi. "Reduction of the radiative decay of atomic coherence in squeezed vacuum". *Nature* 499.7456 (July 2013), pp. 62–65.

[289] D. M. Toyli, A. W. Eddins, S. Boutin, S. Puri, D. Hover, V. Bolkhovsky, W. D. Oliver, A. Blais, and I. Siddiqi. "Resonance Fluorescence from an Artificial Atom in Squeezed Vacuum". *Physical Review X* 6.3 (July 2016), p. 031004.

[290] H.S. Zeng, N. Tang, Y.P. Zheng, and T.T. Xu. "Non-Markovian Dynamics for an Open Two-Level System without Rotating Wave Approximation: Indivisibility versus Backflow of Information". *The European Physical Journal D* 66.10 (Oct. 2012), p. 255.

[291] H. Mäkelä and M. Möttönen. "Effects of the Rotating-Wave and Secular Approximations on Non-Markovianity". *Physical Review A* 88.5 (Nov. 2013), p. 052111.

[292] N. W. Hendrickx, L. Massai, M. Mergenthaler, F. J. Schupp, S. Paredes, S. W. Bedell, G. Salis, and A. Fuhrer. "Sweet-Spot Operation of a Germanium Hole Spin Qubit with Highly Anisotropic Noise Sensitivity". *Nature Materials* 23.7 (July 2024), pp. 920–927.

[293] Aashish A Clerk, Michel H Devoret, Steven M Girvin, Florian Marquardt, and Robert J Schoelkopf. "Introduction to quantum noise, measurement, and amplification". *Reviews of Modern Physics* 82.2 (2010), pp. 1155–1208.

[294] Clemens Gneiting, Felix R. Anger, and Andreas Buchleitner. "Incoherent Ensemble Dynamics in Disordered Systems". *Physical Review A* 93.3 (Mar. 2016), p. 032139.

[295] Clemens Gneiting. "Disorder-Dressed Quantum Evolution". *Physical Review B* 101.21 (June 2020), p. 214203.

[296] Ulrik L. Andersen, Tobias Gehring, Christoph Marquardt, and Gerd Leuchs. "30 Years of Squeezed Light Generation". *Physica Scripta* 91.5 (Apr. 2016), p. 053001.

[297] Jack Y. Qiu et al. "Broadband Squeezed Microwaves and Amplification with a Josephson Travelling-Wave Parametric Amplifier". *Nature Physics* 19.5 (May 2023), pp. 706–713.

[298] Goran Lindblad. “On the Generators of Quantum Dynamical Semigroups”. *Communications in Mathematical Physics* 48 (1976), p. 119.

[299] Vittorio Gorini, Andrzej Kossakowski, and E. C. G. Sudarshan. “Completely Positive Dynamical Semigroups of N Level Systems”. *Journal of Mathematical Physics* 17 (1976), p. 821.

[300] John Preskill. *Lecture Notes for Physics 229: Quantum Information and Computation*. https://web.gps.caltech.edu/~rls/book.pdf. Sept. 1998.

[301] M. Ko źbiał, L. Elson, L. M. Rushton, A. Akbar, A. Meraki, K. Jensen, and J. Kołody ński. “Spin noise spectroscopy of an alignment-based atomic magnetometer”. *Physical Review A* 110 (1 July 2024), p. 013125.

[302] Clemens Müller, Jared H. Cole, and Jürgen Lisenfeld. “Towards Understanding Two-Level-Systems in Amorphous Solids: Insights from Quantum Circuits”. *Reports on Progress in Physics* 82.12 (Oct. 2019), p. 124501.

[303] Hantao Sun et al. “Characterization of Loss Mechanisms in a Fluxonium Qubit”. *Physical Review Applied* 20.3 (Sept. 2023), p. 034016.

[304] Lamia Ateshian. “Temperature and Magnetic-Field Dependence of Relaxation in a Fluxonium Qubit”. *In Preparation* (2024).

[305] O. Astafiev, Yu. Pashkin, Y. Nakamura, T. Yamamoto, and J. Tsai. “Quantum Noise in the Josephson Charge Qubit”. *Physical Review Letters* 93.26 (Dec. 2004), p. 267007.

[306] C. M. Quintana et al. “Observation of Classical-Quantum Crossover of $1/f$ Flux Noise and Its Paramagnetic Temperature Dependence”. *Physical Review Letters* 118.5 (Jan. 2017), p. 057702.

[307] A. D. Leu, M. F. Gely, M. A. Weber, M. C. Smith, D. P. Nadlinger, and D. M. Lucas. “Fast, High-Fidelity Addressed Single-Qubit Gates Using Efficient Composite Pulse Sequences”. *Physical Review Letters* 131.12 (Sept. 2023), p. 120601.

[308] Daniel L. Campbell, Yun-Pil Shim, Bharath Kannan, Roni Winik, Alexander Melville, Bethany M. Niedzielski, Jonilyn L. Yoder, Charles Tahan, Simon Gustavsson, and William D. Oliver. “Universal Non-Adiabatic Control of Small-Gap Superconducting Qubits”. *Physical Review X* 10.4 (Dec. 2020), p. 041051.

[309] H. Levine et al. “Demonstrating a Long-Coherence Dual-Rail Erasure Qubit Using Tunable Transmons”. *Physical Review X* 14.1 (Mar. 2024), p. 011051.

[310] Matthew Reagor et al. “Demonstration of Universal Parametric Entangling Gates on a Multi-Qubit Lattice”. *Science Advances* 4.2 (Feb. 2018), eaao3603.

[311] Florian N. M. Froning, Leon C. Camenzind, Orson A. H. van der Molen, Ang Li, Erik P. A. M. Bakkers, Dominik M. Zumbühl, and Floris R. Braakman. “Ultrafast Hole Spin Qubit with Gate-Tunable Spin–Orbit Switch Functionality”. *Nature Nanotechnology* 16.3 (Mar. 2021), pp. 308–312.

[312] Ke Wang et al. “Ultrafast Coherent Control of a Hole Spin Qubit in a Germanium Quantum Dot”. *Nature Communications* 13.1 (Jan. 2022), p. 206.

[313] W. I. L. Lawrie, M. Rimbach-Russ, F. van Riggelen, N. W. Hendrickx, S. L. de Snoo, A. Sammak, G. Scappucci, J. Helsen, and M. Veldhorst. “Simultaneous Single-Qubit Driving of Semiconductor Spin Qubits at the Fault-Tolerant Threshold”. *Nature Communications* 14.1 (June 2023), p. 3617.

[314] B.-L. Najera-Santos et al. “High-Sensitivity Ac-Charge Detection with a MHz-Frequency Fluxonium Qubit”. *Physical Review X* 14.1 (Jan. 2024), p. 011007.